ELECTRIC VEHICLE (EV) WIRELESS CHARGERS: DESIGN AND OPTIMIZATION

ELECTRIC VEHICLE (EV) WIRELESS CHARGERS: DESIGN AND OPTIMIZATION

BY

ALI RAMEZANI

A THRSIS

SUBMITTED TO THE DEPARTMENT OF ELECTRICAL & COMPUTER ENGINEERING

AND THE SCHOOL OF GRADUATE STUDIES

OF MCMASTER UNIVERSITY

INPARTIAL FULFILMENT OF THE REQUIREMENTS

FOR THE DEGREE OF

Doctor Of Philosophy

Docror of Philosophy (2021) McMaster University

(Electrical & Computer Engineering) Hamilton, Ontario, Canada

TITLE:	Electric Vehicle (EV) Wireless Chargers: Design And Optimization
AUTHOR:	Ali Ramezani
	M.Sc., (Power Electronics)
	University of Tehran, Tehran, Iran
SUPERVISOR:	Dr. Mehdi Narimani
NUMBER OF PAGES:	XXVI, 298

To My Family

Abstract

Wireless charging of the EVs offers a convenient, reliable, and automatic charging of the autonomous vehicles without user interference. The focus of this thesis is the design and optimization of new structures for stationary EV wireless charging applications.

The fundamentals of the Wireless Power Transfer (WPT) system and its main components including the magnetic couplers, transmitter and receiver power converters, and control methods are studied in depth. The requirements of the EV wireless charging application and design criteria are discussed in detail. The advantages and disadvantages of each topology are highlighted, and possible candidates for EV wireless charging applications are selected.

Optimization of the resonant networks in terms of maximum efficiency and misalignment tolerance is studied. Different resonant topologies are studied in detail and their sensitivity functions are extracted. For each topology, an efficiency model is presented that includes the inverter, resonant capacitors, resonant inductor, diode-bridge, and core and conduction losses. Each topology is optimized with two different objective functions and the results are compared through the simulation and experiments. According to the optimization results, suitable topologies for the EV wireless charging application are selected.

In order to increase the power density of the wireless charging system, and save ferrite material, integrated inductors into the magnetic couplers are proposed. In this structure,

the DC-DC inductor is integrated into the receiver main coil and the resonant inductor is integrated into the transmitter coil. This integration introduces new challenges to the design of the resonant network and magnetic coupler due to the unwanted cross-coupling effect. To address this issue, the fully-integrated magnetic structure is optimally designed to have minimum cross-coupling. Moreover, the resonant network is designed based on an optimization problem that includes the cross-coupling into the system equations to ensure maximum efficiency. The proposed fully-integrated magnetic structure is built and experimental tests are presented to validate the performance of the proposed magnetic structure and its optimization method.

To reduce the implementation cost, size and weight a PCB-based magnetic coupler is proposed to replace the Litz wire in the magnetic coupler of the WPT system. Moreover, the proposed PCB-magnetic coupler increases the repeatability of the design and reduces manufacturing errors. The PCB-based magnetic coupler is studied through Finite Element Analysis (FEA) to minimize the AC resistance of the coil. Different parameters such including the number of the PCB layers, copper cross-section, and layer thickness are studied in detail to evaluate their effect on the coil resistance. Thermal analysis is performed to ensure the feasibility of the design under different loading conditions. A 3.3 kW/85 kHz wireless charging system is built and experimental tests are presented.

A novel modular resonant topology for fast wireless charging is proposed. A modular structure offers reliability, scalability, and better thermal management. The proposed topology is made by multi-parallel inverter legs connected to an LCC resonant network. The outputs of the resonant networks are connected in parallel to feed the transmitter coil with a high excitation current. The proposed modular system is compared with a conventional system and it showed superior performance in different aspects.

Acknowledgments

I would like to express my gratitude to my supervisor Dr. Mehdi Narimani for his endless encouragement, support, and guidance throughout my Ph.D. study. His inspirational leadership and motivation helped me to reach my goals in graduate studies. Also, I would like to thank Dr. Ali Emadi and Dr. Jennifer Bauman for their insightful comments and guidance of my research as my supervisory committee members.

I would like to thank the High Power Electronics Lab (HiPEL) team at McMaster University. It was an honor for me to be a part of this wonderful team. The technical discussions and debates helped me to expand my knowledge of power electronics.

This research was supported by Natural Sciences and Engineering Research Council (NSERC) of Canada. I gratefully acknowledge ANSYS for their support with Maxwell, and CMC Microsystems for their support with Altium Designer software.

Finally, I would express my deepest love and gratitude to my family and friends who supported me through the ups and downs of my life. I will be forever grateful to my parents and my brother who never stopped encouraging me.

Contents

List of Figures

List of Tables

Notation

Abbreviations

2D	Two-Dimensional
3D	Three-Dimensional
AC	Alternating Current
BARON	Branch-And-Reduced Optimization Navigation
CC	Constant Current
CP	Constant Power
CV	Constant Voltage
DC	Direct Current
DD	Double-D
DSMC	Discrete Sliding Mode Control
EMI	Electro-Magnetic Interference
ESR	Equivalent Series Resistance

EV	Electric Vehicle
FEA	Finite Element Analysis
FHA	Fundamental Harmonic Analysis
GA	Genetic Algorithm
IB	Integration into a Bipolar
ICT	Intercell Transformers
IU	Integration into a Unipolar
KVL	Kirchhoff's Voltage Law
LCT	Loosely Coupled Transformer
MFP	Metalized Film Propylene
PCB	Printed Circuit Board
PFC	Power Factor Correction
PID	Proportional Integral Derivative
PSO	Particle Swarm Optimization
PWM	Pulse Width Modulation
RMS	Root Mean Square
SAE	Society of Automotive Engineering
SCC	Switched Controlled Capacitor
SOC	State Of Charge
SRF	Self-Resonance Frequency
TWAE	Time-Weighted Average Efficiency

V2G	Vehicle to Grid
VA	Voltampere
WPT	Wireless Power Transfer
ZCS	Zero Current Switching
ZPA	Zero Phase Angle
ZVS	Zero Voltage Switching

Symbols

$C_1{}^{max}$	Maximum value of the primary side LCC capacitor
C_{1s}	Primary side series capacitor
$C_{1s}{}^{max}$	Maximum value of the primary side series capacitor
$C_2{}^{max}$	Maximum value of the secondary side LCC capacitor
C_{2s}	Secondary side series capacitor
$C_{2s}{}^{max}$	Maximum value of the secondary side series capacitor
C_f	Primary side parallel capacitor of the LCC network
D	DC-DC converter duty cycle
D_{in}	Inverter duty cycle
D_s	Strand diameter of Litz wire
D_w	Litz wire outer diameter
E_{Cp}	Total energy of the resonant capacitors
E_{Lp}	Total energy of the resonant inductor

f	Operating frequency
f_b	Buck converter switching frequency
f_o	Resonant frequency
f_{sw}	Inverter switching frequency
G_v	Voltage gain
I_b	DC-DC inductor current
I_{bat}	Battery current
I_{d_ave}	Diode bridge average current
I_{d_rms}	Diode bridge RMS current
I_{diode_ave}	Average current of the anti-parallel diode of the switch
I_{diode_rms}	RMS current of the anti-parallel diode of the switch
I_{in}	Inverter output current
I_{Load}	Load current
I_{mosfet}	Turn-on value of the current flows in the Mosfet
I_{mosfet_rms}	Mosfet RMS current
I_o	Output current
I_p	Primary side coil current
I_p^{max}	Maximum current of the primary side coil
I_s	Secondary side coil current
I_s^{max}	Maximum current of the secondary side coil
J_w	Desired current density

k	Coupling factor
k_f	Litz wire filling factor
K_n	Set of the nominal coupling factors
k_{pb}	Coupling factor between primary side coil and DC-DC inductor
k_{pf}	Coupling factor between primary side coil and resonant inductor
k_{ps}	Coupling factor between primary and secondary sides
k_{sb}	Coupling factor between secondary side coil and DC-DC inductor
k_{sf}	Coupling factor between secondary side coil and resonant inductor
$L_1{}^{max}$	Maximum value of the primary side LCC inductor
$L_2{}^{max}$	Maximum value of the secondary side LCC inductor
L_b	DC-DC inductor self-inductance
L_f	Resonant inductor of the primary side
L_p	Primary side self-inductance
L_s	Secondary side self-inductance
M	Mutual inductance
$M_{parasitic}$	Total cross coupling
n	Number of the modules
N_b	DC-DC inductor number of turns
N_{br}	Number of parallel branches
N_f	Resonant inductor number of turns
N_p	Primary side coil number of turns

N_p	Primary side number of turns
N_s	Secondary side coil number of turns
n_s	Number of the Litz wire strands
N_s	Secondary side number of turns
P_{bridge}	Diode bridge loss
P_{cap}	Capacitor loss
P_{cond_coup}	Magnetic coupler conduction loss
P_{core_coup}	Magnetic coupler core loss
$P_{coupler}$	Magnetic coupler losses
P_{diode}	Total loss of the antiparallel diodes
P_{in}	Input power
P_{inv}	Total loss of the inverter
P_L	Resonant inductor total loss
P_{L_cond}	Resonant inductor conduction loss
P_{L_core}	Resonant inductor core loss
P_{max}	Maximum power
P_{mosfet}	Total loss of the Mosfet switches
P_n	Set of the nominal output powers
P_{out}	Output power
$P^p{}_{cond}$	Primary side magnetic coupler conduction loss
$P^s{}_{cond}$	Secondary side magnetic coupler conduction loss

Q	Quality factor
Q_p	Primary side coil quality factor
Q_s	Secondary side coil quality factor
r_b	DC-DC inductor AC resistance
R_{d_bridge}	Equivalent series resistance of the diode bridge
R_{diode}	Equivalent resistance of the anti-parallel diode of the switch
$R_{ds(on)}$	On-state equivalent resistance of the Mosfet
R_{eq}	Equivalent resistance seen by the resonant network
r_f	Resonant inductor AC resistance
r_n	Index of the physical size
R_o	Load resistance
r_p	Primary side coil AC resistance
r_s	Secondary side coil AC resistance
S_{eff}	Effective cross-section area
S_{req}	Required cross-section area
$tan\delta(f)$	Dissipation factor of the capacitors as a function of frequency
T_{cu}	Copper cross-section
t_f	Fall-time of the switch
T_f	Ferrite thickness
T_{fw}	Ferrite width
T_L	Layer insulation thickness

t_r	Rise-time of the switch
T_w	Track width
U_{d0}	Turn-on voltage-drop of the anti-parallel diode of the switch
U_{d0_bridge}	Forward voltage of the diodes of the diode bridge
V_{bat}	Battery Voltage
V_{Cf}	Voltage of the primary side parallel capacitor
V_{Cs}	Voltage of the primary side series capacitor
V_d	Output DC voltage
V_{dc}	DC-link voltage
V_{in}	Inverter output voltage
${V_{in}}^{RMS}$	RMS value of the inverter output voltage
V_{Load}	Load voltage
V_o	Output voltage
${V_s}^{oc}$	Open circuit induced voltage
Y_b	Inner size of the integrated coil in Y-direction
Y_b	Inner size of the integrated coil in X-direction
Z_{in}	Input impedance
Z_p	Primary side branch impedance
Z_r	Reflected impedance to the primary side
Z_s	Secondary side impedance including mutual inductance
Z_{sec}	Secondary side impedance

a	Power density
β	Sensitivity index
δ	Skin depth
Δk	Coupling factor variation
ΔU	Output voltage factor variation
η	Efficiency
η_{di}	Desired Efficiency
η_{ki}	Efficiency at coupling factor k_i
θ	Inverter phase-shift
μ	Magnetic permeability
ϱ	Copper resistivity
ϕ	Input impedance phase angle
ϕ^{min}	Input impedance minimum phase angle
ω	Angular frequency
ω_0	Resonant angular frequency

Chapter 1

Introduction

1.1. Background

Nowadays, concerns regarding global warming due to the greenhouse gasses caused by CO_2 emissions are increasing. It is estimated that the planet's surface temperature is increased around 1 $^{\circ}$C since the 19^{th} century [1]. Electric Vehicles (EV's) are considered as a promising technology to replace traditional gasoline engines and reduces environmental issues. The global market share of electric passenger cars is increased by 40% compared to 2018 and this trend is estimated to continue and reach to 50 million by 2025 with an annual growth rate of 30% [2]. Although the EV industry is growing, there are several adaptation barriers that need to be addressed [2]. In particular, availability of the charging infrastructure,

battery technology, and initial cost of the EV compared to conventional vehicles are the main barriers [2].

Lithium-ion (Li-ion) battery technology is one of the main energy storage components used in EVs. Li-ion offers higher efficiency (94-98 %), higher energy density (200-300 Wh/kg), and higher lifetime (1500-3000 cycles) compared to Lead-acid batteries (30-40 Wh/kg) and other alternative solutions [3]. Although the energy density is improved and the cost of Li-ion battery dropped in recent years, the energy density of the current technology is still significantly lower than a conventional gasoline system (12,000 Wh/kg) [4]. Moreover, the charging process of the EVs is not as fast as refueling conventional gasoline vehicles. Therefore, the weight of the energy storage system, range anxiety, and slow charging process are major barriers that limited the market penetration of the EV industry [5].

Each year, 1.2 million people die due to traffic accidents [6]. Besides personal vehicles and public transportation, EVs can be used for autonomous driving by employing deep learning methods [7]. Autonomous Vehicles (AVs) avoid accidents, improve energy consumption by controlling the driving pattern, help people with disabilities to commute [6], improving traffic flow, and car-sharing [7]. Moreover, AV can be considered as a solution to support the grid in case of power fluctuations in future smart cities [8]. Despite these promising benefits, autonomous vehicles

face new practical challenges. For instance, the charging process should happen seamlessly without user interference and the size of the battery should be small to keep the cost of the AVs as low as possible [9].

Current battery charging technology relies on conductive (plug-in) transferring of the power to the on-board battery [10]. In this method, the grid electric energy transfers through conductive copper cables. Recently, extreme fast chargers offer lower charging time by increasing the DC voltage to reduce the conductive loss [5]. For instance, Terra HP made by ABB is a 350 kW DC fast charger that adds 200 miles to the EV driving range in a 10 min charging session [4]. Although the conductive fast chargers can reduce the charging time, the size and cost of the on-board battery still is an issue. Moreover, the charging process of the AVs still requires human interference.

Alternatively, wireless charging of the EVs offers a convenient, reliable, and automatic charging of the autonomous vehicles without user interference. Wireless Power Transfer (WPT) can benefit the EV industry in two major aspects: reduction of the battery size and automatic charging process [9]. The EV wireless charging systems can be categorized into dynamic charging, quasi-dynamic, and stationary charging [11].

In a dynamic charging system, ideally, all the roadway is powered by transmitter converters that can transfer the power to the moving vehicle. In the quasi-dynamic EV wireless charging, the transmitter converters are only installed in proximity of the traffic lights, taxi stations, or electric-bus stops [12]. Therefore, in the dynamic and quasi-dynamic wireless charging applications, the size of the battery can be reduced significantly [9]. On the other hand, in the stationary wireless charging systems, the EV position is fixed during the charging process [13]. Considering the infrastructure cost to implement wireless charging for all the roads, stationary charging is a suitable candidate that can be realized in near future.

An early attempt at transferring power using radio waves is conducted by Nikola Tesla in 1890 [13]. However, the efficiency of the power transmission was very low. Nowadays, with the progress of semiconductor devices and power electronics, the wireless power transmission efficiency increased significantly which makes this technology an attractive solution for EV charging. The distance between the transmitter and receiver can be in the range of few millimeters up to a few meters [14]. Currently, high-power wireless chargers are introduced that can deliver up to 200 kW on a relatively large air-gap [15]. Considering these features, wireless charging can be considered not only as a catalyst but also as an essential technology

that brings more satisfaction to the EV market by offering convenience, reliability, and fast charging capabilities.

1.2. Challenges and Motivation

In order to compete with conventional plug-in battery chargers, the wireless charging system should offer competitive cost, power density, and efficiency. Although wireless power transfer is studied in recent publications, there are several challenges moving toward high-power applications such as EV wireless charging. These challenges are related to different parts of the wireless charging system such as resonant networks, magnetic couplers, control, and implementation cost. These challenges are addressed in this thesis to improve the power density, efficiency and reduce the implementation cost.

The current wireless charging system technology is based on the conventional design of resonant networks. Also, the conventional design of the magnetic couplers limits the performance and maximum efficiency of the system which is only achievable in a limited range close to nominal loading conditions. Moreover, the misalignment of the magnetic couplers results in a reduction of the coupling factor that can significantly reduce the efficiency of the system and affect the output voltage. Besides, several trial-and-error corrections are required for designing the resonant networks based on the conventional tuning methods. One of the main

objectives of this thesis is to propose a new design procedure to optimally tune the resonant network for a wide range of load and coupling factor variations.

Typically, a resonant network on the transmitter and receiver sides of the system exists that helps to realize soft switching, constant current output versus load and coupling factor variation. To regulate the output voltage, a DC-DC converter is a suitable candidate that helps to realize Constant Current (CC) and Constant Voltage (CV) modes for the EV battery charging. Both the resonant network and the DC-DC converter require a bulky inductor in their structures. Considering the high cost of ferromagnetic materials, integrated magnetic solutions are a suitable solution to reduce the cost and put the magnetic material to better use. Especially on the vehicle side, the space is limited and it is beneficial to shrink the size of the converter as much as possible. Therefore, an integrated magnetic structure is proposed in this thesis to address this issue.

The EV wireless charging system is operating at 85 kHz band according to SAE 2954 standard which is a relatively high operating frequency. Operating at this frequency results in higher coil AC resistance due to skin effect and proximity effect caused by eddy current. As the AC resistance of the coils increases, the quality factor and the efficiency of the system reduces consequently. Therefore, Litz wire is typically employed to overcome this issue. The ratio of the AC resistance to

the DC resistance will be lower as the diameter of the strands in the Litz wire reduces. However, as the number of strands increases and the diameter of the strands of the Litz wire reduces the cost of the Litz wire increases significantly. Therefore, finding alternatives for replacing the Litz wire is a promising objective. An integrated magnetic structure combined with a PCB-based magnetic structure is proposed in this thesis to improve the power density, reduce the implementation cost and offer competitive performance in EV wireless charging applications.

As the power level of the system increases, the converter design faces several challenges. First, the semiconductor device's cost increases significantly as the voltage and current rating increases. Second, considering the inverter switching frequency, the maximum dv/dt of the switches is another challenge. Third, as the power rating of the system increases, the cost of the resonant elements and their V.A rating increases. Different approaches are proposed to solve this issue such as using parallel switches, multilevel inverters, and multi-parallel inverters. Since the inverter is operating at a relatively high frequency, the inverter requires a complex gate driver design to avoid current imbalance and ensure synchronized switching. Moreover, using the multilevel inverters results in losing soft switching and multi-parallel inverters require a complex transformer design to eliminate the circulating

current which increases the implementation cost. Therefore, a new AC-DC topology that can solve the aforementioned issues is another objective of this thesis.

1.3. Contributions

The author has contributed to several technical, and analytical advances of the EV wireless charging application that briefly described below:

- A comprehensive review of the fundamentals of the wireless power transfer systems focusing on misalignment tolerance;
- Developing a new method to design resonant networks for EV wireless chargers;
- Developing a new magnetic coupler structure to integrate the resonant and DC-DC inductors into the main wireless charging coils and increases the power density and reduce the cost;
- Developing a new PCB-based magnetic coupler design for EV wireless charging;
- Developing a new modular LCC-based resonant network with a passive current sharing for high-power EV wireless charging.

1.4. Publications

The author has contributed several journal and conference papers as listed below.

- Thesis Related Journal Publications

[J.1] A. Ramezani and M. Narimani, "A New Wireless EV Charging System with Integrated DC-DC Magnetic Element," *IEEE Transactions on Transportation Electrification,* vol. 5, no. 4, pp. 1112-1123, 2019.

[J.2] A. Ramezani and M. Narimani, "Optimized Electric Vehicle Wireless Chargers With Reduced Output Voltage Sensitivity to Misalignment," *IEEE Journal of Emerging and Selected Topics in Power Electronics,* vol. 8, no. 4, pp. 3569-3581, 2020.

[J.3] A. Ramezani and M. Narimani, "Optimal Design of Fully-Integrated Magnetic Structure for Wireless Charging of Electric Vehicles," *IEEE Transactions on Transportation Electrification,* 2021.

[J.4] A. Ramezani and M. Narimani, "An Efficient PCB Based Magnetic Coupler Design for Electric Vehicle Wireless Charging," *Under review IEEE Transactions on Transportation Electrification,* 2021.

[J.5] A. Ramezani and M. Narimani, "Modular LCC-Based Resonant Compensation for High-Power EV Wireless Charging," *Under review IEEE Transactions on Transportation Electrification,* 2021.

[J.6] A. Ramezani, M. Narimani, and B. Vu, "Operation of High-Power Inductive Power Transfer Systems under Misalignment Conditions: A Review," *to be submitted to IEEE Transactions on Transportation Electrification,* 2021.

- Thesis Related Conference Publications

[C.1] A. Ramezani and M. Narimani, "A Wireless Power Transfer System with Reduced Output Voltage Sensitivity for EV Applications," in *2018 IEEE PELS Workshop on Emerging Technologies: Wireless Power Transfer (WoW)*, 2018, pp. 1-5.

[C.2] A. Ramezani and M. Narimani, "High Misalignment Tolerant Wireless Charger Designs for EV Applications," in *2019 IEEE Transportation Electrification Conference and Expo (ITEC)*, 2019, pp. 1-5.

[C.3] A. Ramezani and M. Narimani, "A Modular Coil Design for High-Power Wireless EV Charging," *Under review in IEEE Energy Conversion Congress and Exposition (ECCE)*, Vancouver, BC, Canada, 2021.

- Side Research Journal Publications

[J.7] A. R. Dekka, A. Ramezani, S. Ounie, and M. Narimani, "A New Five-Level Voltage Source Inverter: Modulation and Control," *IEEE Transactions on Industry Applications,* vol. 56, no. 5, pp. 5553-5564, 2020.

- Side Research Conference Publications

[C.4] A. Ramezani and M. Narimani, "A Dynamic Wireless Charging System with a Robust Output Voltage Respect to Misalignment," in *2019 IEEE PELS Workshop on Emerging Technologies: Wireless Power Transfer (WoW)*, 2019, pp. 292-296.

[C.5] A. Ramezani and M. Narimani, "A New Configuration and Bypassing Strategy for Dynamic Wireless EV Charging," in *2020 IEEE Transportation Electrification Conference & Expo (ITEC)*, 2020, pp. 821-825.

[C.6] A. Dekka, A. Ramezani, S. Ounie, and M. Narimani, "A New 5–Level Voltage Source Inverter," in *2019 IEEE Applied Power Electronics Conference and Exposition (APEC)*, 2019, pp. 2511-2515.

1.5. Thesis Outline

This thesis is organized into seven chapters, focuses on the optimization and design of the resonant network, magnetic couplers, and converter topology for EV wireless charging.

Chapter 1 presents the research motivation of wireless power transmission for EV charging applications. Moreover, the thesis contributions are outlined.

Chapter 2 presents the fundamentals of the wireless power transfer for EV battery charging applications. Different types of wireless power transmission are categorized at first. Then, the main components of the wireless power transfer system are described and studied individually. The designing challenges of each component are described and current solutions are studied.

Chapter 3 presents the proposed design strategy to optimize the resonant network of the wireless charging system. The issues with the conventional design methods are described and advantages of the proposed method are highlighted. The analytical models for four different resonant topologies are presented. By defining an optimization problem, each of the resonant networks is optimally designed. A prototype is built and experimental measurements are presented. The conclusions of this chapter are considered as the basis of the other chapters.

Chapter 4 presents a proposed integrated magnetic structure for wireless charging of EVs. At first, the partial integration of the DC-DC inductor into the main wireless charging magnetic couplers is presented. Then, integration of both the DC-DC inductor and the resonant inductor into the main wireless charging magnetic couplers is introduced. The design challenges of the fully-integrated

system are presented and an optimization approach is proposed to address this issue. Finally, the experimental setup of both partial and fully-integrated wireless charging systems is built and experimental results are compared with the simulation results.

Chapter 5 introduces a new approach for designing the magnetic couplers based on PCB to reduce the implementation cost while maintaining high efficiency. At first, a theoretical analysis is presented to study the sensitivity of the efficiency to the coil AC resistance. Second, 2D FEA analysis is presented and the effect of different design parameters on the coil AC resistance is studied. Then, 3D FEA analysis based on the conclusions of the 2D studies is presented and an optimal design is selected. Thermal analysis of the coil under different loading conditions is studied to verify the feasibility of the design. Finally, an experimental setup is built to verify the simulation results.

Chapter 6 presents a new modular resonant topology for high-power EV wireless charging systems. The proposed topology is analyzed in-depth and a tuning method for the resonant network is presented. Then the current sharing of the modules is analyzed and the influence of resonant elements tolerance on the current sharing is studied. In the next step, a high-power wireless charging system is

designed based on the proposed topology and the effect of the number of the modules on the system power density and efficiency is analyzed.

Chapter 7 is dedicated to conclusions and future work.

Chapter 2

Fundamentals of a Wireless Power Transfer System for EV Applications

2.1. Introduction

Wireless Power Transfer (WPT) is a general technology that can be implemented using different methods. Fig. 2-1 categorizes different types of wireless power transmission based on the employed technology. Generally, three types of wireless power transfer are introduced: near-field, far-field, and mechanical [11, 13]. The power and distance between the transmitter and receiver for these technologies are compared in Table 2-1.

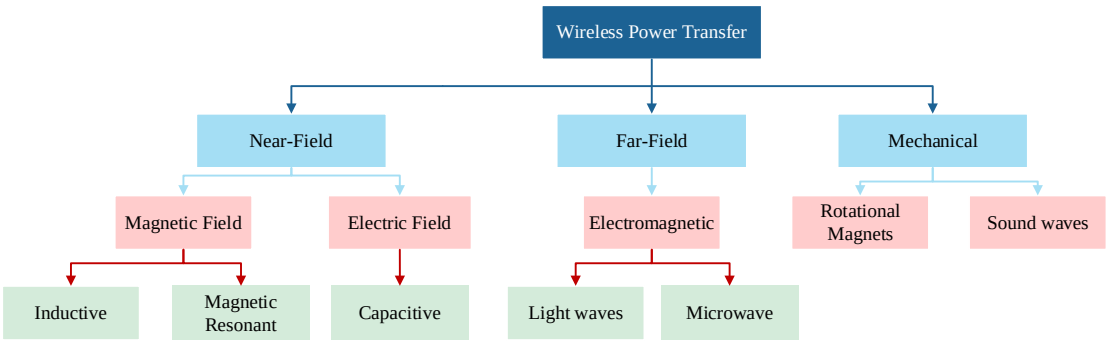

Fig. 2-1.Categories of wireless power transfer based on the power transfer technology [11, 13].

TABLE 2-1
COMPARISON OF DIFFERENT WPT TECHNOLOGIES [11, 13]

WPT	Technology	Power	Distance	Frequency
Mechanical	Sound waves	Less than 10 W	70-300 mm	0.5-3 MHz
	Rotational magnets	Up to few kilowatts	100-150 mm	150-300 Hz
Far-Field	Electromagnetic	Up to few megawatts	Up to several kilometers	300 MHz-300 GHz
Near-Field	Capacitive	Up to few kilowatts	Up to few centimeters	1 kHz-40 MHz
	Magnetic resonant	Up to few kilowatts	Up to few meters	100 kHz-10 MHz
	Inductive	Up to few hundred kilowatts	Up to 400 mm	3 kHz-1 MHz

In the mechanical-based WPT, a mechanical force transfers the power from the transmitter to the receiver. For instance, magnetic gear technology can be used to mechanically transfer the power to the receiver. However, having moving parts in the system results in lower reliability, lower efficiency, and more mechanical noises [16]. Similarly, the sound waves can propagate to the air and apply a motion on the receiver side's transducer [17]. However, the maximum transferable power

and the distance between the transmitter and receiver are limited as described in Table 2-1.

Far-field (radiative) WPT systems are based on the propagation of electromagnetic waves through the air. In this case, the frequency is in the range of 0.3-300 GHz, the distance and maximum transferable power are relatively large. However, this method requires a huge antenna, complex tracking control methods, and the system efficiency is low [11, 13]. Moreover, issues regarding microwave radiation on the human body are another drawback of this technology [18].

Near-field (non-radiative) WPT systems can be categorized into three methods: capacitive, magnetic resonant, and inductive. The Capacitive Power Transfer (CPT) is based on the electric field between the two pairs of plates on the transmitter and receiver to form a capacitor. CPT does not require any winding on the receiver of the transmitter which makes it light-weight and cheaper than other technologies [18]. However, the capacitance between the transmitter and receiver is limited to the size of the plates. Consequently, the maximum transferable power is low. Therefore, the operating frequency should be increased up to the MHz range to compensate for the low capacitive coupling between the transmitter and receivers. However, the maximum rating of the existing power semiconductor devices and voltage stress of the resonant components are the main barriers of this technology [18].

Both the magnetic resonant and Inductive Power Transfer (IPT) technologies are based on the magnetic coupling between a transmitter and receiver coils. In the magnetic resonant technology, the transmitter, and receiver are in the self-oscillating condition and tuned at the operating frequency [19]. In contrast, external resonant capacitors are required for inductive power transfer [20]. In order to operate at self-oscillation mode, the operating frequency should be increased. Therefore, the switching frequency of the magnetic resonant technology is in the range of MHz to achieve a self-oscillating magnetic coupler. The efficiency and maximum transferable power of the near-field WPT systems are typically higher than other technologies at small air-gaps.

In conclusion, inductive power transfer offers high-efficiency, simple implementation, autonomous, and reliable operation features. Moreover, the physical size of the transmitter and receiver, and the feasibility of high-power transmission over a relatively low-frequency band using existing power electronics technology are other advantages of the inductive power transmission technology.

Recently, WPT is proposed as a convenient alternative for charging the battery of Electric Vehicles (EVs). One of the advantages of wireless charging systems is that the charging process can be done without the interference of the user [21]. This convenient feature enables the autonomous vehicles to charge automatically and reduce the size of the on-board battery [9]. In comparison with the conventional

plug-in (conductive) charging stations, expensive and bulky plugs and copper cables are not needed in wireless charging systems [22].

Considering the power level and practical limitations of the switching devices such as switching frequency, inductive wireless power transfer is a great candidate for EV wireless charging applications. Fig. 2-2 illustrates the basic concept of a typical inductive wireless charging system for EV applications.

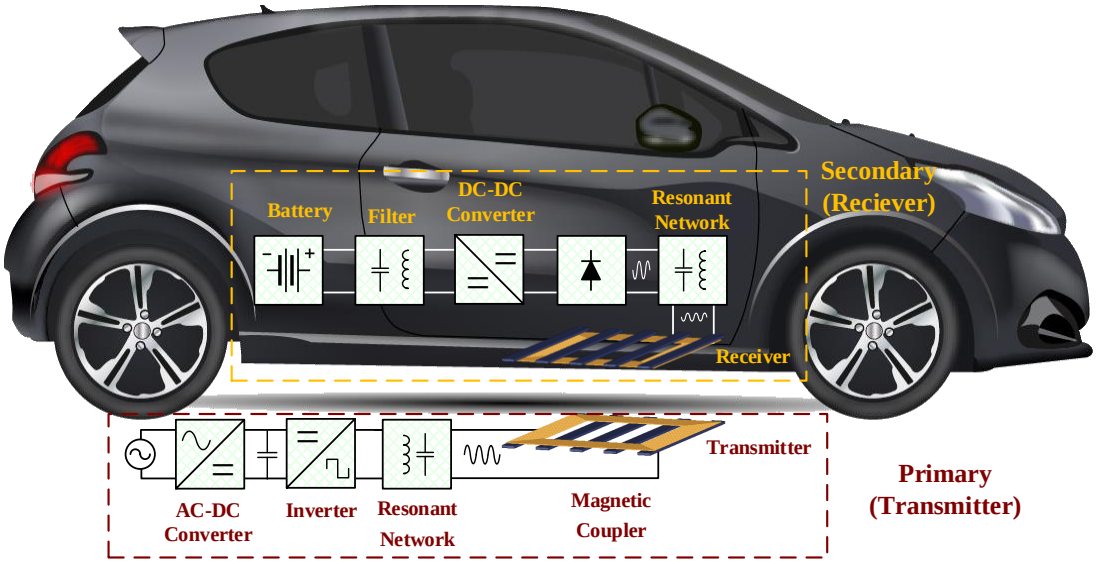

Fig. 2-2.The concept of wireless charging for EV applications.

Inductive WPT systems are operating based on the magnetic coupling between the transmitter and receiver coils. This magnetic coupling brings inherent isolation between the grid and load side which eliminates the need for bulky isolation transformers [11]. Moreover, this feature makes the inductive WPT system suitable for operation in wet environments. Since there is no moving part in this system,

inductive wireless power transfer requires low maintenance and offers high reliability.

A typical inductive wireless charging system is consisting of the following components:

- **Primary Side AC-DC Converter:** This converter usually is a diode bridge or a boost converter with the ability of Power Factor Correction (PFC). This stage provides a constant DC voltage for the inverter.
- **Inverter:** The inverter converts the DC input voltage into a high-frequency square voltage waveform to feed the resonant network.
- **Resonant Network:** This circuit is made by capacitors and inductors tuned at the switching frequency. The resonant network can be designed to provide the soft-switching condition for the inverter to reduce switching losses.
- **Magnetic Couplers:** The magnetic coupler is made by a set of transmitter and receiver coils that are magnetically coupled. The time-varying primary side flux induces an alternative voltage on the secondary side coil which is called the open-circuit voltage. The magnetic coupler is also known as a Loosely Coupler Transformer (LCT).
- **Rectifier and Pickup Converter:** This stage converts the high-frequency voltage induced on the receiver coil into a DC voltage which is suitable for the energy management system on the vehicle. This stage may contain only a diode bridge in the simplest case or a boost, buck, or an active rectifier.

- **Control:** The control system provides appropriate gating signals for the primary side converter and also the secondary side converter to charge the battery in Constant Current (CC) and Constant Voltage (CV) modes.

2.2. Transmitter Converter

The transmitter converter includes a rectification circuit, a Power Factor Correction (PFC) circuit, and an inverter as shown in Fig. 2-3 [23]. The rectification circuit converts the input voltage from the grid to a DC voltage. The PFC stage is typically a boost converter that acts as a power factor correction unit. The output of the PFC stage is a stable DC voltage that feeds the inverter. In a simplified model of the WPT systems, it can be assumed that the input DC voltage is provided by an AC-DC PFC converter [24].

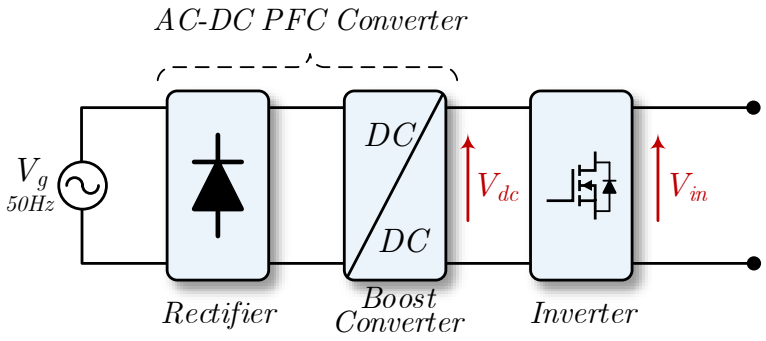

Fig. 2-3. A typical transmitter side converter of the EV wireless charging system.

Fig. 2-4 shows the full-bridge inverter topology used for wireless charging applications. In this figure, the input voltage is V_{dc} generated by the PFC stage and S_1-S_4 are the power switching devices. The output voltage of the inverter, V_{in},

is dependent on the switching modulation scheme. Different Pulse Width Modulation (PWM) schemes can be applied to command the switches of the inverter. Commonly, a phase-shifted modulation scheme is used in WPT systems to realize Zero Voltage Switching (ZVS) [25]. The gate signals of this modulation scheme and the output voltage are shown in Fig. 2-5.

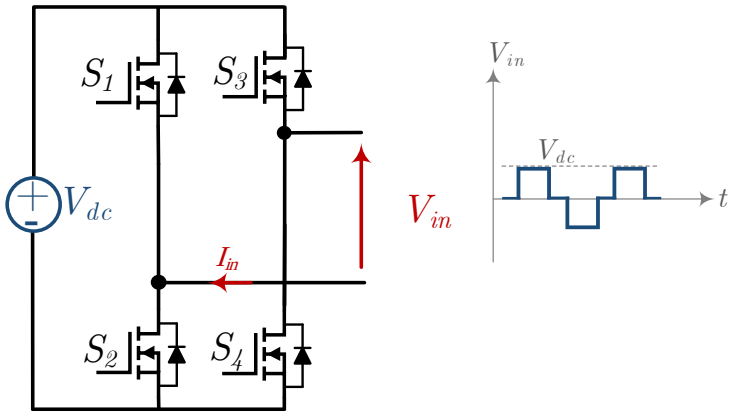

Fig. 2-4. The full-bridge inverter topology and its typical output voltage waveform.

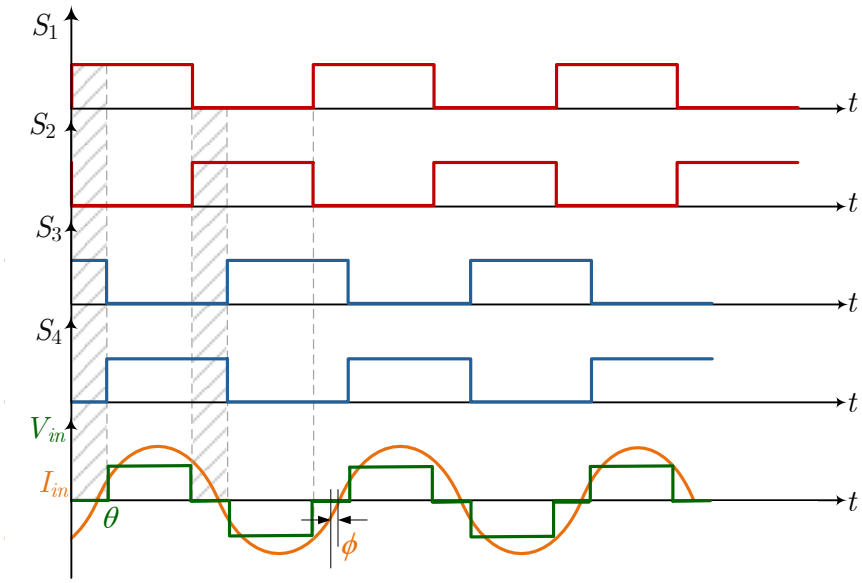

Fig. 2-5. A typical waveform of the gating signals of a full-bridge inverter and its output voltage and current.

According to Fig. 2-5, the output voltage of the inverter is connected to $+V_{dc}$ when S_1 and S_4 are conducting. Similarly, the output voltage is equal to $-V_{dc}$ when S_2 and S_3 are conducting. The phase-shift between the two inverter legs is θ. When θ is equal to zero, the legs of the inverter are synchronized and the output voltage would be zero. When the phase-shift is equal to 180 ° the inverter output voltage would be a square waveform with a 50% duty cycle. By calculating the Fourier series of the inverter output voltage, the RMS value of the first harmonic of the inverter voltage, V_{in}, can be expressed by:

$$V_{in}(t) = \frac{4V_{dc}}{\pi}\sum_{n=1}^{\infty}\sin(\frac{\theta}{2})\sin(n\omega t) \tag{2.1}$$

$$V_{in} = \frac{\sqrt{8}}{\pi}V_{dc}\sin(\frac{\theta}{2}) \tag{2.2}$$

where θ is the phase-shift angle, and ω is the angular switching frequency of the inverter. Due to the band-pass filtering effect of the resonant network, only the fundamental harmonic of the inverter voltage can be considered for analyzing the WPT system [23, 26-28].

The phase angle between the inverter voltage (V_{in}) and its current (I_{in}) is defined by ϕ. This phase angle is dependent on the input impedance at the switching frequency (Z_{in}). In order to realize ZVS, the inverter current should lag the inverter voltage.

Single-stage solutions are also proposed for the WPT systems to combine the PFC stage with the inverter and improve the power density. In [29], a 2.5 kW/110 kHz bridge-less single-stage converter for WPT application is proposed. In this study, SiC switches are used to gain high efficiency for the converter. Fig. 2-6 depicts this single-stage topology. The main disadvantage of this circuit is the variable DC-link voltage when the converter is not operating on the nominal loading condition.

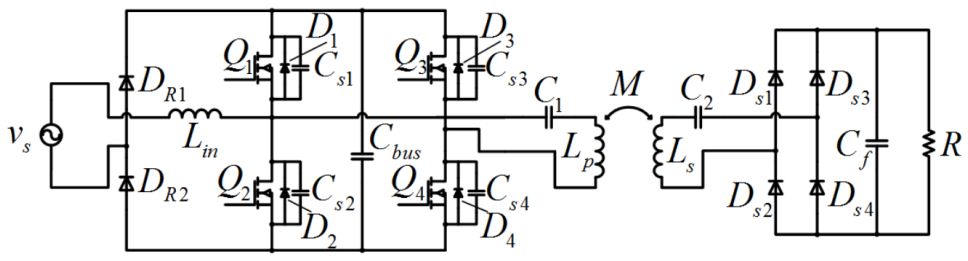

Fig. 2-6. Single-stage inverter topology for WPT application [29].

2.3. Resonant Networks

In a WPT system the magnetic coupler absorbs a large value of reactive power due to the large leakage inductances [24]. Therefore, it is essential to compensate the reactive power of the magnetic couplers by using resonant topologies. The resonant circuits also offer interesting features such as soft switching, high efficiency, high power density, flexible voltage gain and current gain [11].

2.3.1. Requirements and Challenges

Position of the magnetic couplers results in deviation of the coupling factor (k) from the nominal value. The coupling factor deviation affects the input impedance (Z_{in}), input phase angle (ϕ), output power (P_{out}), and efficiency (η) of the system. Therefore, the proper design of resonant network can help to reduce the sensitivity of the efficiency to variation of the coupling factor (k) [30].

Zero voltage switching reduces the switching loss of the inverter switches and increases the system efficiency. ZVS can be realized when the input current (I_{in}) of the resonant network has a lagging phase angle respect to the input voltage (V_{in}). In other words, the resonant network should have a resistive-inductive impedance characteristic. In this situation, the switches of the inverter will see a negative current at the moment of switching and the current passes through the anti-parallel

diode of the switch and clamps the voltage of the switch to zero [26]. Therefore, an inductive input impedance results in ZVS realization for the inverter.

The resonant network should be designed to maintain ZVS at all operating conditions and keep the efficiency as high as possible. In EV charging application, limited current of the transmitter side converter in the safe region in case of the absence of the receiver coil is an important factor to avoid damaging the inverter and resonant elements. These parameters should also be considered in the selection and design of the resonant network for a wireless charging system.

2.3.2. Topologies

The structure of the resonant topologies can be divided into three groups as shown in Fig. 2-7. Input impedance, efficiency, and output voltage gain ($G_v = V_o / V_{in}$) are key functions that need to be defined for analyzing each resonant topology. The input impedance can be used to calculate the input phase angle, and the input current. The voltage gain shows the ratio of the output voltage to the input voltage as a function of the resonant elements.

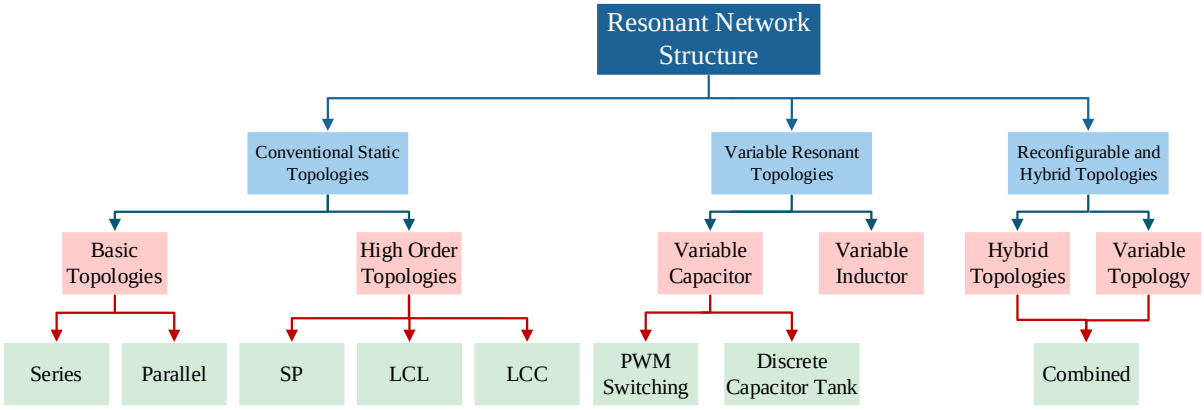

Fig. 2-7. Resonant network structures for WPT systems.

The schematics of the commonly used topologies are summarized in Table 2-2. In this table, Series, Parallel, LCC, and Series-Parallel topologies are labeled by S, P, LCC, SP. The advantages and disadvantages of each topology will be discussed in the next section of this chapter in detail. In this thesis, the reflected impedance is defined by $Z_r = (M\omega)^2 / Z_{\text{sec}}$, where Z_{sec} is the impedance of the secondary side circuit. In the following, some of the common resonant network topologies and their design challenges are studied.

TABLE 2-2
SCHEMATIC OF DIFFERENT RESONANT TOPOLOGIES

Name	Schematic
Series-Series (S-S)	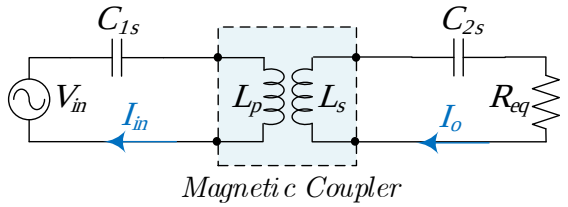
Series-Parallel (S-P)	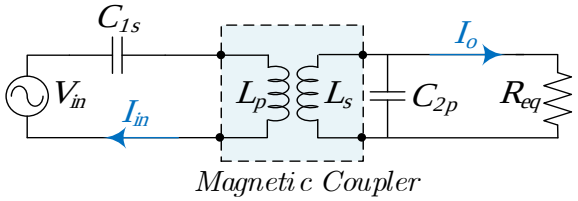
Parallel-Parallel (P-P)	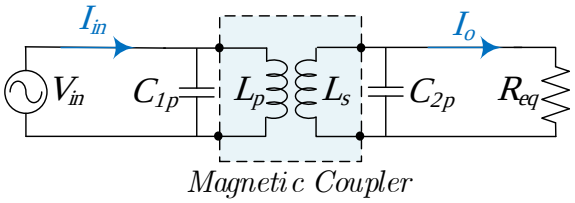
Parallel-Series (P-S)	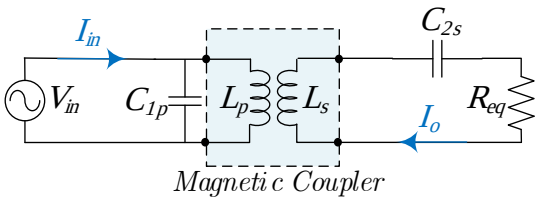
LCC-Series (LCC-S)	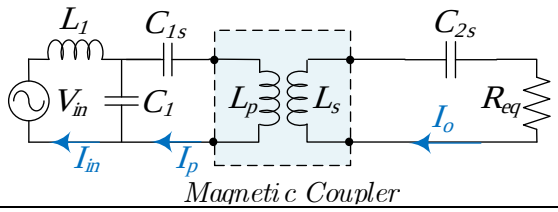
LCC-Parallel (LCC-P)	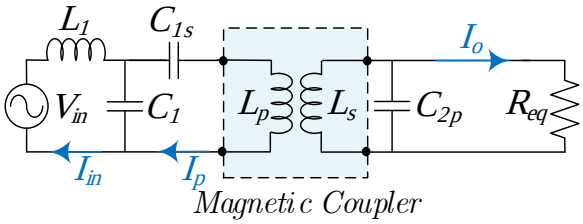

Name	Schematic
LCC-Series Parallel (LCC-SP)	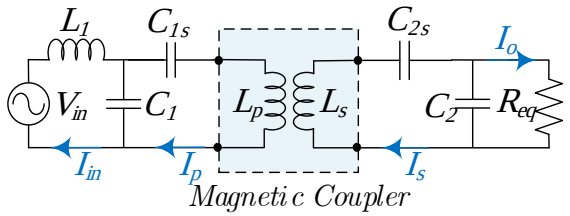
LCC-LCC	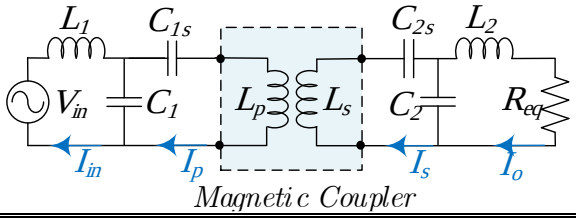

A. Basic Topologies

Four basic topologies can be obtained using a single resonant element on each side of the magnetic couplers: Series-Series (S-S), Series-Parallel (S-P), Parallel-Parallel (P-P), Parallel-Series (P-S). Due to the simplicity of the design, low component count, and high efficiency at the nominal operating point, S-S topology is selected in many applications [31-35]. Generally, in the topologies with a series of primary side resonant network (S-S and S-P), the input current is unbounded in absence of the receiver coil and it is essential to add a protection circuit [11, 36, 37]. In S-S and S-P topology, the input impedance phase angle is highly dependent on the load and coupling condition which results in low power transfer efficiency of the system [11, 38].

Compared to series primary side resonant network, the primary side of a parallel compensated (S-P and P-P) WPT system can operate normally in case of the absence of the receiver coil. Generally, the topologies with a parallel resonant network on the secondary side suffer from excessive output voltage at light-load conditions [26] and are highly sensitive to the misalignment of the magnetic couplers [36]. Moreover, the P-P topology is suffering from the low input power factor seen by the inverter [11], and dependency of the maximum output power point frequency to the mutual inductance [39].

B. LCL and LCC Based topologies

LCL and LCC resonant topologies are extensively used in the primary side of the WPT systems to supply the transmitter coil with a constant current which induces a constant voltage on the secondary side coil. The LCC network is commonly used instead of the LCL topology since it offers more degree of freedom for the designers to achieve desired characteristics [40]. By using the LCC topology, the constant amplitude of the primary side current independent of the load and mutual inductance [41, 42], limited inverter current in case of misalignment, and improvement of light load efficiency [23] can be achieved. The LCC-based topologies are widely used in the WPT application due to their suitable performance. For instance, the LCC-S [43-46], the LCCC-S [47], the LCC-SP [22], the LCC-P [48, 49] and the LCC-LCC [50-54] are analyzed.

Although the LCC-P topology has a constant output current behavior, in this operation mode, ZVS is not achievable [49]. In contrast, the LCC-S topology can be designed to supply the load as a constant voltage source independent of the load [55]. The LCC-LCC topology converts the constant voltage of the input to a Constant Current (CC) in the output of the system at resonant frequency [38] and also can achieve both the CV and CC modes if the resonant elements are tuned for two different resonant frequencies [54]. The LCC-LCC topology has outstanding performance compared to the other topologies. However, due to the number of components, the power density and efficiency of the system will decrease.

2.4. Magnetic Couplers

2.4.1. Principles

Magnetic couplers are the key elements of inductive WPT systems. These couplers consist of a winding, magnetic core material, and a magnetic shield [11, 24, 56, 57]. In Fig. 2-8, a typical magnetic coupler is shown as an example.

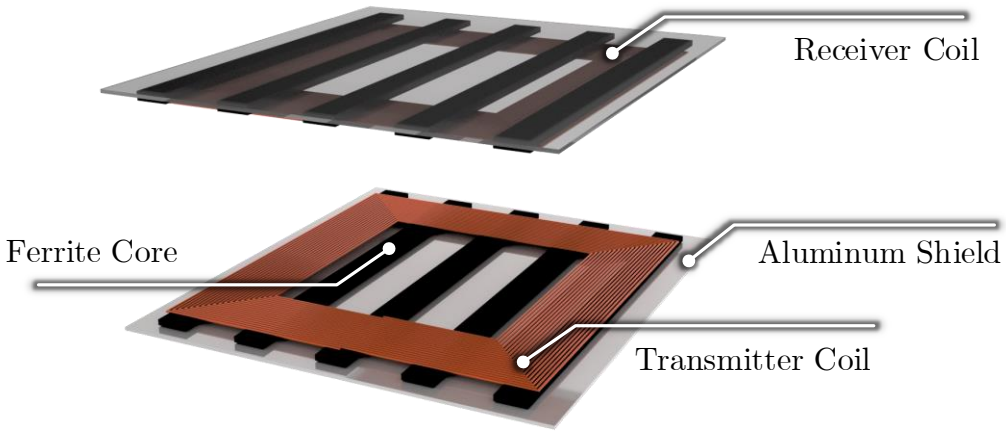

Fig. 2-8. A typical magnetic coupler layout.

Typically, the transmitter coil and receiver coil are also known as primary and secondary side coils, respectively. The magnetic coupling factor (k) for two sets of coils is defined as follows:

$$k = \frac{M}{\sqrt{L_p L_s}} \tag{2.3}$$

where L_p and L_s are the primary and secondary side self-inductances, and M is the mutual inductance between the primary and secondary coils. The nominal magnetic coupling factor (k_n) is dependent on the magnetic material, structure layout, spacing between the turns, and the number of turns. Mutual inductance can also be affected by the distance air-gap and misalignment of the magnetic couplers. Misalignment is the distance between the two coil centers. These parameters are defined in Fig. 2-9. The equivalent circuit model of a magnetic coupler can be

presented as a T-type model as shown in Fig. 2-10. This model can be used for analyzing the wireless charging system.

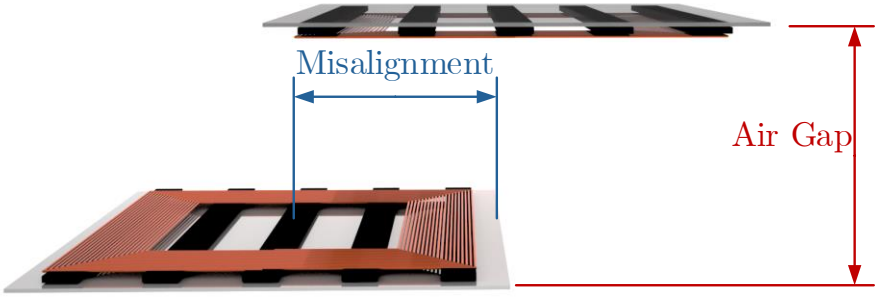

Fig. 2-9. Misalignment and air-gap definition for a magnetic coupler.

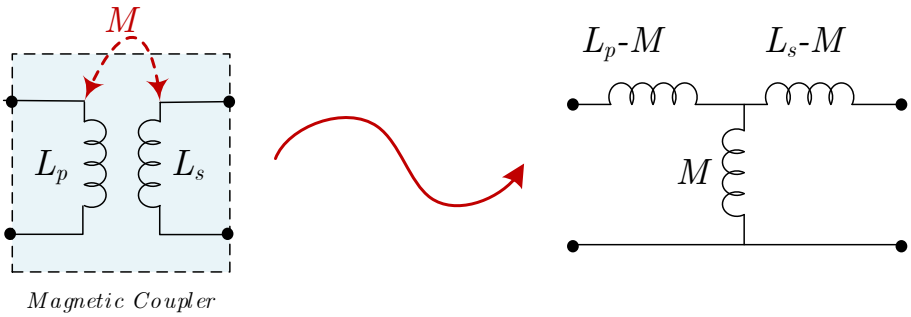

Fig. 2-10. The equivalent circuit model of the magnetic coupler.

The equivalent quality factor of the magnetic couplers (Q) and each coil inherent quality factor are defined as follows [11, 24, 57]:

$$Q = \sqrt{Q_p Q_s} \tag{2.4}$$

$$Q_p = \frac{L_p \omega}{r_p}, Q_s = \frac{L_s \omega}{r_s} \tag{2.5}$$

In (2.5), ω is the angular frequency, L_p and L_s are the primary and secondary side self-inductances and r_p and r_s are the internal AC resistance of the coil

respectively. Therefore, by increasing the operating frequency the quality factor of the coil can be improved. However, by increasing the frequency, the internal AC resistance of the coil will be increased due to the skin and proximity effects [58, 59]. Alternatively, if the AC resistance of the coil is reduced the quality factor will be increased significantly.

In order to reduce the AC resistance of the coils, Litz wire is employed and the selection of appropriate diameter and number of strands is presented in [60-62]. In [63] copper loss analysis of the magnetic couplers for a WPT system is studied. In this study, the Litz wire is modeled in a Finite Element Analysis (FEA) software to investigate the effect of the excitation frequency on the copper losses of the windings. Generally, using a smaller diameter for each strand of the Litz wire and more number of strands results in smaller AC resistance. However, the price of Litz wire increases exponentially with the number of strands. It should be noted that the filling factor of the Litz wire also decreases by increasing the number of strands. Therefore, a higher cross-section area is needed for a higher number of stranded Litz wire [64]. Moreover, a higher number of strands are rarely available in the market [64].

In order to avoid any magnetic field leakage to the back of the magnetic couplers, a magnetic shield is required. Although the ferrite material absorbs the majority of the magnetic field, typically an aluminum plate is plate on the back of

the magnetic couplers as shown in Fig. 2-8 [65]. Alternatively, active shielding can be considered instead of the aluminum plate. In this way, a winding is placed in the back of the magnetic coupler instead of the aluminum plate. The current flowing in the shield winding creates an opposite magnetic field that cancels out the total flux on the back of the magnetic coupler [66].

2.4.2. Magnetic Coupler Layouts

Several magnetic coupler layouts are introduced for WPT systems, among them, circular, rectangular, Double-D (DD) are the most common layouts [13]. The layout and main flux path (ϕ_p) between the transmitter and receiver of these topologies are shown in Fig. 2-11.

As it can be seen in Fig. 2-11, the coil layout is planner and the ferrite material is placed underneath of the coil. In this way, the flux will only flow between the transmitter and receiver coils and turns back into the ferrite plate. Therefore, the ferrite act as a low reluctance path, and the magnetic flux will not leak into the chassis of the vehicle.

One of the magnetic layouts is the circular magnetic coupler [67]. The layout of this structure and its magnetic flux path are illustrated in Fig. 2-11 (a). In this layout, the ferrite bars are placed radially and the coils are placed on top of the

ferrite bars. The magnetic flux of the coil flows outward of the magnetic plane and returns from the outer side of the magnetic coupler.

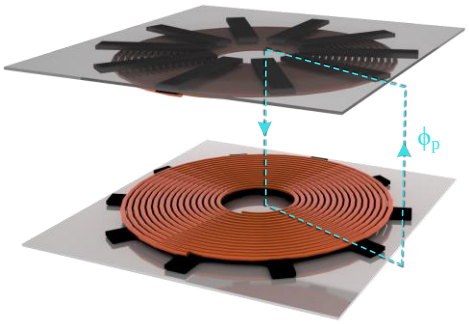

(a) Circular magentic coupler

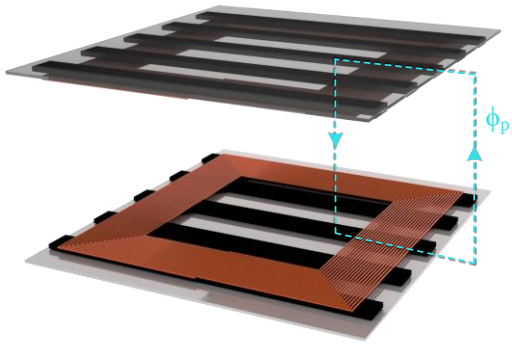

(b) Rectangular magentic coupler

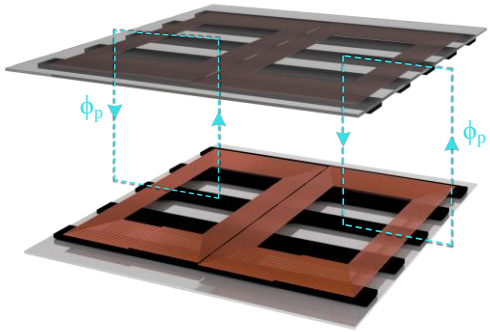

(c) DD magentic coupler

Fig. 2-11. The layout of common magnetic couplers.

The rectangular magnetic coupler is similar to the circular magnetic coupler and is known as Quadrature (Q). The layout of the rectangular magnetic coupler is shown in Fig. 2-11 (b). In this layout, the ferrite bars are placed in parallel.

Similar to the circular magnetic coupler, the flux path is outward the transmitter plane and returns from the other side of the magnetic coupler.

The DD magnetic coupler is one of the well-known layouts introduced in [31] which is shown in Fig. 2-11 (c). In this magnetic coupler, the flux has two opposite directions at the magnetic coupler plane. In the DD layout, the flux path is approximately equal to half of the magnetic coupler's length [11, 24, 57, 68]. However, in [69] it is concluded that the circular layout has a better coupling coefficient in comparison with the DD magnetic couplers with the same occupied area.

Multi-pole structures are proposed to improve the misalignment tolerance [70], increase the power level [71], or supply multiple loads at the same time [72, 73]. Typically, the magnetic couplers have one magnetic pole (unipolar) or two poles (bipolar) as shown in Fig. 2-12. As the number of the poles increases the complexity of the design, cost, and weight of the structure increases [70].

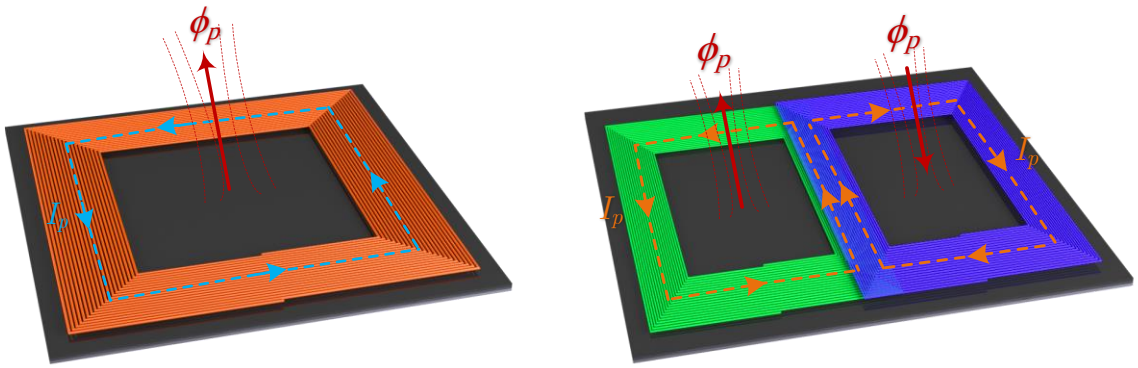

(a) Unipolar (b) bipolar

Fig. 2-12. Current flow and flux path of the unipolar and bipolar magnetic couplers.

In [64], rectangular, square, and circular geometries of the windings are compared. The comparison results are shown in Fig. 2-13. In this comparison, it is concluded that for the same coil area, circular magnetic couplers have a better coupling coefficient in comparison with the rectangular and square coils.

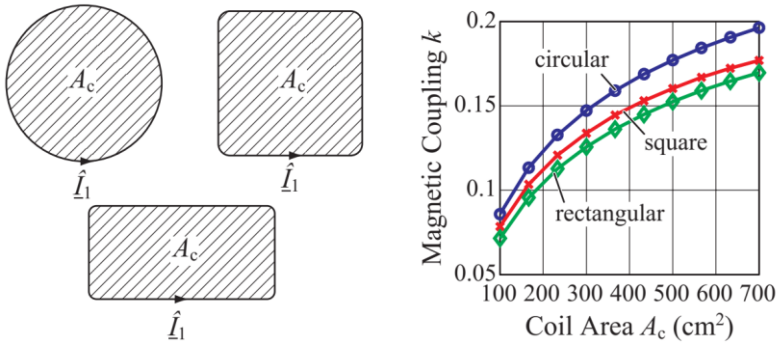

Fig. 2-13. Comparison of the magnetic coupler layouts [64].

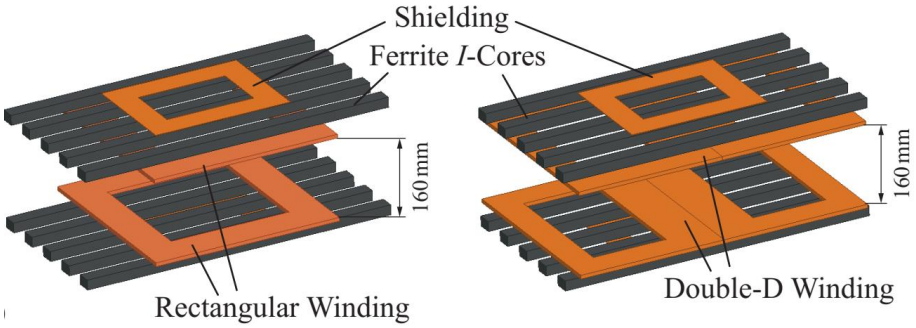

Fig. 2-14. The layout of the rectangular and DD magnetic couplers [74].

In [74], rectangular and DD structures are compared. Fig. 2-14 illustrates the layouts of these magnetic couplers. In this comparison, a 50 kW/85 kHz WPT system for a public transportation is considered. The coupling factor comparison results are shown in Fig. 2-15. As it is shown, the magnetic coupling of the DD

structure is less than the rectangular layout in most of the misalignment points. Moreover, the conduction and core loss of the magnetic couplers are included in a basic loss analysis to compare the performance of these two magnetic couplers. Fig. 2-16 illustrates the loss analysis results. In this figure, $P_{sh,i}$ is the eddy current losses in the shield, $P_{fe,i}$ is the core loss, and $P_{cu,i}$ is for the Litz wire copper loss.

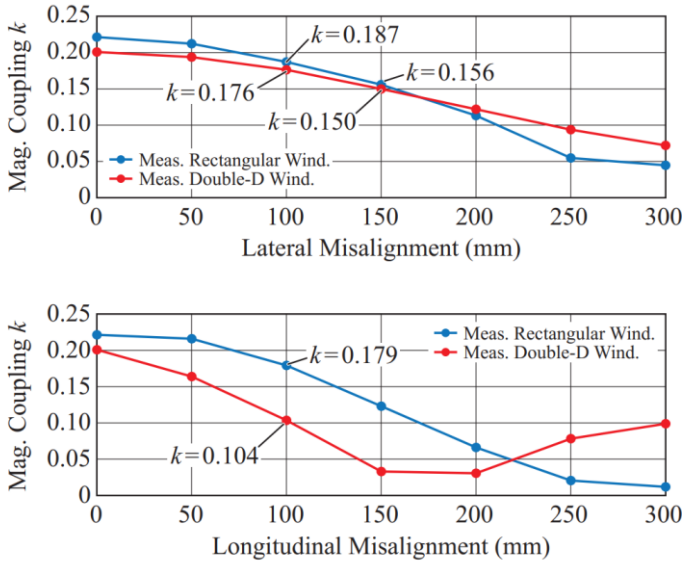

Fig. 2-15. Coupling coefficient comparison of the rectangular and DD magnetic couplers [74].

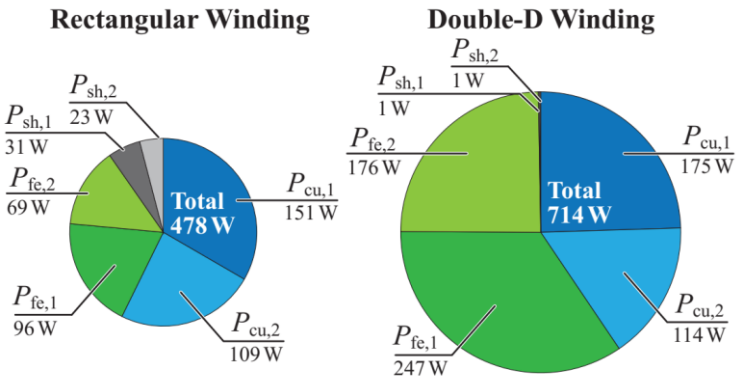

Fig. 2-16. Loss analysis of the DD and Rectangular magnetic couplers [74].

This result shows that the total loss of the rectangular magnetic coupler due to having only one winding is significantly less than the DD magnetic couplers. Moreover, the rectangular magnetic coupler showed a better longitudinal misalignment tolerance. Therefore, rectangular magnetic couplers are more preferable for stationary EV wireless charging applications.

2.4.3. Magnetic Coupler Design

Design, parameter analysis, and optimization of the circular magnetic structures are presented in [67]. It was shown that the number of ferrite strips has the most impact on the uncompensated transferred power which is related to the coupling coefficient. Moreover, it can also be concluded that the thickness of the ferrite strips has less effect on the magnetic coupling. Therefore, the thickness of ferrite could be selected as the minimum value which meets the core saturation criteria [67].

Fig. 2-17 illustrates the effect of ferrite core dimensions in the circular layout. Similarly, the effect of the total diameter is also studied and the results are shown in Fig. 2-18 for a 23A RMS/ 34 kHz excited primary side coil. It was shown that the total magnetic coupler diameter has a significant impact on the transferable output power. Therefore, based on the output power level and available area, the total diameter should be selected.

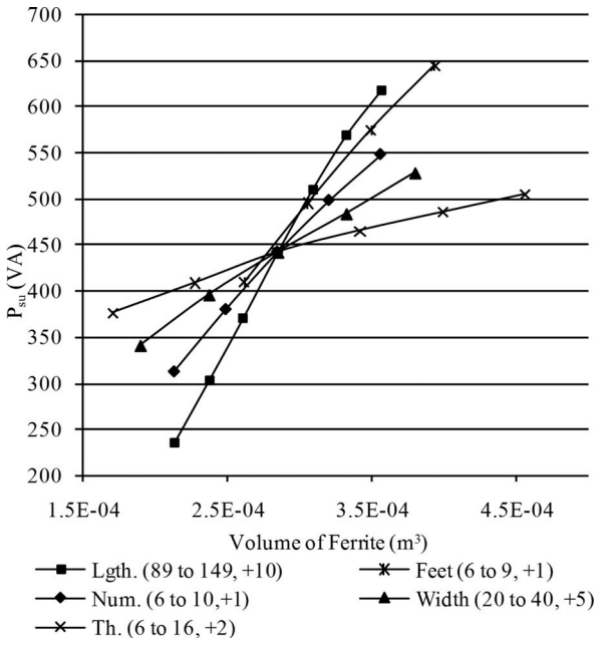

Fig. 2-17. Ferrite dimension effect on the magnetic coupling of the circular magnetic coupler [67].

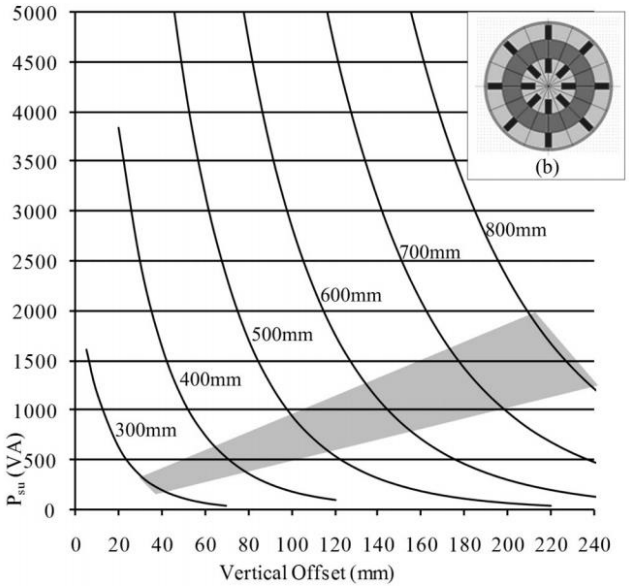

Fig. 2-18. Uncompensated power versus vertical offset profile with different diameters [67].

In [75], the effect of the Litz wire parameters is studied. It turned out that this parameter has not a noticeable impact on the magnetic coupling. Besides, the effect

of the inner radius (R_i) of the coil is investigated in [21, 64]. The effect of the coil inner radius and Litz wire diameter (d_w) are shown in Fig. 2-19. The effect of the spacing between each turn of the winding (S_w) and Litz wire diameter on the coil quality factor are presented in Fig. 2-20.

It can be seen that as the inner radius increases, assuming the outer diameter remains constant, the coupling factor decreases as shown in Fig. 2-19. Moreover, increasing the wire diameter reduces the AC resistance which results in increasing the quality factor. As the turn spacing (S_w) increases the quality factor decreases as shown in Fig. 2-20.

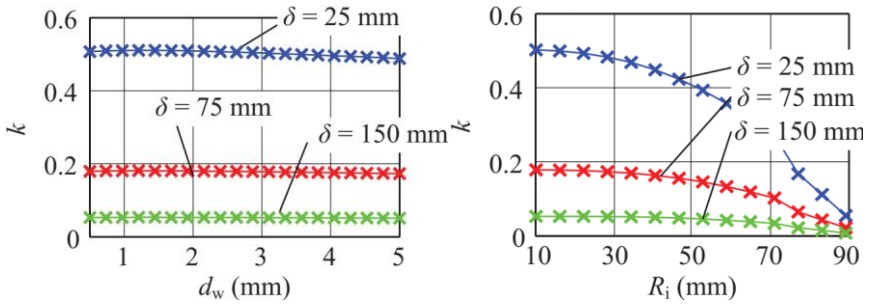

Fig. 2-19. The effect of the Litz wire diameter (d_w) and inner radius of the coil (R_i) on the magnetic coupling in different air-gaps (δ) [75].

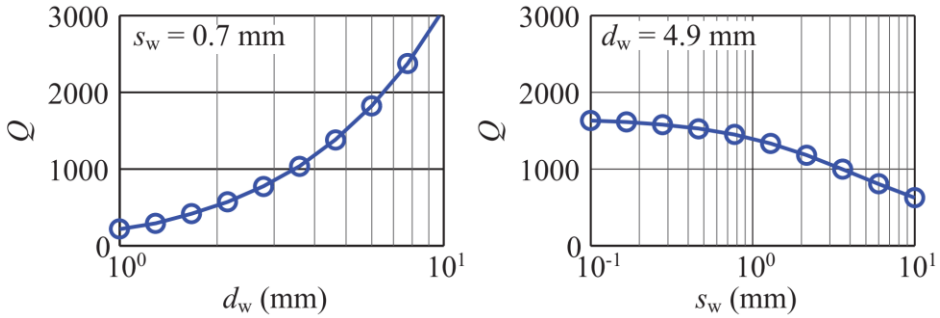

Fig. 2-20. The effect of the Litz wire diameter (d_w) and turn spacing (S_w) on the quality factor [75].

2.5. Pickup Converter

The induced voltage on the receiver coil of the wireless charging system passes through the receiver side resonant network and should be converted to a DC voltage to charge the EV battery. One of the simple methods to convert the high-frequency voltage to a DC voltage to supply the load is using passive rectifiers. In this case, the load voltage should be controlled by a primary side control method. For instance, phase-shifted control of the transmitter side inverter or controlling the amplitude of the input DC voltage can be considered [76].

In order to regulate the output voltage or current and realizing Constant Current (CC) and Constant Voltage (CV) modes in the battery charging process, DC-DC converters can also be considered [18]. Moreover, having DC-DC converters on the receiver side enables the WPT system to deliver power to multiple consumers at the same time [49]. In this case, each receiver regulates the output voltage based on the loading condition and misalignment of the magnetic couplers.

Fig. 2-21 illustrates a typical pickup converter. In this figure, the battery is modeled as a resistance ($R_o = V_{bat}/I_{bat}$), where V_{bat} and I_{bat} are the battery voltage and current, respectively. The equivalent AC resistance, R_{eq}, seen by the resonant network of the receiver side can be expressed by [26, 77]:

$$R_{eq} = \frac{8}{\pi^2} R_L \tag{2.6}$$

where R_L is the resistance seen by the diode bridge from the DC-DC converter. The equivalent resistance of the conventional buck and boost converters can be expressed by [78]:

$$R_L^{buck} = \frac{1}{D^2} R_o \tag{2.7}$$

$$R_L^{boost} = (1-D)^2 R_o \tag{2.8}$$

where D is the duty cycle of the DC-DC converter and R_o is the equivalent resistance of the battery.

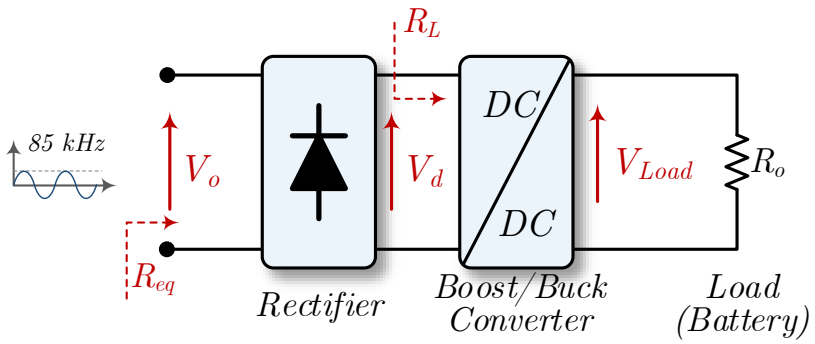

Fig. 2-21. A typical pickup converter of the EV wireless charging system.

Besides the conventional full-bridge rectifier in the AC-DC stage, a semi-active rectifier can be used [79, 80]. In this case, the output voltage can be control without using a DC-DC converter on the receiver side [81]. The schematic of the semi-active rectifier is shown in Fig. 2-22. In this figure, the two top devices are regular power diodes and the two bottom devices are power switches. By controlling the conduction time of the two switches, the output voltage can be controlled.

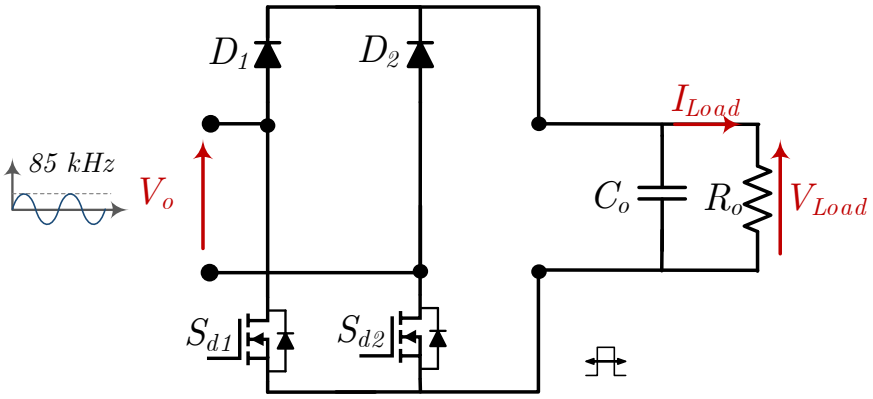

Fig. 2-22. A typical semi-active rectifier topology.

Nowadays, Vehicle to Grid (V2G) is considered as an option in smart grids. A WPT system also can be designed to be used in this operation mode. In [82], a bidirectional WPT system is proposed which is shown in Fig. 2-23. In this topology, instead of a regular diode-bridge, a full-bridge converter is used.

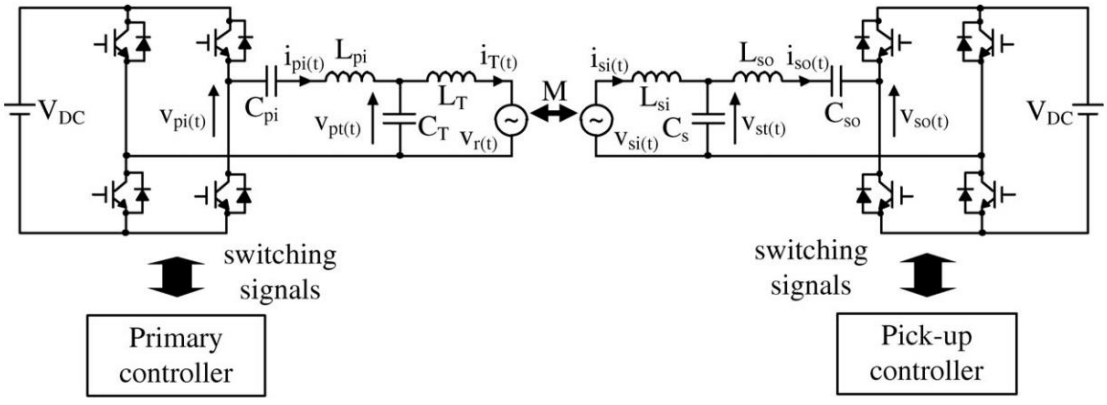

Fig. 2-23. Bidirectional WPT system [82].

2.6. Control Methods

Depending on the circuit topology, different control methods can be considered. For instance, if a DC-DC converter is used on the vehicle side, the inverter output voltage can only be dedicated to regulating the transmitter coil current and the DC-DC converter is responsible for regulating the output voltage. Typically, realizing soft-switching, safe operation under different loading conditions, and safe operation in case of the receiver coil absence are essential features that should be considered. In this case, a safe operation is referring to the limited output voltage and limited inverter current in any operating condition.

2.6.1. Primary Side Control

In the simplest case, a diode bridge can be used on the secondary side. In this case, the output voltage or output current should be controlled by the primary side converter. In this case, the following parameters can be used as a control variable [76]:

- Inverter phase-shift θ [25]
- DC-link voltage (V_{dc})
- Switching frequency (f)
- Inverter duty-cycle (D_{in})

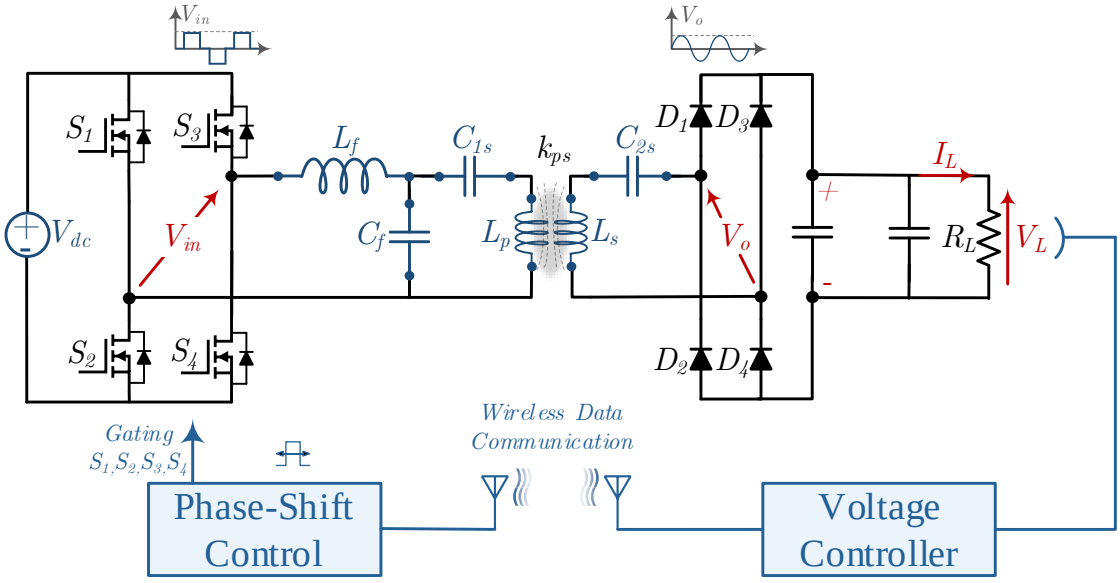

Fig. 2-24. Primary side phase-shifted control.

In the phase-shifted control of the primary side inverter, the phase angle between the inverter legs will be considered as a control variable. Fig. 2-24 illustrates the primary side control concept for the phase-shifted method. The output voltage of the inverter is a semi-rectangular waveform that its RMS value is dependent on the phase-shift (θ)[83]. When the phase difference is 180 degrees, the inverter voltage is a complete rectangular waveform with the amplitude of the DC-link voltage. When the phase-shift is set to 0 degrees the inverter legs will be synchronized and the output voltage of the inverter will be nullified.

Alternatively, the inverter can operate at a fixed 180 degrees phase-shift (conventionally) and the input DC-link voltage can be considered as a control variable as shown in Fig. 2-25. By changing the input DC voltage, the inverter

output voltage changes which affects the output voltage of the WPT system consequently. One of the drawbacks of this method is the requirement of a DC-DC stage to supply the inverter with a variable voltage which increases the implementation cost and complexity [76].

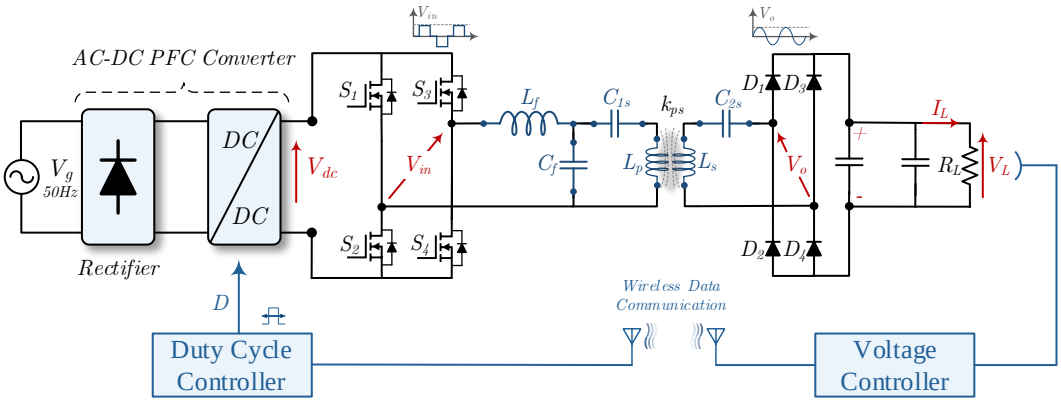

Fig. 2-25. Primary side DC-link voltage control.

The frequency control method can also be considered to control the output voltage of the wireless charging system. This method relies on the frequency response of the voltage gain (G_v) of the resonant network. However, typically the output voltage gain versus frequency shows a nonlinear behavior, especially when high-order resonant networks are used [84]. Moreover, the resonant element components should be rated for a wide range of frequencies which increases the implementation cost and possibility of interference with other signals [76]. Furthermore, different parasitic elements such as parasitic capacitance of the

magnetic couplers may be large in a specific range of frequencies. Therefore, the frequency control method is not preferable in practice.

The inverter duty-cycle (D_{in}) can also be considered as a control variable to change inverter RMS output voltage. However, in this case, it is possible to lose the soft-switching capability of the inverter [76]. It should be noted that having a soft-switching feature is essential for the wireless charging system to ensure maximum power transmission efficiency.

The primary side control method requires a reliable communication between the transmitter and receiver sides to send the output voltage feedback. The voltage feedback to the primary side generates the control signal for the full-bridge inverter (frequency or phase-shift) or the PFC stage (duty cycle). This can increase the complexity, reduce the reliability and generate a delay in the control loop which may affect the performance of the overall system [85, 86].

2.6.2. Secondary Side Control

In this control method, the primary side converter only regulates the primary side coil current (I_p) and the secondary side converter is responsible for controlling the output voltage (V_o). In [64], a boost converter is employed to regulate the output voltage. The main advantage of this method is the simplicity of the design

and supplying the battery in CC and CV modes. However, the number of components is increased in comparison with the primary side control method.

In [79, 87], an active rectifier is used to regulate the output voltage. Moreover, by varying the phase angle of the bridge current, mismatching of the resonant network is compensated to keep the system efficiency near to its maximum value [87]. The system efficiency is compared to the conventional methods and active rectifier in Fig. 2-26.

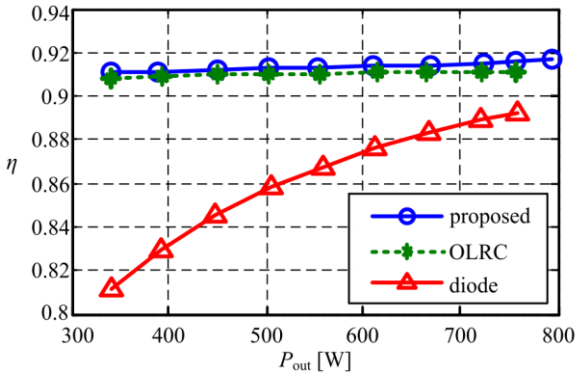

Fig. 2-26. Comparison of the efficiency of the active rectifier and conventional methods [87].

2.6.3. Dual Side Control

In [22], a dual-side control method is proposed for the WPT system by controlling the output voltage using a boost converter on the secondary side. This scheme is shown in Fig. 2-27. However, compared to a conventional WPT system the number of components and complexity are increased. Moreover, a

communication link between the transmitter and receiver is essential in this control method. This communication can introduce some delay in the control loop [85].

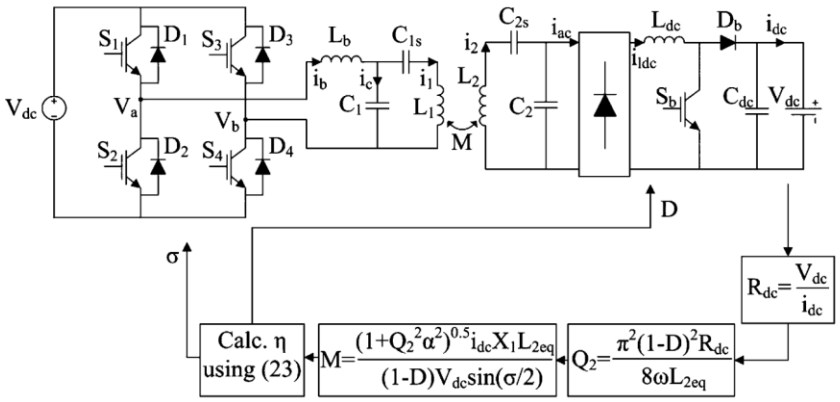

Fig. 2-27. Dual-side control with boost converter on the secondary side [22].

In order to reduce the number of components on the vehicle side, in [81], an active rectifier for the pickup converter is used to regulate the output voltage. Fig. 2-28 shows this configuration and its control method. Similar to other dual-side control methods, this configuration requires a communication link between the primary and secondary sides which can increase the control complexity.

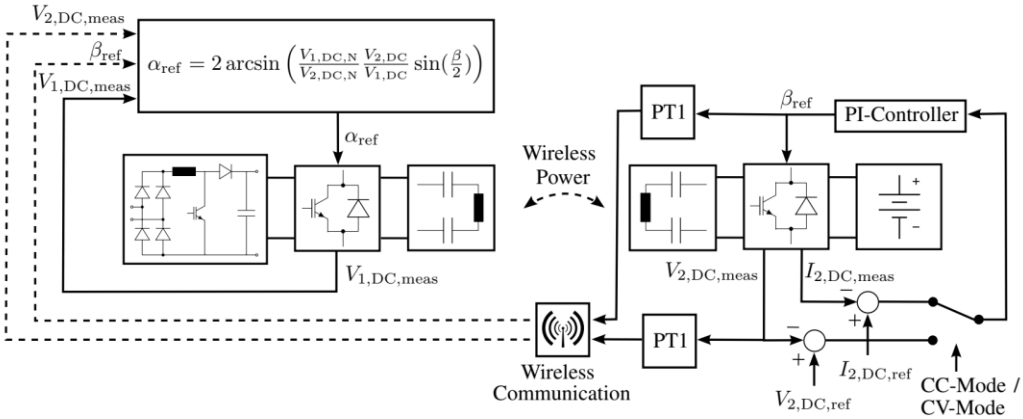

Fig. 2-28. Dual-side control with an active rectifier on the receiver side [81].

2.6.4. Decoupled Control

Transmitter side and receiver side converters are located on separated systems. Therefore, wireless communication is needed for controlling both converters from a central controller. In [88], a decoupled control scheme is proposed to eliminate the need for wireless communication. The concept of this control technique is shown in Fig. 2-29.

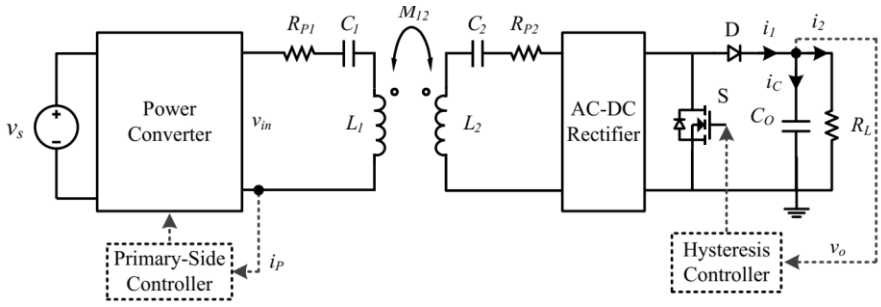

Fig. 2-29. Decoupled control for a Series-Series WPT system [88].

The decoupled concept proposed in [88] is also implemented using a Discrete Sliding Mode Control (DSMC) scheme in [89]. This method offers a faster dynamic response in comparison with the conventional PI methods. The dynamic response of the SMC and conventional PI controller is shown in Fig. 2-30.

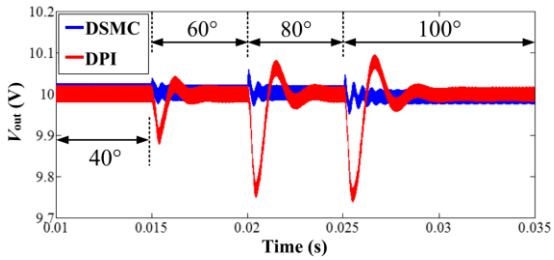

Fig. 2-30. Decoupled control with SMC in comparison with PI controller [89].

2.7. Design Challenges

In the following, the design challenges of a WPT system will be reviewed:

2.7.1. Misalignment Tolerance

The coupling factor (k) between the transmitter and receiver coils is highly dependent on the horizontal and vertical distances of the two coils. Fig. 2-31 illustrates the definition of the air-gap and misalignment of an inductive WPT system for EV charging applications.

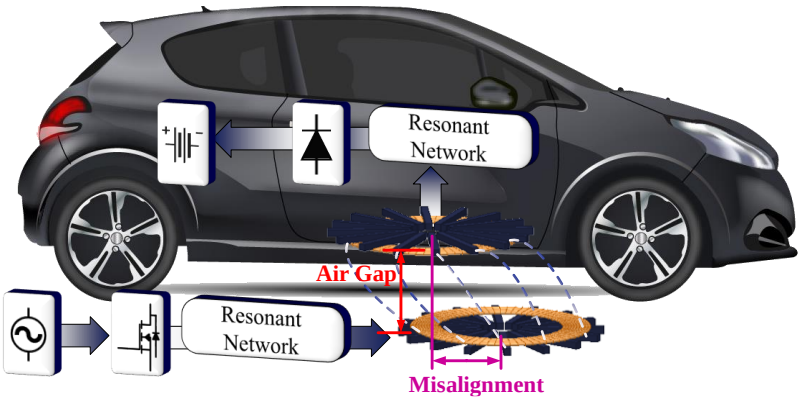

Fig. 2-31. A typical EV wireless charging system.

Occurring misalignment between the transmitter and receiver coils is inevitable in the wireless charging of the EVs. Misalignment of the magnetic couplers results in the variation of coupling factor, k, from its nominal value which affects the output voltage and efficiency of the overall system [11, 24]. In order to overcome the aforementioned issues, two approaches are studied:

1) Output voltage control through control of power converters on the primary and secondary sides [28, 90], and

2) Optimal design of resonant network [91-93].

These methods are employed to supply the load with a constant voltage independent of the coupling factor changes. Control of the power converters either on the transmitter side or the receiver side of the WPT system can help to regulate the output voltage [28, 88, 94, 95]. On the primary side, by phase-shifted control of a full-bridge inverter, the output voltage can be regulated [25, 96]. However, in this method, reliable communication between the primary and secondary sides is essential to send the output voltage feedback to the primary side and control the full-bridge inverter. This can also generate a delay in the control loop which may affect the performance of the overall system [85]. An active rectifier can also be used on the secondary side instead of a passive diode bridge to regulate the output voltage [28, 87, 97]. The main advantage of this method is to control output voltage without the need for communication between the primary and secondary side converters. However, this method increases the complexity and cost of the system [98, 99].

Another solution is to regulate the output voltage through the use of a DC-DC converter after the passive diode-bridge rectifier on the secondary side. The DC-

DC converter can help to regulate the output voltage while the coupling factor is changing [69, 80, 100]. The main advantage of this method is that it can be used without the need for a communication link between the primary and secondary side converters.

A. Tuning of the Resonant Network

The self-inductances of the magnetic couplers are changed when misalignment occurs which results in lower efficiency and variation in the voltage gain of the system. In [101], a variable-tuning LCL pickup converter and an active variable inductor implementation are introduced. A similar approach is introduced in [102, 103], in which, the primary side resonant inductor of the LCC network is considered as a variable inductor to keep the inverter at the optimal switching point.

Another method of active tuning of the resonant network is using switching capacitors [104-106]. In this approach, a fixed size capacitor is switched in PWM mode to form a variable capacitor.

In [107], a dual-side control with online mutual inductance estimation is implemented is shown in Fig. 2-32 (a). In this method, the output voltage is regulated by the inverter, and active rectifier ensures the maximum power delivery. The efficiency comparison between a regular diode-bridge pickup converter (green),

a dual-side controlled system (blue), and the switched controlled capacitor (red) is shown in Fig. 2-32 (b).

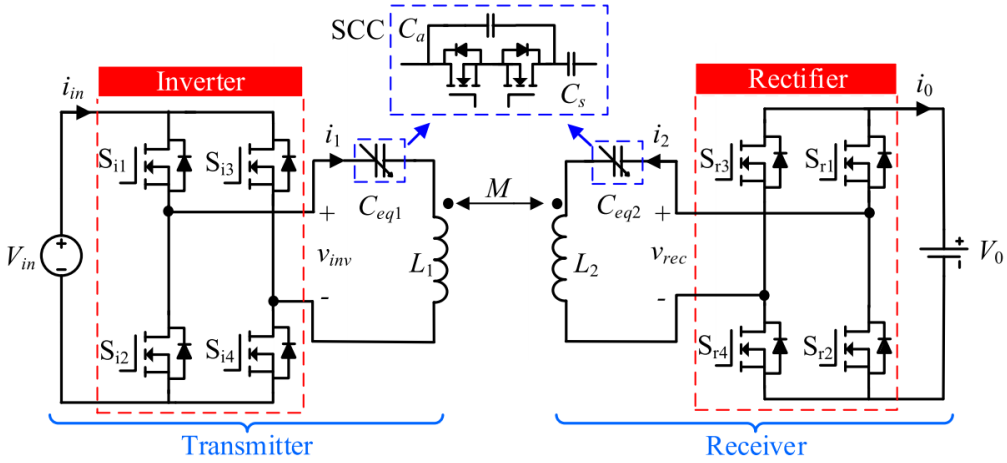

(a) Schematic of the WPT system with dual SCC

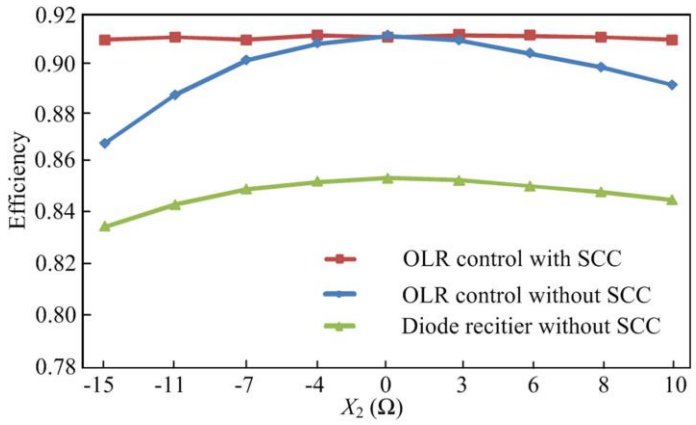

(a) Efficiency comparison

Fig. 2-32. Combination of the switched controlled capacitor (SCC) and dual-side control method [107].

B. Hybrid and Reconfigurable Resonant Topologies

Hybrid topologies combine the benefits of each resonant topology and gain a robust system against the coupling factor and load variations. For instance, a Series and LCC topology can be combined in both the transmitter and receiver of a WPT system to provide constant power over a wide range of misalignment [108]. In such a system as the misalignment increases, the input current of the Series resonant network branch will be increased inherently. Therefore, the total transmitted power to the secondary side will remain constant.

Instead of continuous tuning of the resonant network (active tuning), a reconfigurable topology can also be used. In this approach, the resonant topology will be changed between a limited number of configurations. Compared to the switched controlled capacitor method, the reconfigurable topologies do not require a PWM switching of the resonant elements. Thus, the control complexity and cost will be reduced. In [109], a reconfigurable topology is proposed which switches between the S-S and S-LCC to implement CC and CV modes respectively. This topology is shown in Fig. 2-33. The main advantage of this method is achieving inherent CV and CC without using any DC-DC converter in the output of the system. Therefore, this topology can be used in a fixed coupling factor condition for a wide range of load variations such as battery charging applications [109-111].

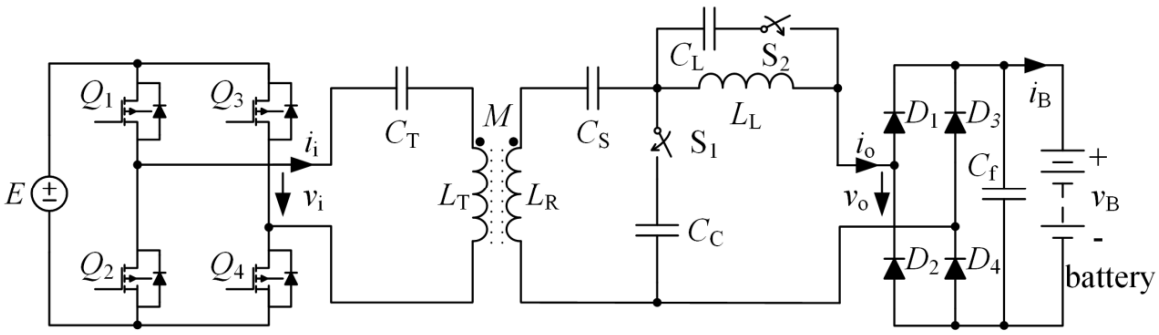

Fig. 2-33. A reconfigurable resonant topology that switches between SS and S-LCC [109].

The hybrid topology and reconfigurable resonant network can also be combined and form a robust resonant network against both the misalignment and load variations [112]. The schematic of this circuit is shown in Fig. 2-34. This circuit combines the LCC-S and S-LCC topology and supplies the load in CC or CV modes for a wide range of load and coupling factor variations.

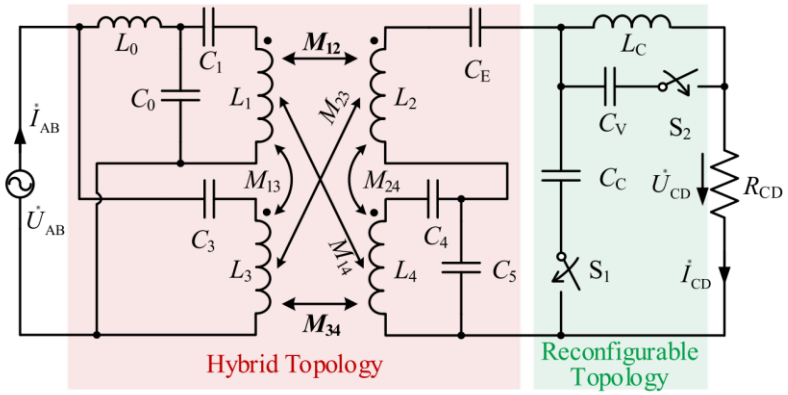

Fig. 2-34. Combination of the switched controlled capacitor (SCC) and dual-side control method [112].

C. Resonant Network Tuning and Optimization

Regardless of the resonant topology selection, tuning of the resonant network plays a vital role in achieving the desired power transmission efficiency, output features (CC or CV mode), and ZVS operation. Fig. 2-35 illustrates different tuning methods that can be considered for designing a resonant network for EV wireless charging applications.

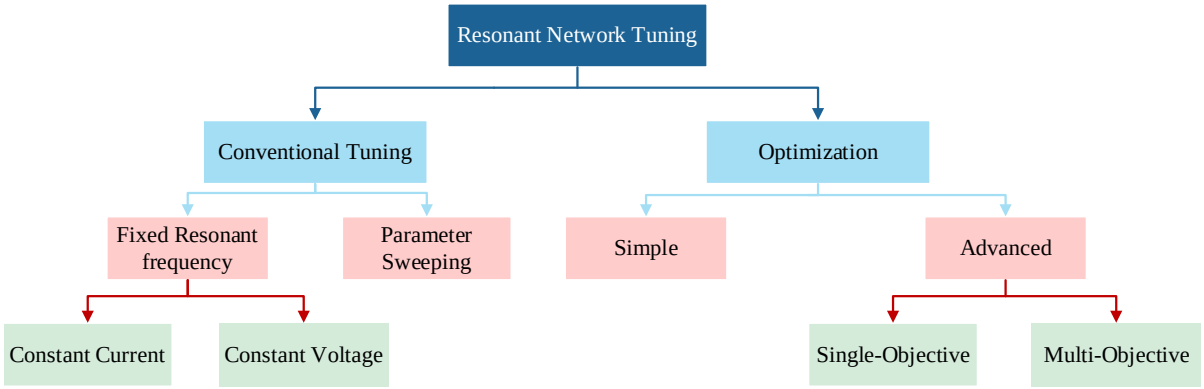

Fig. 2-35. Tuning methods of the resonant networks in WPT systems.

Conventionally, the resonant elements are selected to resonate at a fixed operation frequency, or by parameter sweeping desired output features are achieved. There are several drawbacks in tuning the resonant network by conventional methods that worth mentioning. First, by increasing the number of resonant elements and non-linear behavior of the system, conventional methods are time-consuming and require multiply try and errors. Second, it is not guaranteed that the final solution is the best possible solution. Third, the losses of the resonant

network, inverter, and other elements are not considered [55]. Finally, practical constraints and objectives cannot easily be included in conventional methods [55].

On the other hand, an optimization problem can be defined to select the resonant elements. In basic optimization methods, a lossless, simplified model, and single objective is considered in the optimization problem. For instance, in [99], a detuned S-S topology, and in [40] the LCC-S topology is designed to offers less output power variation respect to the coupling factor variation. However, in both studies, the losses of the system, variation of the self-inductance of the magnetic couplers were not included. Similarly, in [113], a general T-type resonant network is analyzed and the tuning method to achieve a misalignment tolerant output power is presented. In [114], the resonant capacitor of a four coil system is optimally selected to supply the load with a stable output power over a wide range of coupling coefficients. However, the losses of the system are not included completely and it requires two additional passive repeaters.

In advanced optimization of the resonant networks, the boundaries of the system, losses, and multiple objective functions can be included. In [115], a particle swarm optimization method with the objective function of load and coupling factor independent output behavior is presented for an S-CLC compensated WPT system. The same objective function is used in [116] for an S-SP compensated system to achieve load-independent and misalignment tolerant features. However, in both

studies, the primary side resonant network is a Series type that suffers from unbounded current in case of load absence. To improve the optimization of the resonant network, the losses of the coils for an LCC-S topology are also included in the optimization problem in [44]. Although the output power fluctuation reduced, the efficiency of the system was not accurately calculated due to the lack of the inverter and core loss modeling in the optimization problem. Table 2-3 summarizes and compares different tuning methods from different aspects. In this table, β is a sensitivity index defined as the ratio of the output fluctuation ΔU [%] to the magnetic coupling factor variation Δk [%]. Since each reference had different rated values, this index can be used to simplify the comparison. Lower β can be interpreted to lower output sensitivity to misalignment.

TABLE 2-3
COMPARISON OF THE TUNING METHODS

Ref.	Topology	Optimization Method	Reported Output	Robustness Against	Core Loss Inclusion	Inverter Loss Inclusion	Coupling Factor Variation Δk [%]	Output Fluctuation ΔU [%]	Sensitivity Index β
[99]	S-S	Basic	CP	Misalignment	NO	NO	60	21	0.35
[40]	LCC-S	Basic	CP	Misalignment	NO	NO	44	7.1	0.16
[117]	S-SP	Basic	CV	Misalignment and Load	NO	NO	28.5	2.7	0.09
[115]	S-CLC	Advanced	CV	Misalignment and Load	NO	NO	50	11.7	0.23
[116]	S-SP	Advanced	CV	Misalignment and Load	NO	NO	50.8	8.9	0.18
[44]	LCC-S	Advanced	CP	Misalignment	NO	NO	37.1	8.6	0.23

To reduce the misalignment effect on the output voltage and efficiency of a wireless charger system, an optimization-based design procedure for the resonant networks of the WPT system is proposed and studied in Chapter 3.

2.7.2. Efficiency

In order to gain the highest efficiency from a WPT system, the quality factor of the coils should be as high as possible [24, 57]. Fig. 2-36 shows the typical efficiency of the WPT system versus different quality factors under different coupling coefficients. Both the quality factor (Q) and coupling coefficient (k) can affect the system efficiency.

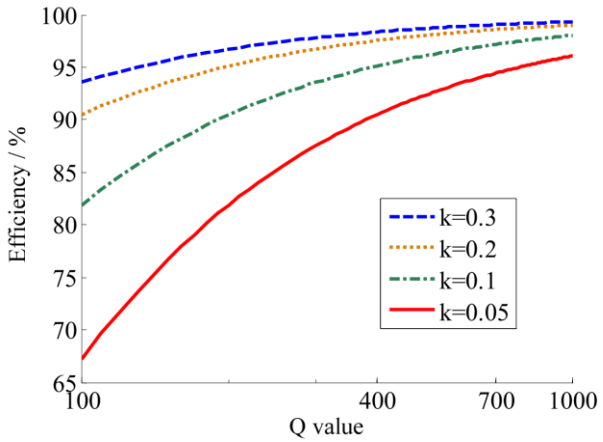

Fig. 2-36. The theoretical efficiency of the WPT system [24].

For instance, the maximum transferable power efficiency of a WPT system with a Series-Series resonant network can be calculated as follows [24]:

$$\eta_{\max} = \frac{\left(kQ\right)^2}{\left(1+\sqrt{1+\left(kQ\right)^2}\right)^2} \tag{2.9}$$

where k is the coupling coefficient and Q is the quality factor of the magnetic couplers.

Typically, the coupling factor increases as the size of the magnetic coupler increases. The quality factor of the magnetic coupler is dependent on the coil AC resistance, frequency, and coil self-inductance. To reduce the AC resistance, a higher wire gauge with smaller strands is required. Generally, in a conventional WPT system, the power density and efficiency are in the opposite direction of the design objective. Therefore, a trade-off between power density and efficiency is essential. To address this trade-off, a multi-objective optimization problem is defined in [33] to select the optimal design. In this optimization, power density (a) and system efficiency (η) are considered as the two objective functions. Fig. 2-37 presents the optimization results for different quality factors, operation frequencies, and coupling coefficients. Every point on the Pareto front is the optimal solution to this problem and the selection of the optimal point is based on the designer experience and desired profiles such as efficiency or power density.

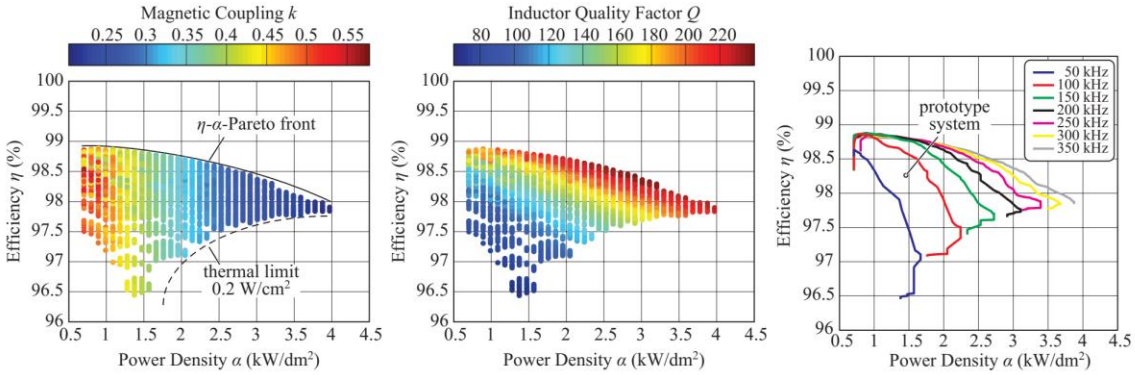

(a) Coupling factor effect (b) Quality factor effect (c) Frequency effect

Fig. 2-37. Multi-objective Pareto optimization of the WPT system [64].

According to Fig. 2-37 (a), as the power density increases the maximum achievable efficiency decreases. Moreover, Fig. 2-37 (b) shows that increasing the quality factor of the coils generally results in having more power density for the system. The increase of the quality factor can be achieved by increasing the switching frequency. The effect of the switching frequency on the system efficiency and power density is shown in Fig. 2-37 (c). This figure shows that increasing the switching frequency from 50 kHz to 100 kHz has a significant influence on improving the system efficiency [64]. However, by increasing the switching frequency beyond 100 kHz, the system efficiency is not affected significantly. Moreover, by increasing the switching frequency gate driver losses are also increases which are not considered in this figure [64]. Also, by increasing the switching frequency, a thinner strand of the Litz wire is needed. However, thinner Litz wires cost more and they are rarely available in the market [64]. Considering these points,

a designer will select an optimal point that meets the desired practical requirements.

In Chapter 3, an optimal procedure is developed to demonstrate how to design the resonant network components to achieve high efficiency.

2.7.3. Power Density

In order to reduce the WPT design size, and increase the power density of the whole system, a new design of magnetic coupler called integrated magnetic structure is proposed in [118-123]. In this design, the inductor of the LCC resonant network is integrated with the magnetic couplers. In [123], a DD coil topology is used for the main WPT magnetic couplers and the resonant network inductance is made by another DD coil, shown in Fig. 2-38. The whole structure is made of three mechanical layers. Moreover, design procedures, different mode analysis, and capacitor tuning methods are presented in [118].

The main challenge of the WPT systems with integrated resonant inductor is the difficulty of the design caused by the interaction of the main coils with the integrated resonant coils. Therefore, in [119], a new simplified resonant network design method for the integrated WPT system is presented. The study in [119] was performed on an integrated WPT system with bipolar main coils and rectangular resonant coil. Similarly, a bipolar layout is used for both the main and integrated

coils on the receiver side [120]. In these topologies, the materials used in the magnetic couplers will be shared with the main coils.

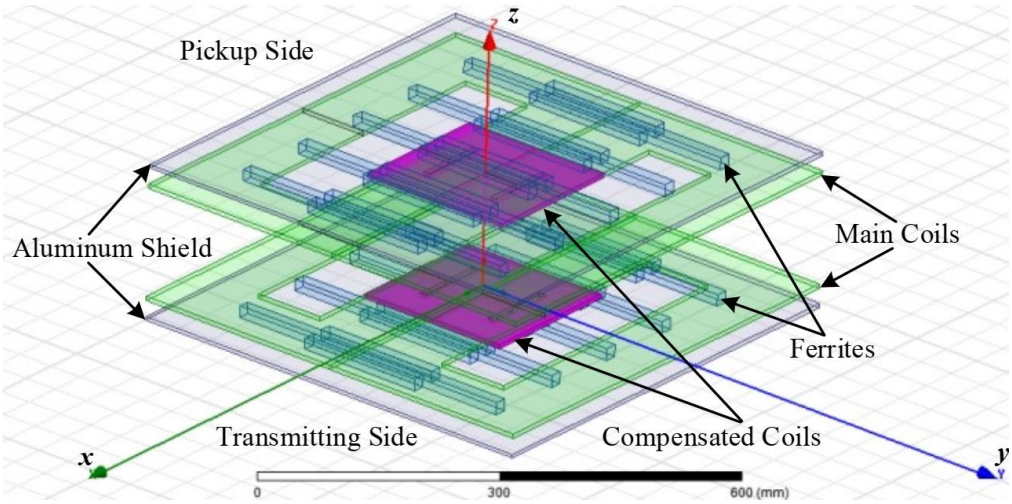

Fig. 2-38. Integration of the LCC inductor into the magnetic coupler [123].

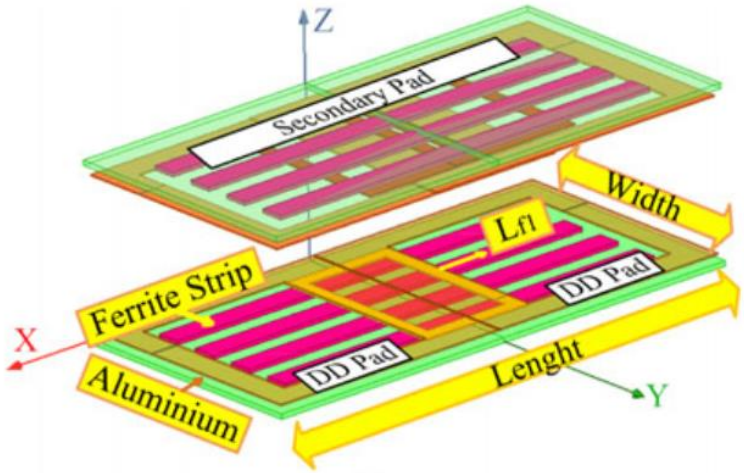

Fig. 2-39. Integration of the LCC inductor into the bipolar magnetic coupler [120].

On the other hand, the pickup converter is placed on the vehicle to convert the high-frequency induced voltage on the receiver coil to a DC voltage for charging the batteries. Typically, a DC-DC converter is used to regulate the output voltage

and provide constant current (CC) and constant voltage (CV) modes for charging the batteries for EV applications [49]. Using a DC-DC converter on the vehicle side enables the system to have a different DC-link voltage from the output (battery pack). However, the DC-DC stage requires an inductor to supply the load which affects the size, weight, and cost of the receiver on the EV side. In order to improve the power density of the pick-up, a new integrated structure which integrates the DC-DC inductor into the magnetic coupler is introduce in Chapter 4 of this thesis.

In order to further improve the power density of the transmitter side, Printed Circuit Board (PCB) can be used instead of wire-wound coils. The PCB magnetic coupler can simplify production, reduce labor work, weight and cost; however, the existing PCB coils are limited to low-power WPT systems. The main challenges and limiting factors for moving toward the high-power applications are coil AC resistance, high-frequency operation, thermal management due to conduction loss, and the large size of the coil. These challenges are studied in Chapter 5 and a solution with a comparable efficiency is provided.

2.7.4. High-Power Wireless Charging

In high-power wireless charging applications, such as electric buses, a high-power transmitter circuit to supply hundreds of kW is a requirement [18]. To increase the output power level of a wireless power transfer system, the transmitter

side inverter power rating should be increased. Increasing the power rating of the inverter could be achieved by increasing the rating of the semiconductors, using the multilevel topologies [124-126], and modular structures [127].

Currently, the voltage rating of high-frequency switches such as SiC devices is limited in commercialized products. Moreover, at high voltage operation, the dv/dt and maximum current rating of the switches are other limiting factors [128]. Furthermore, the cost of the inverter switches increases significantly by increasing the switch ratings. Alternatively, parallel switches can be used to increase the current rating. However, careful design of the gate driver circuit and active control of the switches is essential to avoid device failure [129, 130]. Moreover, in case of failure in one of the switches, all the inverter switches will be involved. Therefore, using parallel switches to increase the current rating may reduce the reliability of the system and increase the complexity of the control.

By using multilevel topologies, the voltage rating of each semiconductor switch will be reduced [131]. In [132], a multilevel topology for the WPT system by a combination of IGBT and MOSFET switches is proposed to increase the power rating of the inverter, shown in Fig. 2-40. Similarly, a new multilevel topology is proposed in [133]. However, the requirement of bulky flying capacitors, the complexity of control and modulation, uneven loss distribution, losing the soft-

switching capability are a few examples of the disadvantages of the multilevel topologies for wireless charging applications [131].

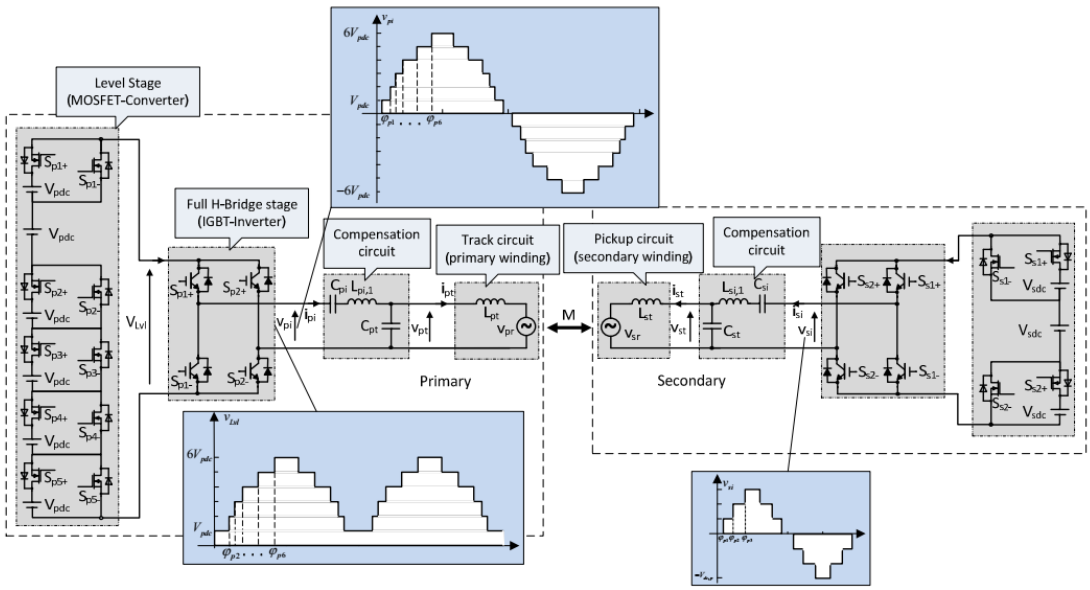

Fig. 2-40. Hybrid multilevel WPT system [132].

Alternatively, in [134, 135], a multiphase structure is proposed for wireless charging applications, shown in Fig. 2-41. This structure is constructed by a half-bridge and a series capacitor for each phase. In order to limit the circulating current between the legs of the multi-phase inverter, Intercell Transformers (ICT) are used. The optimization of this modular structure and increased power level is studied in [128]. It should be noted that in this system, the phase angle of the voltage of each phase can be controlled to regulated the output voltage. Similarly, an extended version of the multi-phase topology with ICTs is proposed in [136], and modeling and control of this topology are studied in [137].

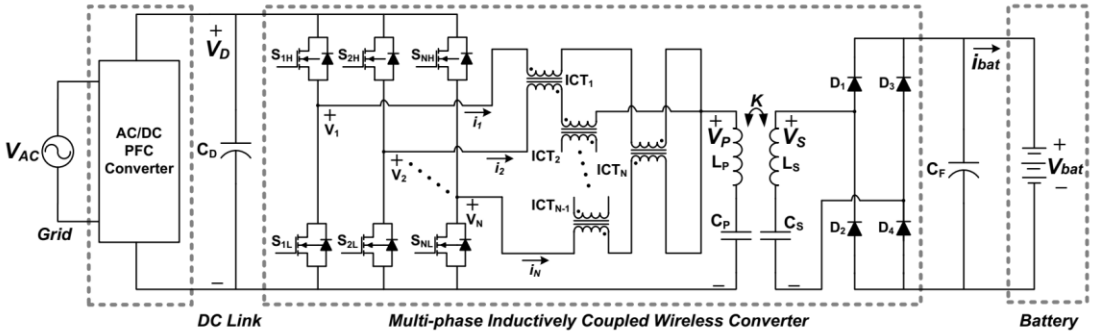

Fig. 2-41. Multi-phase inductively coupled WPT system [134].

Although the circulating current can be eliminated by using ICTs, the implementation cost and complexity of the system are increased. Moreover, because of using the series resonant topology, the transmitter side of the wireless charging system has an unbounded inverter current when the vehicle side is in absence. In another word, in the case of the absence of the receiver coil, the reflected impedance would be zero which puts the transmitter side in the short-circuit operating condition [11]. This could damage the switches, transmitter coil, and resonant capacitors.

In [138], multi-parallel H-bridge converters are proposed for a WPT system. This configuration is suitable for high-power charging applications to feed each resonant converter by a separated H-bridge inverter to minimize the VA rating of each converter. Moreover, the modularity of the converter is another benefit of this topology [11]. This topology is shown in Fig. 2-42. Although the modularity is realized, designing a modular magnetically decoupled structure is a challenge for

this topology. For instance, the transmitter coils should have a large spacing to have a low cross-coupling. Therefore, this configuration can be used for electric train applications where space is less restricted.

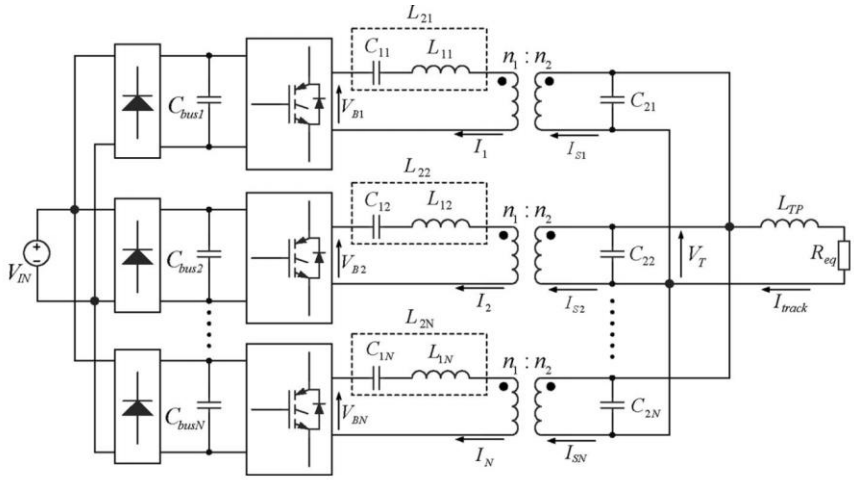

Fig. 2-42. Parallel H-bridge primary side converters for WPT system [138].

In order to eliminate the bulky DC-link capacitors and diode bridge of the transmitter side inverter, a direct Matrix converter can be used [139-142]. Initially, in [142], a low power matrix converter for WPT systems is proposed which is shown in Fig. 2-43.

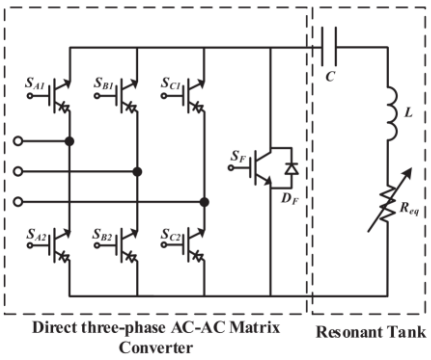

Fig. 2-43. Matrix converter for a WPT system [142].

Similarly, in [141], a bidirectional Matrix converter is proposed for WPT application which is illustrated in Fig. 2-44. This converter can operate in a grid-connected application to transfer the stored energy from the vehicle to the grid. This converter is implemented on a 1 kW/ 20 kHz WPT system. The reported maximum efficiency of this converter with the DD magnetic couplers at a 17 cm gap (k=0.29) is 89%. The drawback of this configuration is that it is only applicable to low-power systems [11].

To address the aforementioned problems, Chapter 6 proposes a new modular inverter based on the LCC resonant network.

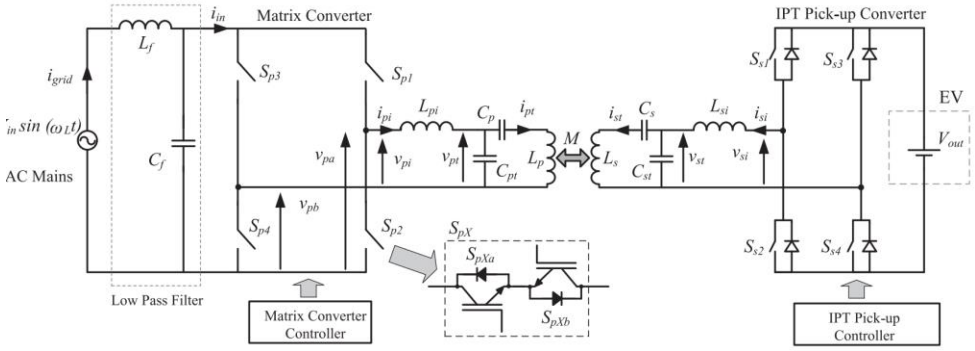

Fig. 2-44. Matrix converter for a WPT system [142].

2.8. Conclusion

In this chapter, the fundamentals of wireless charging were reviewed in detail. The main components of the wireless charging system including the magnetic couplers, resonant networks, transmitter, and pickup converters were studied in detail. An overview of the conventional topologies for each component of the system

was presented. The advantages and drawbacks of each design were outlined, and the design challenges of the state-of-the-art solutions were discussed and analyzed.

It was concluded that circular and rectangular magnetic couplers are more preferable for stationary EV wireless charging applications due to higher power density and lower power loss. By comparing different resonant topologies, it was shown that basic topologies are not satisfying all the requirements of EV wireless charging applications. Moreover, active tuning and hybrid topologies suffer from lower reliability and increase the complexity of the system. Therefore, high-order resonant networks should be optimally designed to maximize efficiency and offer a misalignment tolerant WPT system. Requirements of the power converters for high power EV wireless charging applications were discussed and it was concluded that the intercell transformers are the main drawback of the existing modular topologies for EV wireless charging applications.

Chapter 3

Optimal Design of the Resonant Networks for EV Wireless Charging Systems Respect to Misalignments

3.1. Introduction

As discussed in the previous chapter, misalignment is a big challenge in EV wireless charging systems. To reduce the misalignment effect on the output voltage and efficiency of the wireless charger system, an optimization-based design procedure for the resonant networks of the WPT system is proposed in this chapter. The proposed method is based on the optimal tuning of the resonant network without adding any extra element to the circuit. The proposed design method is

applied to four possible combinations of LCC and Series topology on the primary and secondary sides.

According to comparison studies presented in Chapter 2, the LCC and Series resonant networks are the possible candidates for the EV wireless charging applications. The outstanding constant output current of the LCC topology, its wide range ZVS operation, and high efficiency profile in different loading conditions are the main advantages of this topology. The constant output voltage, simplicity of design, high efficiency, and a low number of components are the attractive features of the Series resonant network. Therefore, different combinations of the LCC and Series resonant networks are considered in this chapter: S-S, S-LCC, LCC-S, and LCC-LCC.

All the topologies are optimized to operate at the same design conditions such as power level, magnetic couplers, and input/output voltage to have a fair comparison between all of these topologies. Two optimization problems are defined;

1) optimal design of the resonant network to achieve constant voltage at different loading conditions (Case I),

2) optimal design of the resonant network to achieve maximum efficiency at different loading conditions (Case II).

In Case I, the proposed optimized circuit results in achieving low voltage variation versus coupling factor, k. A constant voltage in the output of the WPT system can be beneficial to eliminate the DC-DC conversion stage at the output. If a well-regulated output voltage is needed, a DC-DC converter can be added at the secondary side. The proposed method still can help to design the power converter optimally. This is because a constant voltage on the receiver circuit helps the DC-DC converter to maintain its optimal designed duty-cycle and helps to operate at its maximum efficiency for a wide range of coupling and load variations [85]. Moreover, the size of the required passive components like the dc-link capacitors on the secondary side can be reduced [117].

In Case II, the efficiency-oriented optimization is presented. The results of both cases outline a general conclusion and show the trade-off between these two objectives. Therefore, this comparison can help to select the topology according to the objective requirements.

The chapter is structured in five sections: in Section 3.2, analytical models for each circuit topology are extracted and output voltage sensitivity functions are developed. In Section 3.3, at first, the design procedure is explained and the optimization problem is defined. Then, a case study is considered and each topology is optimized and studied. The output voltage profiles, efficiency, resonant network

size, and power loss distribution of each topology are presented for each objective function. Experimental results are presented in Section 3.4 to compare the results with simulation studies and validate the design and optimization procedure. Finally, conclusions are outlined in Section 3.5.

3.2. Circuit Modeling and Sensitivity Analysis

As discussed, a WPT system consists of three main parts: an inverter, resonant networks, and magnetic couplers. The load in the EV charging application can be considered as an equal resistance at each output power (R_L). The circuit diagram of a typical WPT system with a full-bridge inverter and a simple diode rectifier is illustrated in Fig. 3-1.

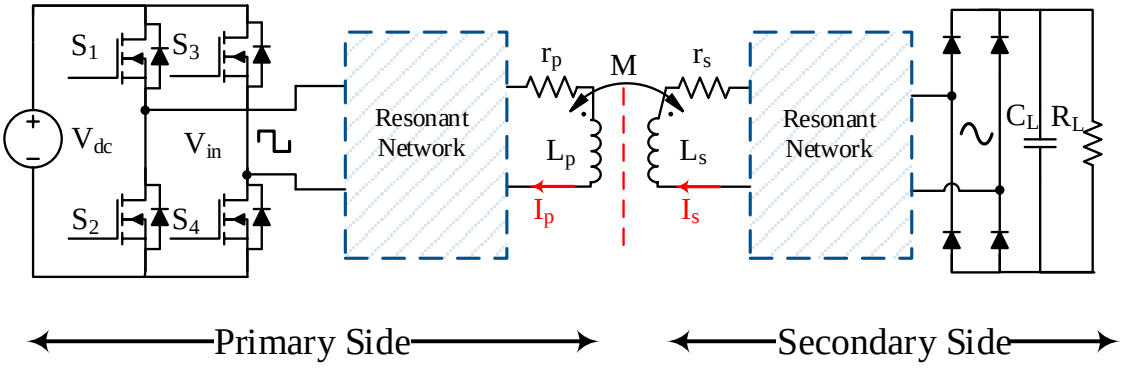

Fig. 3-1. Circuit diagram of a typical WPT system.

In this figure, L_p and L_s are the primary and secondary side coil self-inductance respectively. M is the mutual coupling of the couplers and the coupling factor for the coils is defined as: $k = M/\sqrt{L_p L_s}$. Moreover, r_p and r_s are the parasitic AC

resistance of the coils. The AC resistance of the coils reduces the coil quality factor which has a significant effect on the system maximum efficiency.

To reduce the complexity of the analysis and design, commonly Fundamental Harmonic Analysis (FHA) is used for resonant converters. In this method, only the fundamental harmonic of the generated voltage of the inverter is considered. The RMS value of this waveform is calculated as $V_{in}^{rms} = (2\sqrt{2}\mathrm{V}_{\mathrm{dc}}/\pi)\sin(\theta/2)$ [26]. In this equation, θ is the phase shift applied on the inverter legs. This phase shift controls the RMS value of the input voltage and can be used in the control loop. Similarly, the equivalent AC resistance seen by the secondary side from the diode bridge is expressed as $R_{eq} = 8/\pi^2 R_L$ [26]. The magnetic couplers can also be replaced by a T-type model. Fig. 3-2 shows the simplified circuit diagram of the WPT system with two unknown resonant networks.

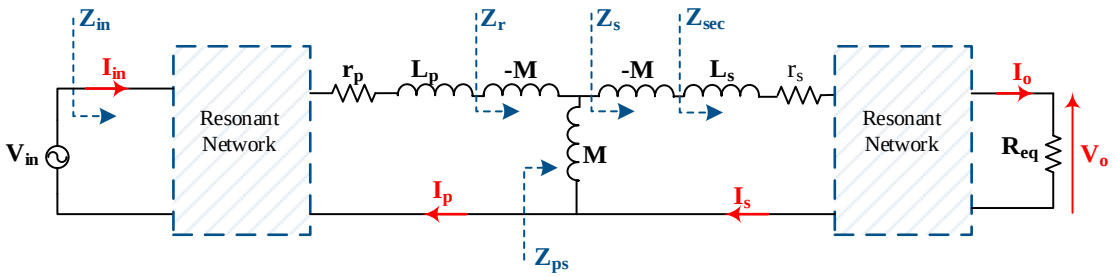

Fig. 3-2. Equivalent circuit diagram of the WPT system.

In this figure, the fundamental harmonic of the voltage generated by the inverter is replaced by the voltage source (V_{in}). The reflected impedance from the secondary side to the primary circuit, Z_r, is defined as follows:

$$Z_r = \left(Z_s \,||\, j\omega M\right) - j\omega M = \frac{\left(M\omega\right)^2}{Z_{\text{sec}}} \tag{3.1}$$

where ω is the angular frequency of the fundamental harmonic of the inverter voltage. To further analyze the circuit, the resonant topologies need to be known. In the following, four combinations of LCC and series networks are studied in detail and the sensitivity function of the output voltage with respect to the mutual impedance (M) is derived. As discussed in Chapter 2, the misalignment of the transmitter and receiver coil results in variation of the mutual inductance from its nominal value.

3.2.1. Series-Series Topology

In this configuration, both the primary and secondary side resonant networks are simple series capacitors (C_{s1} and C_{s2}) as shown in Fig. 3-3.

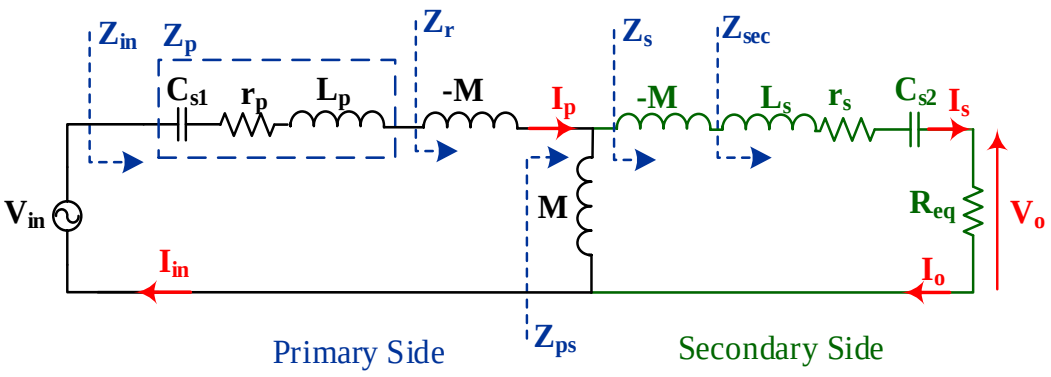

Fig. 3-3. A WPT system with Series-Series resonant network.

In this circuit, the impedance seen by the secondary side coil, Z_{sec}, is expressed as:

$$Z_s = Z_{\text{sec}} - \omega M j \tag{3.2}$$

where

$$Z_{\text{sec}} = R_{eq} + r_s + \left(L_s\omega - 1/\omega C_{2s}\right)j$$

The input impedance of the circuit seen by the inverter (Z_{in}) is given as:

$$Z_{in} = Z_r + Z_p = r_p + j\left(L_p\omega - 1/\omega C_{1s}\right) + Z_r \tag{3.3}$$

Using the defined impedances of the circuit, the input current (I_{in}), primary side current (I_p), and secondary side current (I_s) are derived as:

$$\begin{cases} I_{in} = I_p = \dfrac{V_{in}}{Z_{in}} \\ I_s = I_{in}\dfrac{j\omega M}{Z_s + j\omega M} = I_{in}\dfrac{j\omega M}{Z_{\text{sec}}} \end{cases} \tag{3.4}$$

Since the output current, I_o, is equal to the secondary side coil current, the output voltage can be expressed as:

$$V_o = R_{eq} I_s = I_p \frac{j\omega M R_{eq}}{Z_{\text{sec}}} \tag{3.5}$$

The output voltage sensitivity with respect to the mutual inductance variation is derived as follows:

$$\frac{\partial V_o}{\partial M} = \frac{R_{eq}\omega}{Z_{\text{sec}}}\left(I_p + M \frac{\partial I_p}{\partial M} \right) \tag{3.6}$$

As it can be seen, the sensitivity of the voltage is dependent on both the variation of M and I_p. The variation of primary side coil current is calculated as:

$$\frac{\partial I_p}{\partial M} = V_{in}\left(\frac{\partial Z_{in}^{-1}}{\partial M} \right) = \frac{-V_{in}}{Z_{in}^2}\left(\frac{\partial Z_r}{\partial M} \right) \tag{3.7}$$

where the variation of reflected impedance is calculated as:

$$\frac{\partial Z_r}{\partial M} = \frac{\partial\left(\frac{(M\omega)^2}{Z_s} \right)}{\partial M} = \frac{2M\omega^2 Z_s - (M\omega)^2 \frac{\partial Z_s}{\partial M}}{Z_s^{\,2}} = \frac{2M\omega^2 Z_s + j(M\omega)^2 \omega}{Z_s^{\,2}} \tag{3.8}$$

By putting (3.7) and (3.8) into (3.6), the variations of the output voltage, $\partial V_o / \partial M$, is simplified as:

$$\frac{\partial V_o}{\partial M} = \frac{jR_{eq}\omega V_{in}}{Z_{in} Z_{\text{sec}}}\left(1 - \frac{M}{Z_{in}}\left(2M\omega^2 + j\frac{(M\omega)^2}{Z_s} \right) \right) \tag{3.9}$$

Eq. (3.9) shows the sensitivity of the output voltage respect to the mutual coupling.

3.2.2. LCC-Series Topology

In this topology, an LCC resonant network and a series capacitor are considered for primary and secondary circuits, respectively, as shown in Fig. 3-4.

In this topology, secondary impedances are the same as Series-Series topology. The circuit input impedance is given by:

$$Z_{in} = r_1 + j\omega L_1 + Z_{pin} \tag{3.10}$$

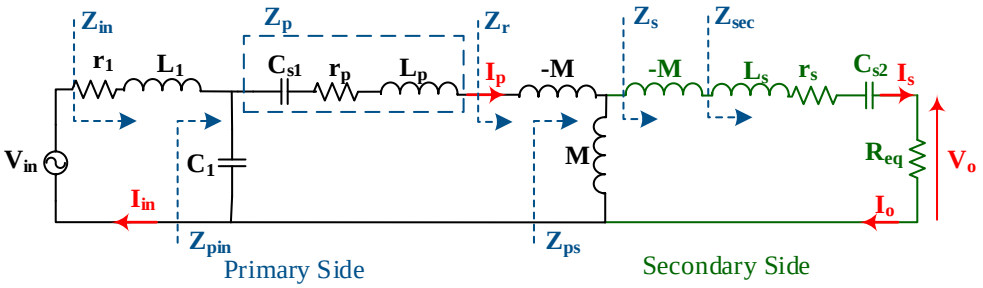

Fig. 3-4. A WPT system with LCC-Series resonant topology.

where the parameter Z_{pin} is obtained as follows:

$$Z_{pin} = \left(Z_r + Z_p\right) \| \frac{1}{j\omega C_1} \tag{3.11}$$

The reflected impedance is defined for a general resonant network in (3.1), and I_{in}, and I_p, and I_s are given by:

$$I_{in} = \frac{V_{in}}{Z_{in}} \tag{3.12}$$

$$I_p = I_{in} \frac{1}{1 + j\omega C_1 \left(Z_p + Z_r\right)} \tag{3.13}$$

$$I_s = I_p \frac{j\omega M}{Z_s + j\omega M} = I_p \frac{j\omega M}{Z_{\text{sec}}} \tag{3.14}$$

Since, the secondary side of this topology is the same as Series-Series topology, the output voltage, and its sensitivity function are obtained similarly and can be expressed as:

$$\frac{\partial V_o}{\partial M} = \frac{jR_{eq}\omega V_{in}}{Z_{in}Z_{\text{sec}}}\left(1 - \frac{M}{Z_{in}}\left(2M\omega^2 + j\frac{(M\omega)^2}{Z_s}\right)\right) \tag{3.15}$$

3.2.3. LCC-LCC Topology

Fig. 3-5 illustrates the circuit diagram of the LCC-LCC compensated WPT system.

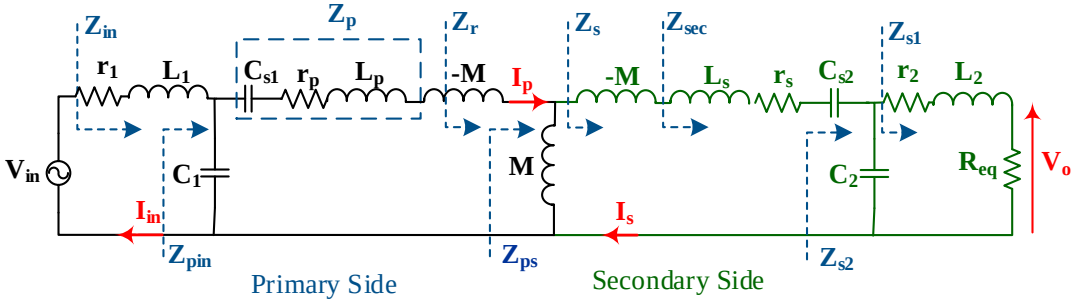

Fig. 3-5. A WPT system with LCC-LCC resonant networks.

Similar to (3.10) and (3.11) the input impedance of this circuit can be expressed. However, the secondary side network impedances are given by:

$$Z_{\text{sec}} = Z_{s2} + r_s + \left(L_s\omega - \frac{1}{\omega C_{2s}}\right)j \tag{3.16}$$

where Z_{s2} and Z_{s1} are defined as follows:

$$Z_{s2} = \frac{Z_{s1}}{1 + j\omega C_2 Z_{s1}}$$
$$Z_{s1} = R_{eq} + r_2 + (L_2\omega)\, j \tag{3.17}$$

Similar to (3.12)-(3.14), currents of each branch of the primary side converter can be expressed. However, the equation for the output current needs to be defined. The output current and voltage are given by:

$$I_o = I_s \frac{1}{1 + j\omega C_2 Z_{s1}} \tag{3.18}$$

$$V_o = R_{eq} I_o = I_s \frac{R_{eq}}{1 + j\omega C_2 Z_{s1}} \tag{3.19}$$

By inserting (3.14) into (3.18), the output current can be derived:

$$I_o = \left(I_p \frac{j\omega M}{Z_{\text{sec}}} \right) \frac{1}{1 + j\omega C_2 Z_{s1}} \tag{3.20}$$

Therefore, the output voltage can be simplified according to (3.19) and it can be expressed by:

$$V_o = \left(I_p \frac{j\omega M}{Z_{\text{sec}}} \right) \frac{R_{eq}}{1 + j\omega C_2 Z_{s1}} \tag{3.21}$$

The sensitivity of the output voltage can be calculated as:

$$\frac{\partial V_o}{\partial M} = \frac{R_{eq}\omega j}{(1 + jC_2 Z_{s1}) Z_{\text{sec}}} \left(I_p + M \frac{\partial I_p}{\partial M} \right) \tag{3.22}$$

Comparing (3.22) and (3.6) reveals that the sensitivity functions are similar and just a coefficient value is multiplied to (3.6). This coefficient is a function of the selected resonant topology for primary and secondary.

3.2.4. Series-LCC Topology

The diagram of the Series-LCC compensated WPT system is depicted in Fig. 3-6.

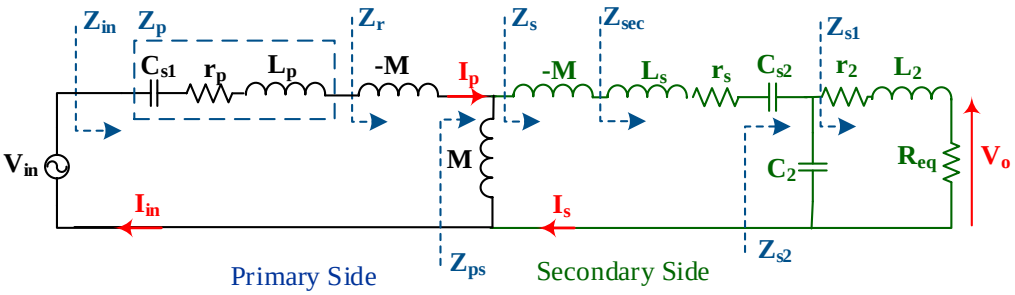

Fig. 3-6. A WPT system with Series-LCC resonant topology.

The input impedance for this topology is expressed as:

$$Z_{in} = r_p + j\left(L_p\omega - \frac{1}{\omega C_{1s}}\right) + Z_r = Z_r + Z_p \tag{3.23}$$

The reflected impedance and impedance seen by the secondary side coil are also defined as follows:

$$Z_r = \frac{(M\omega)^2}{Z_{\text{sec}}} \tag{3.24}$$

$$Z_{\text{sec}} = Z_{s2} + r_s + \left(L_s\omega - \frac{1}{\omega C_{2s}} \right) j$$

where Z_{s1} and Z_{s2} are defined in (3.17). In a similar procedure to the Series-Series topology, the input impedance and the primary side current are obtained as follows:

$$\begin{cases} I_{in} = I_p = \dfrac{V_{in}}{Z_{in}} \\ Z_{in} = Z_r + Z_p = r_p + j\left(L_p\omega - {}^{1}\!\!\diagup\!\!{}_{\omega C_{1s}} \right) + Z_r \end{cases} \tag{3.25}$$

Similar to the LCC-LCC topology, the secondary side currents, and output voltage, can be expressed by:

$$I_s = I_p \frac{j\omega M}{Z_s + j\omega M} = I_p \frac{j\omega M}{Z_{\text{sec}}} \tag{3.26}$$

$$I_o = I_s \frac{1}{1 + j\omega C_2 Z_{s1}} \tag{3.27}$$

$$V_o = R_{eq} I_o = I_s \frac{R_{eq}}{1 + j\omega C_2 Z_{s1}} \tag{3.28}$$

and its sensitivity function of this topology are similar to the LCC-LCC topology that can be calculated by:

$$\frac{\partial V_o}{\partial M} = \frac{R_{eq}\omega j}{\left(1 + jC_2 Z_{s1}\right) Z_{\text{sec}}} \left(I_p + M \frac{\partial I_p}{\partial M} \right) \tag{3.29}$$

3.3. The Proposed Design Optimization Procedure

In Section 3.2, steady-state equations of each topology are presented. In this section, a framework for the design of the resonant networks of the WPT system is presented. Selecting the resonant components for these high-order circuits is not an easy task. In order to design these topologies, the application requirements, different criteria and boundaries should be considered. Moreover, due to the non-linearity of the system, different solutions are possible. Therefore, an optimization problem should be defined to include the objective function, system equations, and constraints.

3.3.1. Objective Functions

As discussed before, in this chapter two different cases are considered for the design of the resonant topologies:

A. Case I: Reduced Output Voltage Sensitivity Respect to Misalignment

In this case, the main design objective is minimizing the voltage variation respect to the variation of M. This function is defined as:

$$Min(\frac{\partial V_o(P_{out}, M)}{\partial M}) \approx Min(\frac{\Delta V_o(P_{out}, M)}{\Delta M}) \tag{3.30}$$

The result of this optimization provides the least sensitivity of the output voltage respect to the misalignment. However, this may result in poor efficiency for

the system without considering a lower boundary for the efficiency. Therefore, appropriate boundaries for the system efficiency needs to be defined in the problem constraints.

B. Case II: Maximum Efficiency Respect to Misalignment

In a conventional design of the WPT systems, only the efficiency of the converter at its nominal operating point is considered. However, in practice misalignment occurs and it can affect the system efficiency. Therefore, achieving maximum efficiency in all the coupling factors also can be considered as an objective function. This function is defined as:

$$Max(\sum_{i} \eta_{k_i})$$

where (3.31)

$$\eta_{k_i} = \frac{P_{out,k_i}}{P_{out,k_i} + P_{loss,k_i}} \qquad \forall k_i \in K_n$$

where P_{out,k_i} is the value of the output power at $k{=}k_i$, K_n is a finite set of the nominal operating points which is related to different misalignment conditions, and P_{loss,k_i} is the system losses at the operating point. This objective function includes all the operating coupling factors in which the converter needs to gain the highest efficiency values. In the following, the power loss calculation and constraints that need to be considered in the objective function will be discussed:

3.3.2. Power Loss Calculation

Different parameters affect the efficiency of the WPT system. The main sources of the power losses are inverter switches, resonant capacitors, resonant inductors, magnetic couplers, and diode-bridge. In order to solve the optimization problem, each of the loss components should be modeled and included in the optimization problem. In the following, each of the loss components is discussed in detail:

A. Magnetic couplers losses ($\mathbf{P_{coupler}}$)

The magnetic couplers loss includes the conduction loss (P_{cond_coup}) and core (P_{core_coup}) loss. Total magnetic coupler losses can be express by:

$$P_{coupler} = P_{cond\_coup} + P_{core\_coup} \tag{3.32}$$

Each of these losses is explained in details in the following:

A.1. Conduction losses of the magnetic couplers ($\mathbf{P_{cond}}$)

Conduction losses of the magnetic couplers are equal to the power losses of their AC resistances at the operating frequency [143]. The AC resistance of the coils is higher than the initial dc resistance. The AC resistance is caused by the skin effect and proximity effect between the turns. The skin effect is caused by the eddy current inside the inductors which reduces the effective cross-section of the wire. Therefore, Litz wire is commonly used to reduce the skin effect by using multiple

strands of small diameter wires instead of a single conductor wire. The primary and secondary side conduction losses of the magnetic couplers is calculated by:

$$P_{cond}^{p} = r_p I_p^2 \tag{3.33}$$

$$P_{cond}^{s} = r_s I_s^2 \tag{3.34}$$

where r_p and r_s are the AC resistance of the primary and secondary side magnetic couplers, respectively. The AC resistance of the magnetic couplers is measured at 85 kHz and used in these equations and then include in the optimization problem to calculate the losses.

A.2. Core losses of the magnetic couplers ($\mathbf{P_{core\_coup}}$)

The core loss of the magnetic couplers is the sum of the hysteresis and eddy losses. In order to calculate the core loss of the magnetic couplers, FEA is used. Since the system is operating at a constant frequency (85 kHz), for a given volume of the core material and a constant number of turns, the core loss is only a function of the field density, and field density is also a function of the coupler excitation current [144].

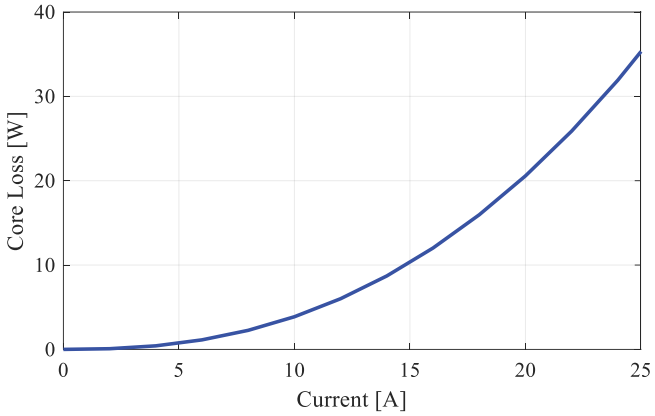

Fig. 3-7. FEA results of the magnetic coupler core loss versus excitation current at 85 kHz

Therefore, the core loss can be calculated for each excitation current at 85 kHz using FEA. Fig. 3-7 illustrates the calculated core losses versus the excitation current of the magnetic coupler. The results are approximated by a polynomial to have an analytical model of the losses and it is included in the optimization problem.

B. Diode bridge losses ($\mathbf{P_{bridge}}$)

The diode bridge losses are modeled as a drop voltage at turn-on state and series equivalent resistance losses which is calculated by [143]:

$$P_{bridge} = 4\left(U_{d0\_bridge} I_{d\_ave} + R_{d\_bridge} I_{d\_rms}^2\right) \tag{3.35}$$

In (3.35), the diode is assumed to have a voltage drop of U_{d0_bridge} and the series equivalent resistance of R_{d_bridge}, and I_{d_ave} and I_{d_rms} are the diode current average and RMS values, respectively. Since there are four diodes in a full-bridge rectifier, the power loss is multiplied by four. Assuming I_o is the output current,

half of the output current at each cycle passes through each leg, therefore, $I_o/2$ is considered for diode average current and $I_o^2/2$ is equal to the RMS current of each diode which is used to calculate diode conductive power loss [143]. Therefore, the diode bridge losses can be simplified as follows:

$$P_{bridge} = 4\left(U_{d0\_bridge}\frac{I_o}{2} + R_{d\_bridge}\frac{I_o^2}{2}\right) \tag{3.36}$$

C. Resonant capacitors losses ($\mathbf{P_{cap}}$)

The losses of the resonant capacitors are dependent on the dissipation factor of the selected capacitor, operating frequency, and the current of the resonant capacitors. Based on the equations of each branch current for different topologies, the resonant capacitor losses can be calculated by [64]:

$$P_{cap} = \sum \frac{\tan\delta(f)}{2\pi f C_i} I_i^2 \tag{3.37}$$

where $\tan\delta(f)$ is the dissipation factor of the resonant capacitors as a function of frequency which includes the Equivalent Series Resistance (ESR) losses. This value is given in the datasheet of the selected capacitors. Moreover, I_i is the RMS current flowing into the capacitor with the value of C_i. In the following, capacitor losses are calculated for each topology:

C.1. Series-Series configuration

In this topology, the current flowing in C_{s1} and C_{s2} capacitors are equal to the primary side (I_p) and secondary side current (I_s), respectively. Then the total capacitor loss of the Series-Series topology is calculated by:

$$P_{cap}^{S-S} = \frac{\tan\delta(f)}{2\pi f}\left(\frac{I_p^2}{C_{s1}} + \frac{I_s^2}{C_{s2}}\right) \tag{3.38}$$

C.2. LCC-Series configuration

In the LCC-Series topology, the primary side capacitor current is equal to the primary side coil current (I_p) and the secondary side capacitor current is equal to the secondary side coil current (I_s) than can be calculated according to (3.13) and (3.14), respectively. According to Fig. 3-4, the current flows through the C_1 can be calculated from the current division between C_1 and (Z_p+Z_r) branches and expressed as:

$$I_{C_1} = I_{in}\left(\frac{1}{C_1\omega j} \,||\, \left(Z_p + Z_r\right)\right)C_1\omega j \tag{3.39}$$

Therefore, the total capacitor loss is expressed by:

$$P_{cap}^{LCC-S} = \frac{\tan\delta(f)}{2\pi f}\left(\frac{I_p^2}{C_{s1}} + \frac{I_s^2}{C_{s2}} + \frac{I_{C_1}^2}{C_1}\right) \tag{3.40}$$

C.3. LCC-LCC configuration

In this topology, the current flows in C_{s1} and C_{s2} capacitors are equal to the primary side (I_p) and secondary side current (I_s) that can be calculated by (3.13)

and (3.14), respectively. The current flows to the capacitor C_1 can be calculated by (3.39) and the current flows in C_2 is calculated by the current division between the C_2 and Z_{s1} and expressed by:

$$I_{C_2} = I_s \frac{Z_{s1} C_2 \omega j}{Z_{s1} C_2 \omega j + 1} \tag{3.41}$$

Therefore, the total capacitor loss in LCC-LCC topology is given in:

$$P_{cap}^{LCC-S} = \frac{\tan\delta(f)}{2\pi f}\left(\frac{I_p^2}{C_{s1}} + \frac{I_s^2}{C_{s2}} + \frac{I_{C_1}^2}{C_1} + \frac{I_{C_2}^2}{C_2}\right) \tag{3.42}$$

C.4. Series-LCC configuration

Similarly, in the Series-LCC topology, the current flows in C_{s1} and C_{s2} capacitors are the primary side (I_p) and secondary side current (I_s) that can be calculated by (3.25) and (3.26), respectively. The current of C_2 is calculated according to Fig. 3-6 which is given by:

$$I_{C_2} = I_s \frac{Z_{s1} C_2 \omega j}{Z_{s1} C_2 \omega j + 1} \tag{3.43}$$

The total capacitor loss in this topology is expressed by:

$$P_{cap}^{LCC-S} = \frac{\tan\delta(f)}{2\pi f}\left(\frac{I_p^2}{C_{s1}} + \frac{I_s^2}{C_{s2}} + \frac{I_{C_2}^2}{C_2}\right) \tag{3.44}$$

C. Inverter losses ($\mathbf{P_{inv}}$)

The inverter losses of with four MOSFET switches consist of conduction and can be modeled as [55, 143]:

$$P_{mosfet} \simeq 4R_{ds(on)}I^2_{mosfet\_rms} + 2V_{dc}I_{mosfet}f\left(t_r + t_f\right) \tag{3.45}$$

where $R_{ds(on)}$ is the on-state equivalent resistance of the Mosfet switches extracted from the datasheets. The parameters t_r and t_f are rise time and fall time related to the dynamic characteristics of the selected switch. Moreover, I_{mosfet_rms} and I_{mosfet} are the RMS value, and turn-on value of the current flows in the Mosfet switch.

The losses of the anti-parallel diodes are calculated as follows [143]:

$$P_{diode} \simeq 4\left(U_{d0}I_{diode\_ave} + R_{diode}I^2_{diode\_rms}\right) \tag{3.46}$$

where U_{d0} and R_{diode} are the turn-on voltage drop and resistance of the antiparallel diode of the Mosfet switches respectively. These values can be found in the datasheet of the selected switch.

The total loss of the inverter is the sum of the Mosfet switches and their anti-parallel diodes losses, which is expressed by:

$$P_{inv} = P_{mosfet} + P_{diode} \tag{3.47}$$

D. Resonant inductor losses ($\mathbf{P_L}$)

The resonant inductor losses include the conduction and core losses, can be expressed as:

$$P_L = P_{L\_cond} + P_{L\_core} = r_L I_L^2 + P_{L\_core} \tag{3.48}$$

The AC resistance of the inductors (r_L) is measured experimentally. Similar to the magnetic couplers, the core losses of the resonant inductors are calculated through FEA. In this case, the value of the core loss not only is dependent on the excitation current but also is a function of the inductor size. Fig. 3-8 presents the FEA results of a resonant inductor loss versus the current and size of the inductor for a typical 500W WPT system.

It can be seen that the variation of core loss versus current and inductance is negligible compared to the rated power of the system. Therefore, the average of the core loss is considered in this chapter instead of curve fitting. All the aforementioned loss calculations for different components of the circuit are included in the optimization problem.

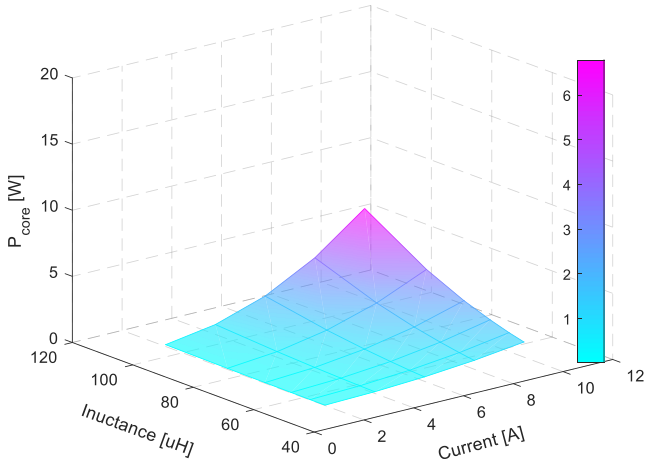

Fig. 3-8. FEA results of the inductor core loss versus excitation current and inductor size at 85kHz.

3.3.3. Constraints

For any physical system, there are several boundaries that limit the variables of the system. These constraints can be defined based on each application requirement. Some of the constraints are caused by the limited possible size, cost, or volume of the system:

A. Size of the Resonant Network:

In this optimization problem, the size of the resonant network should be limited to avoid an unacceptable design from a practical point of view. These boundaries are defined as a vector given by:

$$\{L_1, L_2, C_1, C_2, C_{1s}, C_{2s}\} \leq \left\{\mathrm{L_1}^{\max}, \mathrm{L_2}^{\max}, \mathrm{C_1}^{\max}, \mathrm{C_2}^{\max}, \mathrm{C_{1s}}^{\max}, \mathrm{C_{2s}}^{\max}\right\} \tag{3.49}$$

B. Thermal Limit:

Other practical constraints like the thermal limits of the system should be considered in a practical problem. Therefore, maximum values for the primary and secondary side coils are also defined as:

$$I_p(P_{out}, k_i) \leq \mathrm{I_p^{max}} \tag{3.50}$$

$$I_s(P_{out}, k_i) \leq \mathrm{I_s^{max}} \tag{3.51}$$

C. Voltage Gain:

To satisfy application requirements, an acceptable range for the output voltage gain should also be taken into account. The voltage gain is the ratio of the output voltage to the input voltage of the system. This constraint is defined by setting lower and upper boundaries as follows:

$$\mathrm{G}_{\mathrm{V_o^{min}}} \leq G_{V_o(P_{out},k_i)} \leq \mathrm{G}_{\mathrm{V_o^{max}}} \qquad \forall k_i \in K_n \tag{3.52}$$

D. ZVS Operation and Efficiency:

The resonant network should be designed to provide ZVS conditions for the inverter. As discussed in Chapter 2, the input impedance seen by the inverter should have a resistive-inductive characteristic at the switching frequency and its phase angle should be a positive value. The ZVS satisfaction constraint is defined by:

$$\phi^{\min} \leq \phi(P_{out},k) \leq \pi/2 \tag{3.53}$$

where ϕ is the input impedance phase angle and $\phi^{\min}$ is the minimum phase angle selected by the designer. Moreover, as discussed in the previous part, it is essential for the system efficiency to have a lower boundary in Case I. This boundary eliminates the solutions in which the output voltage profile is optimized and the

system efficiency is poor. This constraint for a desired acceptable energy efficiency is included as:

$$\eta_{k_i} \geq \eta_{di} \qquad \forall k_i \in K_n \tag{3.54}$$

3.3.4. Optimization

In order to solve the proposed non-linear optimization problem, Brand-And-Reduce Optimization Navigation (BARON) is used [145, 146]. BARON is an optimization solver capable of solving non-convex and mixed-integer programming. In addition, it can also find the global optimal point for the optimization problem in certain conditions [147]. Fig. 3-9 shows the proposed procedure to design the resonant networks components optimally for EV wireless charging applications.

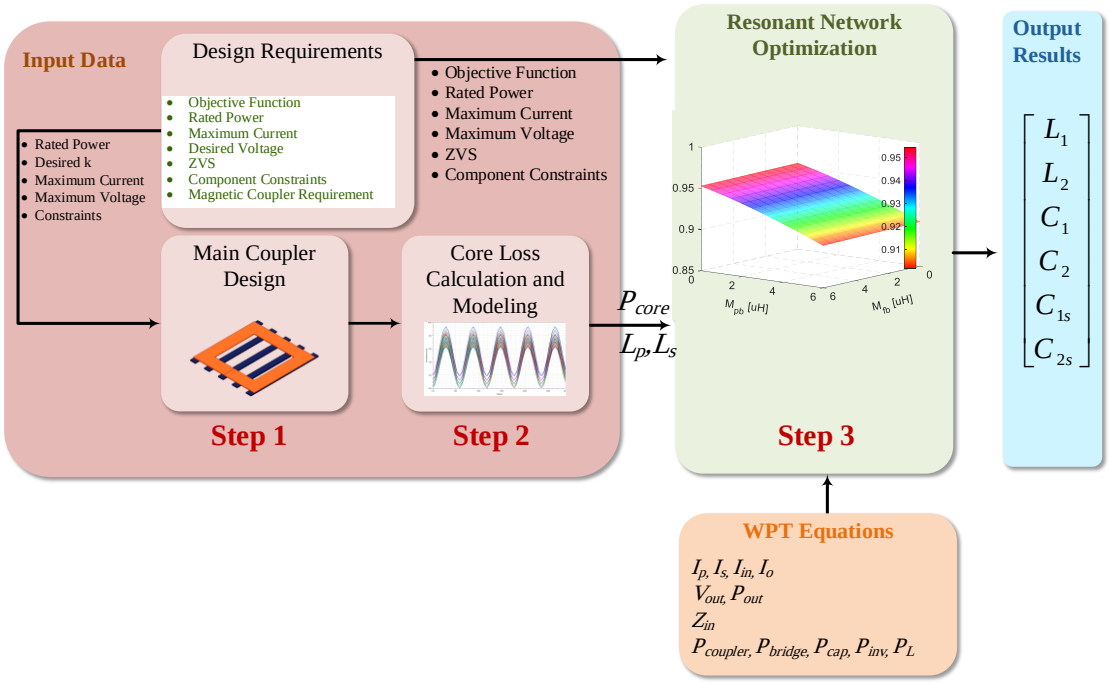

Fig. 3-9. Procedure of the proposed optimized resonant network design.

To define the optimization problem, different parts of the problem should be defined as follows:

1. *Input parameters*: f, V_{dc}, FEA results, measurements, datasheets.
2. *Variables*: currents, resonant elements (C_1, C_{s1}, C_{s2}, C_2, L_1, L_2), k.
3. *Constraints*: upper and lower boundaries of currents, voltages, input phase angle, efficiency, and values of the resonant elements.
4. *Equations*: P_{out}, P_{loss}, V_{out}, I_{in}, I_p, impedances of the circuit.
5. *Objective function*: Maximum efficiency or Minimum voltage variation.

In this chapter, a 500 W/85 kHz WPT system is considered as a case study. The switching frequency is set to 85 kHz based on SAE J2954 standard for light-duty EV charging system. Other design parameters and constraints are presented in Table 3-1. Table 3-2 lists the obtained values from the optimization for each of the resonant topologies. The results are given for both cases I and II.

TABLE 3-1
VARIABLES BOUNDARIES AND FIXED PARAMETERS

Variable/Parameter	Min.	Max./Fix Value
L_p, L_s	-	270-278 µH
L_1, L_2	1 µH	200 µH
C_1, C_2, C_{1s}, C_{2s}	1 nF	200 nF
G_{Vo}	0.725	0.775
K_n	-	0.18,0.25,0.32
I_p(P_{out},k)	0	15 A
I_s(P_{out},k)	0	15 A
ϕ	0.2	π/2
η_{di}	-	0.80
V_{dc}	-	200 V
$R_{ds(on)}$	-	37 mΩ
r_1, r_2	-	50 mΩ
r_p, r_s	-	110 mΩ
tanδ(f)	-	10^{-3}

TABLE 3-2
OPTIMIZATION RESULT FOR DIFFERENT TOPOLOGIES

Topology	Objective (Case)	Design Values						Total Inductor [μH]	Total Capacitor [nF]
		L_1[nf]	L_2[nf]	C_1[nf]	C_2[nf]	C_{1s}[nf]	C_{2s}[nf]		
Series-Series	I	-	-	-	-	16.90	14.43	0	31.33
	II	-	-	-	-	15.25	12.53	0	27.78
LCC-Series	I	54.85	-	108.90	-	15.68	20.12	54.85	144.70
	II	15.40	-	29.73	-	15.53	13.10	15.40	58.36
LCC-LCC	I	55.53	66.16	91.00	71.83	16.55	22.10	121.69	201.48
	II	28.97	138.69	23.62	26.75	15.16	26.11	167.66	91.64
Series-LCC	I	-	66.57	-	30.26	14.83	12.60	66.57	57.69
	II	-	80.79	-	31.78	15.25	21.44	80.76	68.47

Fig. 3-10 shows the output voltage and efficiency profiles of the different resonant topologies in both cases where coupling factor changes; Case I: reduced output voltage sensitivity and Case II: maximum efficiency. It should be noted that the output power is 500 W constant in all the cases.

Fig. 3-10 shows that where the constant output voltage is considered (Case I), all the designed topologies can effectively reduce the output voltage variation at different coupling factors. However, the overall system efficiency in Case II is always higher than the efficiency of the Case I designs as expected.

In Case II, the objective was defined as maximum efficiency at each coupling factor. In Fig. 3-10, it can be seen that this objective pushed the efficiency of the system into the higher values however the output voltage changes when the coupling factor changes. It can be seen that the LCC-Series, Series-LCC, and LCC-LCC topologies, have the highest average efficiencies respectively in Case II.

However, for all the topologies in Case II, the voltage regulation is very poor, and the output voltage is significantly influenced by the coupling. Among them, LCC-Series and Series LCC have the highest voltage variation with respect to k.

In this optimization problem, different constraints are included, therefore, the topology of the system needs to have enough degree of freedom to satisfy the design requirements and reach the optimum value.

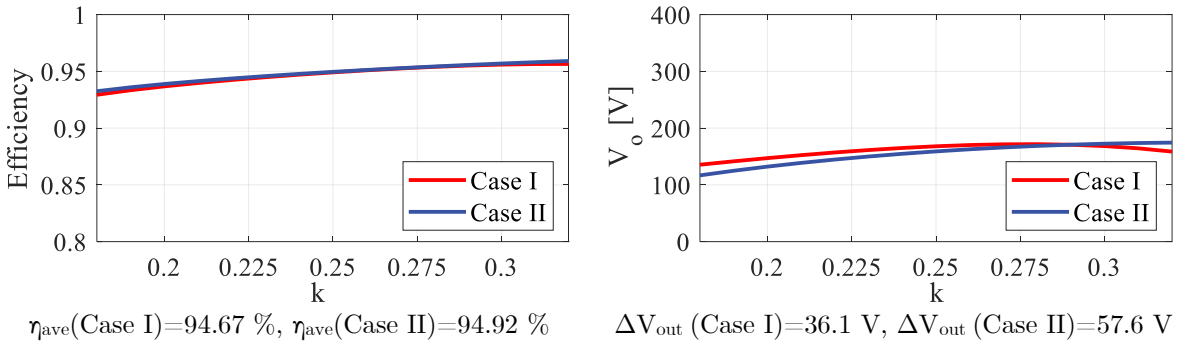

η_{ave}(Case I)=94.67 %, η_{ave}(Case II)=94.92 % ΔV_{out} (Case I)=36.1 V, ΔV_{out} (Case II)=57.6 V

(a) Series-Series

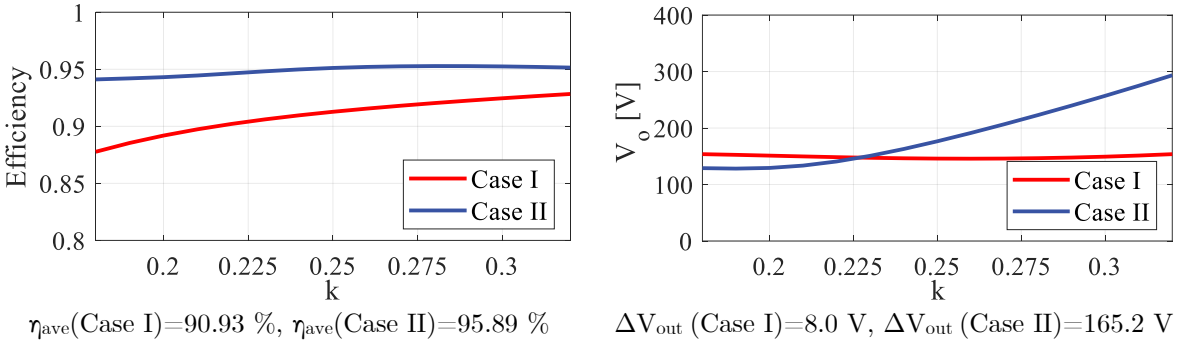

η_{ave}(Case I)=90.93 %, η_{ave}(Case II)=95.89 % ΔV_{out} (Case I)=8.0 V, ΔV_{out} (Case II)=165.2 V

(b) LCC-Series

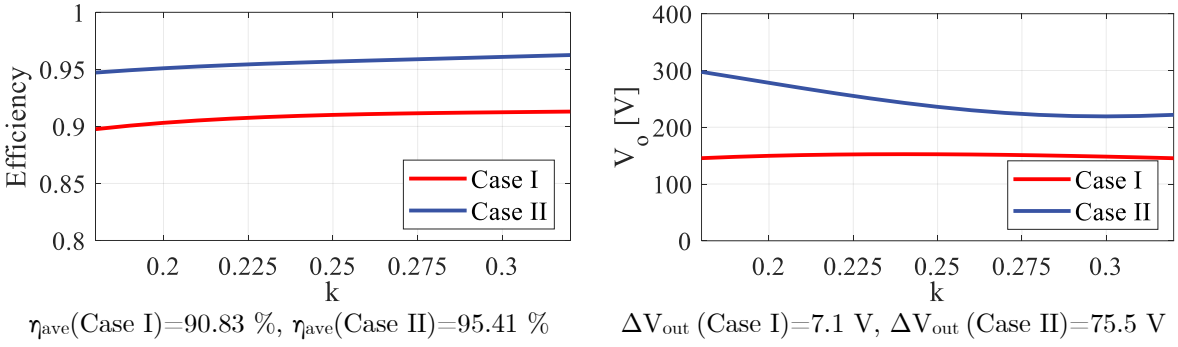

η_{ave}(Case I)=90.83 %, η_{ave}(Case II)=95.41 % ΔV_{out} (Case I)=7.1 V, ΔV_{out} (Case II)=75.5 V

(c) LCC-LCC

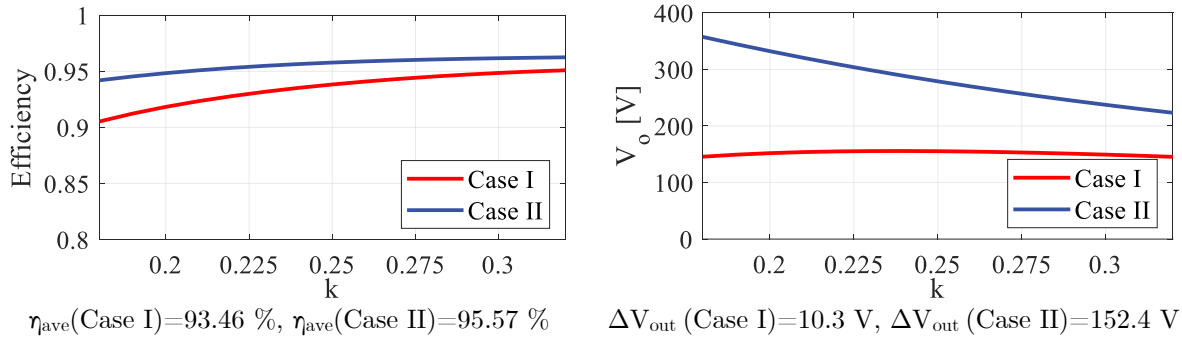

η_{ave}(Case I)=93.46 %, η_{ave}(Case II)=95.57 % ΔV_{out} (Case I)=10.3 V, ΔV_{out} (Case II)=152.4 V

(d) Series-LCC

Fig. 3-10. Comparison of the performance of different resonant topologies at 500 W rated load.

The LCC-LCC topology has six resonant elements in its structure which give the highest degree of freedom in the optimization problem. In the LCC-Series and Series-LCC circuit, there are four resonant elements defined as the problem variables. On the other hand, the Series-Series topology has only two resonant capacitors which restrict its design area. Therefore, for Series-Series topology, the feasible area is so tight that it cannot be flexible enough to satisfy the constraints and reach Max./Min. of the objective functions. Consequently, the difference between the results in Case I and II for the Series-Series topology is not significant. By comparing the output voltage variation of the topologies in Fig. 3-10, it can be seen that there is a correlation between the number of resonant elements and their output voltage variation.

A. Voltage Comparison

By comparing all the topologies in Case I (minimum voltage variation), it can be seen that the voltage variation is significantly reduced for all the topologies except the Series-Series topology. This is because of the fact that this topology has a lower degree of freedom in comparison with the others. Three other topologies presented a very good voltage regulation for a wide range of coupling factor variation. The LCC-LCC and LCC-Series designs presented 7.1 V and 8 V variations respectively which are the least voltage variation in Case I. The reported voltage variation in [40] was above 7% for the LCC-S topology with a constant

resistance load. The measured voltage variation reported in [115] was 8 V for a 72 V nominal voltage (more than 11%).

Further reduction of voltage variation or a wider range of coupling factors could be considered in the optimization problem. However, those constraints will tight the feasible region in which the problem may not be converged or results in lower efficiency profiles. Therefore, the range of 0.18-0.32 for k is selected in this chapter to not only present a constant voltage in the output but also ensures high-efficiency energy transmission.

B. Efficiency Comparison

Comparing the average efficiency of these three topologies in Case I shows that Series-Series and Series-LCC have presented the highest efficiency for the whole operating range. Moreover, it can be seen that the variation of the system efficiency for LCC-LCC topology is very small compared to the other topologies. Therefore, if the constant output voltage within a wide range of coupling factors is a requirement, without considering other parameters, LCC-LCC is preferable due to its flat efficiency curve.

C. Component Size Comparison

The other key parameter for comparing these topologies in each case is the size of the resonant networks. The size of the resonant network has a crucial impact on

the total cost and volume of the design. As can be seen from Table 3-2, in both cases, Series-Series and Series-LCC have the lowest required capacitor values. However, since the voltage variation of Series-Series topology even in Case I is very high, this topology is not a good candidate for wide range operation of coupling factor.

The total inductor value needed for the LCC-Series and Series-LCC in Case I are close which is approximately half of the required inductance for LCC-LCC topology in Case I. Similarly, in Case II (maximum efficiency), the total required inductance for LCC-Series is 15.4 µH which is much lower than LCC-LCC network. In summary, the total required inductance of the LCC-Series is the lowest in both cases. Therefore, considering Case I, it can be concluded that Series-LCC (if lower capacitor value is required) and LCC-Series (if lower inductor value is required) are the most cost-effective topologies with the least voltage variation.

D. Input Phase Angle

The phase angle of the input impedance seen by the inverter determines the reactive current that the inverter should provide. To compare the four topologies, input phase angles of the optimized resonant networks are compared in Fig. 3-11.

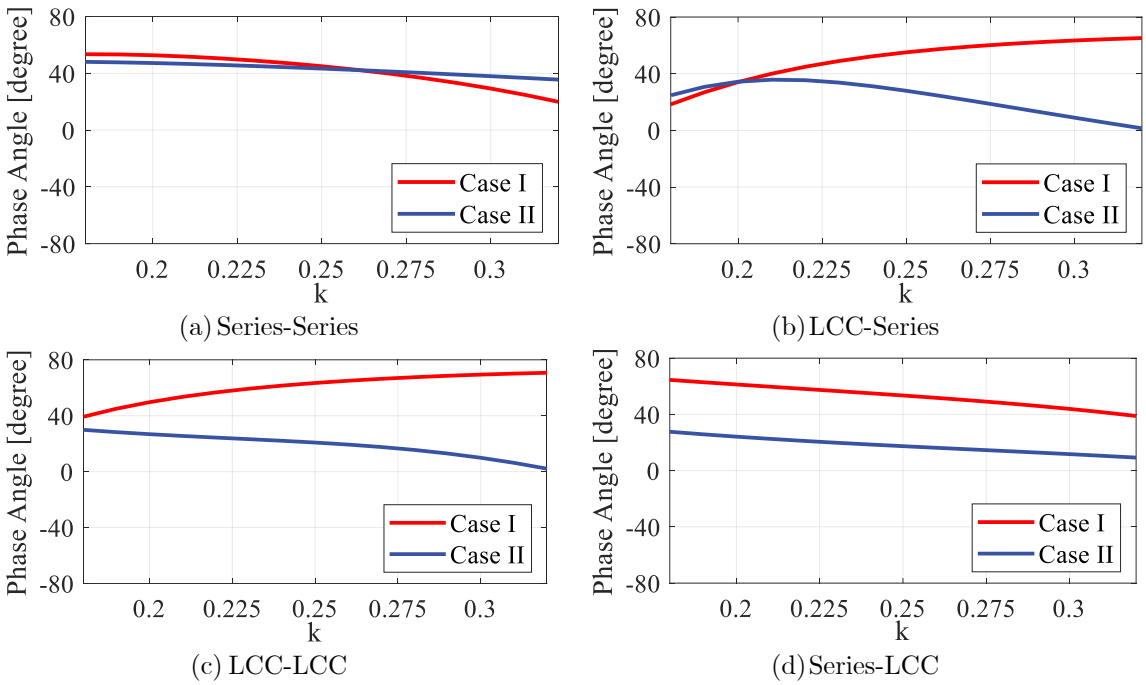

(a) Series-Series (b) LCC-Series

(c) LCC-LCC (d) Series-LCC

Fig. 3-11. Comparison of the input phase angle versus k.

It can be seen that the phase angle remains a positive value for the whole operating range which ensures the ZVS operation of the inverter switches. Moreover, it can be seen that generally, the phase angle of Case II is lower than Case I because the optimization program tried to reduce the inverter losses.

The contribution of the inverter loss in the efficiency of the system is lower than other parameters. Therefore, the optimized circuits have a higher input phase angle compared to conventional design methods. Although having a Zero Phase Angle (ZPA) minimizes the inverter losses, it cannot guarantee the optimality of the maximum efficiency of the whole WPT system. Furthermore, in Case I the

objective function was minimizing the voltage variation versus coupling factor; therefore, the optimized circuit showed more inverter losses compared to Case II.

E. Power Loss Distribution Comparison

Fig. 3-12, shows the calculated power loss distribution for each topology at 500W rated loading condition. In this calculation, the coil resistance, and inductor resistances are considered for conduction losses, and the coil losses only take the core loss into account. As expected, the total amount of power loss is higher in all the topologies in Case I compared to Case II. Moreover, it can be seen that generally, the power losses are increasing as the misalignment increases (k decreases).

In Case II, for Series-Series and LCC-Series since the output voltage drops when k decreases, for constant power, the output current increases. Therefore, the diode-bridge loss increases as shown in Fig. 3-12. On the other hand, LCC-LCC and Series-LCC topologies have an increasing output voltage when the coupling factor reduces (more misalignment). Therefore, their diode-bride loss is higher when the coils are fully aligned in Case II.

It can be seen in Fig. 3-12 that the rate of change of the coils losses in Case I is higher than Case II when the coupling factor decreases from 0.32 to 0.18. Since in Case I, the converter is designed to reduce the output voltage variation, the

primary side coils current increases to compensate for the reduction of induced voltage on the secondary side coil. This resulted in higher conduction and core losses for the coils. From this aspect, the LCC-Series topology has the highest coil loss portion in comparison with other topologies in Case I. On the other hand, the LCC-LCC network has the lowest coil loss in comparison with the other topologies in Case I (except Series-Series).

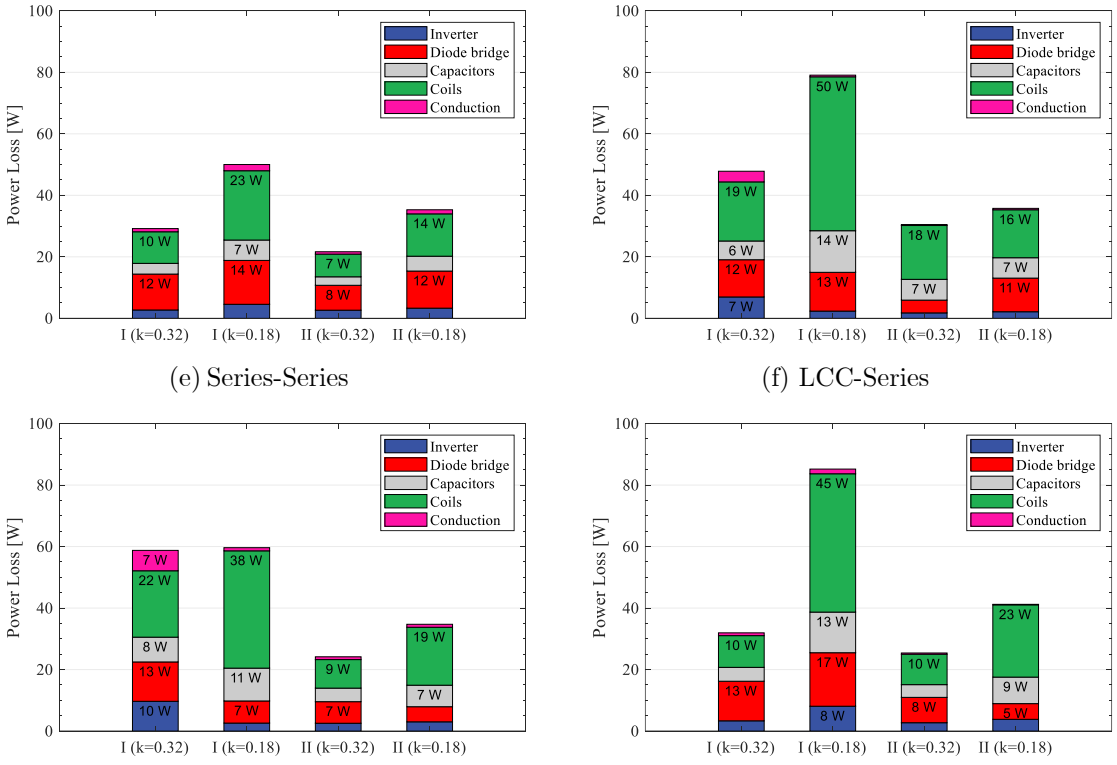

(e) Series-Series (f) LCC-Series

(g) LCC-LCC (h) Series-LCC

Fig. 3-12. Comparison of the loss distribution at different coupling factors of the resonant topologies.

3.3.5. Discussion

In a conventional tuning of an LCC network, the primary side current was load-independent which resulted in high sensitivity of the output voltage with respect to misalignment. Conversely, the developed optimization method resulted in having a more flexible current on the primary side. The optimization in Case I, pushed the primary side current to follow and compensate for the variation of the coupling factor effect on the output voltage of the system.

A wider range of the coupling factors could be considered in the optimization of the resonant networks. To evaluate the optimization results presented in Table 3-2 in a wider range of k (k=0.14-0.4), output voltages of the resonant networks are presented in Fig. 3-13. Although the resonant networks are optimized in the range of k=0.18-0.36, the result of the output voltage at a wider range of coupling factors was acceptable. The output voltage variation with respect to misalignment was significantly lower than conventional tuning of the resonant networks.

In summary, considering the poor performance of the Series-Series topology in Case I and the high total required resonant capacitors and inductors in LCC-LCC topologies, LCC-Series, and Series-LCC topologies are the best candidates for satisfying the constant output voltage application requirements when k varies in a

wide range. Table 3-3 summarizes the comparison conclusions discussed in this section.

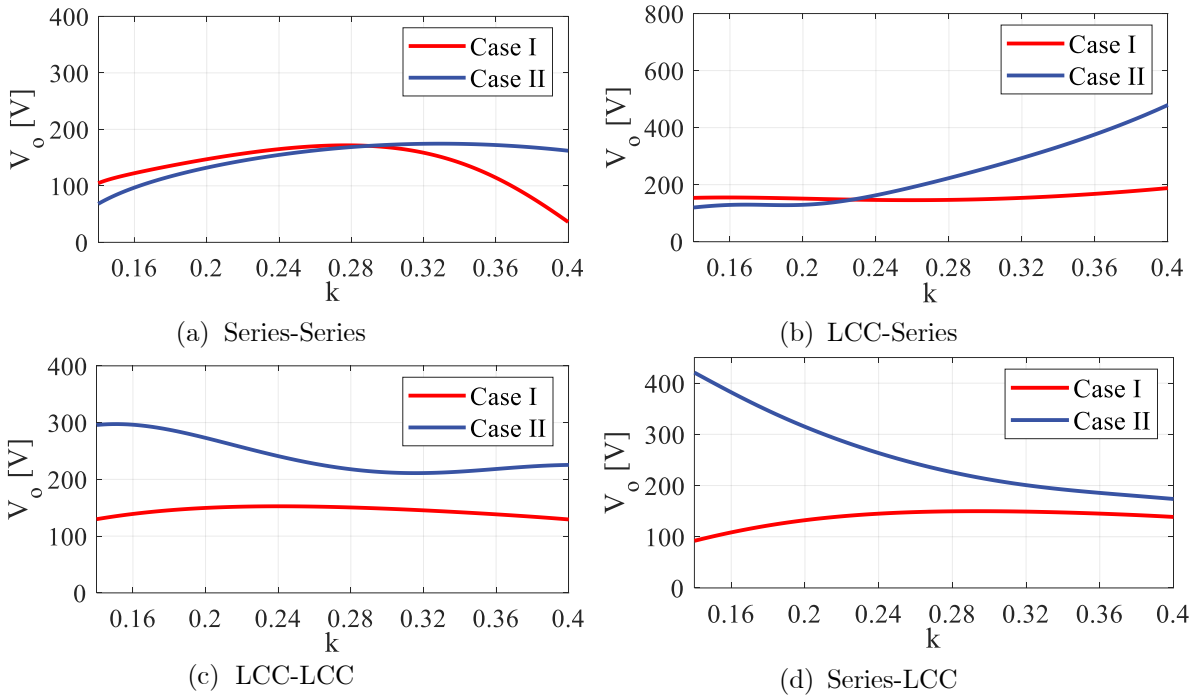

(a) Series-Series (b) LCC-Series

(c) LCC-LCC (d) Series-LCC

Fig. 3-13. Output voltage variation versus coupling factor (k=0.14-0.4).

TABLE 3-3
COMPARISON OF THE TOPOLOGIES IN CASE I

Topology	Number of Components	Capacitor Size	Inductor Size	Average Efficiency	Voltage Variation
Series-Series	Good	Good	-	Good	Poor
LCC-Series	Normal	Normal	Good	Good	Good
LCC-LCC	Poor	Poor	Normal	Good	Good
Series-LCC	Normal	Good	Good	Good	Good

The frequency splitting issue, also known as bifurcation, can be a concern in the WPT systems when the frequency control method is used to control the output voltage. This phenomenon is studied in [148], and design guidelines to avoid

bifurcation for a Series-Series compensation are presented in [149]. In order to study this phenomenon, the frequency response of the output voltage of the four studied topologies are shown in Fig. 3-15.

It can be seen that there are two maximum output voltage points for each topology. This phenomenon is known as bifurcation of the output voltage. However, in this thesis a fixed frequency of 85 kHz is used for the inverter; therefore, the bifurcation does not affect the performance of the system.

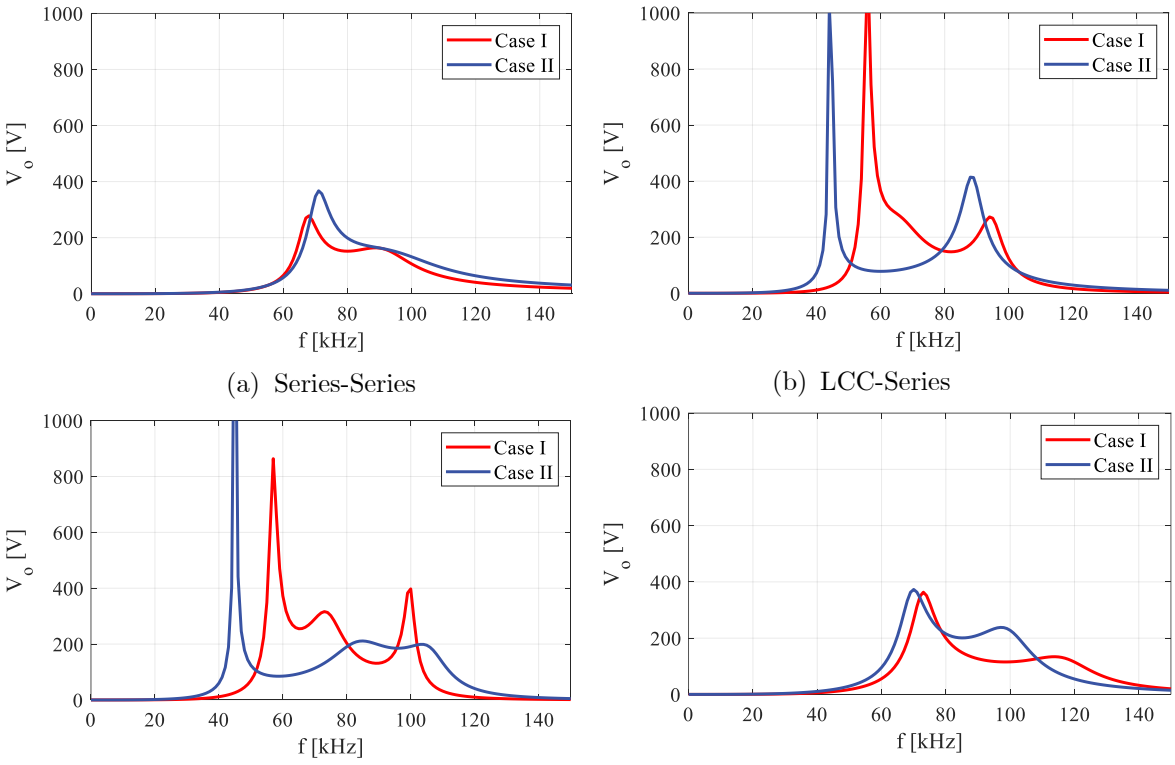

(a) Series-Series (b) LCC-Series

(c) LCC-LCC (d) Series-LCC

Fig. 3-14. Frequency response of the output voltage.

3.4. Experimental Results

Since the main focus of this chapter is the optimization comparison of constant voltage characteristics of different resonant topologies, only Case I is implemented for experimental evaluation. A 500 W/85 kHz prototype was built to validate the performance of the proposed resonant network design. Fig. 3-15 shows the experimental setup with the parameters shown in Table 3-2 for Case I.

In this setup, IPW60R037P7 power MOSFETs are used which has a 37 mΩ turn-on resistance and a good switching dynamic.

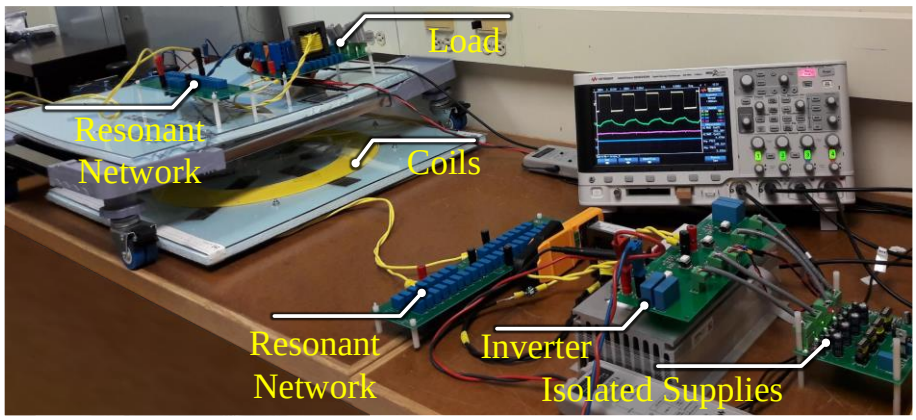

Fig. 3-15. Realized prototype of the WPT system.

Diode-bridge is built by DSEI120-06A. In this chapter, a circular magnetic coupler with 19 turns is considered for both primary and secondary sides. The sizing and number of turns of the magnetic couplers are based on the FEA simulations. The total diameter of the magnetic couplers is limited to 500 mm and their self-inductance is in the range of 272-280 μH. A Litz wire with 500 strands of AWG 38

is used to provide a high-quality factor for the coils by reducing the AC resistance at 85 kHz. FEA simulation results and experimental measurement of the coupling factor are compared in Fig. 3-16.

Fig. 3-16 shows very good accordance between the simulation results and measured values. In order to validate the voltage regulation performance of the optimized topology, an open-loop test is carried out in this section.

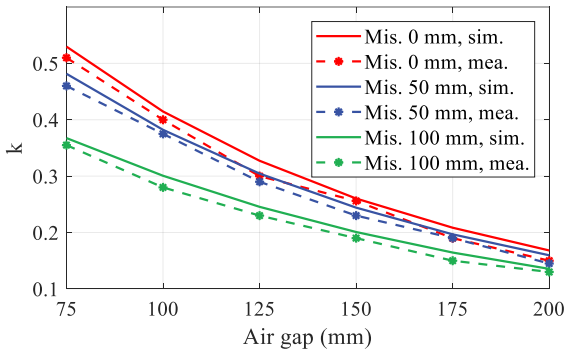

Fig. 3-16. Comparison of FEA and measured coupling factor at different positions.

Fig. 3-17 shows the experimental results for two different coupling factor conditions. As can be seen, the output voltage is almost constant for the two coupling conditions. Moreover, ZVS is achieved for the converter in all the operating points to ensure operation in high efficiency for a wide range of coupling. As can be seen from Fig. 3-17, for variation of k from 0.2 to 0.32, the output voltage variation is very low. Fig. 3-18 shows the output voltage and Efficiency of the optimized Series-LCC topology under different values of k. As discussed before, the

efficiency of this case is not as high as in Case II. However, the voltage regulation characteristics are very satisfying as expected.

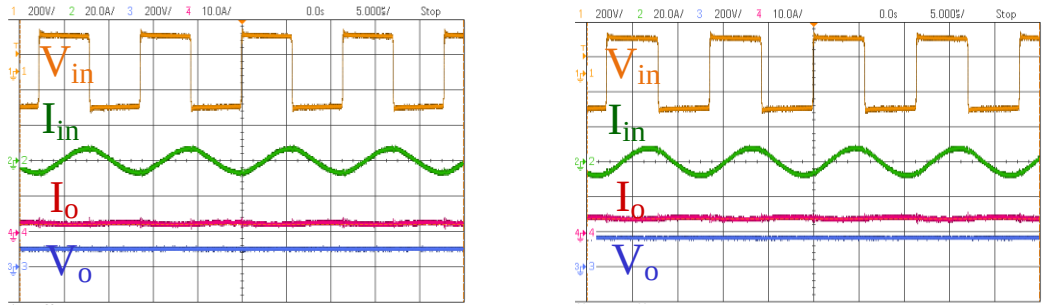

k=0.2 *k*=0.32

(a) Series-Series

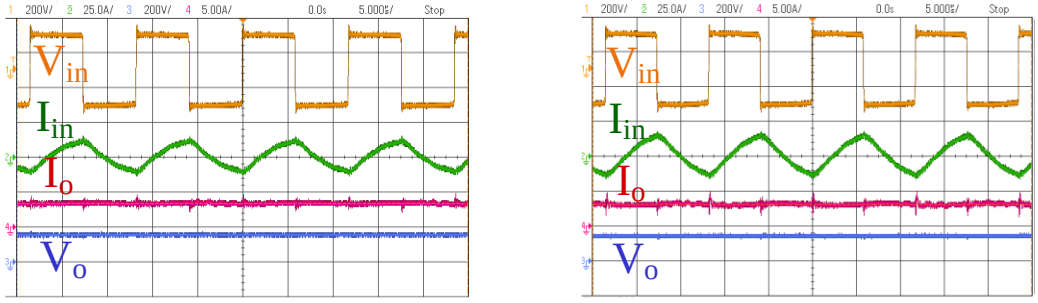

k=0.2 *k*=0.32

(b) LCC-Series

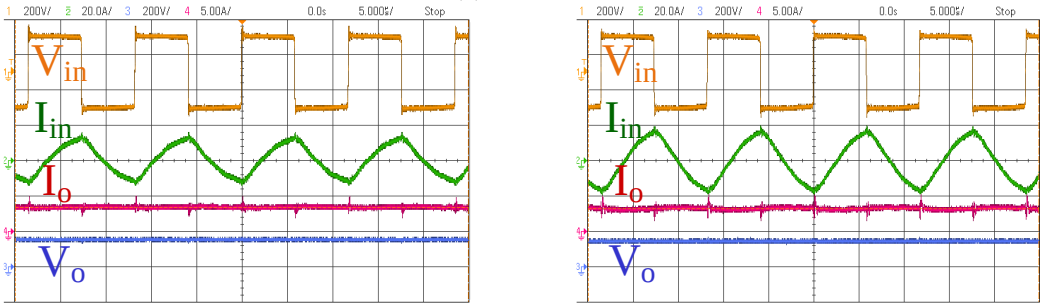

k=0.2 *k*=0.32

(c) LCC-LCC

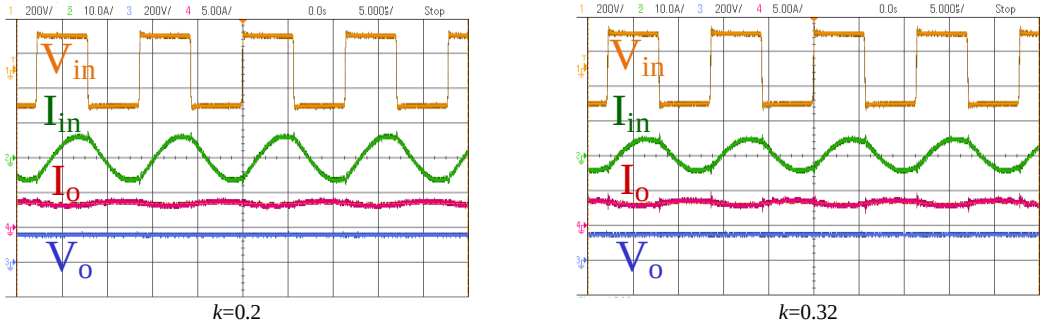

k=0.2 *k*=0.32

(d) Series-LCC

Fig. 3-17. Experimental voltage and current waveforms under different coupling conditions at 500 W load.

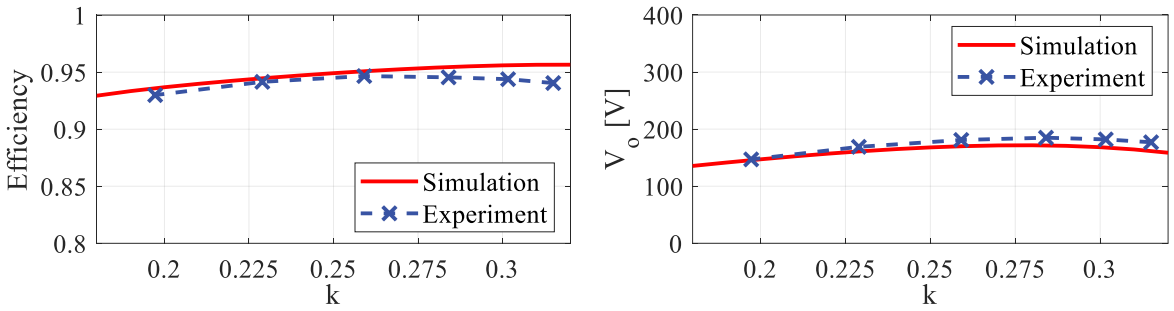

(a) Series-Series

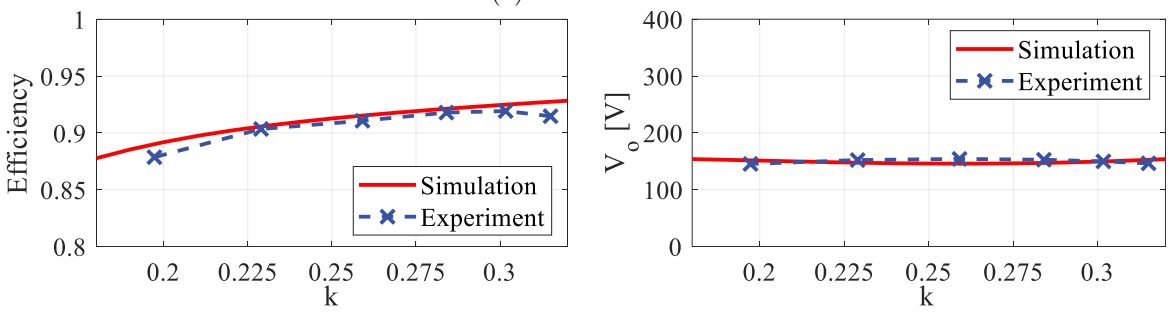

(b) LCC-Series

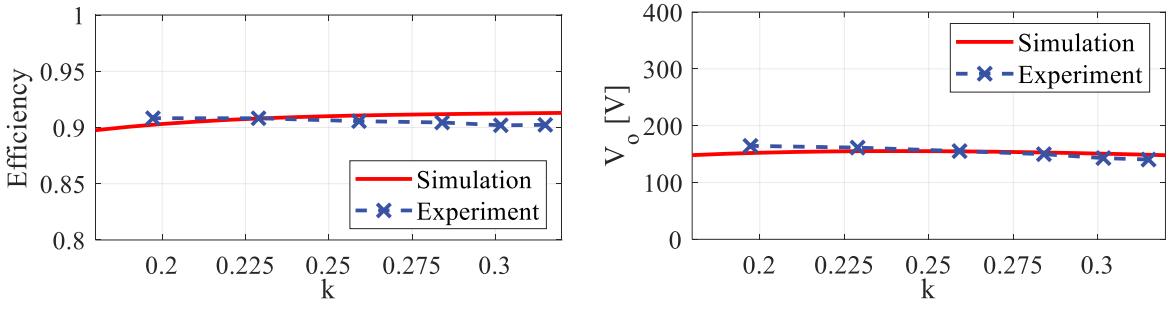

(c) LCC-LCC

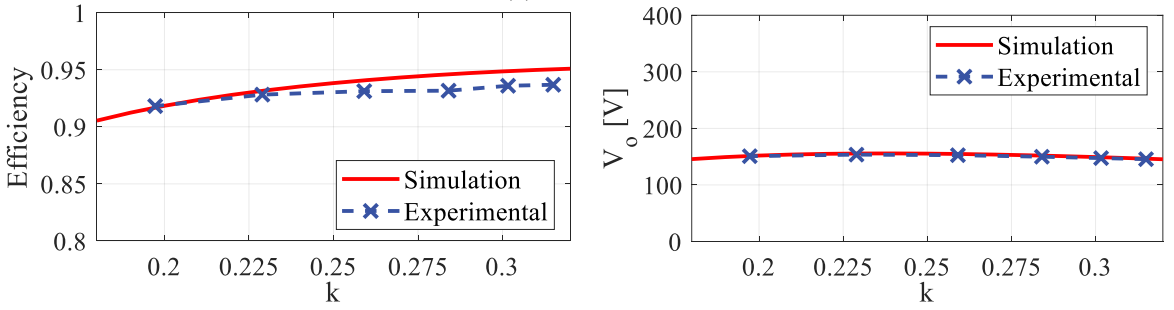

(d) Series-LCC

Fig. 3-18. Comparison of experimental and simulation results under different coupling conditions for Case I.

3.5. Conclusion

This chapter presents an optimal design of resonant networks in a WPT System for EV applications. The design has been done for two case scenarios: Case I: achieve a constant output voltage with respect to misalignments, and Case II: achieve the highest possible efficiency with respect to misalignments.

Different topologies are studied and optimized and the results are compared. To design the resonant networks, an optimization problem is defined to minimize the output voltage variation with respect to the misalignment. Moreover, practical constraints, losses, and ZVS conditions are also included in the design framework. All the topologies are optimized and compared from different aspects such as output voltage variations, average efficiency, number and size of the components, and power loss distribution. Among the different resonant topologies, LCC-LCC presented the best performance in terms of output voltage variation (4.7%) for the wide range of coupling factors between 0.18 to 0.32. Considering the average efficiency of the topologies, LCC-LCC is also the best topology at misalignment occurrences.

However, the number of components and their values in the LCC-LCC topology are higher than the other topologies. The next best candidate considering the number of components is LCC-Series with 5.3% output voltage fluctuation in

the desired misalignment range. Moreover, the average efficiency of LCC-Series was slightly lower than LCC-LCC. Therefore, taking the volume and weight of the design (power density) into account, especially in EV applications, LCC-Series can be considered as the best candidate with the least output voltage sensitivity and good average efficiency over a wide range of coupling factor variations.

By proposing the reduced voltage sensitivity WPT system, the variation of the output voltage reduced compared to conventional designs. Therefore, in the case of misalignment occurrence, the output voltage will not be affected significantly. In order to validate the proposed design procedure and the comparison of the topologies, a 500 W/85 kHz WPT system is built with circular magnetic couplers. The output voltage and efficiency of the converters are compared. The experimental results validated this conclusion and verified the performance of the optimized resonant network under different misalignments.

Chapter 4

A New Integrated Magnetic Structure for EV Wireless Charging Applications

4.1. Introduction

In Chapter 3, an optimization procedure for designing the resonant network of the wireless charging system with respect to misalignments is developed. It is shown that the LCC-S topology offers outstanding efficiency and misalignment tolerance. In this chapter, a new integrated wireless charging system is developed to improve the power density and reduces the implementation cost by reduction of the required ferrite material. Moreover, system-level optimization and magnetic structure optimization are developed to maximize efficiency of the wireless power transmission system.

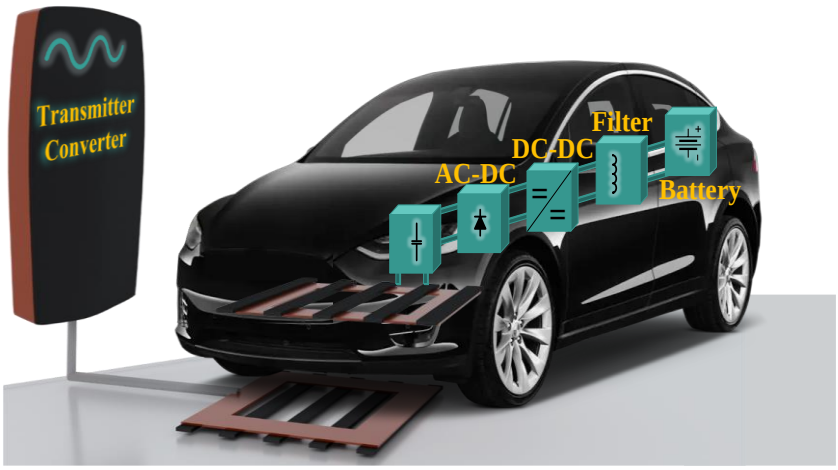

Fig. 4-1. A typical wireless EV charging system.

In a typical EV wireless charging system, as shown in Fig. 4-1, the receiver side consists of a resonant network, rectifier, and a DC-DC converter [69]. The DC-DC converter also requires a filter before connecting to the battery.

In this chapter, the LCC-S topology is selected. The LCC-S not only offers outstanding efficiency and misalignment tolerance, but also this topology presents suitable features for stationary charging such as high efficiency, low partial load losses, ZVS realization, and constant current on the primary side coil. The other attractive advantage of LCC-S topology for EV applications is the component counts [55]. This topology has only one capacitor on the vehicle side which reduces the weight, size, and cost. Especially, for EV application the power density of the system is crucial since space is limited on the vehicle side [119].

As discussed in Chapter 2, integration of the resonant inductors and magnetic couplers can reduce the use of ferrites and thus help to reduce the cost and improve the power density of the converter. Since the receiver converter is located on the vehicle side, the power density is more challenging and important.

In this chapter, a new structure is proposed to integrate the inductors needed for the DC-DC conversion stage on the vehicle side into the main magnetic couplers.

Table 4-1 compares the features of the proposed integration method with recently proposed integrated WPT systems.

TABLE 4-1
INTEGRATION METHOD AND POWER LEVEL COMPARISON

Ref.	Resonant inductor integration	DC-DC inductor integration	Power [kW]	Integrated coil
[119]	✓	×	3	Rectangular
[121]	✓	×	3.5	DD
[122]	✓	×	3	Bipolar
[123]	✓	×	5.6	DD
[120]	✓	×	3	Bipolar
Proposed	✓	✓	3.3	Bipolar

4.2. The Proposed Integrated Magnetic Structure

The proposed structure is shown in Fig. 4-2. In this structure, the space on the receiver magnetic coupler is used to place the DC-DC inductor and thus shrink the size of the receiver converter.

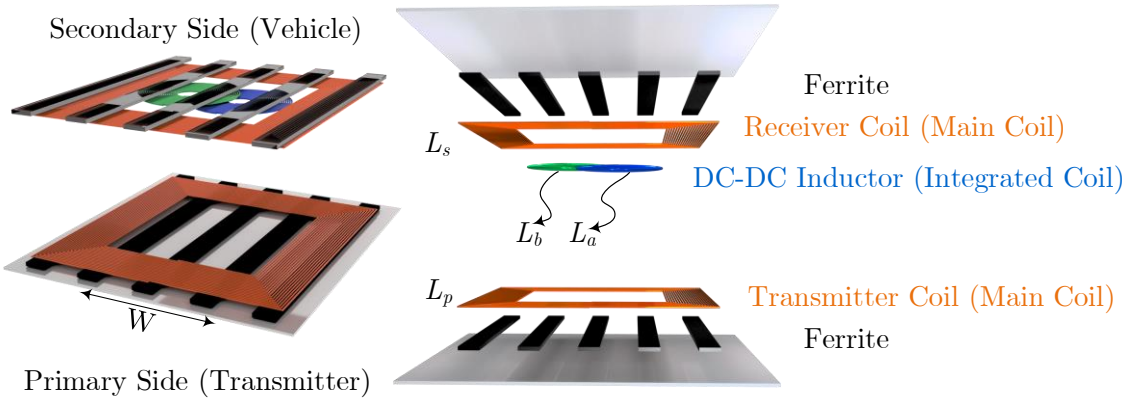

Fig. 4-2. Proposed WPT magnetic structure with integrated DC-DC converter inductor.

As discussed in Chapter 2, the rectangular and circular magnetic couplers are suitable candidates for stationary EV wireless charging applications. The rectangular magnetic coupler is chosen in this chapter because of two main reasons. First, the integrated coils should be placed in the inner space of the main coils. A rectangular magnetic coupler offers more inner space for the integrated coils compared to a circular magnetic coupler. Second, the middle area of the circular pad is not covered by ferrite and there is a hole in the middle of the structure. Therefore, the self-inductance of the integrated inductor will be low due to higher magnetic reluctance. The rectangular magnetic structure has more ferrite material

in the inner space of the magnetic coupler which is suitable for the integrated inductor.

The magnetic coupler structure is made of ferrite bars and rectangular coils as shown in Fig. 4-2. The DC-DC converter inductor coil (called integrated coil), is placed in the middle of the rectangular receiver coil (called main coil). The energy will be transferred through the main coils and the integrated coil is only be used for the DC-DC power conversion stage.

Integrating the magnetic structure of the magnetic couplers with the DC-DC inductor results in the mutual coupling between the DC-DC inductor and the magnetic couplers. This mutual inductance induces an unwanted voltage on the DC-DC inductor. To eliminate the effect of the coupling and the induced voltage, the DC-DC inductor can be divided into two coils. The two integrated coils (L_a and L_b) are placed in an opposing direction (bipolar type) to have opposing induced voltage from the main coils. By connecting the L_a and L_b coils in series, the DC-DC inductor is formed. Therefore, the unwanted induced voltage will be eliminated which will be discussed in detail in Section 4.2.3.

4.2.1. Case Study

In this case study, it is assumed that the magnetic coupler is designed and the total dimensions of the magnetic couplers are limited by 550mm×550mm. The

integrated coil is a bi-polar type coil that is required to be located inside the main coil. In this case, the available space is 190mm×190mm for each of them. The thickness and number of the ferrite bars are selected based on the finite element analysis to avoid saturation and excessive core losses. In this design, five ferrite bars with a dimension of 510mm×38mm×7mm are considered. The ferrite bars are N87 material from EPCOS which present a good performance in high-frequency power transmission.

The proposed magnetic coupler structure is modeled in ANSYS Maxwell and FEA results to calculate the self-inductance and mutual inductance between the main coils and integrated coils. The mutual inductance between the main coils is also affected by the position of the magnetic couplers respect to each other which is considered here by applying X and Y-direction misalignments. The x-axis misalignment (X-Mis.) and y-axis (Y-Mis.) tolerances are considered to be ±200mm. The self-inductance of the main coils (L_p and L_s) and integrated coils (L_a and L_b) with respect to misalignments are shown in Fig. 4-3. It can be seen that the self-inductances variations are negligible in the studied range. Therefore, these values are assumed constant for the simplicity of the circuit analysis.

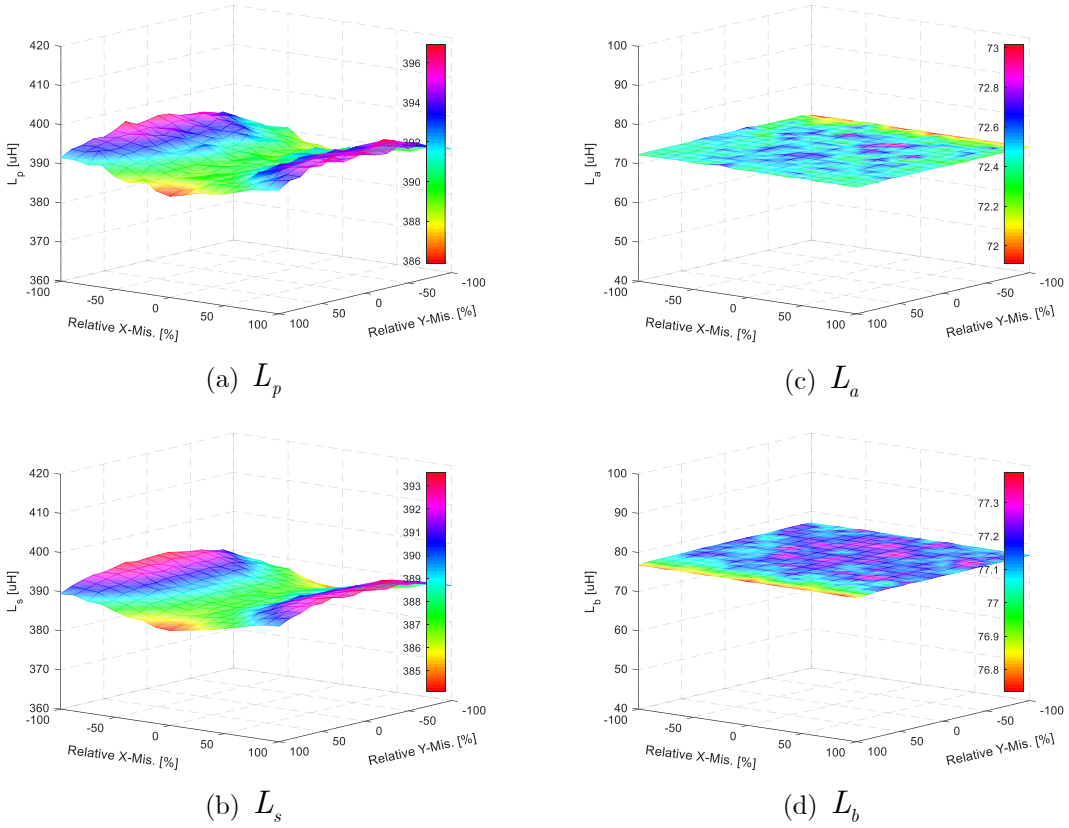

(a) L_p (c) L_a

(b) L_s (d) L_b

Fig. 4-3. Self-inductance variation of the proposed integrated magnetic structure under different misalignments.

The coupling coefficients can also be defined as:

$$k_{ps} = M_{ps}\Big/\sqrt{L_pL_s}\ ,\ k_{pa} = M_{pa}\Big/\sqrt{L_pL_a}\ ,\ k_{pb} = M_{pb}\Big/\sqrt{L_pL_b}$$
$$k_{sa} = M_{sa}\Big/\sqrt{L_sL_a}\ ,\ k_{sb} = M_{sb}\Big/\sqrt{L_sL_b}\ ,\ k_{ab} = M_{ab}\Big/\sqrt{L_aL_b} \tag{4.1}$$

where k_{ps} is the mutual coupling coefficient between primary and secondary side coil, k_{pa} is the mutual coupling coefficient between primary and integrated coil A, and k_{pb} is the mutual coupling coefficient between primary and integrated coil B at the nominal air gap.

The results are shown in Fig. 4-4. In Fig. 4-4 (a), the coupling factor is varied from 0.32 to 0.034 when there is a ±200mm misalignment between the centers of the two magnetic couplers. The coupling factors and self-inductance values are presented relative to 200 mm for 100% misalignment.

The variation of the magnetic coupler position results in the variation of the mutual inductance between the primary coil and DC-DC inductors. It can be seen that k_{pa} and k_{pb} values at different misalignment conditions are close to each other. This feature is used to connect the two coils in a reverse connection to cancel out the unwanted induce voltage from the primary side coil on the DC-DC inductors. In other words, the integrated coil is decoupled from the main coils. This feature will be further elaborated in Section 4.2.3.

The mutual coupling between the secondary side coil and auxiliary coils (k_{sa}, k_{sb}) and the mutual coupling factor of the two integrated coils (k_{ab}) are shown in Fig. 4-4 (d), (e), and (f) respectively. In Fig. 4-4 (d) and (e), it can be seen that the coupling factor between the secondary side main coil remains almost constant for different misalignment variations. Similarly, the coupling factor between the two integrated coils, k_{ab}, is also remained constant in this region as shown in Fig. 4-4 (f). This is because of the fact that the position of the two DC-DC inductors is not

changed by applying X and Y-misalignment between the primary and secondary main coils.

It should be noted that it is possible to place the integrated coils in the back of the ferrite bars. In that case, more space is available for the integrated coils and the inductance value could be increased. Moreover, the values of k_{pa}, k_{pb}, k_{sa}, and k_{sb} are reduced compared to the proposed design, and the values of k_{ps} and k_{ab} have remained the same as the originally proposed structure. Therefore, the mutual inductances between the DC-DC coils, primary and secondary side coils will be reduced which reduces the unwanted induce voltage. However, in that case, an extra layer of shielding is needed to avoid excessive magnetic flux flowing into the vehicle and passenger to meet the safety standards. Therefore, to avoid adding an extra layer to the magnetic structure and magnetic flux leakage in the vehicle side, the first approach is selected.

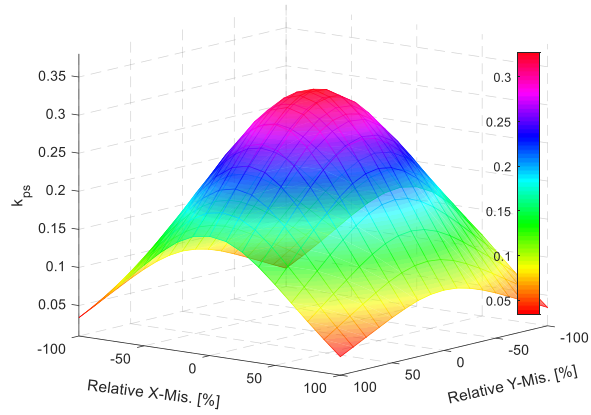

(a) k_{ps}

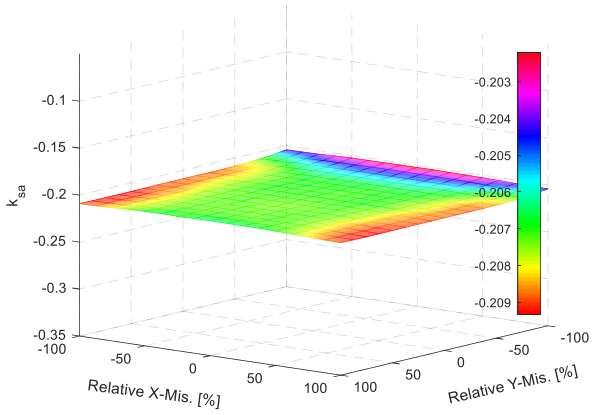

(d) k_{sa}

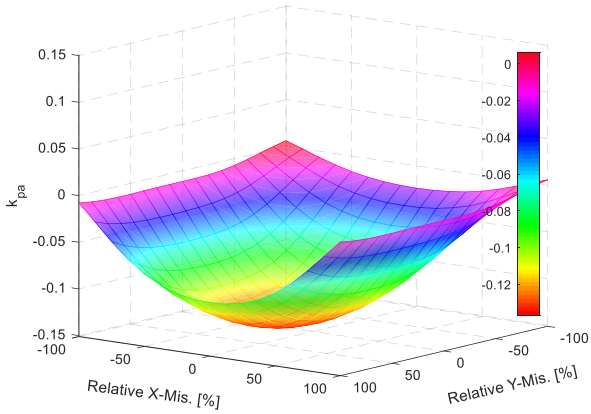

(b) k_{pa}

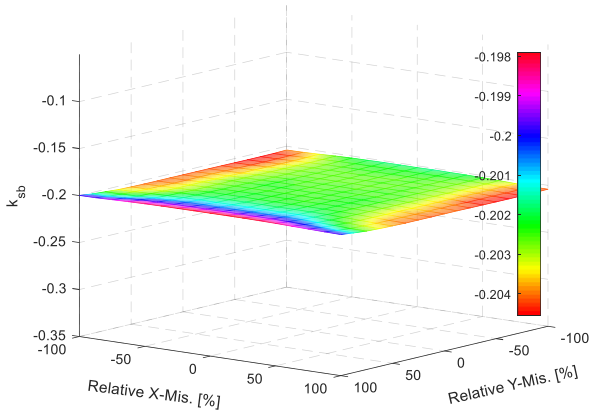

(e) k_{sb}

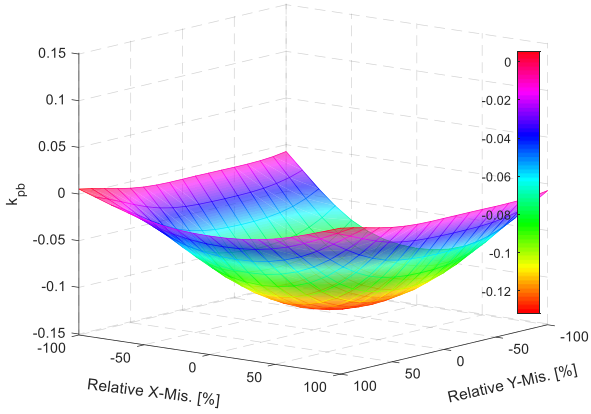

(c) k_{pb}

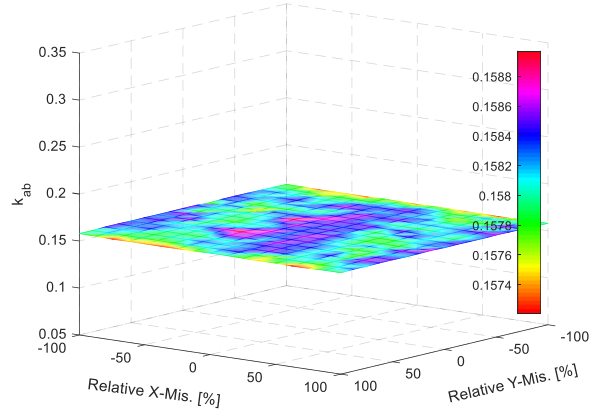

(f) k_{ab}

Fig. 4-4. Coupling factor variation of the proposed integrated magnetic structure under different misalignments.

4.2.2. Design Guidelines

The size of the magnetic coupler is related to the uncompensated power which is equivalent to the short-circuit current times open-circuit voltage. The open-circuit voltage is dependent on the coupling factor of the magnetic couplers and the primary side current.

First, according to the required power level and the available space for the magnetic coupler, an initial structure will be designed. The diameter of Litz wire is selected according to the current rating of the coils. Each strand diameter should be selected according to the skin depth at the operating frequency. Then the total required number of strands can be calculated.

Different design parameters with several iterations should be considered for the proper design;

- The ferrite bars used in the structure are the I-type ferrite cores. Limited variations of these bars are available in the market. Therefore, the size of the ferrite bars should be considered as a discrete variable in the design process.
- To have an optimal design, some constraints should be considered in the design process. For instance, the size of the integrated coils should be less than the internal diameter of the magnetic coupler. Moreover,

the self-inductance value of the main coils should be limited to avoid excessive voltages on the winding.

- The volume of ferrite material or copper should be minimized. The volume of ferrite not only improves the coupling factor but also affects the self-inductance values.

- The self-inductance value of the DC-DC inductor can be determined by the ferrite bars dimension, the number of turns, and outer diameter. The outer diameter of the integrated coils is limited to the inner width of the main coil to avoid adding an extra layer to the structure.

- FEA studies are also done to show the effect of the number of ferrite bars on the self-inductance of the DC-DC inductor and k_{ps}. The results are presented in Table 4-2.

TABLE 4-2
EFFECT OF FERRITE VOLUME ON THE COUPLING FACTOR AND SELF-INDUCTANCES

Number of ferrite bars	Ferrite Weight [kg]	Ferrite Volume [mm^3]	Max. k_{ps}	L_p, L_s [µH]	L_a, L_b [µH]
4	2.6	542640	0.3158	363.5, 361.3	71.2, 75.3
5	3.3	678300	0.3273	390.7, 387.9	72.6, 77.3
6	3.9	813960	0.3337	408.1, 406.2	76.3, 81.9
Fully covered	7.9	1635060	0.3738	504, 501.6	89.8, 98.5

According to Table 4-2, the increase in the volume of ferrite will lead to increase maximum coupling factor and self-inductance values. However, large self-inductance of the main coils results in increasing their voltage stress. Moreover, there is not a significant difference between the results of five ferrite and six bars. Therefore, five number of bars are selected in this study to save ferrite and reduce the implementation cost.

4.2.3. Analysis and Design of the Integrated Magnetic Structure

A. Circuit Modeling and Analysis

To design the resonant network and analyze the effect of the mutual inductance between the main coils and integrated coils (DC-DC inductor), a frequency domain analysis is presented in this section. The presented model is used in an optimization program to optimally design the resonant elements of the EV wireless charging system. By using the presented model of the system, the unwanted voltage induced on the DC-DC inductors is analyzed and a new method is presented to eliminate this unwanted voltage.

The primary side converter is a full-bridge inverter fed by the dc source and the output of the inverter is connected to the primary side resonant network. The LCC-S topology is selected for the resonant and is shown in Fig. 4-5.

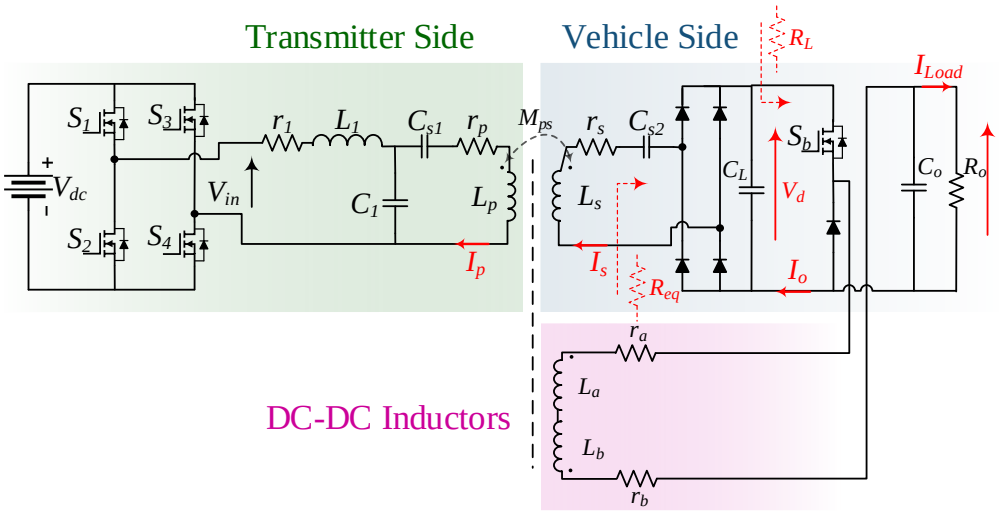

Fig. 4-5. A WPT system with an LCC-S resonant network and proposed integrated DC-DC conversion stage coils.

The high-order resonant network absorbs the higher harmonics of the inverter voltage. Therefore, for the simplicity of the analysis and design of the resonant network, fundamental harmonic analysis is commonly used. The RMS value of the voltage waveform generated by the voltage source inverter is calculated as $V_{in}^{RMS} = (\sqrt{8}\mathrm{V}_{\mathrm{dc}}/\pi)\sin(\theta/2)$ [26].

In this equation, θ is the phase-shift of the inverter legs with operating angular frequency of ω. The phase-shift angle can be used to control the RMS value of the input voltage of the resonant network to control the output voltage.

Similarly, considering a high value for the output dc-link capacitor, the resistance seen by the vehicle side resonant network from the diode bridge is

expressed as $R_{eq} = 8/\pi^2 R_L$ [26]. The value of R_L is dependent on the duty cycle of the DC-DC converter which is a buck converter in this chapter. According to these assumptions, the equivalent circuit is shown in Fig. 4-6.

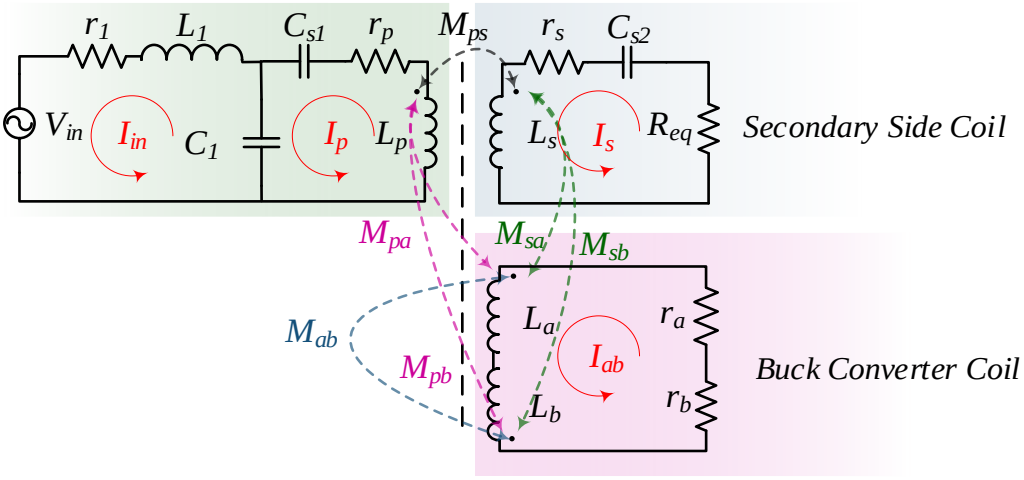

Fig. 4-6. Simplified circuit of the LCC-S compensated topology with integrated DC-DC coils.

In this figure, r_p and r_s are the primary and secondary side coils AC resistances, and parameters r_a and r_b are the integrated coils parasitic AC resistance. In this circuit, L_a and L_b forms the inductors of the DC-DC converter.

According to Kirchhoff's Voltage Law (KVL), the steady-state of the LCC-S topology shown in Fig. 4-6 is described as $V = ZI$, where:

$$[V]^T = \begin{bmatrix} V_{in} & 0 & 0 & 0 \end{bmatrix},$$
$$[I]^T = \begin{bmatrix} I_{in} & I_p & I_s & I_{ab} \end{bmatrix}, \tag{4.2}$$

$$Z = \begin{bmatrix} Z_{11} & -Z_{12} & 0 & 0 \\ -Z_{12} & Z_{22} & -Z_{23} & -Z_{24} \\ 0 & -Z_{23} & Z_{33} & -Z_{34} \\ 0 & -Z_{24} & -Z_{34} & Z_{44} \end{bmatrix}$$

The diagonal elements of the impedance matrix are defined as follows:

$$\begin{aligned} Z_{11} &= r_1 + j\omega\left(L_1 - \frac{1}{\omega^2 C_1}\right) \\ Z_{22} &= r_p + j\omega\left(L_p - \frac{1}{\omega^2 C_{1s}} - \frac{1}{\omega^2 C_1}\right) \\ Z_{33} &= R_{eq} + r_s + j\omega\left(L_s - \frac{1}{\omega^2 C_{2s}}\right) \\ Z_{44} &= r_a + r_b + j\omega\left(L_a + L_b - 2M_{ab}\right) \end{aligned} \tag{4.3}$$

Similarly, the non-diagonal elements are defined as:

$$\begin{aligned} Z_{12} &= \frac{1}{\omega^2 C_1} \\ Z_{23} &= j\omega M_{ps} \\ Z_{24} &= j\omega\left(M_{pa} - M_{pb}\right) \\ Z_{34} &= j\omega\left(M_{sb} - M_{sa}\right) \end{aligned} \tag{4.4}$$

According to the presented analysis, the input current of the circuit is calculated as follows:

$$I_{in} = -V_{in} \times \frac{Z_{12}Z_{33}Z_{44}}{Z_{33}Z_{44}{Z_{12}}^2 + Z_{11}\left(Z_{44}{Z_{23}}^2 + Z_{33}{Z_{24}}^2 - Z_{22}Z_{33}Z_{44}\right)} \tag{4.5}$$

The transmitter coil current (I_p) and secondary side coil current (I_s) can be expressed by:

$$I_p = -I_{in} \times \frac{Z_{12}(Z_{33}Z_{44} - {Z_{34}}^2)}{Z_{44}{Z_{23}}^2 + Z_{22}{Z_{34}}^2 + 2Z_{24}Z_{23}Z_{34} - Z_{33}(Z_{22}Z_{44} - {Z_{24}}^2)}$$
$$I_s = I_p \frac{Z_{24}Z_{34} + Z_{23}Z_{44}}{Z_{33}Z_{44} - {Z_{34}}^2} \tag{4.6}$$

It should also be noted that the secondary side coil current is equal to the load current. The induced voltage on the series-connected integrated coils (DC-DC) can be written as:

$$V_{ab}^{oc} = j\omega\left[\left(M_{pa} - M_{pb}\right)I_p + \left(M_{sb} - M_{sa}\right)I_s\right] \tag{4.7}$$

It can be concluded from (4.7) that the induced voltage on the integrated coils is dependent on the difference of their mutual inductances with primary and secondary coils. If the integrated coils are placed in a way to have equal mutual inductances, they will cancel out their effects and the induced voltage will be minimized. In order to eliminate the induced voltage from the main coils, the DC-DC coil is divided into two parts which are connected reversely. In the fully-aligned condition, the induced voltage will be zero. In case of misalignment, the mutual couplings are not equal to cancel out each other. In that case, a small AC voltage will be induced on the DC-DC coil which will discuss further in the next part. The output voltage of the wireless charging system on the equivalent resistance is defined by:

$$V_o = R_{eq} I_o = R_{eq} \frac{Z_{24} Z_{34} + Z_{23} Z_{44}}{Z_{33} Z_{44} - Z_{34}^{\ 2}} \tag{4.8}$$

The coupling between the primary and secondary side (k_{ps}), directly affects the induced voltage on the secondary side coil, V_s^{oc}:

$$V_s^{oc} = j\omega \left[\left(M_{ps} \right) I_p + \left(M_{sb} - M_{sa} \right) I_{ab} \right] \tag{4.9}$$

The induced voltage on the secondary side also affects the input voltage of the buck converter, V_d:

$$I_s = \frac{V_s^{oc}}{r_s + j\omega \left(L_s - \dfrac{1}{\omega^2 C_{s2}} \right)} \tag{4.10}$$

$$V_d = \frac{\pi}{\sqrt{8}} R_{eq} I_s \tag{4.11}$$

In this analysis, it is assumed that the buck stage filter will absorb high-frequency components that are induced from the main coils. The DC-DC inductor is modeled in the analysis as an inductance series with its AC resistance as shown in Fig. 4-7 (a) and (b).

The unwanted induced voltage V_{ab}^{oc} is in series with the buck converter inductor. Fig. 4-7 (c) shows the simplified model of the buck converter circuit with the integrated coils. Then, the DC-DC inductor is divided into two coils which are connected reversely as shown in Fig. 4-7 (d). The RC component of the buck

converter itself acts as a low-pass filter which converts the square waveform into a ripple-free output voltage. Therefore, any high-frequency voltage component in the input of the filter of the buck converter will be absorbed and only dc component contributes to dc voltage at the output. As a result, the induced voltages on the coils will cancel out at fully-aligned conditions and the circuit can be simplified as Fig. 4-7 (e). Moreover, by analyzing the filtering effect of the RC network in the buck converter, it can be shown that the high-frequency component will not appear on the load.

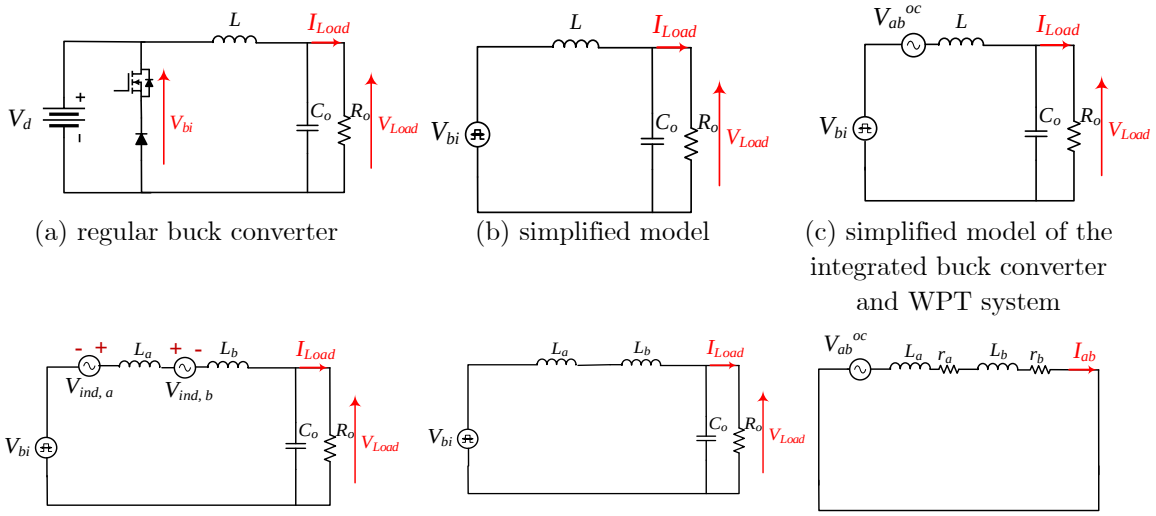

(a) regular buck converter (b) simplified model (c) simplified model of the integrated buck converter and WPT system

(d) inductor divided and connected reversely (e) the induced voltage canceled out (f) integrated inductor seen from the WPT system

Fig. 4-7. Circuit schematic of the wireless charging system with integrated magnetic coupler.

From the WPT circuit point of view, the buck converter circuit acts as a low-pass filter. Therefore, the integrated inductor can be modeled as an inductance series with their AC resistances and induced voltages from primary and secondary side coils as shown in Fig. 4-7 (f).

B. Optimization

The optimization is applied to the design of the WPT resonant elements. The resonant circuit is optimized to present high efficiency for the whole operating range. The nominal load is 3.3 kW; however, the converter will not operate at its maximum power for the whole charging process. Therefore, the Time-Weighted Average Efficiency (TWAE) optimization method for WPT systems [55] is adopted on the problem and Brand-And-Reduce Optimization Navigation (BARON) is used [145, 146]. BARON is a powerful optimization solver that can be used to solve non-convex and mixed-integer optimization problems. Besides, it can also find the global optimal point for the optimization problem if the boundaries are selected properly [147].

According to the SAE standard for stationary charging, the switching frequency of the transmitter side converter is limited to 85 kHz band. The output voltage is limited in the range of 300-600 V considering the voltage rating of the semiconductor devices on the vehicle side converter. To consider the heat generated

by the losses of the coils, the primary, and secondary side coil currents are limited to 15 A. In order to satisfy the ZVS condition, the imaginary part of the impedance seen by the full-bridge inverter should be a positive value. Therefore, the soft switching satisfaction condition is defined by the following constraint:

$$0 \le \phi = \measuredangle Z_{in} \le \pi/2 \tag{4.12}$$

In this section, the operating range for the WPT system is limited in the range of 0.22-0.32 for k_{ps} and the nominal power set for TWAE is $P_n = \{2100, 2400, 2700, 540\}$. In this range of coupling factors, the x and y-direction misalignments are limited to $\pm 115mm$ at the nominal air-gap. Table 4-3 lists the designed 3.3 kW/85 kHz WPT system with the proposed magnetic structure and discussed constraints.

TABLE 4-3
DESIGN SPECIFICATIONS

Variable	Selected Value
L_1	66.1 µH
C_1	48.4 nF
C_{s1}	11.6 nF
C_{s2}	9.7 nF

The efficiency and output voltage of the designed WPT system (without considering the DC-DC stage on the vehicle side) are shown in Fig. 4-8. It can be seen that the efficiency curve is almost flat for the acceptable desired operating range.

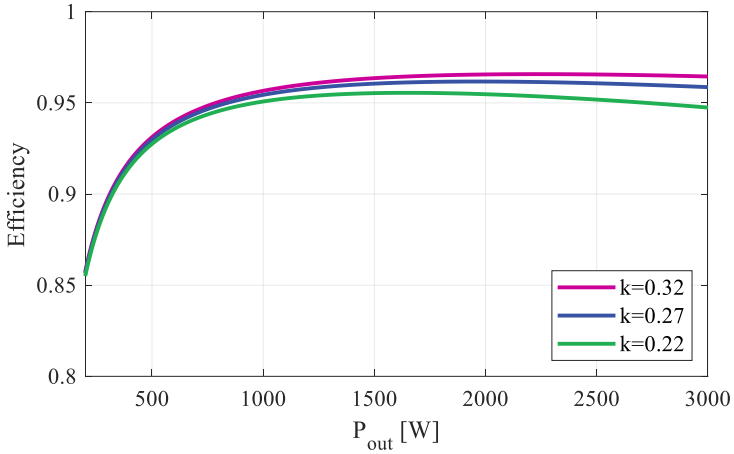

Fig. 4-8. The efficiency of the WPT system under different coupling conditions versus output power.

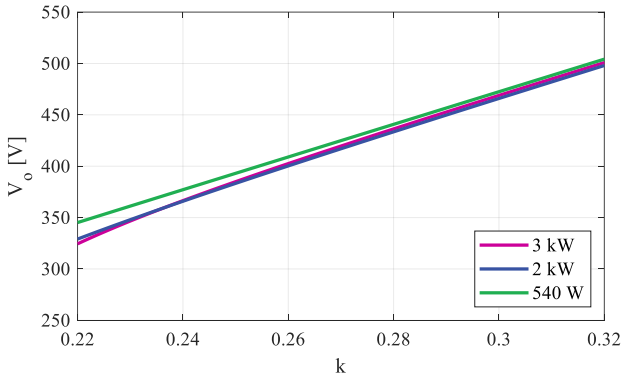

(a) output voltage versus coupling factor

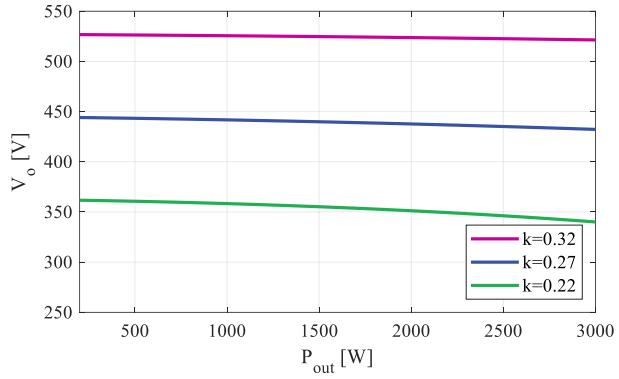

(b) Output voltage versus output power

Fig. 4-9. The output voltage of the WPT system under different loading conditions.

The output voltage has an increasing trend as the coupling factor increases as shown in Fig. 4-9 (a). Moreover, from Fig. 4-9 (b) it can be concluded that the output voltage is not sensitive to the load since at each coupling factor the value of the output voltage remained almost constant when the load increased from light-load to full-load condition.

C. Design Challenges

Although integration of the magnetic couplers and DC-DC inductor results in a more compact design and reduces cost by saving ferrite material, it also brings some challenges for the design. Since the magnetic couplers are placed in the same plane as the secondary side main coil, there are parasitic mutual inductances between the primary, secondary, and DC-DC coils as discussed in Section 4.2.2.

As discussed, to improve the performance of the system and reduce the induced voltage, the DC-DC inductor is divided into two coils. The two integrated coils are connected reversely to cancel out their induced voltages at fully-aligned operation. However, due to the misalignment occurrence, the values of their mutual inductance and their corresponding induced voltages will not be eliminated. In case of the misalignment, the induced voltage is described in (4.7). This voltage results slightly more losses in the system.

According to the calculated values of the mutual inductances in the FEA results and (4.7), the induced voltage on the auxiliary coils is calculated and illustrated in Fig. 4-10. In Fig. 4-10 (a), the induced voltage at the nominal air-gap under different X-misalignment is shown and it can be seen that the induced voltage on these coils is negligible as expected. Thanks to the symmetrical design of the integrated coils, at zero Y-Mis. their mutual inductance with transmitter (primary) coil is canceled out and resulted in a very low induced voltage on them. However, the magnetic structure is not symmetrical when Y-direction misalignments happen.

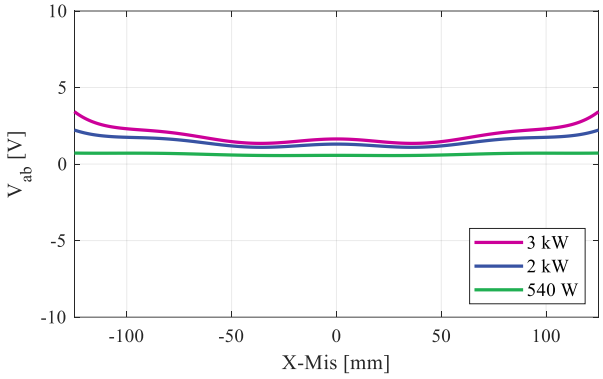

(a) Induced voltage versus Y-Mis

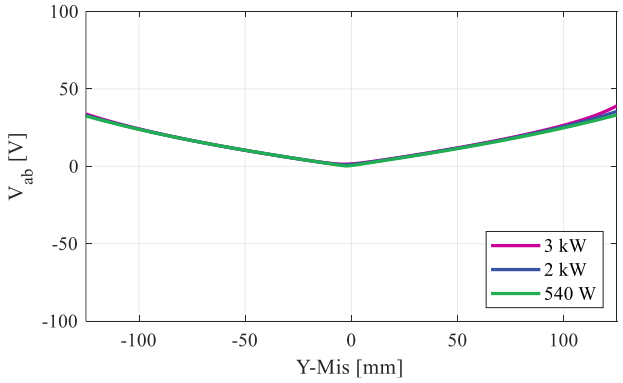

(b) Induced voltage versus Y-Mis

Fig. 4-10. Induced voltage on the auxiliary coils versus X-Mis. and Y-Mis.

Therefore, the value of mutual inductances can induce a low voltage on the integrated coils. Since the circuit seen by the induced voltage on the integrated coil behaves as a low-pass filter, the 85 kHz voltage generated by the WPT is not affecting the DC-DC conversion stage and not contributing to generating more power loss. Moreover, since a closed-loop controller is used on the DC-DC converter, any ripple caused by the induced voltage will be eliminated.

Due to the limited space available in the magnetic coupler of the wireless charger, the size of the integrated DC-DC inductor is limited too. In some applications that need more inductance value, this issue needs to be considered. By increasing the volume of the utilized ferrite in the structure, both main coil self-inductance and integrated coil self-inductance will increase. However, increasing the volume of ferrite is contradicting with the idea of reduction of the utilized ferrite material. Alternatively, by increasing the number of turns the value of the self-inductance can be controlled. In this case, if the same plane with the secondary side coils was not enough, the back of the ferrite material can be considered to be fully covered by the integrated inductor. The third solution for increasing the value of the inductance in the proposed integration method is swapping the integrated inductor and main coils. In that case, the value of the integrated coil self-inductance will be much higher than the presented design in this section.

D. Dynamic Performance

The dynamic performance of the integrated buck converter is similar to the conventional buck converter. The impedance seen from the unwanted induce voltage (V_{ab}) is a low-pass filter. Therefore, high-frequency components of the voltage will not change the performance and dynamic response of the buck converter. The presented charging system is for stationary charging applications in which the coupling factor will not change during the charging process. Therefore, except for the start-up of the system, no transient and dynamic response is expected in the operation of the buck stage.

In order to evaluate the dynamic response of the integrated buck converter variation of output power from half to full-load at k=0.32 and k=0.22 is presented in Fig. 4-11. It can be seen that at lower coupling factors, there are less fluctuations in the output voltage. Because at lower coupling factors both the unwanted induced voltage and input voltage of the buck stage have lower amplitudes compared to the fully-aligned condition.

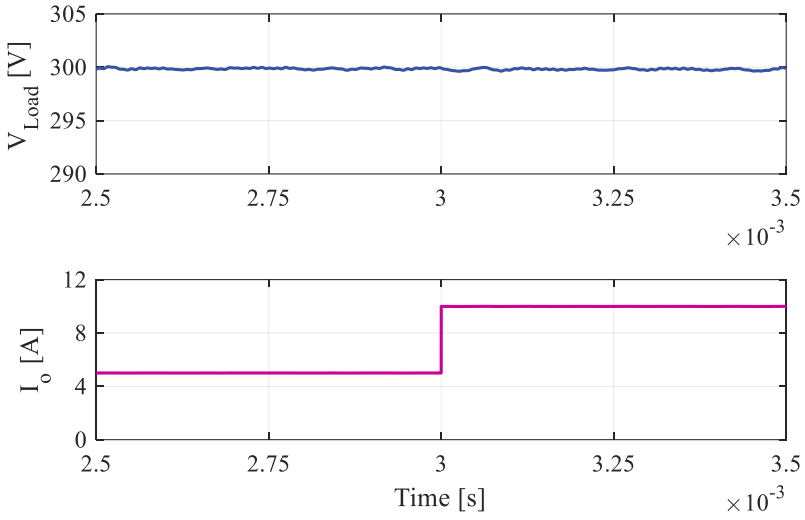

(a) k=0.32

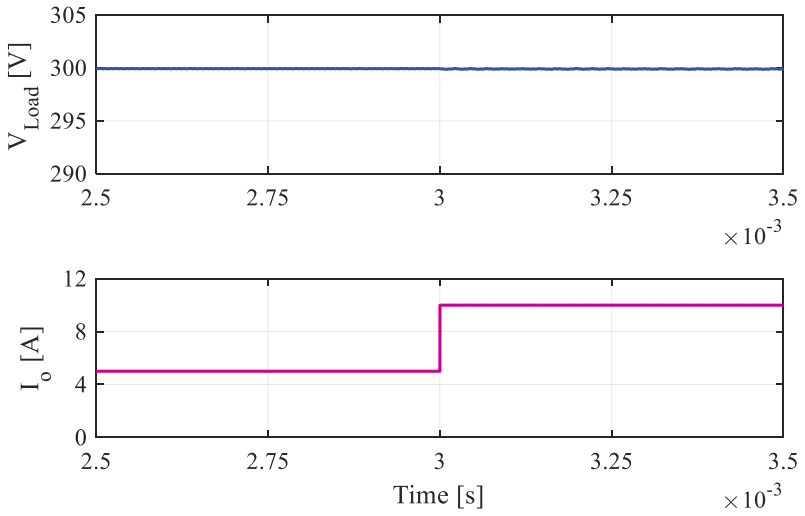

(b) k=0.22

Fig. 4-11. Dynamic response of the buck converter from half to the full-load loading condition

E. Comparison with Conventional Buck Converter

Compared to a conventional buck converter, the proposed integrated converter has slightly lower efficiency. The magnetic coupling between the main coils and integrated coils generates an induced voltage on the buck converter inductor. This

voltage causes more losses in the system. However, the output ripple is not affected because of the filtering effect of the low-pass filter in the output of the buck stage.

In order to compare the losses of the proposed integrated structure with the conventional WPT system with a regular buck converter, the core and conduction losses are calculated using 3D-FEA. In this comparison, the DC-DC inductor of the regular buck converter is made by an E65 ferrite core with 15 turns of Litz wire. At the nominal loading condition, the total magnetic elements loss of the conventional WPT system including the conventional DC-DC inductor and main couplers is calculated 44.1 W. The total magnetic elements loss of the proposed integrated structure in the fully-aligned position at rated load is calculated 52.21 W. Although the total magnetic loss of the proposed system is slightly higher, considering the rated power of 3.3 kW, the difference of efficiency is ~0.2% increase which is negligible.

4.2.4. Experimental Results

To validate the proposed integrated magnetic structure, a prototype of the WPT system with rectangular magnetic coupler is built. The rated power for the system is 3.3 kW and the nominal air-gap is set to 150mm. Fig. 4-12 illustrates the 3.3-kW setup built in the lab. The realized integrated magnetic structure is shown in Fig. 4-13.

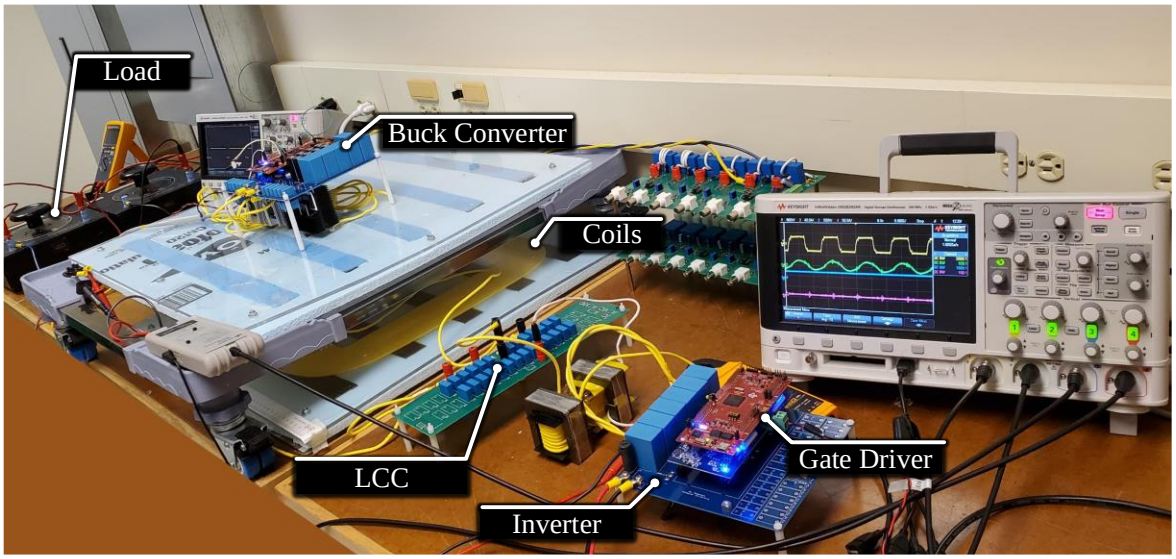

Fig. 4-12. Realized prototype of the WPT system.

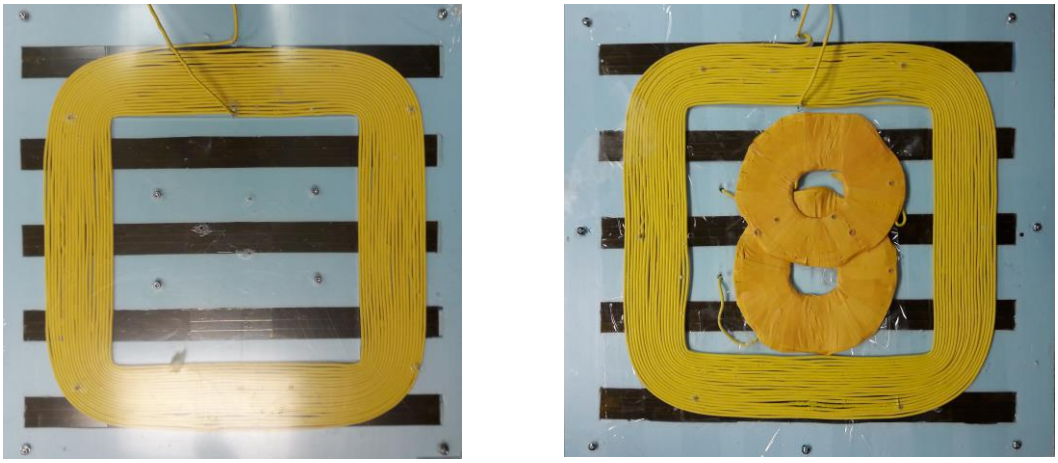

(a) primary side coil (b) secondary side coil

Fig. 4-13. Realized proposed integrated magnetic structure.

Since the inner rectangle of the auxiliary coils was small compared to the large diameter of the Litz wire, their shape turned into a circular form. In this setup, the coils are made by 500 strands of AWG 38 and the ferrites are type N87 from EPCOS. In the primary side converter, IPW65R037C6 *CoolMOS* is used which has

a 37 mΩ turn-on resistance. The resonant capacitors are selected based on their withstand voltage at 85 kHz operation. In this design, film metalized polypropylene capacitors from EPCOS are used to reduce the capacitor losses. The switching frequency of the buck converter is selected to be 120 kHz.

The 3D-model of the designed PCB for the secondary side converter and its realized final assembly is shown in Fig. 4-14. In order to ensure the reliable operation of the converter, additional thermal analysis based on the calculated power losses is also performed on the 3D-model. According to the thermal analysis, heatsinks and PCB dimensions are selected after several iterations which are out of the scope of this thesis. The value of the DC-link capacitors is selected based on the time-domain analysis. For simplicity, the DC-DC integrated coils are used for a simple buck converter. However, these inductors can be used for any other DC-DC converter on the secondary side too.

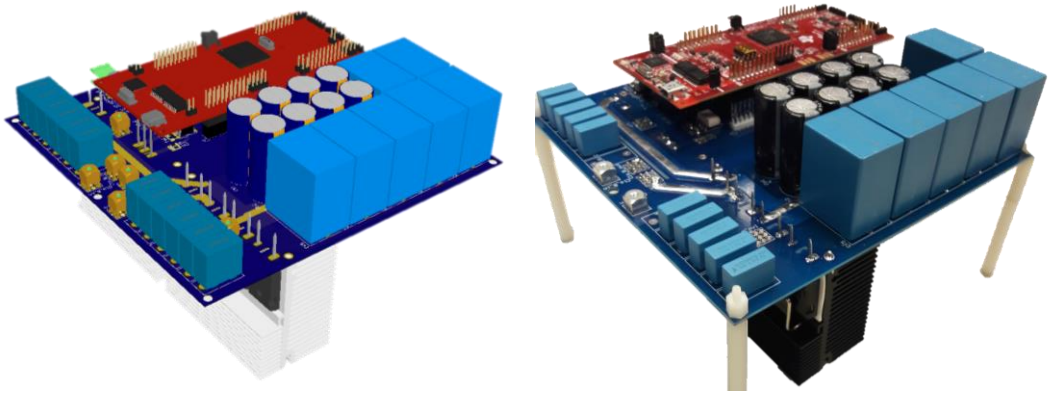

(a) 3D-model (b) Final assembly

Fig. 4-14. The secondary side converter including the resonant network, rectifier, and DC-DC converter.

Fig. 4-15 shows the experimental results at three different loading condition coils at the nominal air-gap and fully-aligned condition and under misalignment occurrence. In this figure, the input voltage of the buck converter is shown which is the WPT system output voltage before the final DC-DC conversion stage. The ZVS operation can be verified in Fig. 4-15 which the inverter current has a phase lag compared to the inverter output voltage. Besides, the output voltage remained almost constant as expected when the output power changed from full-load to half-load condition.

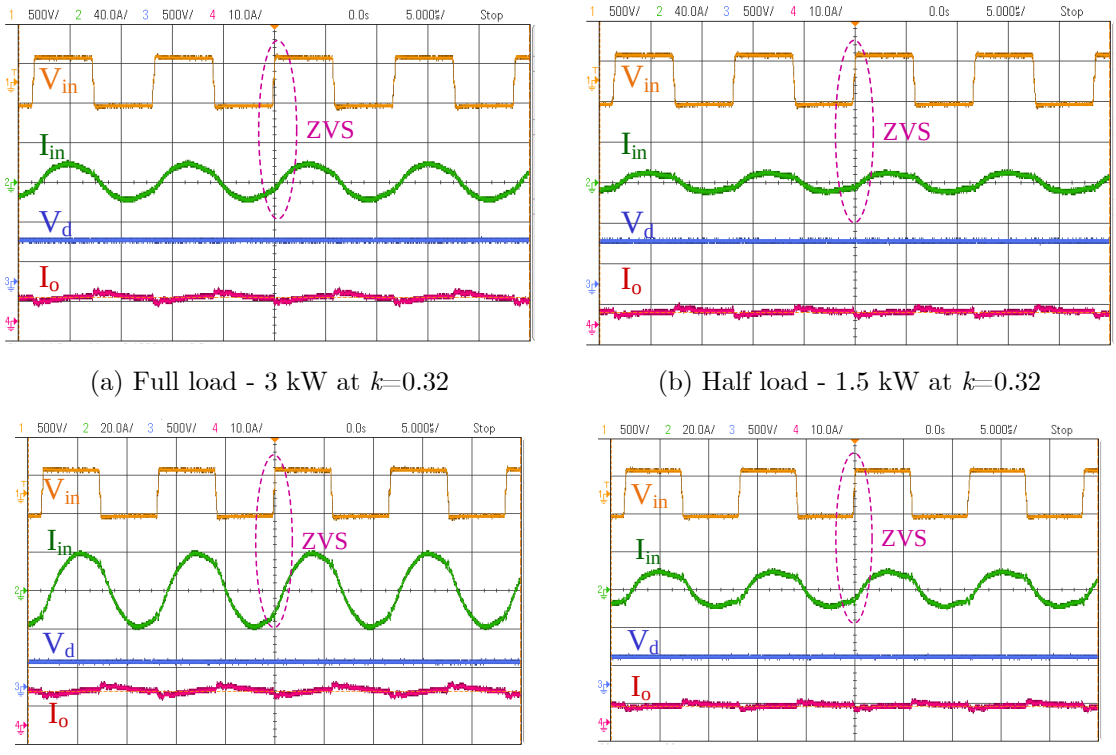

(a) Full load - 3 kW at k=0.32

(b) Half load - 1.5 kW at k=0.32

(c) Full load - 3 kW at k=0.22

(d) Half load - 1.5 kW at k=0.22

Fig. 4-15. Experimental output waveforms.

The measured efficiency and output voltages of the system are close to the calculated values. Moreover, the efficiency of the system maintained higher than 90 % even at partial output power conditions. Fig. 4-16 (b) illustrates the output voltage of the WPT system (input of the buck stage) at three different coupling factors from low output power to the rated power.

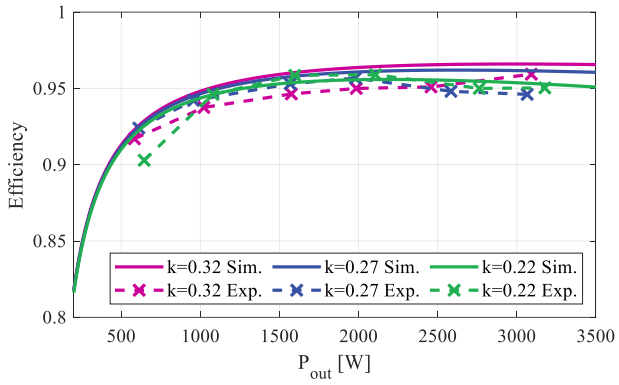

(a) Efficiency of the WPT system

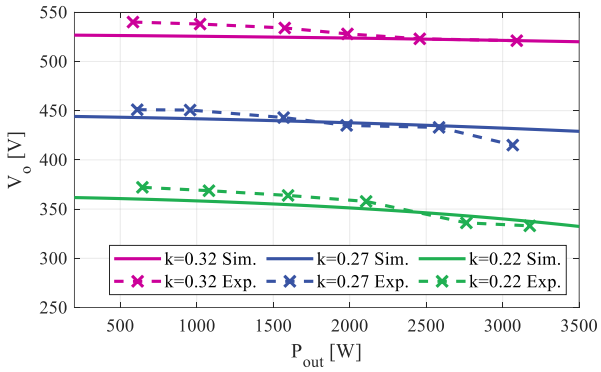

(b) Output voltage of the WPT system before buck stage V_d

Fig. 4-16. Comparison of the experimental and simulation results versus output power under different coupling factors.

It can be seen that the output voltage presented an almost constant profile for the whole range. Therefore, the duty cycle of the buck converter will almost remain constant at each coupling operating point are shown in Fig. 4-16. Moreover, it can

be seen that the measured voltage is slightly different from the simulation results which can be caused by the tuning of the resonant network errors or magnetic couplers.

In order to verify the proposed integration method, the output voltage of the buck converter in the CV mode is presented in Fig. 4-17. It can be seen that the output voltage is regulated at 300 V. Moreover, the induced voltages from the primary side coil on the DC-DC coils are eliminated in the output voltage in any operating condition.

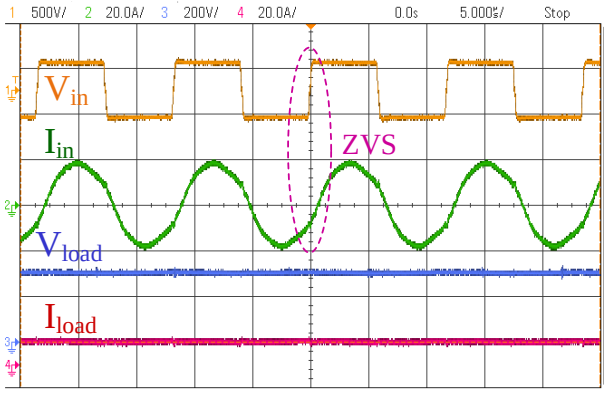

(a) k=0.32

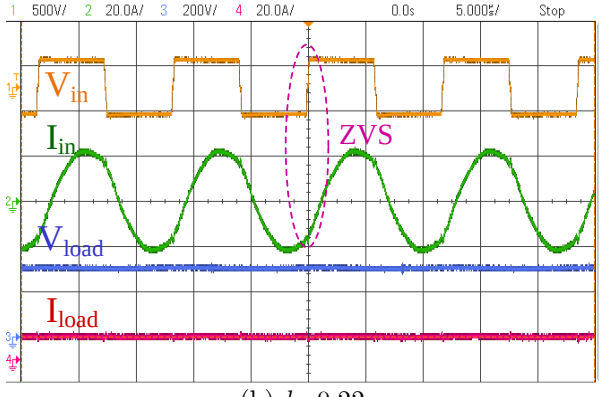

(b) k=0.22

Fig. 4-17. Experimental waveforms under different coupling factors at rated load.

4.3. A Fully-Integrated Magnetic Structure

This section proposes a full integration of resonant inductor with the transmitter side coil and the DC-DC inductor with the receiver side coil to save the overall cost and improve the power density. This full integration approach leads to new challenges; when the DC-DC inductor integrates into the receiver side coil, the cross-coupling effect will induce an extra voltage on integrated coils especially under misalignment conditions. The additional induced voltage results in more conduction loss in the system. Having two integrated coils in the magnetic couplers results in an additional cross-coupling between the resonant inductor and DC-DC inductor. The cross-coupling is large enough to affect system efficiency.

In this section, the side effects of the integration of the magnetic components on the efficiency of the system are analyzed and sensitive parameters are discussed in detail. The magnetic structure is simulated through finite element analysis. The losses of the magnetic structure are modeled. An optimization problem is defined to select the optimal magnetic structure and determine the optimal value of resonant elements. The optimization problem is based on the design requirements and constraints, the FEA results of the magnetic structures, and losses of the system including core losses. The result of the proposed integration method is an efficient wireless charger with a lower number of components and compact

converters. The performance of the proposed integration method is evaluated through experiments in both steady-state and transient operation modes.

4.3.1. The Layout of the Fully Integrated Magnetic Structure

In order to integrate the resonant and DC-DC inductors (called integrated inductors) into the transmitter/receiver coils (called main coils), the integrated inductors should be decoupled from the main coils. The integration can be done in two methods: Integration into a Unipolar (IU) structure and Integration into a Bipolar (IB) structure [122]. Fig. 4-18 illustrates the layout of IU and IB integration structures.

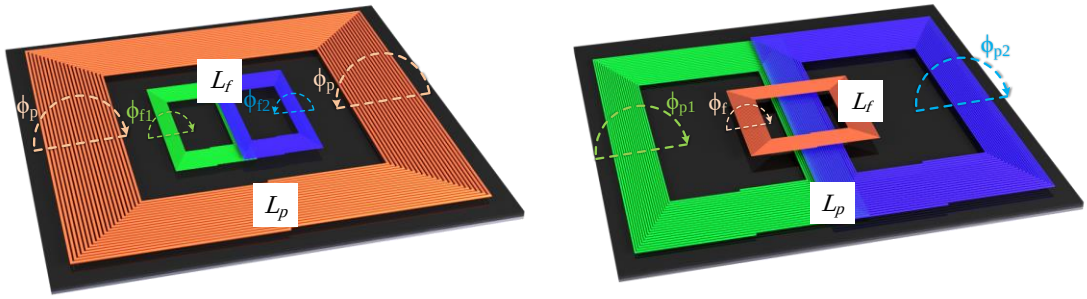

(a) Integration to Unipolar (IU) (b) Integration to Bipolar (IB)

Fig. 4-18. Integration methods of the inductor into the main magnetic couplers.

In the IU structure, the main coil is unipolar (i.e., rectangular coil) and the integrated coil is a DD coil. The DD coil is made by two rectangular coils that are connected in series (L_{f1} and L_{f2}) as shown in Fig. 4-18 (a). The electrical connection of the bipolar coil is in a way that the two rectangular coils generate opposite

magnetic flux. In an ideal condition, the amplitude of the generated flux of the first coil (ϕ_{f1}) is equal to the flux of the second rectangular coil (ϕ_{f2}). Ideally, the total magnetic flux of the integrated coil that passes through the primary side coil (L_p) would be zero and the main coil of the magnetic coupler (L_p) would be decoupled from the integrated inductor (L_f).

In the IB structure, the main coil is a DD coil and the integrated coil is a rectangular coil placed in the middle of the main coil as shown in Fig. 4-18 (b). In this layout, the sum of the flux of the main bipolar coil (ϕ_{p1} and ϕ_{p2}) that passes through the integrated rectangular coil (L_f) should be zero. In this layout, the electrical connection of the main coil is in a way that the two main rectangular coils are generating magnetic flux in the opposite direction [150].

It has been studied and concluded that the IU structure has more misalignment tolerance and a better efficiency profile for different loading conditions compared to the IB structure [122]. In this thesis, the IU structure is used to design the transmitter (L_p) and receiver (L_s) coils.

Fig. 4-19 illustrates the structure of the proposed approach with the integration of both resonant inductor and DC-DC inductor into the transmitter and receiver coils respectively. Similar to the resonant inductor (L_f), the DC-DC inductor (L_b) of the vehicle side converter is integrated with the receiver main coil (L_s). The

bipolar coils are placed in the middle space of the main wireless couplers to be decoupled from the main wireless charging coils. It should be noted that the shape of the integrated coils can be selected differently. For instance, a rectangular bipolar coil could be used for L_f and L_b. In this thesis, a circular coil layout is used due to its simplicity of implementation.

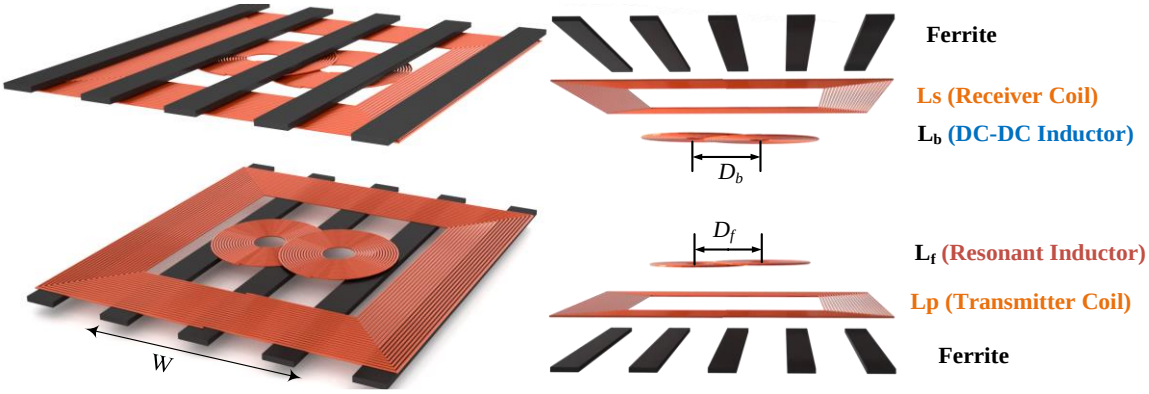

Fig. 4-19. The proposed fully-integrated magnetic structure.

Fig. 4-20 shows the schematic of the circuit with the proposed fully integrated magnetic structure. The coupling coefficient between the coil i and j can be expressed as:

$$k_{ij} = M_{ij} \Big/ \sqrt{L_i L_j} \qquad i, j \in \{p, s, f, b\} \tag{4.13}$$

where p refers to the transmitter coil (L_p), s refers to the receiver coil (L_s), f refers to the resonant inductor (L_f), b refers to the DC-DC converter (buck) inductor (L_b) and M_{ij} is the mutual inductance between the coil i and coil j.

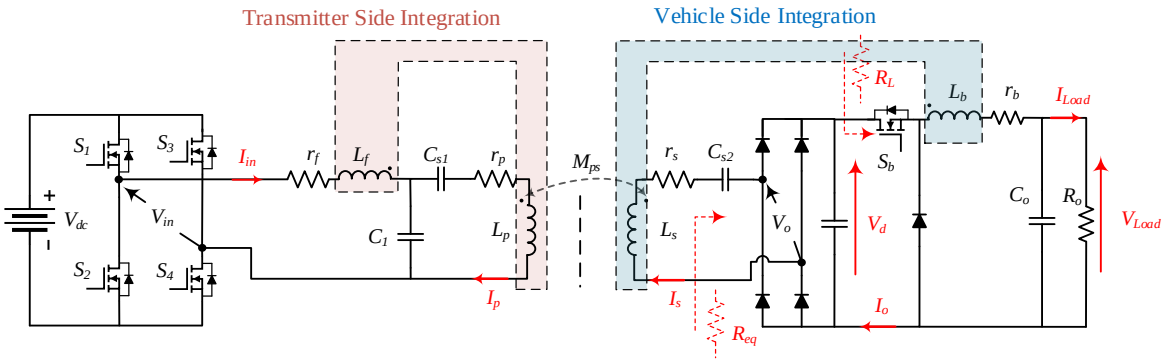

Fig. 4-20. Circuit diagram of the LCC-S resonant topology with the fully-integrated magnetic structure.

4.3.2. Circuit Modeling

According to FHA, the circuit shown in Fig. 4-20 can be simplified and shown in Fig. 4-21. In this simplification, the inverter can be replaced by a voltage source that its RMS value is equal to the first harmonic voltage $V_{in}^{RMS} = (\sqrt{8}\mathrm{V}_{\mathrm{dc}}/\pi)\sin(\theta/2)$, and the equivalent load seen by the resonant network is equal to $R_{eq} = 8/\pi^2\, R_L = 8/(\mathrm{D}\pi)^2\, R_o$; where θ is the switching phase-shift between the inverter legs and D is the duty cycle of the buck converter. Although the equivalent resistance cannot represent the battery model completely, it simplifies the analysis of the circuit. The battery can be modeled by $R_o = V_{bat}/I_{bat}$ where V_{bat} and I_{bat} are the battery voltage and current respectively.

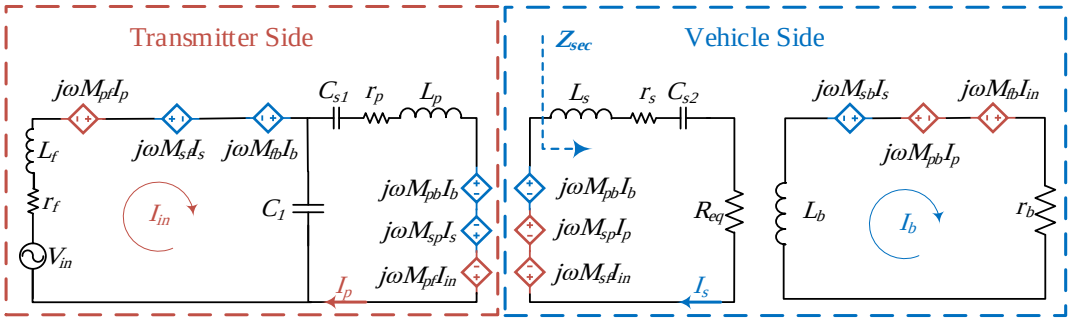

(a) Resonant network

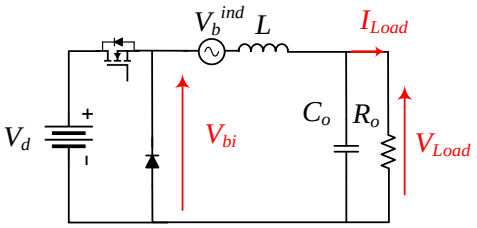

(b) Integrated buck converter

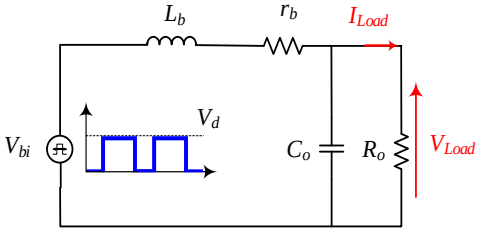

(c) Simplified integrated buck converter

Fig. 4-21. Simplified circuit of the proposed integrated wireless charging system.

As the battery charges in the CC mode, the SOC increases, and the battery voltage will increase until the battery voltage reaches the CV set point. Then, the DC-DC converter switches from CC mode to CV mode to charge the battery in this stage. During the CC mode, the voltage of the battery will change, and during the CV mode, the current of the battery will change. Therefore, the battery equivalent resistance can be considered as a time-dependent variable. However, due to the selection of LCC-S topology, a load-independent output voltage is provided. The DC-DC converter will regulate the output voltage or current by changing the duty cycle.

Since the buck converter acts as a low-pass filter that absorbs high-frequency components, the buck converter seen by the resonant network is modeled as a loop with the inductance of L_b and its resistance, r_b [151]. The circuit of the buck converter with an integrated magnetic structure is presented in Fig. 4-21 (b). In this circuit, V_{bi} is a square waveform voltage generated by the switch and diode of the buck converter.

Assuming that the induced voltage on the buck converter coil (V_b) is negligible, the equivalent circuit seen by the integrated buck converter is shown in Fig. 4-21 (c). This assumption is evaluated in Section 4.3.4. According to Kirchhoff's Voltage Law (KVL), the currents can be calculated by $I = Z^{-1}V$; where $[V] = [V_{in}, 0, 0, 0]^T$, $[I] = [I_{in}, I_p, I_s, I_b]^T$. KVL in the circuit loops gives:

$$V_{in} = (r_f + j\omega L_f)I_{in} + \frac{1}{\omega C_1}(I_{in} - I_p) - j\omega M_{pf}I_p + j\omega M_{sf}I_s - j\omega M_{fb}I_b \tag{4.14}$$

$$0 = \frac{1}{\omega C_1}(I_p - I_{in}) + (r_p + j\omega L_p + \frac{1}{j\omega C_{s1}})I_p - j\omega M_{ps}I_s - j\omega M_{pf}I_{in} + j\omega M_{pb}I_b \tag{4.15}$$

$$0 = j\omega M_{sf}I_{in} - j\omega M_{sp}I_p + (r_s + j\omega L_s + \frac{1}{j\omega C_{s2}})I_s + R_{eq} - j\omega M_{sb}I_b \tag{4.16}$$

$$0 = (r_b + j\omega L_b)I_b - j\omega M_{fb}I_{in} + j\omega M_{pb}I_p - j\omega M_{sb}I_s \tag{4.17}$$

Therefore, the impedance matrix, Z, is defined by:

$$Z = \begin{bmatrix} Z_{11} & -Z_{12} & -Z_{13} & -Z_{14} \\ -Z_{12} & Z_{22} & -Z_{23} & -Z_{24} \\ -Z_{13} & -Z_{23} & Z_{33} & -Z_{34} \\ -Z_{14} & -Z_{24} & -Z_{34} & Z_{44} \end{bmatrix} \tag{4.18}$$

The non-diagonal elements of the impedance matrix for the integrated LCC-S circuit can be expressed by:

$$Z_{12} = 1/j\omega C_1 + j\omega M_{pf} \ , \ Z_{13} = -j\omega M_{sf} \ , \ Z_{23} = j\omega M_{ps} \ , \ Z_{14} = j\omega M_{fb} \ , \\ Z_{24} = -j\omega M_{pb} \ , Z_{34} = j\omega M_{sb} \tag{4.19}$$

The diagonal elements of Z are defined by the sum of the total impedance of each current loop as follows:

$$Z_{11} = r_f + j\omega\left(L_f - 1/\omega^2 C_1\right) \ ,$$

$$Z_{22} = r_p + j\omega\left(L_p - 1/\omega^2 C_{1s} - 1/\omega^2 C_1\right) \tag{4.20}$$

$$Z_{33} = R_{eq} + r_s + j\omega\left(L_s - 1/\omega^2 C_{2s}\right) \ , \qquad Z_{44} = r_b + j\omega L_b$$

The output voltage of the WPT system (V_o), output dc-link voltage (V_d), and load voltage (V_{Load}) are calculated as follows:

$$V_o = R_{eq} I_s \tag{4.21}$$

$$V_d = V_o \, \pi/\sqrt{8} = R_{eq} I_s \, \pi/\sqrt{8} \tag{4.22}$$

$$V_{Load} = V_d D = R_{eq} I_s \, D\pi/\sqrt{8} \tag{4.23}$$

By solving the circuit according to the impedance matrix, the output voltage can be expressed by:

$$V_o = R_{eq}\left(\frac{Z_{13}Z_{14}Z_{24} + Z_{12}Z_{14}Z_{34} + Z_{11}Z_{24}Z_{34} + Z_{12}Z_{13}Z_{44} + Z_{11}Z_{23}Z_{44} - Z_{14}^2 Z_{23}}{\Delta} I_p - V_{in}\frac{Z_{14}Z_{34} + Z_{13}Z_{44}}{\Delta}\right) \tag{4.24}$$

$$\Delta = Z_{44}Z_{13}^2 + 2Z_{13}Z_{14}Z_{34} + Z_{33}Z_{14}^2 + Z_{11}Z_{34}^2 - Z_{11}Z_{33}Z_{44}$$

By letting the cross-coupling zero, and assuming the circuit tuned at the resonant frequency ($\omega = \omega_0 = \frac{1}{\sqrt{L_f C_1}} = \frac{1}{\sqrt{(L_p - L_f)C_{1s}}} = \frac{1}{\sqrt{L_s C_{2s}}}$) the output voltage can be simplified to:

$$V_o = R_{eq} V_{in}\left(\frac{Z_{12}Z_{23}}{Z_{22}Z_{12}^2 + Z_{11}\left(Z_{23}^2 - Z_{22}Z_{33}\right)}\right) = \frac{M_{ps}}{L_f} V_{in} \tag{4.25}$$

4.3.3. Design Challenges

One of the main challenges with the fully-integrated magnetic structure design is the cross-coupling between the main coils (L_p and L_s) and the integrated inductors (L_f and L_b). The mutual inductance between the main coils and integrated coils can generate unwanted induced voltages if the magnetic structure is not designed appropriately.

Assuming a DC current flows through the DC-DC inductor with a small AC ripple, the induced voltage from L_b on the other coils can be neglected. According to the simplified circuit presented in Fig. 4-21, the induced voltages are calculated. The unwanted induced voltages on the integrated inductors are expressed by:

$$V_f^{ind} = j\omega\left(M_{pf}I_p + M_{sf}I_s\right) \tag{4.26}$$

$$V_b^{ind} = j\omega\left(M_{fb}I_{in} - M_{pb}I_p + M_{sb}I_s\right) \tag{4.27}$$

where V_f and V_b are the induced voltages on L_f and L_b respectively. It can be seen that the induced voltages are dependent on the mutual inductances of the integrated coils with the main coils. The induced voltage on the DC-DC coil, V_b^{ind}, results in higher conduction losses. According to the simplified model shown in Fig. 4-21, this voltage will generate conduction power loss on the DC-DC inductor associate with its AC resistance, r_b. Therefore, the magnetic couplers need to be designed such that to achieve almost zero cross-coupling and eliminate the unwanted induced voltages.

On the other hand, the cross-coupling between the resonant inductor and the transmitter side coil (M_{pf}) as well as the cross-coupling between the resonant inductor and the receiver side coil (M_{sf}) has some other effects. The induced voltage

on the resonant inductor affects the values of the resonant elements as follows [118]:

$$L_f' = L_f + M_{pf} \tag{4.28}$$

$$C_1' = \frac{C_1}{1 + \omega^2 M_{pf} C_1} \tag{4.29}$$

where L_f' and C_1' are the equivalent values of the resonant elements due to the presence of the cross-coupling. These equivalent values should be used for designing the LCC network based on conventional methods presented in [119, 123]. Moreover, it can be seen that by having the cross-coupling between the resonant inductor and main primary side coil (M_{pf}), the actual value of the required L_f will be reduced and the actual value of C_1 will be increased.

According to (4.28) and (4.29), the resonant frequency of the system does not affect by cross-coupling [123]. However, the value of the output voltage and output power for a given resistance will be affected. Therefore, it is necessary to include these mutual inductance values in the designing of the resonant network of the integrated wireless charging system. In this thesis, it is assumed that the self-inductance of the main wireless charging system is predefined.

The induced voltage on the L_b as described in (4.27) increases the system losses [151]. Therefore, the value of the mutual inductances between the DC-DC coil and

other coils should be minimized. The details of optimal designing of the system with the fully integrated magnetic structure will be discussed in Section 4.3.4.

4.3.4. Design Procedure and Optimization

The summary of the proposed design optimization procedure is presented in Fig. 4-22. This procedure helps to design the resonant elements and magnetic structure to ensure the highest efficiency of the system. The design of the proposed fully-integrated WPT system can be divided into four steps:

1. Transmitter/Receiver Coil Design (Main Coils)
2. Resonant and DC-DC inductors Design (Integrated Coils)
3. Core Loss Calculation and Modeling
4. Optimal Resonant Network Design

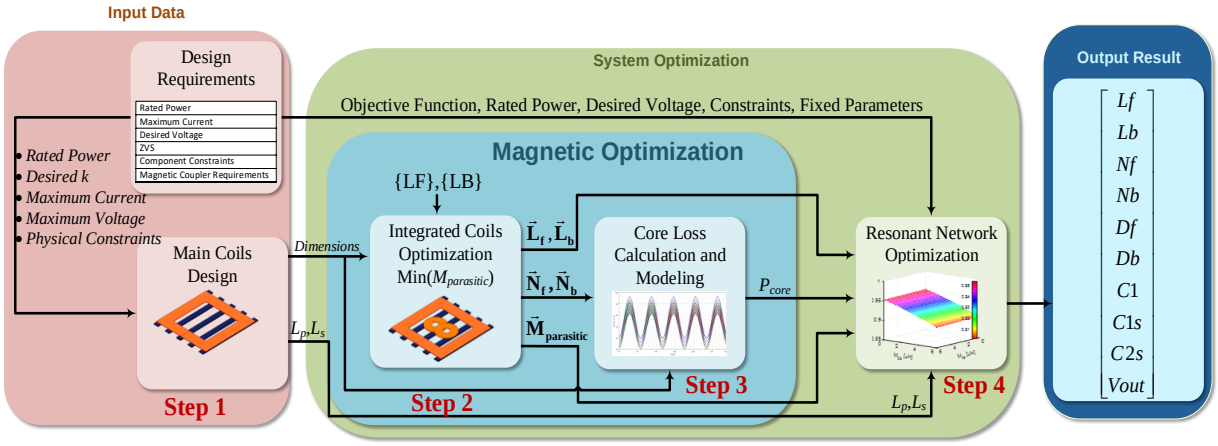

Fig. 4-22. Proposed design optimization procedure for the fully-integrated magnetic structure.

The main coils consist of the transmitter coil, receiver coil, and ferrite bars. In the first step, the main coils are designed based on the defined design requirements such as power rating, desired coupling factor, available space, maximum current, maximum voltage, and physical constraints. In the main coil design block, the size of the windings, the number of turns, and the volume of the ferrite of the main coils will be determined. At this step, it is assumed that there is no resonant inductor and DC-DC inductor. The output of the first step is the value of the transmitter self-inductance (L_p), receiver self-inductance (L_s), and total dimensions of the main coils. The dimension of the main coils is essential as the integrated inductors will be located inside the main coils, and the dimension will limit the size of the integrated inductors.

In the next step, an optimization problem is defined to find the optimal dimension of the resonant inductor and DC-DC inductor to fit into the transmitter and receiver coils, respectively while minimizing cross-coupling. This optimization problem is solved for a range of L_f ($L_f^{\min} < L_f < L_f^{\max}$) and L_b ($L_b^{\min} < L_b < L_b^{\max}$) and the output of this step generates a table (Table 4-4) that shows the optimal dimension for each combination of L_f and L_b. This dimension includes the number of turns (N_f and N_b) and the distance of the coils from the center (D_f and D_b). The

range of L_f and L_b is defined as a set of discrete values. These sets are named by LF and LB respectively as follows:

$$\forall i \in I \qquad LF = \{L_f^{\min} + i \times \Delta L\} \tag{4.30}$$

$$\forall i \in I \qquad LB = \{L_b^{\min} + i \times \Delta L\} \tag{4.31}$$

where I is the set of FEA designs, i is the number of FEA cases, and ΔL is the steps between the desired values. For instance, in this thesis, 64 FEA design cases are considered; therefore, I= (1, 2, ...,64). The value of $L_f^{\min}$ and $L_b^{\min}$ are equal to 40 µH and ΔL is considered 10 µH.

Core loss and conduction loss of all the inductors should be considered in power loss calculations to have an optimal design with respect to efficiency. Therefore, in this step, the core loss versus the excitation current is calculated. These calculated power losses will be used in the next step to design the resonant network, where a mathematical model of the core loss is required to provide a closed-form relationship between the transmitter coil current (I_p), receiver coil current (I_s), and the core loss.

The last step is the optimal design of the resonant network. In this step, the output of the integrated coil design is used and an optimization problem is defined to select the best resonant capacitors to achieve the design requirements. These

requirements are power rating, maximum current, desired voltage, and zero voltage switching (ZVS) conditions. The resonant network optimization process will find the best values of the L_f and L_b combination from Table 4-4. The details of each step are explained in the following:

A. Magnetic Coupler (Main Coils) Design

To design the main wireless charging coils, it should be noted that the coupling factor of the magnetic couplers (k_{ps}) and its quality factor (Q) are the two important parameters that affect the power transmission efficiency significantly [11, 64]. To increase the quality factor of the magnetic couplers, the AC resistance of the coils should be reduced which can be achieved by using the appropriate Litz wire for the operating frequency. Moreover, the coupling factor of the magnetic couplers should be maximized for a specific area to increase the power density of the design [64, 100, 152]. To avoid insulation issues due to large terminal voltage, a high number of turns should be avoided [67].

A main magnetic coupler with exterior dimensions of 510mm×510mm is selected to avoid a large magnetic coupler on the vehicle side. The number of turns and ferrite volume is designed according to the presented guidelines in [74, 100, 153]. The selected design has 20 turns and the coil width is 460mm×460mm. In

order to reduce the weight and cost of the design, a lower volume of ferrite is preferable.

To evaluate the effect of ferrite material in the magnetic couplers, an FEA study is done. In this study, the thickness and width of the ferrite bars are changed and the magnetic coupling factor between the main wireless charging coils and their self-inductance values are calculated as shown in Fig. 4-23. It can be seen that adding the ferrite material to the magnetic couplers significantly increases the magnetic coupling coefficient (k_{ps}). However, the coupling factor changes versus the covered area by ferrite are increasing with a low slope. As an example, in the structure with a ferrite bar with a thickness of 7mm, by increasing the covered area from 20% to 80%, the coupling factor is only increased by 14.8%.

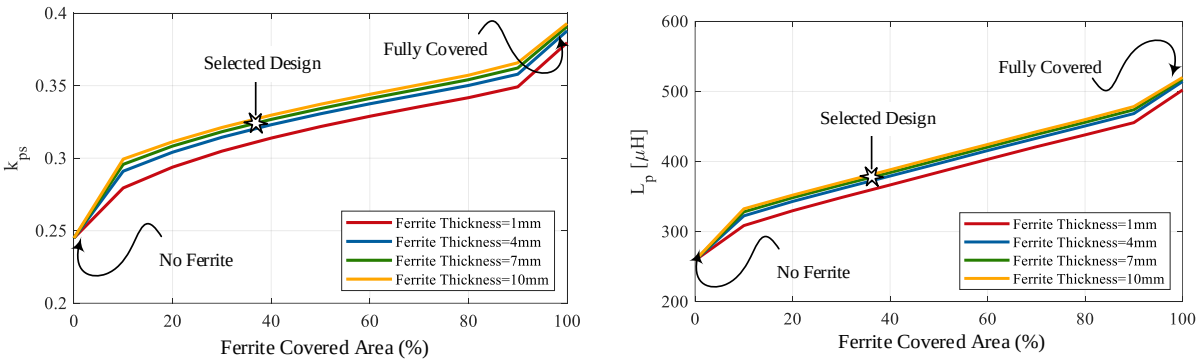

(a) Main coils coupling factor (b) Main coils self-inductance

Fig. 4-23. Ferrite dimension effect on the coupling factor and self-inductance.

Similarly, the self-inductance of the main couplers increased by increasing the covered area by ferrite. Having a magnetic coupler with high self-inductance results in high voltage on the coil terminals due to high-frequency operation (85 kHz). Therefore, it is more desirable to keep the self-inductance lower to avoid insulation issues. Moreover, it can be concluded that the ferrite thickness is not affecting the coupling factor and self-inductance considerably. The thickness of the ferrite material can affect the magnetic field density and impact core loss.

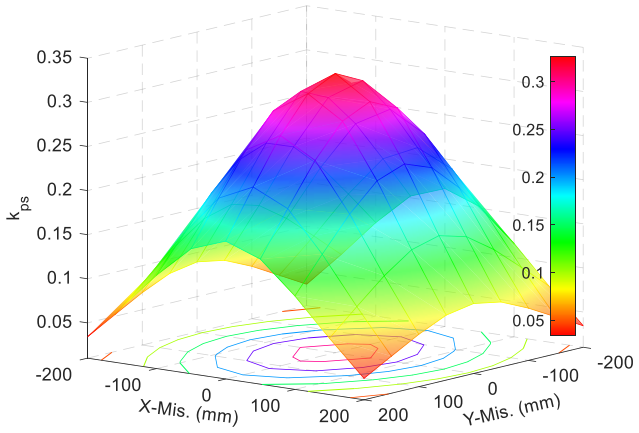

Fig. 4-24. Coupling factor variation of the proposed integrated magnetic structure under different misalignments.

In the selected design, five ferrite bars with dimensions of 510mm×38mm×7mm are placed in the back of the magnetic couplers. This selection is based on the availability of ferrite in the market. Fig. 4-24 shows the variation of the main coils coupling coefficient (k_{ps}) of the selected design versus X and Y-direction

misalignment conditions. The nominal coupling factor of the main coils is around 0.32 which is desired for EV wireless charging.

B. Integrated Coil Optimization

After the selection of main coils, the integrated coils can be optimally designed. According to the results given in Section 4.3.1, the cross-coupling between main coils and integrated coils significantly affects the efficiency of the overall system. Inappropriate design of the fully-integrated structure reduces the system efficiency and as a result, the cross-couplings should be reduced.

Each integrated coil is constructed by two unipolar coils that are connected reversely. The generated flux by each unipolar coil is in the opposite direction of the other coil of the same integrated coil. The distance between the two unipolar coils (D_f and D_b) and their number of turns (N_f and N_b) are considered as design variables. It should be noted that a limited number of design variables should be considered to minimize the search region for the solver; otherwise, due to the nonlinearity of the design, the optimization problem may not converge.

To achieve a fully-integrated magnetic structure with high overall efficiency, minimizing the cross-coupling is considered as the objective function of the magnetic structure optimization. This objective function is defined by:

$$min(M_{parasitic}) = min(\left|M_{pf}\right| + \left|M_{sf}\right| + \left|M_{pb}\right| + \left|M_{sb}\right| + \left|M_{fb}\right|) \tag{4.32}$$

The weighting factors can be considered in the objective function; however, this approach requires a precise selection of the weight factors. A two-layer optimization is proposed in this chapter to address this issue; FEA optimization and system optimization. With this approach, the weighting factors can be eliminated. An equal weighting factor is considered for all the mutual inductances. The second layer of the optimization includes the individual effect of the cross-couplings on the system efficiency. In the second layer, the values of the resonant elements are selected, and the best integrated coil design is selected among the optimized magnetic designs (Table 4-4).

In this optimization, the resonant inductor outer diameter (D_{of}) is limited to the inner width of the main coils (W). The value of D_{of} can be calculated based on the resonant inductor number of turns (N_f), its inner diameter (D_{if}), and the diameter of the Litz wire (D_{Litz}). In this study, the inner diameters of integrated coils (D_{if} and D_{ib}) are fixed at 50 mm to allow the integrated coil to occupy the surface area with the maximum number of turns if needed. The diameter of the Litz wire is selected according to the nominal current. Moreover, the distance between the two coils for each integrated coil (D_f or D_b) should be limited according

to the number of turns. These parameters are included as a system of constraints into the optimization problem as follows:

$$D_f + 2D_{Litz} \times N_f < W - D_{if} \tag{4.33}$$

$$D_b + 2D_{Litz} \times N_b < W - D_{ib} \tag{4.34}$$

For each set of required values for L_f and L_b, an optimized design exists where the cross inductance is minimized. Using the optimization toolbox of ANSYS Electronics, this optimization problem is solved for each set of L_f and L_b.

The result of this optimization is presented in Table 4-4 and this data is used for designing the converter of the wireless charging system. This table lists all the optimal integrated coil designs with minimum cross mutual inductances that can be considered for the magnetic couplers. For instance, if a resonant inductor with the value of 90 µH and DC-DC inductor with the value of 110 µH is desired, the value of D_b, D_f, N_f, and N_b to achieve minimum total cross inductance can be found in Table 4-4. The resonant network optimization process will search among the listed designs in this table and select the best integrated coil design among them.

TABLE 4-4
OPTIMIZED INTEGRATED COIL DESIGNS

Design Number	L_b (μH)	L_f (μH)	D_b (mm)	D_f (mm)	N_b	N_f	M_{pf} (nH)	M_{pb} (nH)	M_{sf} (nH)	M_{sb} (nH)	M_{fb} (nH)
1	110	110	100	100	20	20	28.2	202.5	254.4	133.2	7670.7
2	110	100	100	90	20	20	54.8	203.4	227.2	131.5	7055.2
3	110	90	100	110	20	17	68.0	191.7	163.0	153.6	6511.2
4	110	80	100	130	20	16	1.10	213.6	196.6	144.0	6343.0
5	110	70	100	120	20	15	77.9	221.2	194.9	111.9	5242.9
6	110	60	100	100	20	15	175.1	213.2	236.3	107.0	4604.7
7	110	50	100	80	20	15	147.3	213.8	208.0	110.8	3825.2
8	110	40	100	60	20	15	60.4	215.6	156.1	114.6	2872.5
.	.	.	.	.	.	.	.	.	.	.	.
.	.	.	.	.	.	.	.	.	.	.	.
.	.	.	.	.	.	.	.	.	.	.	.
57	40	110	60	100	15	20	51.0	133.7	241.6	29.43	2922.1
58	40	100	60	90	15	15	8.38	129.9	253.4	21.81	2708.2
59	40	90	60	110	15	18	62.6	139.5	240.4	33.68	2495.7
60	40	80	60	140	15	16	37.9	128.3	156.6	18.21	2110.0
61	40	70	60	120	15	15	259.6	135.7	307.5	25.04	2008.7
62	40	60	60	100	15	15	166.4	120.7	225.9	11.24	1813.2
63	40	50	60	80	15	15	150.5	142.8	211.2	42.77	1538.5
64	40	40	60	60	15	15	65.38	133.8	158.5	29.85	1197.6

C. Core Loss Calculation and Modeling

Since the main coils contain a magnetic material, core loss should be included in the optimization problem. This inclusion of core loss helps to design the optimal resonant circuit to achieve maximum efficiency.

The ferrite material is N87 made by EPCOS which has a low magnetic loss profile at high-frequency operation. The nonlinear B-H curve and magnetic loss versus frequency, provided by the datasheet, are imported into ANSYS Maxwell. The core loss of the proposed magnetic structure is calculated through the FEA. In the FEA simulation, transient time-domain analysis is performed at different operating points. The amplitude of the transmitter (I_p), receiver (I_s), resonant

inductor (I_f), and DC-DC inductor (I_b) currents are varied from 0 to 12 A, and the average value of the core loss is calculated. According to the FEA results, the value of I_f and I_b have a negligible effect on the core loss (less than 3% of the total core loss) of the magnetic structure. Therefore, to simplify the analysis and reduce the complexity of the model, the core loss is defined as a function of I_p and I_s. The FEA results for the core loss versus amplitude of the excitation currents are shown in Fig. 4-25.

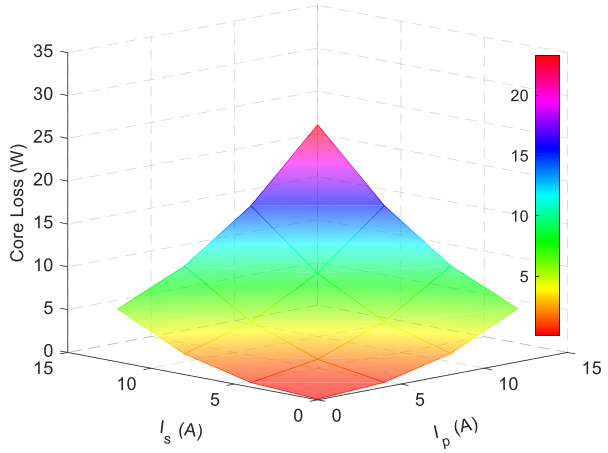

Fig. 4-25. The core loss of the proposed magnetic structure versus primary and secondary side currents.

It can be seen that the core loss value showed a quasi-quadratic pattern versus the I_p and I_s. Therefore, the core loss can be expressed by a polynomial as a function of primary and secondary side currents. This model is used in the resonant converter optimization to find the best resonant network considering the core loss versus transmitter and receiver currents.

4.3.5. Resonant Network Optimization

The following components can define an optimization problem:

1. Objective function
2. Equations and constraints
3. Fixed parameters

A. Objective Function

In this section, the main objective is to maximize the efficiency of the system. The efficiency of a wireless charging system is dependent on the coupling factor and loading condition. As discussed in Section 4.3.1, the equivalent resistance of the load seen by the LCC-S network is a time-dependent variable in the stationary battery charging application. To keep the efficiency of the converter high for a wide range of loads, the whole charging profile of the battery should be considered. The variation of the load resistance can be analyzed by the output power condition and the amount of time that the converter will operate at each point. Therefore, points that have a longer duration should be prioritized for maximum efficiency. In order to achieve this goal, a Time Weighted Average Efficiency (TWAE) function is defined as the objective function to achieve this goal. In this objective function, the sum of the efficiency at different points multiplied by their associated time weight factors should be considered [143]. In this objective function, the important points

have larger weighting factors. Compared to the conventional design of the resonant converters for a specific nominal point (Constant R_{eq}), the TWAE method includes the nonlinear changes of the battery profile, which maximizes the efficiency of the resonant network for the whole charging process [143].

The resonant network for this circuit is optimally designed for a 3.3 kW WPT system based on the presented method in [55]. The nominal power and nominal coupling factor sets are defined by $P_n = \{1540 \quad 1760 \quad 980 \quad 396\}$ and $K_n = \{0.22 \quad 0.27 \quad 0.32\}$, respectively. The maximum average efficiency is defined as the objective function of the optimization as follows:

$$\sum_{k_i \in \mathrm{K_n}} \sum_{P_i \in \mathrm{P_n}} \frac{\mathrm{W}_{Pi} \times \eta_{P_i,k_i}}{n} \tag{4.35}$$

where $W_{pi} = \{0.033 \quad 0.767 \quad 0.126 \quad 0.074\}$ is the time weight factors, K_n is a set of the nominal coupling factors and η_{P_i,k_i} is the efficiency at each operating condition and n is equal to 4. According to this TWAE function, the design point with the power of 1760 W has the highest weight and the design point with 1540 W has the lowest weight on the objective function. In other words, the weight factors define the priority of the design points for the optimization problem.

B. Equations and Constraints

The equations that describe the proposed fully-integrated wireless charging system are presented in Section 4.3.2. These equations are included in the optimization problem to calculate the input current, coil current, losses, output voltage, and efficiency of the system.

The core loss of the system is modeled according to the presented results in Section 4.3.4. Moreover, the conduction losses of the inverter, vehicle side diode bridge, resonant capacitors, and conduction loss of the magnetic couplers are included according to each loss component equation presented in [55, 154].

In this optimization problem, practical constraints are also considered. These constraints are including maximum input current (I_{in}), main coil current (I_p and I_s), maximum and minimum output voltage (V_o), and ZVS condition. The boundaries for resonant components are also defined by:

$$\begin{bmatrix} C_1 \\ C_{s1} \\ C_{s2} \\ L_f \end{bmatrix} \leq \begin{bmatrix} C_1^{\max} \\ C_{s1}^{\max} \\ C_{s2}^{\max} \\ L_f^{\max} \end{bmatrix} \tag{4.36}$$

where the value of L_f should be selected according to the physical boundaries of the magnetic structure dimensions. As discussed in Section 4.3.4, the value $L_f^{\max}$ is selected according to the available space in the magnetic structure where this value

is limited to 110 μH in this study. Based on the presented FEA results in section 4.3.4, the variable L_f should be defined as an integer vector in the optimization problem as follows:

$$L_f = \vec{\mathbf{n}}.\vec{\mathbf{L}}_{\mathbf{f}} = \begin{bmatrix} n_1 & \cdots & n_i \end{bmatrix}.\begin{bmatrix} L_{f1} \\ \vdots \\ L_{fi} \end{bmatrix} \tag{4.37}$$

$$\sum\nolimits_i n_i = 1 \tag{4.38}$$

where $\vec{\mathbf{n}}$ is a vector of binary variables, $i \in I$ is the number of FEA cases, and $\vec{\mathbf{L}}_{\mathbf{f}}$ is a vector of the calculated optimized designs in Section 4.3.4. Each element $\vec{\mathbf{L}}_{\mathbf{f}}$ refers to a unique optimized design with minimum cross-coupling. Since only one design should be selected in the optimization problem, the sum of the binary values should be equal to one as expressed in (4.38). In this section, 64 different FEA cases are optimally designed; therefore, the index i is equal to 64 and $\vec{\mathbf{L}}_{\mathbf{f}}$ has 64 elements. Similarly, the vector of variable L_b is defined. In the next step, the cross mutual inductance values are included in the optimization problem as follows:

$$\vec{\mathbf{M}}_{\mathbf{parasitic\_i}} = \vec{\mathbf{n}}.\vec{\mathbf{M}}_{\mathbf{parasitic}} = \begin{bmatrix} n_1 & \cdots & n_i \end{bmatrix}.\begin{bmatrix} M_{pf1} & M_{pb1} & M_{sf1} & M_{sb1} & M_{fb1} \\ \vdots & \vdots & \vdots & \vdots & \vdots \\ M_{pfi} & M_{pbi} & M_{sfi} & M_{sbi} & M_{fbi} \end{bmatrix} \tag{4.39}$$

where $\vec{\mathbf{M}}_{\mathbf{parasitic}}$ is calculated cross mutual inductance for each optimized design. The optimization problem outputs the resonant elements values and the non-zero elements of the binary vector $\vec{\mathbf{n}}$ show the best magnetic coupler design. In other words, the optimization problem finds the best resonant elements values and picks the best integrated magnetic coupler design for a wireless charging system.

In this problem, the switching and conduction losses of the inverter (P_{inv}), resonant capacitor loss (P_{cap}), core losses (P_{core}), diode bridge losses, and coils conductions losses, and integrated coils conduction losses are included according to [30, 55, 151]. Soft switching should be considered as another constraint in the design process to reduce the switching losses of the inverter. The soft switching condition can be defined as follows:

$$0 < \phi < \pi/2 \tag{4.40}$$

$$\phi = \measuredangle V_{in}/I_{in} \tag{4.41}$$

where ϕ is the input current phase angle which should have a lag phase angle to satisfy the ZVS condition. The constraints and range of the variables are listed in Table 4-5.

C. Fixed Parameters

Some fixed parameters as input should be considered in the optimization problem. The operating frequency of the light-duty EV wireless charger is fixed to 85 kHz according to SAE [155]. The value of the component specifications such as MOSFET on-state resistance ($R_{ds(\text{on})}$), rise-time (t_r) and fall time (t_f) of the switches, and diode forward voltage are included in the optimization. Moreover, the value of the self-inductance and mutual inductances are extracted from FEA and included in the optimization problem. A summary of the design fixed parameters is listed in Table 4-5.

TABLE 4-5
CONSTRAINTS AND FIXED PARAMETERS

Parameter	Symbol	Fixed	Min.	Max.
Resonant inductor	L_f	-	50 µH	150 µH
Transmitter parallel capacitor	C_1	-	1 nF	150 nF
Transmitter series capacitor	C_{s1}	-	1 nF	150 nF
Vehicle side series capacitor	C_{s2}	-	1 nF	150 nF
Self-inductance of the main coils	L_p, L_s	-	384 µH	391 µH
Main coils coupling factor	k_{ps}	-	0.22	0.32
Vehicle side integrated coil self-inductance	L_b	-	50 µH	110 µH
Main wireless charging coil current	I_p, I_s	-	0	15 A
Output voltage range	V_o	-	200	600
Input voltage	V_{dc}	200 V	-	-
Switching frequency	f_{sw}	85 kHz	-	-
Output power range	P_o	-	396 W	2200 W
Mosfet on-state resistance	$R_{ds(\text{on})}$	37mΩ	-	-
Switch rise time and fall time	t_r, t_f	32 ns, 7 ns	-	-
Diode bridge forward voltage at 70A	U_{d0_bridge}	1.12 V	-	-
Resonant capacitor dissipation factor	tan(δ)	1×10^{-3}	-	-

D. Solution

The optimization of the fully integrated system can be solved using any optimization software such as General Algebraic Modeling System (GAMS) or MATLAB. The optimization results and other system specifications are presented in Table 4-6. It can be seen that a design with a lower value of L_f that satisfy the wireless charging requirements, and a larger value of L_b is selected. The larger value of L_b increases the loop impedance value of the buck converter as shown in Fig. 4-21. Therefore, the amplitude of the AC current on that branch (I_b) will be smaller and the integration loss would be smaller. Moreover, a larger DC-DC inductor results in less output ripple.

TABLE 4-6
SYSTEM SPECIFICATIONS AT NOMINAL OPERATING CONDITION

Parameter	Symbol	Value
Optimized resonant inductor	L_f	50 µH
Optimized distance of L_f	D_f	80 mm
Optimized resonant inductor turns	N_f	15
Optimized transmitter parallel capacitor	C_1	72.7 nF
Optimized Transmitter series capacitor	C_{s1}	10.43 nF
Optimized Vehicle side series capacitor	C_{s2}	9.69 nF
Main coils self-inductances	L_p, L_s	387 µH
Integrated coil self-inductance	L_b	110 µH
Optimized distance of L_b	D_b	100 mm
Input voltage	V_{dc}	200 V
Switching frequency	f_{sw}	85 kHz
Switching frequency of the buck converter	f_b	120 kHz
Optimal output power	P_o	2.2 kW
Air gap	-	125 mm
Ferrite dimension	-	510mm×38mm×7mm
Magnetic coupler dimension	-	510mm×510mm
Nominal coupling factor	k	0.32

In general, a smaller value of L_f results in smaller mutual inductance between the resonant inductor and other coils such as M_{fb} and M_{pf}, thus, the total loss will be reduced. Therefore, it can be concluded that larger L_b and smaller L_f results in better performance. The output voltage and efficiency profile of the designed wireless charging system under different coupling factors are calculated and compared with the experimental results.

4.3.6. Integrated Coil Rotation Angle

It is possible to have a rotation of the integrated coils in the design of the integrated wireless charging magnetic couplers. Having a rotation in secondary, primary, or both sides may reduce the cross-coupling and improve the magnetic structure. To evaluate the effect of the rotation of the integrated coils on the cross-coupling, three cases are considered: zero rotation, 90-degree rotation of L_b, and ±45-degree rotation of both L_f and L_b. The FEA results of these three cases with the specification listed in Table 4-6 are shown in Fig. 4-26

Since the misalignment of the magnetic couplers is inevitable, a range of ±200mm misalignment is considered in this simulation. To compare different rotation angles, the cross-coupling between L_f and L_b and the total cross-coupling is studied. Moreover, the RMS value of the mutual inductance should be considered to evaluate the layout for the whole range of misalignment. According to Fig. 4-26

(d)-(f), it can be seen that 90-degree rotation shows a minimum value of M_{fb} which is desired for an integrated magnetic structure. The RMS value of the M_{fb} of the 0-degree and ±45-degree layouts is slightly higher than the 90-degree layout.

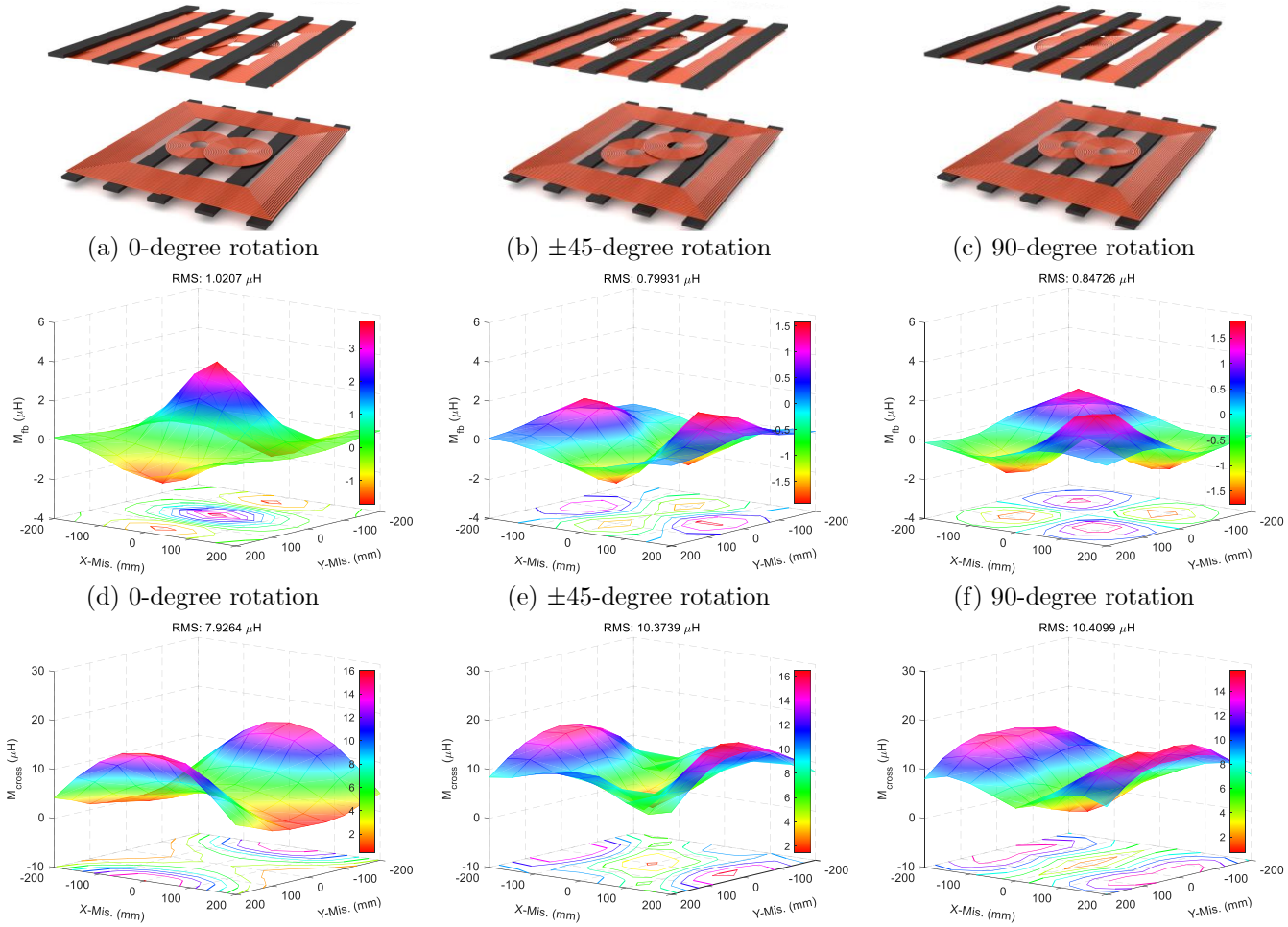

(a) 0-degree rotation (b) ±45-degree rotation (c) 90-degree rotation

(d) 0-degree rotation (e) ±45-degree rotation (f) 90-degree rotation

(g) 0-degree rotation (h) ±45-degree rotation (i) 90-degree rotation

Fig. 4-26. The effect of the integrated coils angle on the: (a) 0-degree rotation (b) 45-degree rotation (c) 90-degree rotation (d) M_{fb} with 0-degree rotation (e) M_{fb} with 45-degree rotation (f) M_{fb} with 90-degree rotation (g) Cross coupling with 0-degree rotation (h) Cross coupling with 45-degree rotation (i) Cross coupling with 90-degree rotation.

Although RMS lower value M_{fb} is desirable, other cross-couplings should be considered for selecting the rotation angle. The total cross-coupling is also calculated and the results are shown in Fig. 4-26 (g)-(i). It can be seen that the 0-degree rotation layout showed the minimum total cross-coupling and the other two layouts showed a similar value of total cross-coupling. Therefore, in this thesis, a 0-degree rotation angle is selected to minimize the total cross-coupling.

4.3.7. Performance Analysis

A. Operation

Based on the parameters given in Table 4-6 the induced voltage on the DC-DC inductor (V_b^{ind}) is calculated under different misalignment conditions, and the results are illustrated in Fig. 4-27. In Fig. 4-27 (a) and (b), the output power is 500 W and 2.2 kW respectively.

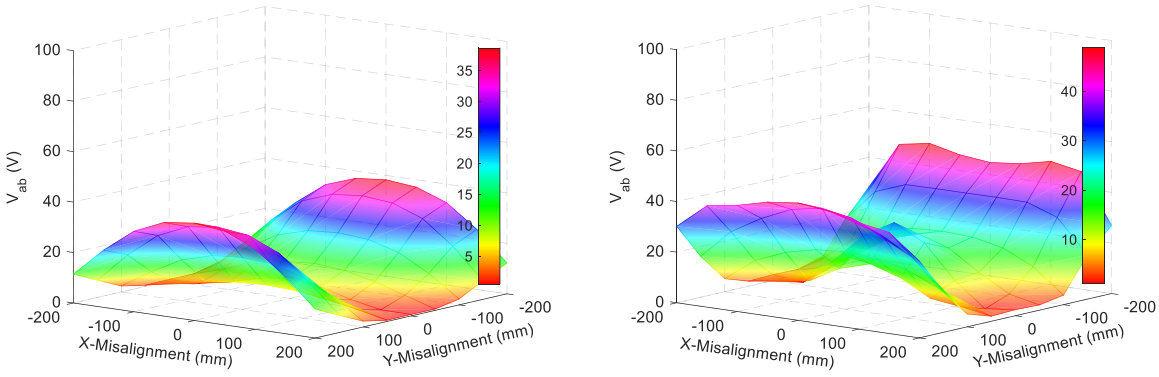

(a) 500 W (b) 2.2 kW

Fig. 4-27. Calculated induced voltage on the integrated DC-DC coil.

It can be seen that the induced voltage is much lower than the rated output voltage (500 V) (almost negligible), and its corresponding power loss is much lower than the rated power (2.2 kW). Moreover, the amplitude of the induced voltage is not affected significantly by the variation of the output power. Therefore, the UI integration structure successfully eliminated the induced voltage at different misalignment conditions.

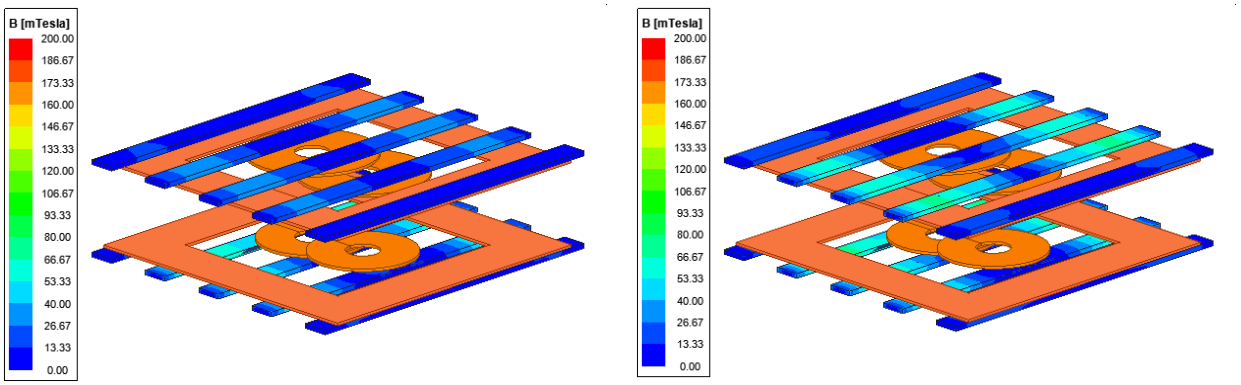

(a) 500 W (b) 2.2 kW

Fig. 4-28. Magnetic field density (B) of the ferrite bars under different loading conditions.

In the next step, a time-domain transient FEA is performed on the magnetic structure to study the magnetic field distribution. The amplitude of the magnetic field density (B) of the fully integrated magnetic structure under full and partial loading conditions at the same time step and the maximum value is presented in Fig. 4-28.

It can be seen that the field density is higher in the region that is covered with main coils, as expected. The field density of the ferrite bars located on the transmitter side does not change when the load power changes from 500 W to 2.2 kW. The unchanged field density of the transmitter side is due to the constant current characteristic of the LCC topology. The field density in the core material is lower than the saturation field density of the selected ferrite material (B_{sat}= 300 mT). Moreover, the DC-DC inductor current effect on the field density is negligible.

B. Comparison

The fully-integrated system can be compared with conventional designs from three design aspects: integrated coil design, resonant network design, and cost:

B.1) Integrated Coil Design

In this case study, the design with L_f=60 µH and L_b=110 µH is considered. It is also assumed that the DC-DC inductor value is fixed, and the overlap distance (D_f) and the number of turns of the resonant inductor (N_f) are varied. Fig. 4-29 shows the FEA results of the self-inductance of the resonant inductor (L_f) and the total cross-coupling.

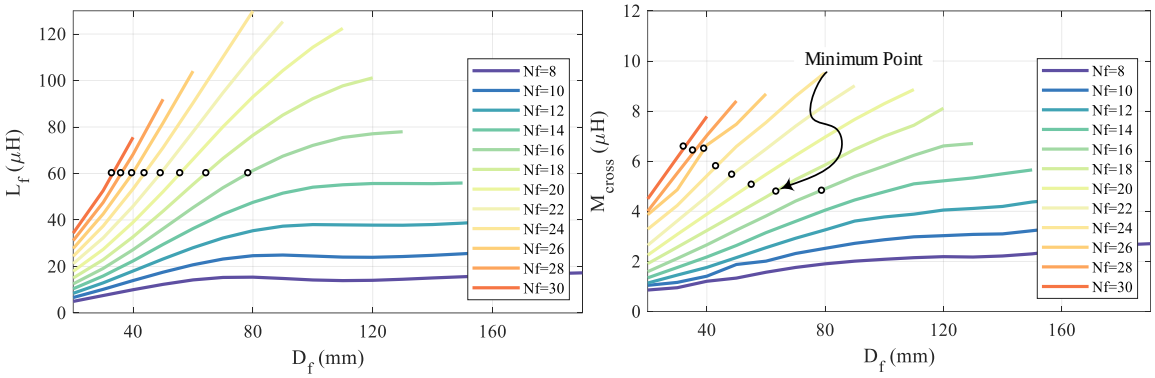

(a) L_f (b) M_{cross}

Fig. 4-29. Example of designing the resonant inductor with low cross-coupling.

The value of L_f=60 µH can be achieved by a different number of turns and overlaps; these points are marked in Fig. 4-29 (a). The corresponding total cross-coupling value of each design is shown in Fig. 4-29 (b). It can be seen that there exists a point that shows a minimum total cross-coupling which is the desired design. The proposed optimization method finds the optimal point among all different design points in a single optimization problem. Therefore, no trial and error is required.

B.2) Resonant Network Design

In this case, the effectiveness of the resonant network optimization is evaluated. It is assumed that the magnetic structure is optimally designed and Table 4-4 is available. According to Table 4-4, the cross-coupling values for design number 8 (L_f=40 µH) are generally lower than design number 7 (L_f=50 µH). For instance, one may look at the cross-coupling values and select design 8 with the lowest

parasitic mutual inductance (L_f=40 µH) and conventionally tune the resonant network on the resonant frequency ($\omega = \omega_0 = \frac{1}{\sqrt{L_f C_1}} = \frac{1}{\sqrt{(L_p - L_f)C_{1s}}} = \frac{1}{\sqrt{L_s C_{2s}}}$).

Fig. 4-30 compares the efficiency of the integrated wireless charging system with the optimized magnetic structure with two different resonant inductor values.

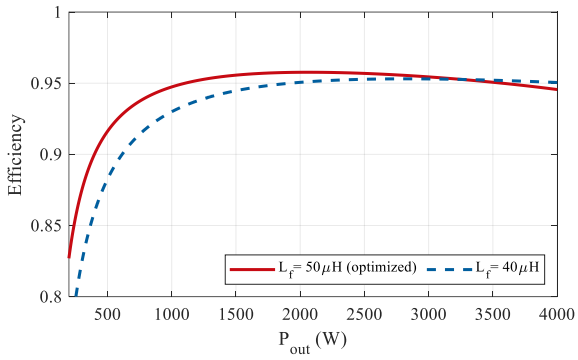

Fig. 4-30. Comparison of the optimized fully-integrated wireless charging system versus the conventional design.

It can be seen that the optimized value of L_f=50 µH showed a better performance in terms of efficiency in the range of nominal output power. However, as the output power increases beyond the nominal point (2.2 kW), the conventional design shows a better efficiency profile. Therefore, the proposed optimization of the fully-integrated wireless charging system picks the best value of the resonant inductor among the optimized magnetic couplers which results in higher efficiency in the desired range of the output power. Moreover, the proposed optimization method includes practical constraints. Therefore, using the proposed optimization

method, no iterations, and trial and error are required and all the constraints are considered at the same time in a single optimization problem.

B.3) Cost and Volume Comparison

Different types of inductors are studied to investigate the cost and volume reduction of the proposed fully-integrated structure. Typically, the inductors can be built using air core, EE type ferrite core, and integrated structure as shown in Fig. 4-31. As an example, a wireless charging system with inductor values of L_f=50 µH and L_b=110 µH is considered. The cost of ferrite, Litz wire, and volume for different types of inductors is listed in Table 4-7. It can be seen that the cost of the inductor will be reduced by using integrated inductors. Since the integrated inductors are placed in the unoccupied space in the center of the main wireless charging coils, the required space for the integrated coils is zero.

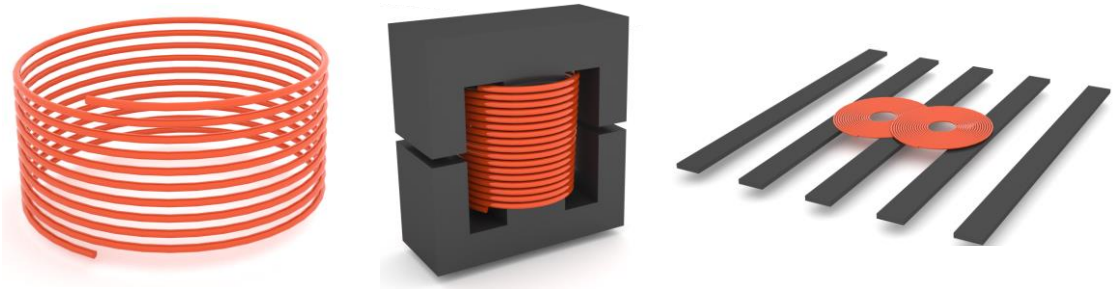

(a) Air core (b) EE core (c) Integrated

Fig. 4-31. Different types of inductors that considered for cost and volume comparison.

TABLE 4-7
COMPARISON OF THE COST AND VOLUME OF THE DIFFERENT TYPES OF INDUCTORS

Type	Inductor	Wire Cost ($)	Ferrite Cost ($)	Total Cost ($)	Required Space (mm^3)
Air Core	L_f	18	0	18	989100
	L_b	30	0	30	1661688
EE Ferrite Core	L_f	3	22	25	139425
	L_b	4	22	26	152100
Integrated	L_f	12	0	12	0
	L_b	20	0	20	0

Compared to the use of an EE-type structure for both resonant and DC-DC inductors, the fully-integrated system reduces the estimated cost by around 35% and saves 2.91×10^5 mm^3 of the volume. If a partially integrated is used, which means that L_f is integrated and L_b is built by EE core, the proposed fully-integrated system can reduce the total estimated cost by around 15% and save 1.52×10^5 mm^3 of the volume.

4.3.8. Experimental Results

To evaluate the proposed fully-integrated wireless charging system, a 3.3 kW system was built in the lab. The switching frequency of 85 kHz was selected according to the SAE standard for stationary chargers. In this setup, the magnetic couplers were made by 500 strands Litz wire of AWG 38 to reduce the skin effect at the operating frequency and the ferrite cores were N87 from EPCOS. The controller is implemented with a Texas Instruments TMS320F28379D DSP to generate gating signals for the inverter and the DC-DC converter. The power

MOSFET switches used in the inverter were IPW65R037C6 *CoolMOS* series with 37 mΩ on-state resistance. Fig. 4-32 shows the experimental setup of the proposed fully-integrated magnetic structure.

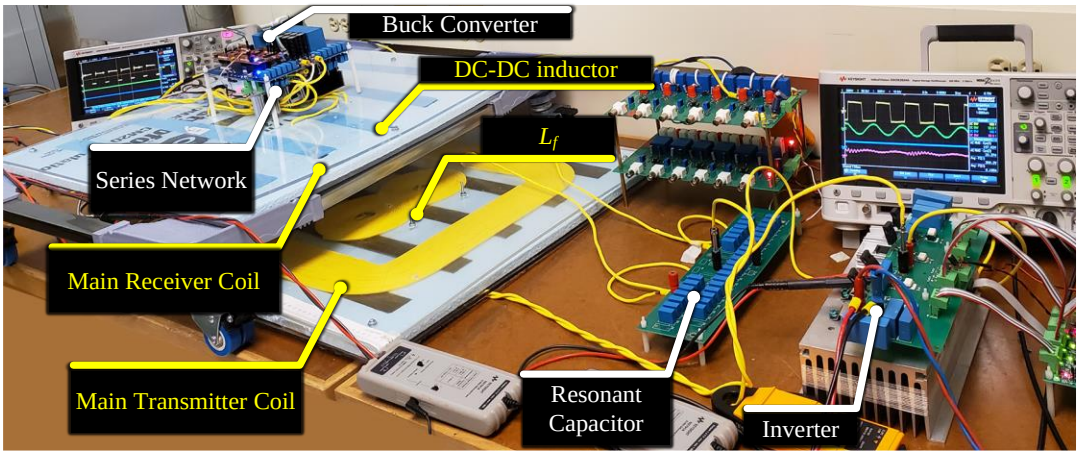

Fig. 4-32. The laboratory prototype of the wireless charging system with a fully-integrated magnetic structure.

In this experiment, the magnetic coupler position was changed from zero to 120 mm misalignment. Fig. 4-33 shows the inverter output voltage (V_{in}), inverter current (I_{in}), output voltage (V_d), and current (I_o) waveforms at the nominal loading (2.2 kW) and partially loading (500 W) conditions. It can be seen that ZVS was achieved for this converter in the whole operating range. Furthermore, to investigate the accuracy of the efficiency and output voltage calculations, different operating points are measured and compared with calculation results. Fig. 4-34 compares the efficiency and output voltage of the WPT system to the experimental results. It can be seen there is good accordance between the simulations and

experimental results. It should be noted that in this experiment only X-direction misalignment is considered. According to the simulation results, X and Y-direction misalignment have a negligible difference in terms of efficiency, and the system efficiency is more sensitive to the main coils coupling factor.

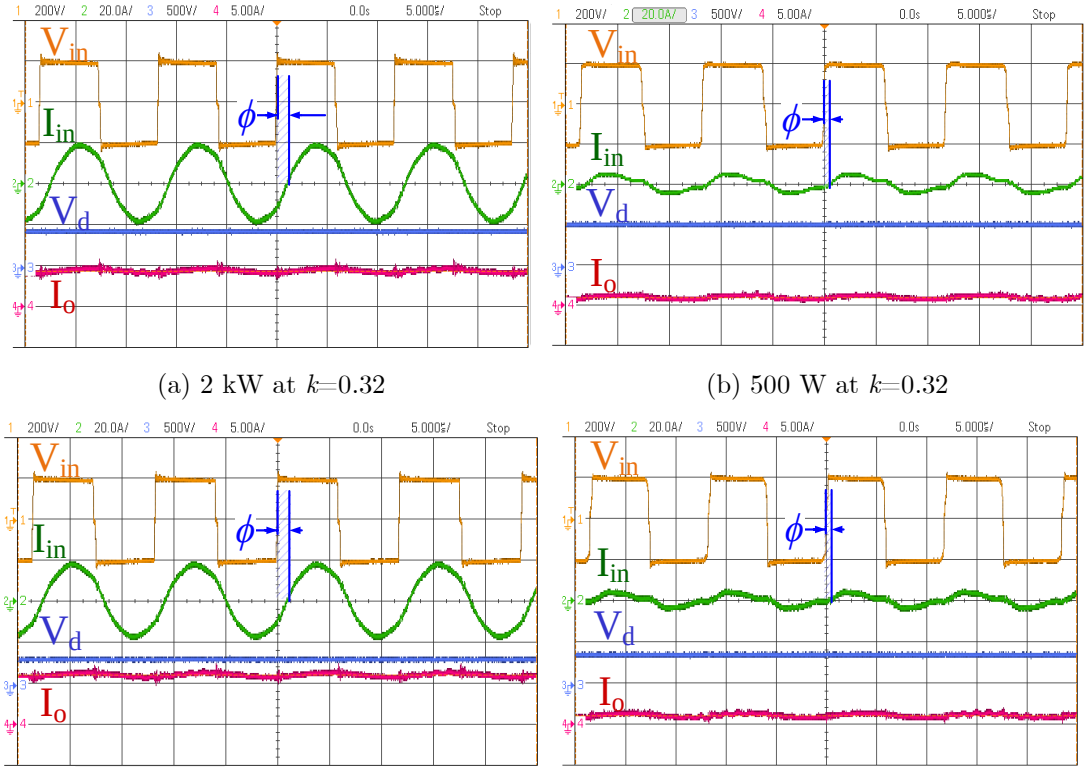

(a) 2 kW at k=0.32 (b) 500 W at k=0.32

(c) 2 kW at k=0.22 (d) 500 W at k=0.22

Fig. 4-33. Experimental output waveforms.

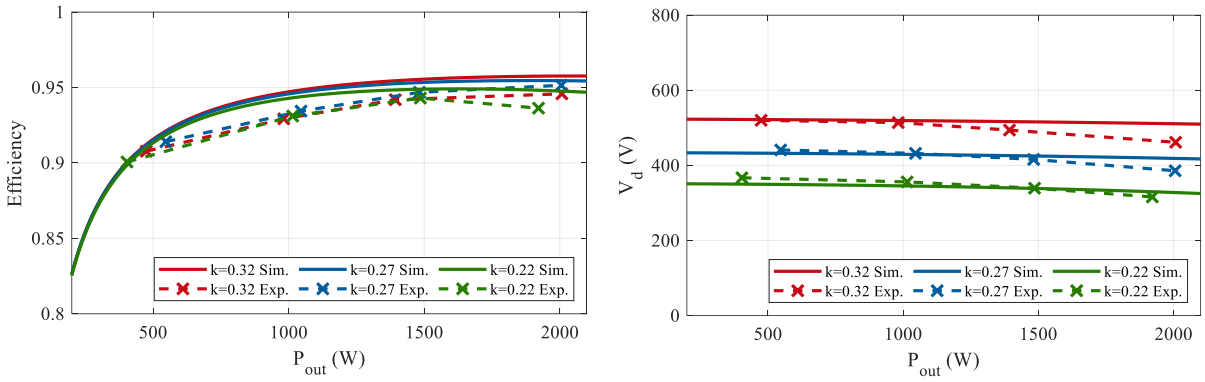

(a) Efficiency (b) Output voltage (V_d)

Fig. 4-34. Comparison of the experimental and simulation results versus output power under different coupling factors.

Finally, the dynamic performance of the proposed integrated system was evaluated by changing the load from 1 kW to 2.2 kW. In this experiment, the coupling factor was 0.32, and the load change by a single step. Fig. 4-35 shows the dynamic performance of the proposed wireless charging system with the integrated DC-DC inductor. It can be seen that the output voltage (V_{Load}) is stabilized with a very short transient time.

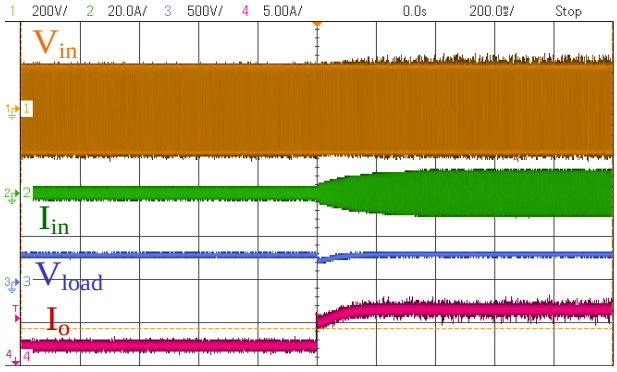

Fig. 4-35. Dynamic performance of the DC-DC converter from half load to full-load condition.

4.4. Conclusion

This chapter studied challenges with the partially-integrated and fully-integrated magnetic structures for EV wireless charging. The proposed integrated structure helps to improve the power density and reduce the cost of the magnetic design by reducing the required ferrite material. A new procedure for the optimal design of the proposed structure is presented. In this chapter, an LCC-S topology is selected to minimize the number of required components on the vehicle side.

In the proposed fully-integration method, the resonant inductor of the LCC network is integrated into the transmitter coil, and the DC-DC inductor is integrated into the receiver main coil. It was shown that the integrated coils have a cross-coupling with each other and with the main wireless charging coils which affects the performance of the system. To reduce the cross-coupling effect, the magnetic structure is optimally designed for different values of self-inductance. The optimized magnetic structures are imported into the resonant network optimization problem to select resonant capacitors. Moreover, the core and conduction losses of the magnetic coupler, inverter, and diode-bridge losses, and resonant capacitor losses are included in the resonant network optimization. The optimization problem also picks the best optimized magnetic structure based on the design requirements and cross-couplings and finds the best values for the resonant capacitors.

According to the system optimization, a lower value of the resonant inductor and a higher value of the buck converter inductor is preferable which results in lower cross inductance, higher overall efficiency, and less output ripple. The converter is analyzed, and the effect of the negligible mutual inductances is studied. A 3.3 kW/85 kHz system was built and compared with the simulation studies to validate the feasibility and performance of the proposed integration and optimization method.

Chapter 5

PCB Based Magnetic Couplers for EV Wireless Charging

5.1. Introduction

As discussed, the EV wireless charging system is operating at 85 kHz. Operating at this frequency results in higher coil AC resistance due to skin effect and proximity effect caused by eddy current. As the AC resistance of the coils increases, the quality factor and the efficiency of the system reduces consequently. Therefore, Litz wire is typically employed to overcome this issue. However, as the number of strands increases and the diameter of the strands of the Litz wire reduces the cost of the Litz wire increases significantly. Therefore, finding alternatives for replacing the Litz wire is an objective of this chapter.

In this chapter, a conventional Litz wire–based magnetic coupler is replaced with a PCB-based planner magnetic structure. Instead of a self-resonator coil, the printed coil is only operating as an inductive coupling between the transmitter and receiver side. Furthermore, the effect of the ferrite material on the structure of the PCB-based magnetic coupler is studied. The PCB layer is analyzed using FEA software to calculate the AC resistance at the operating frequency. The 2-Dimensional (2D) FEA studies are presented to provide a guideline for designing the PCB-based magnetic couplers. In this study, the effects of the copper cross-section, thickness and width, number of the parallel branches per turn, board layer thickness, and dimensions of the ferrite core on the AC resistance are analyzed in depth. The 3-Dimensional (3D) FEA studies are also presented in this chapter to validate the 2D analysis and find a PCB layout with a low conduction loss.

The sensitivity functions of the WPT system efficiency with respect to the coil AC resistances are also calculated. According to the sensitivity functions, possible cases for using PCB-based magnetic couplers are investigated. The magnetic couplers are designed for a 3.3 kW wireless EV charging application. The efficiency of the conventional and proposed PCB-based wireless charging systems are compared through simulation and experiments. The proposed magnetic coupler

design based on PCB shows low AC resistance and competitive efficiency results compared to the system using Litz wire in the magnetic couplers.

5.2. Moving Toward the PCB Magnetic Coupler and Design Challenges

A typical EV wireless charging system based on the inductive coupling is shown in Fig. 5-1.

Fig. 5-1. A typical EV wireless charging system based on the inductive coupling.

5.2.1. Conventional Magnetic Couplers

The switching frequency for a light-duty wireless charger is set to 85 kHz according to SAE standard. At this frequency, due to skin effect, the AC resistance of the single strand wire will be increased significantly compared to its DC resistance. To overcome this issue, multiple insulated strands of copper (Litz wire) are typically employed [18]. The diameter of each strand of the Litz wire is selected according to the skin depth (δ) at the operating frequency (f) and the total number

of the strands (n_s) will be selected according to the total current of the wire and the desired current density (J_w). In this way, the skin effect could be mitigated and the AC resistance of the wire will be close to its DC resistance. However, due to the proximity effect, the AC conduction losses cannot be eliminated.

Fig. 5-2 shows the layout of a conventional rectangular magnetic couplers made by Litz wire. In this structure, the total diameter of the wire is D_w consist of multiple insulated copper strands with a diameter of D_s. The value of skin depth (δ) of the copper in the operating frequency determines the maximum strand diameter of each strand of the wire as follows [29]:

$$\delta = \sqrt{\frac{2\rho}{\omega\mu}} \tag{4.42}$$

$$D_s \leq 2\delta \tag{4.43}$$

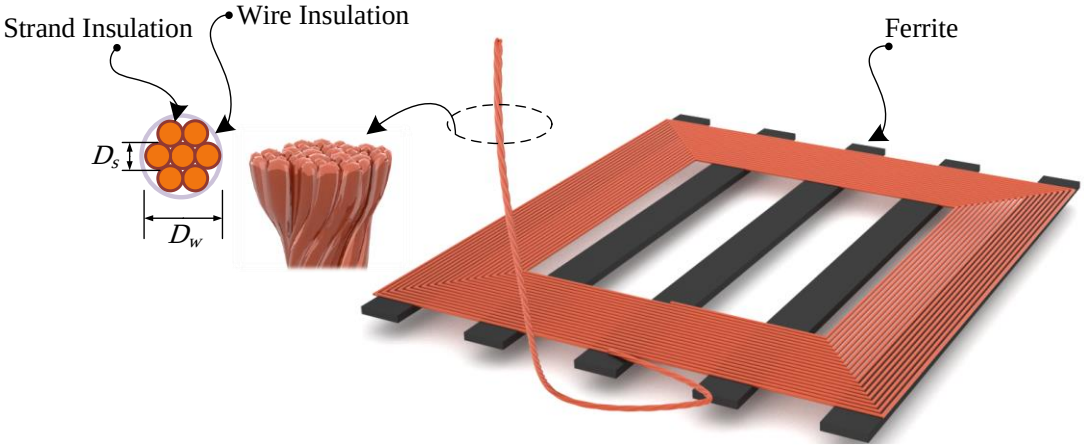

Fig. 5-2. Rectangular magnetic coupler made by Litz wire

where ρ is the conductor resistivity, μ is the permeability, and ω is the angular frequency. The effective cross-section area of each strand is given by:

$$S_{eff} = D_s^2 \pi / 4 \tag{4.44}$$

where D_s is the diameter of each strand in the Litz wire. The required cross-section area of cupper based on the branch current and maximum allowable current density can be calculated as follows:

$$S_{req} = \frac{I}{J_w} \tag{4.45}$$

where I is the branch current and J_w is the desired current density. The current density is restricted to the maximum allowable temperature rise of the wire. The total number of strands can be selected according to the required cross-section as follows:

$$n_s = S_{req} / S_{eff} \tag{4.46}$$

The wire total diameter can be calculated according to the filling factor of the Litz wire as follows:

$$D_w = k_f \sqrt{n_s} D_s \tag{4.47}$$

where k_f is the Litz wire fill factor which is a constant value typically around 1.3-1.6 [78]. Ideally, k_f should be one but due to the shape of the strands, strand insulation, and manufacturing process, some space of the wire will not cover by copper which results in higher k_f values.

According to (4.42), the selected strand size should be smaller than twice the skin depth to reduce the skin effect. However, having very thin strands results in a higher value of k_f[64] that results in larger diameter wires compared to single strand wire with equivalent copper cross-section area. It should be noted that the high value of k_f results in lower copper in a specific area which leads to a low power density design. Additionally, the availability of the Litz wires with a high number of strands and low strand diameter is another limiting factor [64]. Although the Litz wire can mitigate the skin effect and reduce the AC resistance, the cost of the Litz wire increases significantly as the number of strands increases. The price of the Litz wire produced by different manufacturers is considered and the normalized average cost per meter of them versus the number of strands is shown in Fig. 5-3.

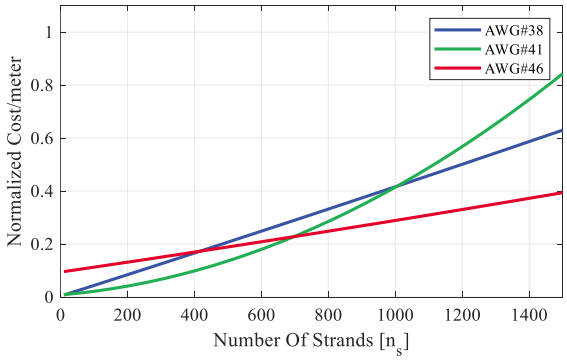

Fig. 5-3. Normalized cost of Litz wire versus number strands.

Besides the significant increase in the cost of the Litz wire for high power applications, the manufacturing errors should be considered. These errors could be related to building the coil or elements of the magnetic coupler including Litz wire.

In the case of using a high gauge wire for the strands (tiny strands), it is possible to have more broken strands due to their fragility [64]. Therefore, the effective number of strands will be reduced and thus increasing the conduction loss. The insulation layer of the Litz wire has some manufacturing tolerance that affects the spacing between the turns. Moreover, space between the wire and ferrite core can have some errors during manufacturing.

5.2.2. PCB Based Magnetic Couplers

A. Layout

A PCB-based magnetic structure offers a simple manufacturing process compared to a conventional Litz wire-based structure. The design tolerance will be limited to PCB production error which is significantly lower compared to manufacturing a conventional wire-wound coil. Additionally, the parasitic elements of the circuit are predictable and thus can be considered and mitigated in the analysis. Moreover, the manufacturing costs will be reduced due to simplicity and machine assembly instead of labor work. Considering the advantages of the PCB-based magnetic structure over conventional wire-wound coils, a planner magnetic structure based on the PCB can be used for wireless charging applications. The proposed magnetic coupler is utilizing a multi-layer PCB as shown in Fig. 5-4.

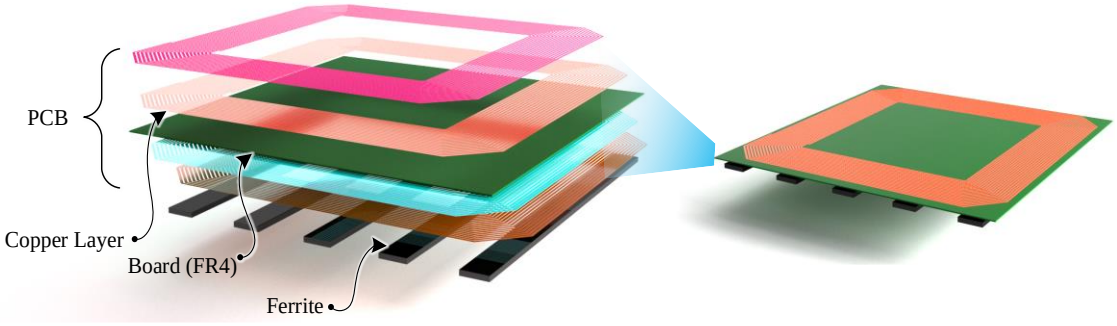

Fig. 5-4. Proposed magnetic coupler made by multi-layer PCB.

In this structure, the coils are printed on the board material. It is possible to have multiple layers to increase the current capability and reduce the conduction loss. The layers of the structure can be connected in parallel to reduce the AC resistance. Similarly, by increasing the trace width and copper weight (thickness), the coil resistance can be reduced. It should be noted that different layers are insulated from each other by a dielectric material (FR4).

Estimation of the cost of the PCB production versus different board parameters is gathered and the normalized values are shown in Fig. 5-5.

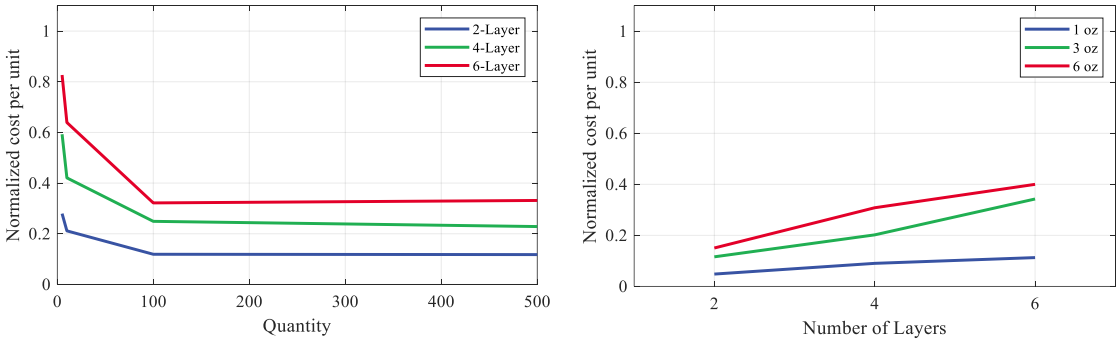

(a) quantity of boards with 3oz copper weight (b) number of layers

Fig. 5-5. Normalized cost of PCB versus.

The size of the board is consistent for all the points. According to Fig. 5-5 (a), the cost of each board will decrease as the quantity of the order increases and it will be an almost constant value for a high number of boards. The cost of PCB production versus the number of layers is shown in Fig. 5-5 (b). It can be seen that as the number of layers increases, the total cost increases too. Moreover, increasing the copper weight also increases the production cost as expected. According to this data, the minimum number of layers and lower copper weight (oz) is preferable.

B. Design Challenges

As discussed, the quality factor of the coils should be high to ensure a high-efficiency profile for the wireless power transmission system. Since the operating frequency for EV application is restricted to 85 kHz, the self-inductance of the coil and its AC resistance are the remaining design parameters to achieve high-quality factor magnetic couplers. The self-inductance is dependent on the number of turns, the dimension of the coil, and the magnetic core material. The coil AC resistance is dependent on the copper cross-section, the spacing between the turns (proximity effect), and its length.

The size of the magnetic couplers should be optimally selected to avoid large structures. Especially for EV applications, the vehicle-side coil size is limited to the available space underneath the vehicle. Moreover, the vehicle side magnetic

structure and pickup converter should be light-weight. Therefore, the core material should be optimally selected.

In a PCB-based magnetic structure, each turn can be made by a limited number of strands compared to the Litz wire-based structure. Therefore, finite element analysis is required to optimally design the PCB-based structure and select the track width (T_w) and the number of parallel branches (N_{br}). Moreover, the current capability of the PCB tracks is limited due to the coil conduction loss. Having high conduction loss on the coils reduces the efficiency of the system and may violate the allowable temperature of the board material.

5.2.3. Circuit Modeling

An LCC-S topology is selected for the compensation network shown in Fig. 5-6. By using the fundamental harmonic analysis, the circuit schematic could be further simplified as shown in Fig. 5-7.

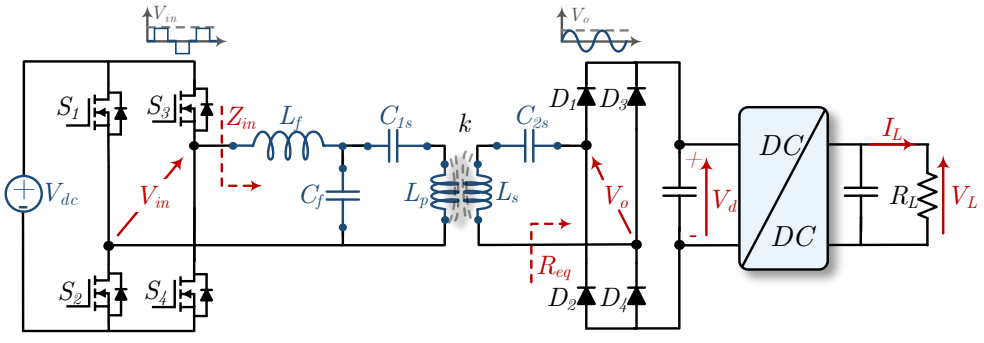

Fig. 5-6. Circuit diagram of the LCC-S compensated WPT system and battery control scheme.

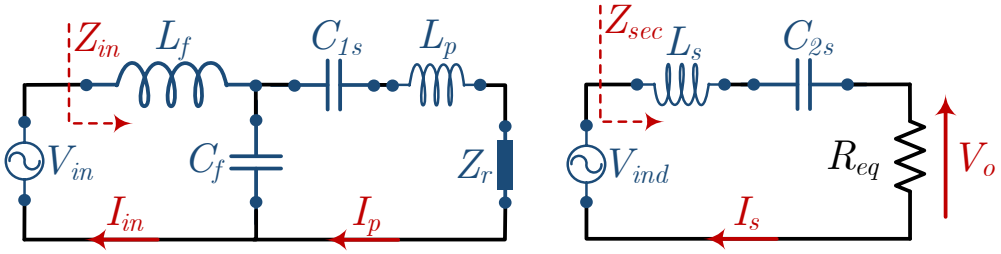

Fig. 5-7. Equivalent circuit of LCC-S topology according to fundamental harmonic approximation.

When the circuit is excited with the resonant frequency, the secondary side circuit reactance will be eliminated ($L_s C_{2s}\omega^2 = 1$) and the output voltage will be equal to the induced voltage. In this condition, the output voltage is independent of the load variation and the voltage source feature of the LCC-S network is achieved. The output power is given by:

$$P_{out} = \frac{M^2}{R_{eq} L_f^2} V_{in} V_o \tag{4.48}$$

where M is the mutual inductance between the primary and secondary side, V_{in} is the RMS voltage of the inverter and V_o is the RMS value of the output voltage before rectification.

5.2.4. Sensitivity Analysis

In this sensitivity analysis, only conduction losses of the magnetic couplers are considered to simplify the analysis and evaluate their effect on the performance of the system. The power loss in the coils and efficiency of the WPT system can also be defined by [55]:

$$P_{loss} = r_p I_p^2 + r_s I_s^2 \tag{4.49}$$

$$\eta = \frac{P_{out}}{P_{out} + P_{loss}} \tag{4.50}$$

In the next step, the sensitivity of the system efficiency to the coil resistances at the resonant frequency of $\omega=\omega_0$ is calculated as follows:

$$S_p = \frac{\partial \eta}{\partial r_p} = -(M_{ps}\omega)^2 \frac{R_{eq}}{\left((M_{ps}\omega)^2 + r_p\left(R_{eq} + r_s\right)\right)} \tag{4.51}$$

$$S_s = \frac{\partial \eta}{\partial r_s} = -(M_{ps}\omega)^2 \frac{1 + 2R_{eq}r_p\left(R_{eq} + r_s\right)}{\left(R_{eq} + r_s\right)\left((M_{ps}\omega)^2 + r_p\left(R_{eq} + r_s\right)\right)^2} \tag{4.52}$$

It can be seen that the sensitivity functions are independent of the magnetic couplers' self-inductances and resonant elements values. The value of R_{eq} can be calculated according to the desired nominal voltage and power. For a 3.3 kW wireless charging system, typically the output voltage is in the range of 300-600 V; therefore, the value of load resistance is around 27-109 Ω. The sensitivity functions versus output power for a typical 3.3 kW WPT system are calculated and the results are shown in Fig. 5-8.

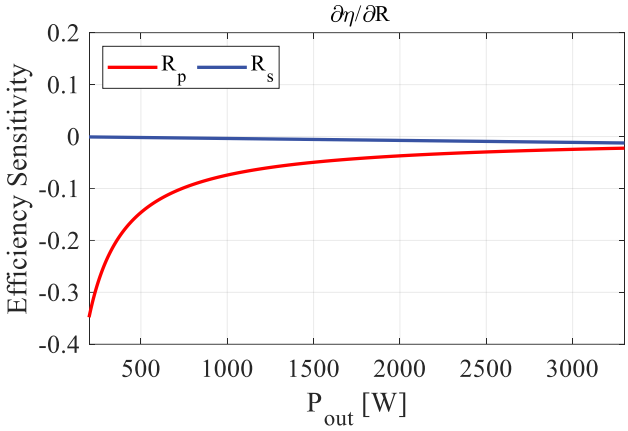

Fig. 5-8. The sensitivity of the efficiency to the primary and secondary side coil resistances.

According to Fig. 5-8, the efficiency of the wireless charging system is highly sensitive to the primary side coil resistance (r_p). The negative sign of the sensitivity value means that by any small variation of the coil resistance, the efficiency of the system will decrease as expected. Moreover, it can be seen that at light-load conditions, the sensitivity of the efficiency to the primary side coil resistance is higher. Therefore, more power loss during light-load operation is expected for a system with higher primary side coil resistance.

Having an LCC compensation on the transmitter side generates a constant current in the transmitter coil. Therefore, the total conduction loss of the transmitter side will remain constant in the charging process. In this case, a slight change of the r_p results in the high variation of efficiency which is leading higher sensitivity at light load conditions. It can be concluded that the small change of the secondary side coil resistance (r_s) has a negligible effect on system efficiency.

Therefore, instead of the high-cost Litz wire-based magnetic coupler, other alternatives such as the proposed PCB-based magnetic structure could be used for the receiver side coil.

5.3. Magnetic Coupler Design

A rectangular Litz wire based magnetic structure is considered to be predetermined. The conventional magnetic structure is used as a benchmark to evaluate the proposed PCB-based magnetic structure. The power rating, input, and output voltage, and misalignment range are considered to be the same for both systems. The coil AC resistance and self-inductance are considered as a figure of merit in this section.

To design the PCB-based structure, 3D-FEA studies are required. However, due to the computationally intensity and complexity of the modeling, 2D-FEA studies are employed. The 2D-FEA study illustrates the effectiveness of each design parameter that leads to minimum coil resistance. The result of the 2D analysis will be used to design the 3D model for further evaluations. Accordingly, the optimal design is selected and misalignment analysis is performed. Finally, the PCB design is compared with the reference design built by Litz wire.

5.3.1. Two-Dimensional Studies

In this part, the effect of different design parameters is studied through a 2D simulation to reduce the computation time. The results and conclusions of this part can be used as the guidelines for designing the 3D model of the PCB. In order to have a fair comparison, the range of the design variables of the PCB structure is selected to be in the range of the reference design (coil made by Litz wire). Therefore, the total coil width is 80 mm, and the PCB coil has 20 turns on each layer. Fig. 5-9 illustrates the procedure of generating the equivalent model of the 3D structure for 2D studies. In this study, the frequency is swept from 10 Hz to 200 kHz to study the skin effect on the coil resistance. This procedure is repeated for boards with 1 to 4 layers.

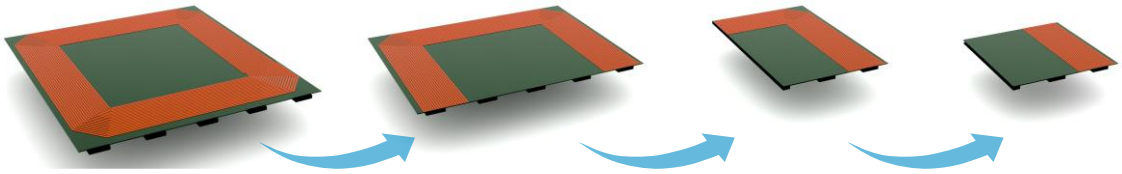

(a) procedure of transformation

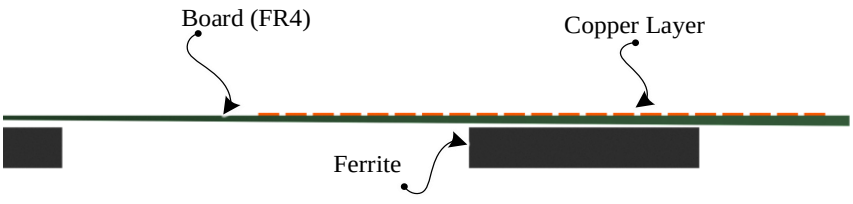

(b) final 2D model

Fig. 5-9. Simplification of the 3D model to a 2D model.

A. Copper Cross Section

In a solid conductor, as the cross-section area increases, the DC resistance decreases. However, due to the skin effect, the AC resistance of the wire will not decrease as the cross-section increases. To evaluate the effect of the track cross-section on the coil resistance, the copper track width (T_w) and copper weight (T_{cu}) is changed in the range of 0.5-3.5 mm and 1-6 oz, respectively. In this part, only the effect of the copper cross-section on the AC resistance is studied. The effect of the ferrite material is studied in the next part.

Fig. 5-10 shows the FEA results of the coil resistance versus the copper cross-section for one, two, and four-layer boards. It can be seen that generally the coil resistance will be reduced as the copper thickness increases. However, the effect of copper thickness will be negligible as the track width is high enough. Moreover, as the number of layers increases, the AC resistance of the coil decreases. However, the designs with a track width of larger than 1.5 mm showed negligible changes to the number of layers and copper weight increase. Therefore, the coil quality factor will not benefit from having an excessive number of layers. Additionally, the lower number of layers is preferable due to the high cost of multi-layer PCB designs. This could be achieved by optimal designing of the copper layer.

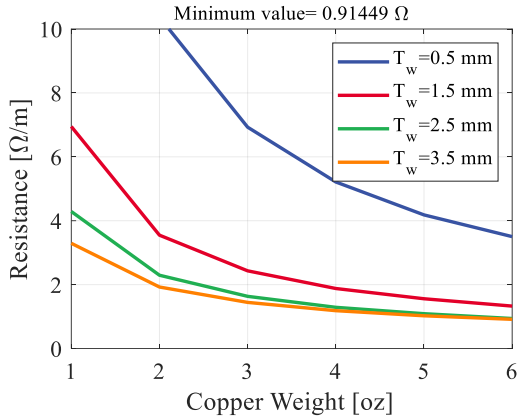

(a) 1-Layer board

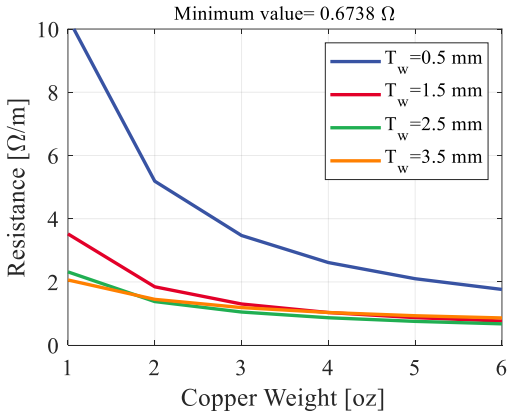

(b) 2-Layer board

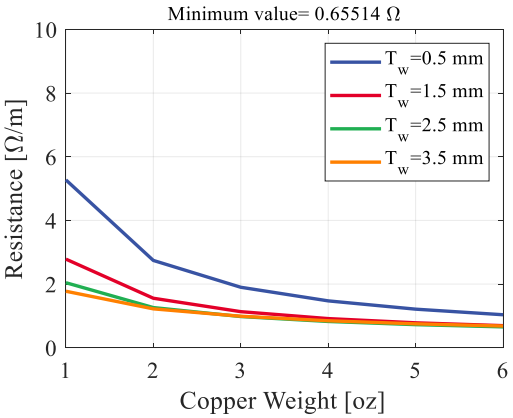

(c) 4-Layer board

Fig. 5-10. Track AC resistance versus copper weight (thickness) at different track width

B. Parallel Branches

Similar to the Litz wire design, the PCB tracks could be designed. In this way, each turn of the coil is divided into multiple parallel branches (N_{br}) as shown in Fig. 5-11. In this part, designs with different numbers of parallel branches are considered to study its effect on the coil AC resistance. Since the skin depth at 100 kHz is around 0.2 mm, the width of parallel branches should be selected close to 0.4 mm according to (4.43). Similar to the previous part, single-layer, two-layer, and four-layer board layouts are considered and the FEA results are shown in Fig. 5-12.

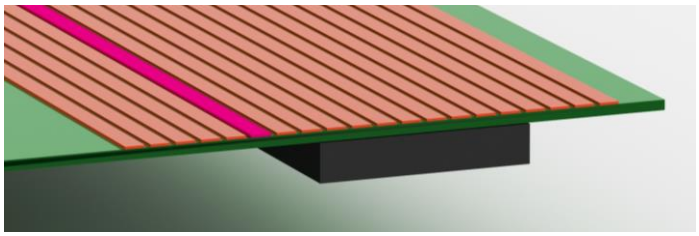

(a)

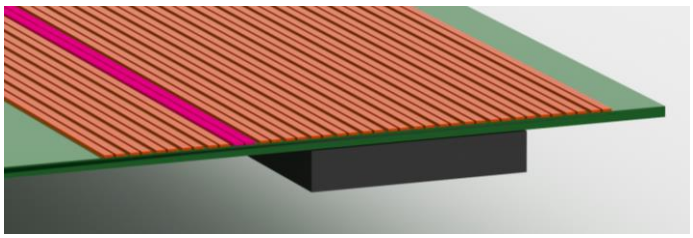

(b)

Fig. 5-11. Coil turns layout: (a) single branch for each turn (b) two parallel branches for each turn.

By comparing the FEA results between the cases with two and three branches, it can be seen that the changes in the minimum achievable value are negligible. It

should be noted that the designs with track width smaller than twice the size of the skin depth are showing the highest resistance even at high copper weights (thickness). It can be seen that as the branch width is larger than 0.4 mm, the resistance of the coil is reduced significantly. However, beyond the 0.4 mm track width, the changes are negligible and the reduction rate of the resistance versus copper weight and track width is saturated. Furthermore, the designs with a 0.2 mm track width showed higher changes when the number of parallel branches is increased.

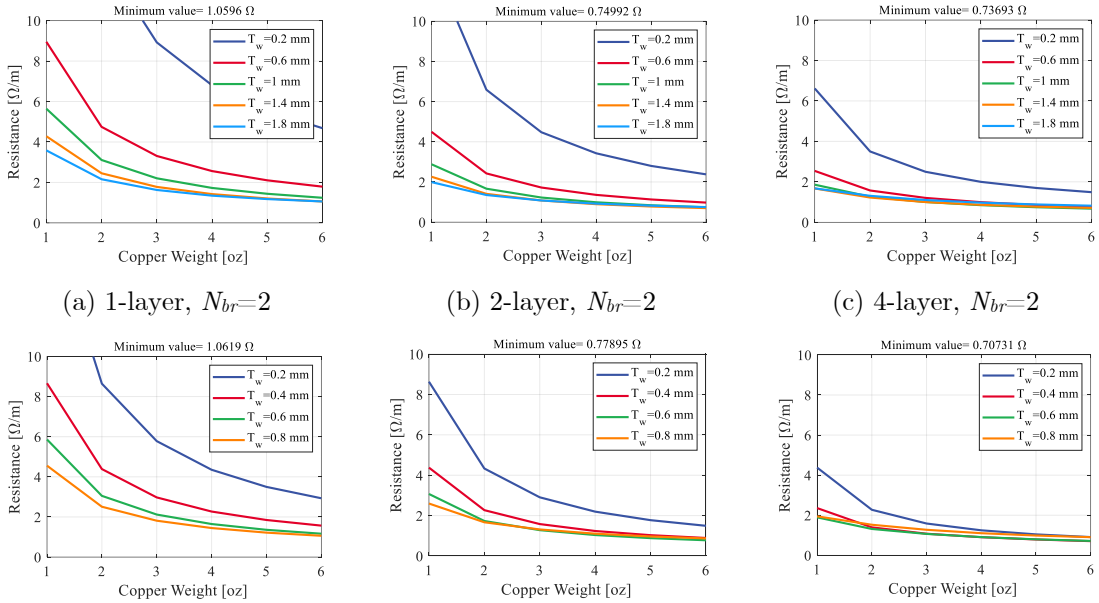

(a) 1-layer, N_{br}=2 (b) 2-layer, N_{br}=2 (c) 4-layer, N_{br}=2

(d) 1-layer, N_{br}=3 (e) 2-layer, N_{br}=3 (f) 4-layer, N_{br}=3

Fig. 5-12. Track AC resistance versus copper weight at different branch widths.

Comparing the presented results in Fig. 5-12 to the single branch layout (Fig. 5-10), it can be seen that when the copper cross-section is lower than twice the skin

depth in each direction, having a higher number of parallel branches (N_{br}) is beneficial. A design with a low copper cross-section can be selected in two scenarios: cost limitation, and space limitation. In any of these cases, the presented results could be helpful for the designer to appropriately select the optimal sizes for the copper layer of the coils. As the copper cross-section or number of layers increases, the parallel branches' effect on the coil resistance is reduced.

Moreover, it can be seen that the minimum achievable resistance for a single branch per turn is lower than multiple parallel branches. This pattern can be seen in all the number of layers. Because of the restriction of the coil total width to 80 mm (to match the reference Litz wire design), as the number of branches increases, the clearance between the branches and different turns will be reduced. It should be noted that in this high-power application, the clearance between the turns is essential to avoid insulation issues. Therefore, the proximity effect will be increased, and coil AC resistance will be increased compared to the single branch case presented in Fig. 5-10. Depending on the requirements of each application, the designer can select the optimal value of the coil width to minimize the coil AC resistance. In this chapter, a comparable equivalent for the reference Litz wire based magnetic coupler is considered as the baseline.

C. Layer Thickness

Due to the proximity effect at high-frequency operation, the AC resistance of the coils could be affected by nearby turns and layers. The layer insulation thickness (T_L) is considered as another design variable in this part as shown in Fig. 5-13. In this study, the dielectric thickness is varied from 0.2 mm to 1.8 mm, and copper thickness (T_{cu}) is changed between 3-6 oz. The branch width is changed between 1.5-3.5 mm, 0.6-1.8 mm, and 0.4-0.8 mm for the single branch, two branches, and three branches designs, respectively. The FEA results of this study are presented in Fig. 5-14 and Fig. 5-15 with the same color maps as Fig. 5-12.

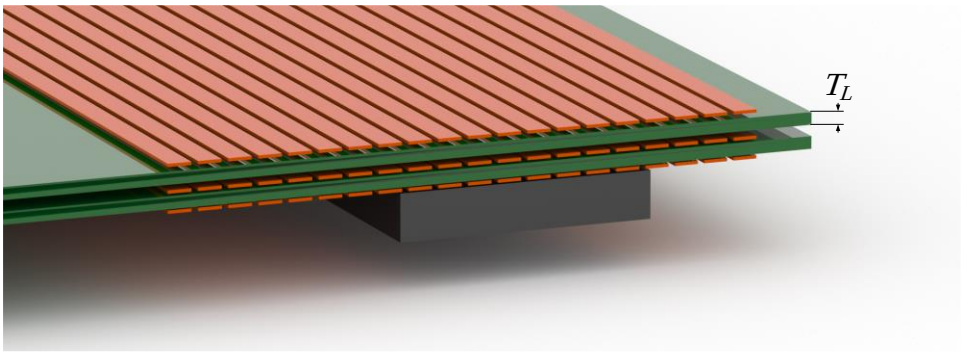

Fig. 5-13. Layer thickness in a multi-layer board.

In Fig. 5-14, the results for 0.5 mm and 0.2 mm are not presented due to high coil resistance according to Fig. 5-12 (dark blue curves). According to Fig. 5-14, it can be seen that in all three types of designs with different copper weights (T_{cu}), the coil resistance is reduced as the spacing between the layers (T_L) reduces. However, as the branch width (T_w) is increased, the variation of the AC resistance

with respect to the layer thickness is increased. However, the changes in the 6 oz designs are close to the 3 oz designs. In another word, the coil resistance is more sensitive to the board layer thickness when wider tracks are used. According to Fig. 5-14 (b) and (e), having wider branches does not necessarily result in lower resistance. It can be seen that the resistance of the designs with T_w=1.8 mm is higher than the designs with T_w=1.4 mm due to the proximity effect as discussed before.

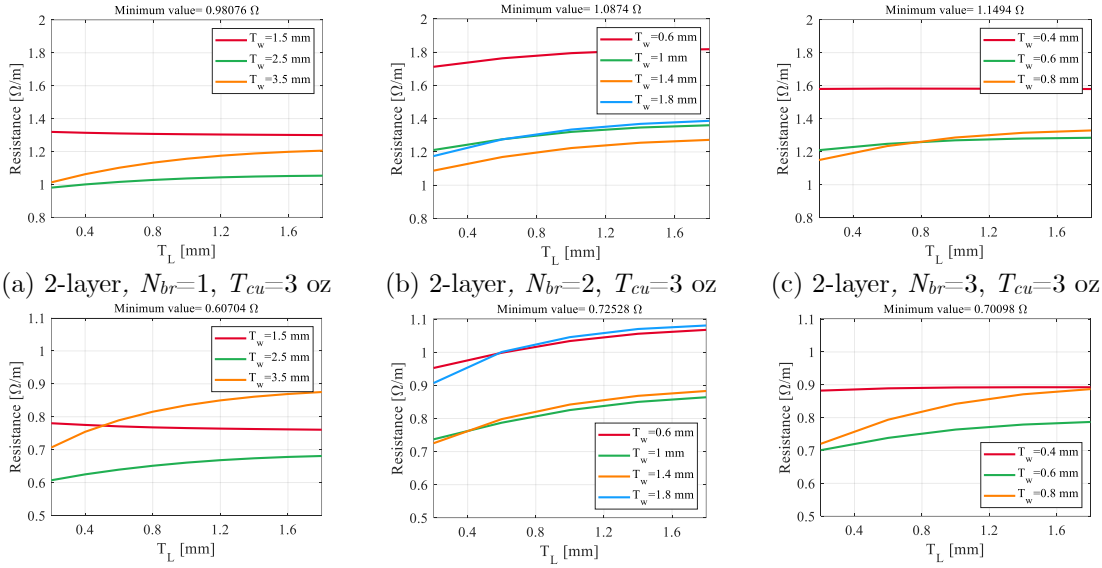

(a) 2-layer, N_{br}=1, T_{cu}=3 oz (b) 2-layer, N_{br}=2, T_{cu}=3 oz (c) 2-layer, N_{br}=3, T_{cu}=3 oz

(d) 2-layer, N_{br}=1, T_{cu}=6 oz (e) 2-layer, N_{br}=2, T_{cu}=6 oz (f) 2-layer, N_{br}=3, T_{cu}=6 oz

Fig. 5-14. Track AC resistance versus layer thickness at different branch widths of a 2-layer board.

Another important point that can be seen in Fig. 5-14 (a) and (d) is that by changing the copper thickness from 3 oz to 6 oz the resistance of the design with 3.5 mm is increase beyond the resistance of 1.5 mm track width design. Having higher copper thickness significantly increases the production cost; it was shown

that it can be nullified if the layer thickness is not selected optimally. Moreover, changing the thickness of the board typically does not affect the production cost. Therefore, the optimal selection of the board thickness is a vital step in designing the PCB magnetic couplers. It should be noted that the effect of layer thickness is only observed on the high-frequency excitation of the coils. The coil resistance under DC or low-frequency operation remains constant versus layer thickness.

Similarly, the 4-layer PCB layout is studied and the FEA results are presented in Fig. 5-15. It can be seen that similar results are achieved and by reducing the layer thickness the coil AC resistance is reduced. Additionally, the minimum possible AC resistance is around 0.54 Ω/m corresponding to the 4-layer board with a branch width of 2.5 mm and 6 oz copper thickness. Although the 2-layer board showed a comparable low resistance at the same design point (Fig. 5-14 (d)), other parameters such as current density and temperature rise should be considered in practice.

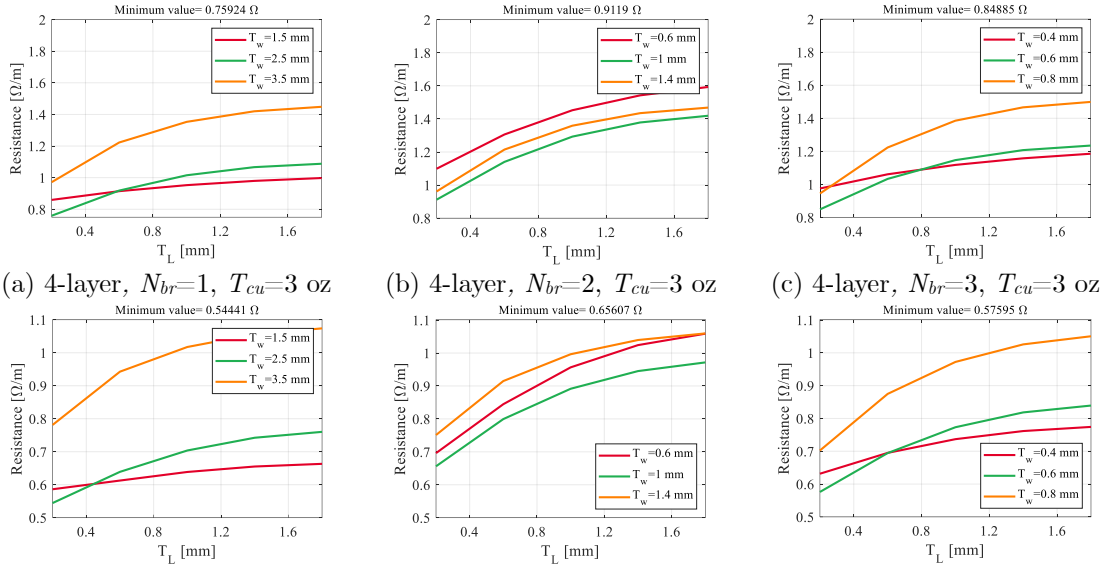

(a) 4-layer, N_{br}=1, T_{cu}=3 oz (b) 4-layer, N_{br}=2, T_{cu}=3 oz (c) 4-layer, N_{br}=3, T_{cu}=3 oz

(d) 4-layer, N_{br}=1, T_{cu}=6 oz (e) 4-layer, N_{br}=2, T_{cu}=6 oz (f) 4-layer, N_{br}=3, T_{cu}=6 oz

Fig. 5-15. Track AC resistance versus layer thickness at different branch widths of a 4-layer board.

In order to study this effect in more depth, magnetic field density (B) and current density (J) distribution in this magnetic system is studied. As an example, the field distribution for the 2-layer board with two different design points is presented in Fig. 5-16. By comparing Fig. 5-16 (a) and (b), it can be seen that the magnetic field density is distributed more uniform in the design with a lower layer thickness (T_L=0.2 mm). Therefore, as it is shown in Fig. 5-16 (c) and (d), the current density is distributed to move evenly with a lower peak-to-peak value at T_L=0.2 mm. In another word, the proximity effect is reduced when the layers are placed close to each other. Therefore, the coil resistance is reduced as shown in Fig. 5-14 and Fig. 5-15.

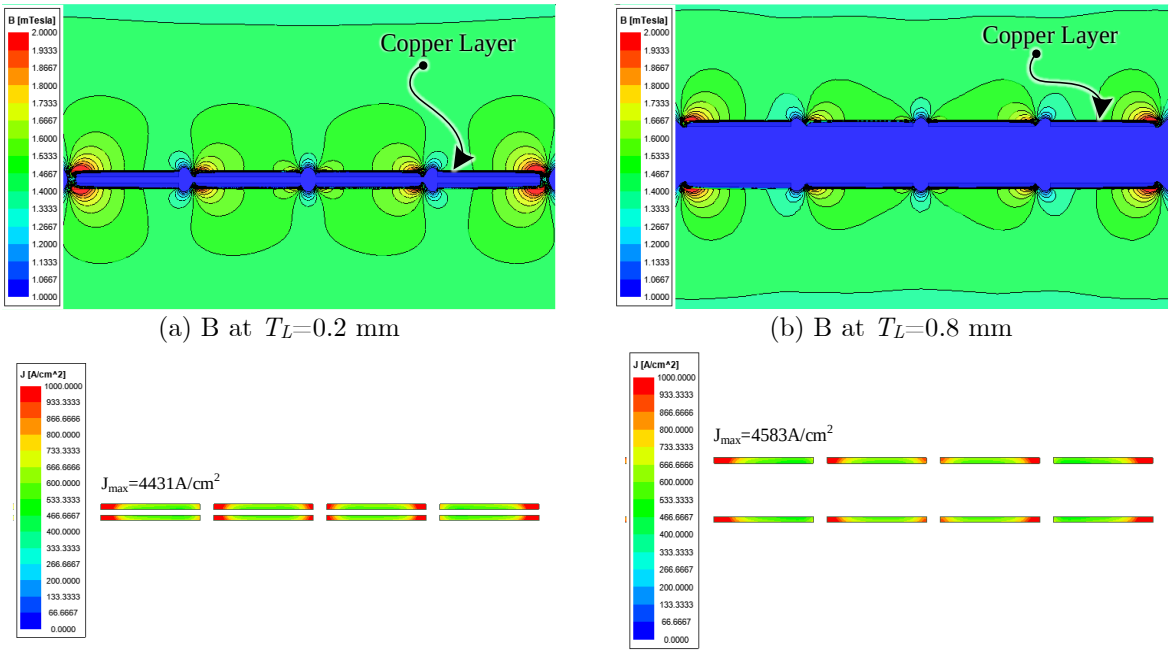

(a) B at T_L=0.2 mm (b) B at T_L=0.8 mm

(c) J at T_L=0.2 mm (d) J at T_L=0.8 mm

Fig. 5-16. Magnetic field density (B) and current density (J) distribution in the 2-layer board with T_w=3.5 mm.

D. Magnetic Core Material

Magnetic core material such as Ferrite can be added to the magnetic couplers to improve the coupling factor, increase the self-inductance and quality factor, and reduce the field emission in the backside of the magnetic couplers. Due to the high permeability of the ferrite, adding it to the magnetic structure can change the magnetic field distribution. Changes in the magnetic field could result in the variation of the coil resistance due to the eddy current effect. Therefore, in this part, the ferrite blocks are added to the 2D analysis to investigate its effect on the AC resistance of the coil at the operating frequency. In this study, different

thickness of ferrite material (T_f) is placed underneath the board and FEA is performed on the 2D model. To save space, as an example, the FEA results for a single branch and 3 branches layouts with the board thickness of 0.2 mm and 6 oz copper thickness are presented in Fig. 5-17.

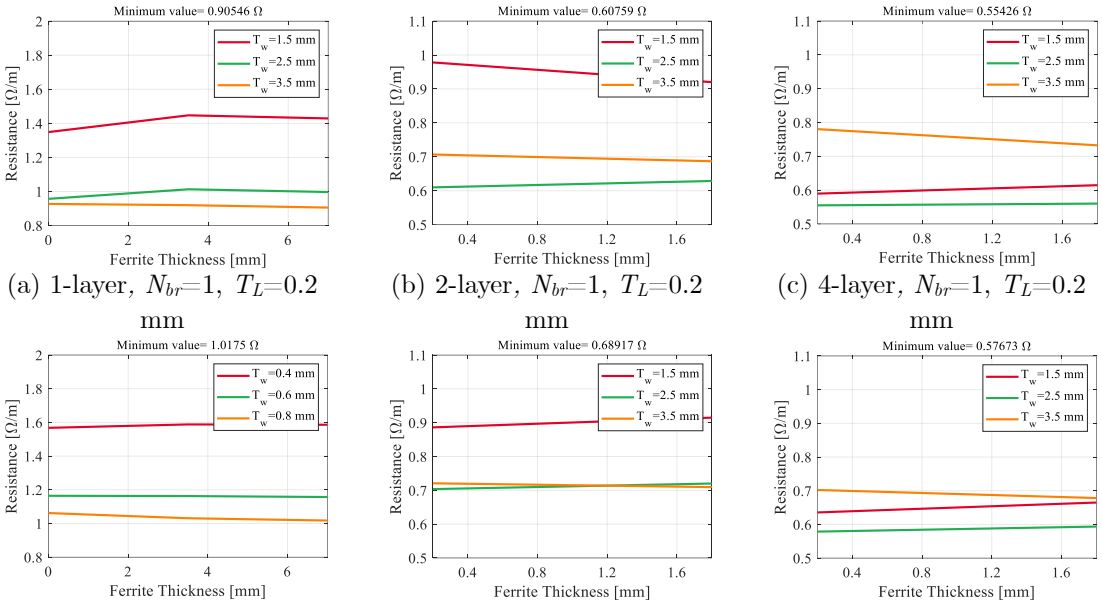

(a) 1-layer, N_{br}=1, T_L=0.2 mm (b) 2-layer, N_{br}=1, T_L=0.2 mm (c) 4-layer, N_{br}=1, T_L=0.2 mm

(d) 1-layer, N_{br}=3, T_L=0.2 mm (e) 2-layer, N_{br}=3, T_L=0.2 mm (f) 4-layer, N_{br}=3, T_L=0.2 mm

Fig. 5-17. Track AC resistance versus ferrite thickness at different branch widths.

As can be seen, the ferrite core has a negligible effect on the coil AC resistance at this frequency. Generally, having ferrite blocks in the structure leads to slightly higher AC resistance. Although introducing the ferrite material will change the magnetic field distribution around the ferrite blocks, the changes in the coil resistance are not large. This is because of the fact that the size of the core is smaller compared to the air surrounding the magnetic couplers.

The changes of the magnetic field due to the ferrite core for a 4-layer board with a single branch per turn are shown in Fig. 5-18. In this figure, the range of B and J are limited to make the differences visible in the plot.

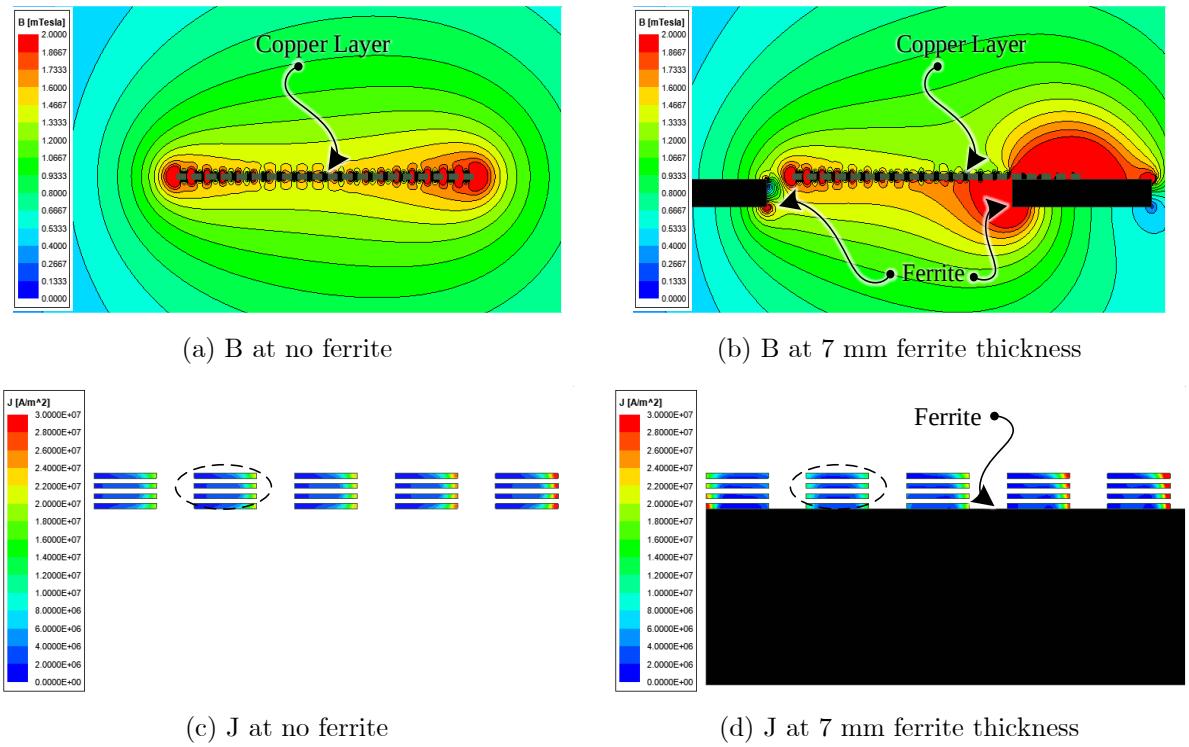

(a) B at no ferrite

(b) B at 7 mm ferrite thickness

(c) J at no ferrite

(d) J at 7 mm ferrite thickness

Fig. 5-18. Magnetic field density (B) and current density (J) distribution in the 2-layer board with T_w=3.5 mm.

It can be seen that the magnetic field density distribution is changed as expected. The magnetic field has a higher density inside and around the ferrite blocks. This has a small impact on the current density as shown in Fig. 5-18 (c) and (d). It can be seen that the points with high current density are on one side of the track in the no-ferrite design. In contrast, the current density is distributed more evenly in the structure with ferrite blocks but the average of the field

magnitude is higher. These small changes in the magnetic field and current density result in changes in the AC resistance of the coil.

5.3.2. Three-Dimensional Studies

Based on the presented 2D-FEA results, the 3D design (Fig. 5-9) parameters can be selected optimally. The 2D FEA results provided the guidelines to optimize the PCB layout of the magnetic couplers. For instance, the effect of the parallel branches and board dielectric thickness on the coil AC resistance is studied in the 2D modeling and the conclusions can be applied to the 3D model. In this way, the computation time and complexity are reduced.

It should be noted that these designs are restricted to the same outer and inner dimensions of the reference Litz wire structure. Therefore, a fair comparison between the two cases can be done. In this study, several iterations are done to find one of the optimal designs which are suitable for EV charging application. To avoid overlength, only a few numbers of 3D iterations are presented in this part as an example.

A. Copper Cross-section

The effect of the copper cross-section on the current density distribution (J) of a 10 A current excitation with the frequency of 100 kHz is illustrated in Fig. 5-19. In this figure, only one corner of the 3D model is shown for better visibility of the

results. It can be seen that as the copper thickness (T_{cu}) increased, the current density is reduced and the surface of the maximum current density is reduced. Moreover, it can be seen that as T_{cu} increased, the proximity effect is reduced. Therefore, having a higher copper weight can be beneficial to avoid hotspots in the PCB-based magnetic structure.

When the track width (T_w) is increased from 1 mm to 1.5 mm, the current density is distributed more evenly. Up to 2.5 mm track width, similar behavior is observed. However, beyond the track width of 2.5 mm, the proximity effect caused higher current density in the corners of the track as shown in Fig. 5-17 (e) and (g), and (f) and (h). This result is similar to the presented results for a 4-layer board in Fig. 5-15 (d). The calculated AC resistance at 100 kHz of the presented designs and the minimum values for 3 oz and 6 oz copper thickness is shown separately for better visibility in Fig. 5-20 (a) and (b).

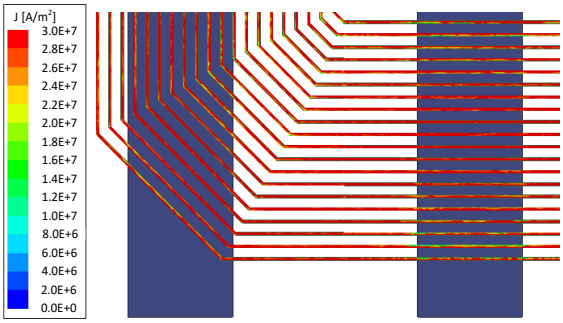

(a) 4-layer, N_{br}=1, T_w=1 mm, T_L=0.2 mm, T_{cu}=3 oz

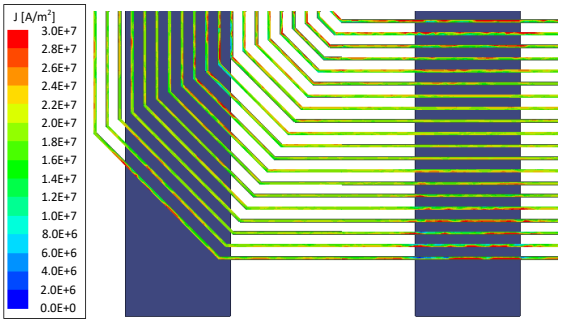

(b) 4-layer, N_{br}=1, T_w=1 mm, T_L=0.2 mm, T_{cu}=6 oz

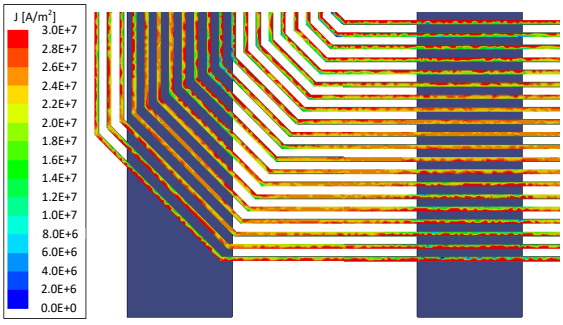

(c) 4-layer, N_{br}=1, T_w=1.5 mm, T_L=0.2 mm, T_{cu}=3 oz

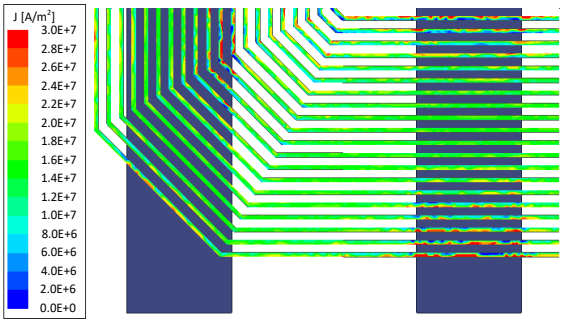

(d) 4-layer, N_{br}=1, T_w=1.5 mm, T_L=0.2 mm, T_{cu}=6 oz

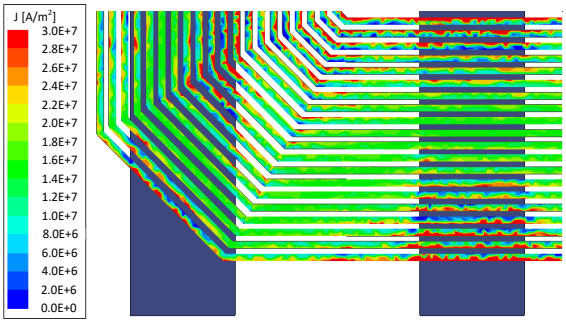

(e) 4-layer, N_{br}=1, T_w=2.5 mm, T_L=0.2 mm, T_{cu}=3 oz

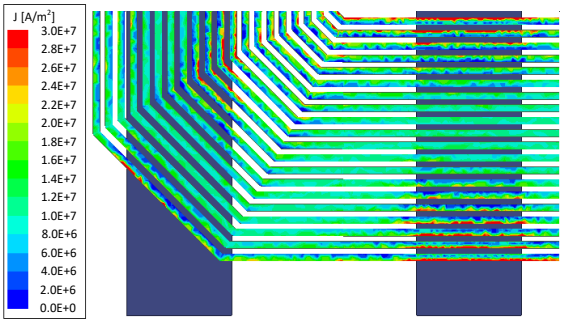

(f) 4-layer, N_{br}=1, T_w=2.5 mm, T_L=0.2 mm, T_{cu}=6 oz

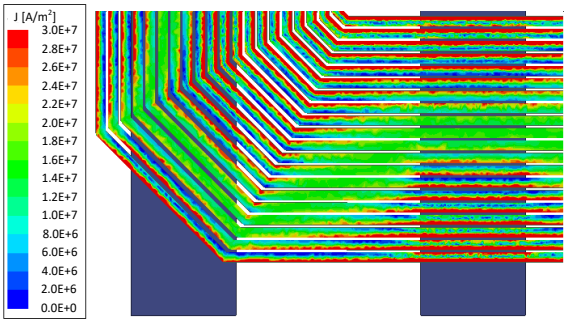

(g) 4-layer, N_{br}=1, T_w=3.5 mm, T_L=0.2 mm, T_{cu}=3 oz

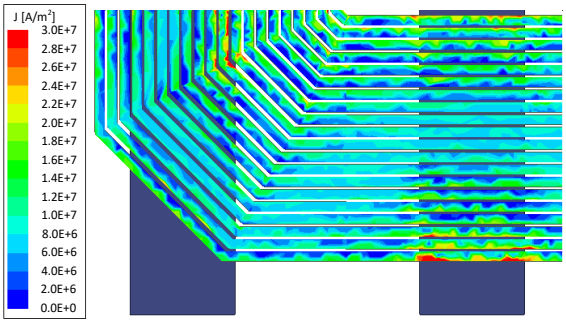

(h) 4-layer, N_{br}=1, T_w=3.5 mm, T_L=0.2 mm, T_{cu}=6 oz

Fig. 5-19. Current density distribution in the 3D models of the 4-layer PCB.

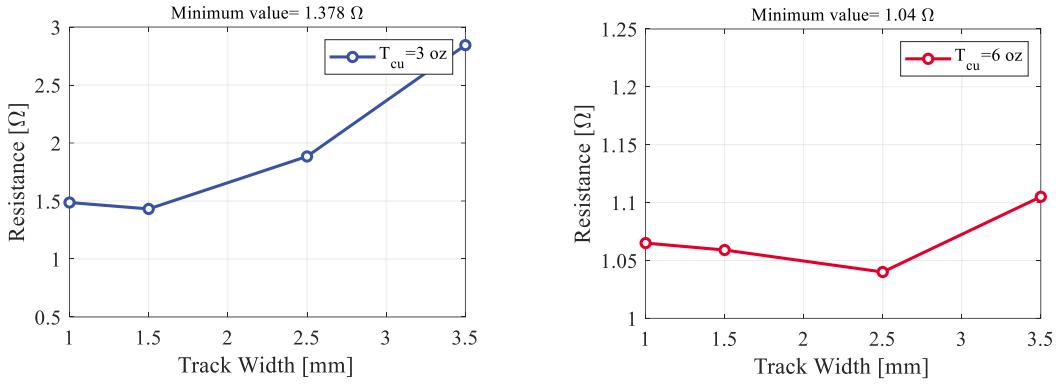

(a) (b)

Fig. 5-20. Calculated AC resistance of the single branch 4-layer PCB designs versus track width.

B. Layer Thickness

In this part, the effect of the dielectric thickness (T_L) on the AC resistance of the actual 3D model is studied. Similar to the 2D studies, a reduction of the coil AC resistance versus T_L is observed. As an example, the current density of a 4-layer PCB layout with a dielectric thickness of 0.7 mm and 0.2 mm is shown in Fig. 5-21 (a) and (b), respectively. It can be seen that there are fewer points that have a current density of 30 A/mm^2 and beyond in the layout with a 0.2 mm layer dielectric thickness. The AC resistance of the coils is also dropped from 1.78Ω to 1.105Ω when the layer thickness is reduced which is close to a 30 % reduction of the AC resistance similar to Fig. 5-15 (d).

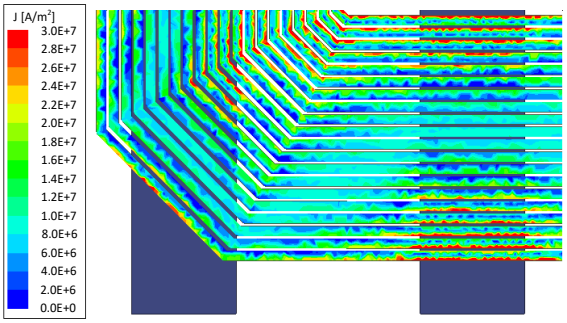

(a) 4-layer, N_{br}=1, T_w=3.5 mm, T_L=0.7 mm, T_{cu}=6 oz

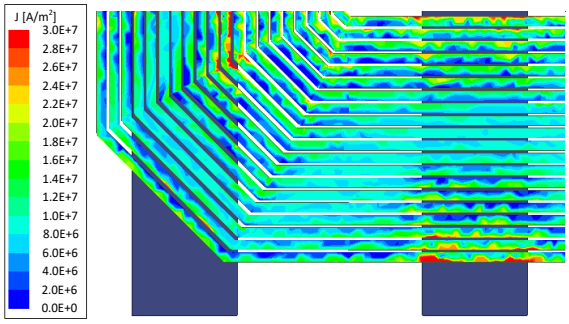

(b) 4-layer, N_{br}=1, T_w=3.5 mm, T_L=0.2 mm, T_{cu}=6 oz

Fig. 5-21. Current density distribution in the 3D models of the 4-layer PCB.

C. Integrated Coil Design

An integrated DC-DC inductor is also designed for the proposed PCB-based magnetic coupler. At first, the effect of the aspect ratio of the integrated coils, and ferrite bar direction on the self-inductance of the integrated coil is calculated. In this case, it is assumed that the number of turns is set to 20 turns. The aspect ratio is the ratio of the inner rectangle X edge size to the Y-direction size (X_b/Y_b). The FEA results of this study are shown in Fig. 5-22.

It can be seen that as the aspect ratio increased the self-inductance value increased. However, when the inner size is larger (Y_b), the effect of the aspect ratio

on the self-inductance is larger. Moreover, as the inner size increased the self-inductance value increased significantly. By comparing Fig. 5-22 (a) and (b), it can be seen that for Y_b=40 mm and Y_b =50 mm, when the ferrite bars are in zero degrees the self-inductance is slightly higher. In another word, the ferrite bars are aligned with the larger side of the integrated coils (x-direction) the self-inductance is slightly larger. According to this result, the aspect ratio of 1.5 is selected for the integrated coils to maximize the self-inductance.

In the next step, the number of the coil turns and the inner size of the coils is changed to study their effect on the self-inductance of the integrated coil. In this study, the aspect ratio is set to 1.5 according to the previous conclusions. The FEA results of this simulation are shown in Fig. 5-23. It can be seen that as the number of the integrated coil turns increases the self-inductance increases as expected. Similar to the previous case, as the inner size of the coil increases the self-inductance increases as well. Moreover, the ferrite direction showed a similar effect here.

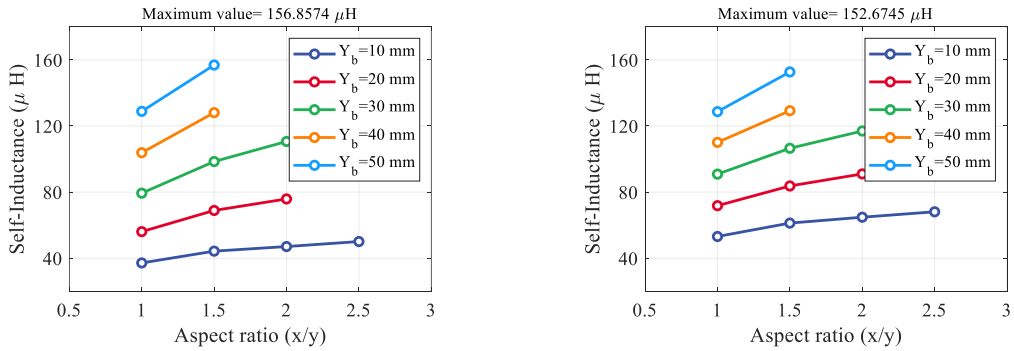

(a) 0-degree ferrite (b) 90-degree ferrite

Fig. 5-22. Calculated self-inductance of the integrated coil in the 4-layer PCB designs.

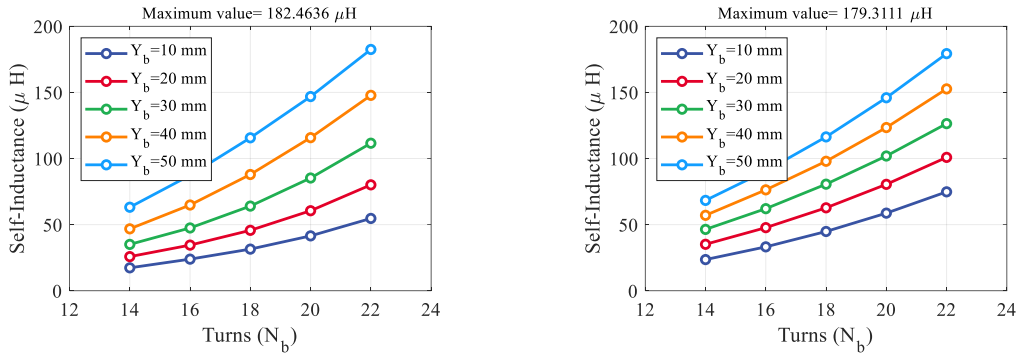

(a) 0-degree ferrite (b) 90-degree ferrite

Fig. 5-23. Calculated self-inductance of the integrated coil in the 4-layer PCB designs.

5.3.3. Selected Design

According to the 2D analysis, 3D designs were analyzed and compared. After several iterations, an optimal design is selected and the specification is listed in Table 5-1.

TABLE 5-1
SELECTED MAGNETIC COUPLER SPECIFICATIONS

Parameter	Symbol	Design Value
Primary side number of turns (Litz)	N_p	20
Secondary side number of turns (PCB)	N_s	20
Copper thickness	T_{cu}	6 oz
Number of parallel branches	N_{br}	1
Track width	T_w	2.5 mm
Board dielectric thickness	T_L	0.2 mm
Ferrite Thickness	T_f	7 mm
Ferrite width	T_{fw}	35 mm

Based on the FEA results, one of the designs which showed the minimum AC resistance is found and selected for the magnetic structure. The aspect ratio of the integrated coil is around 1.5 and the X_b and Y_b are 74 mm and 47 mm respectively. The calculated AC resistance of the main coil and integrated coil are 1.05 Ω and 0.878 Ω at 100 kHz, respectively.

A. Thermal Analysis

To calculate the maximum temperature rise of the board, a steady-state 3D thermal finite element analysis is done. Noting the symmetry of the design, a 50 mm cut of the board is considered to reduce the complexity of the simulation and required computational power.

Fig. 5-24 shows the surface temperature of the PCB when the 10 A sinusoidal current is flowing to the copper traces. In this study, the ambient temperature is assumed to be 23 °C. The maximum temperature of the copper versus the RMS value of the current is calculated and the results are shown in Fig. 5-25. Since the board material used in this thesis is T_g=180 °C, the calculated values of the maximum copper temperature are in the safe operating region.

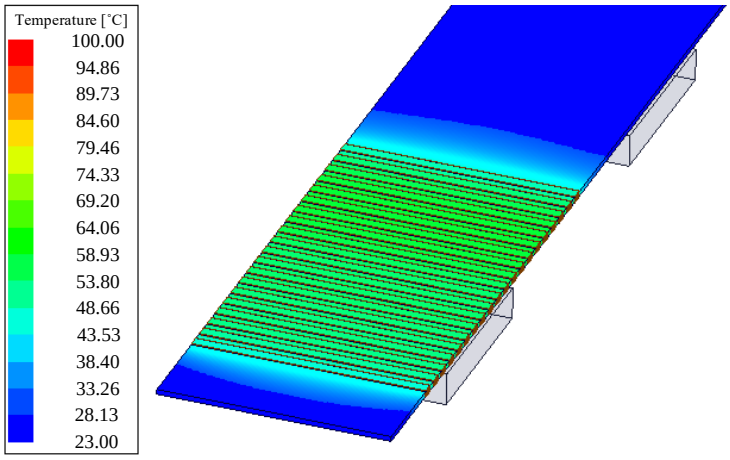

Fig. 5-24. The surface temperature of the proposed magnetic coupler based on PCB flowing I_s=10 A RMS.

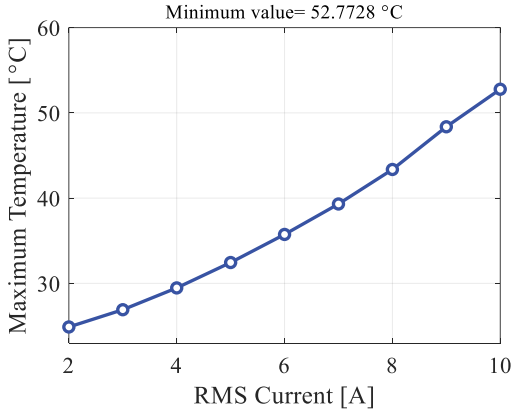

Fig. 5-25. Maximum temperature of the copper versus RMS current.

5.3.4. Comparison

To evaluate the proposed PCB-based magnetic coupler, the secondary side of the conventional wireless charger is replaced by the PCB, and the system efficiency is compared. The efficiency of the two systems with identical parameters except for the coil resistance versus the output power under full-aligned conditions is shown in Fig. 5-26. It can be seen that replacing the secondary side coil with a PCB has

a negligible effect on the efficiency at low power operation and at high power operation conditions, the difference is low. It worth mentioning that the proposed PCB-based magnetic coupler can reduce the volume of the magnetic coupler by around 55% compared to a conventional design due to the small thickness of the coil.

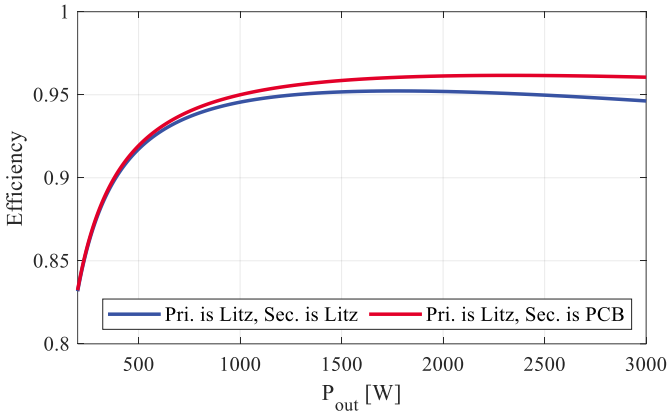

Fig. 5-26. Comparison of the conventional and the proposed wireless charging systems.

5.4. Experimental Results

To evaluate the performance of the proposed magnetic coupler based on PCB, a 3.3 kW wireless power transfer system is built. The LCC-S resonant network is designed optimally for this study. In this design, it is assumed that the input voltage is 200 V and the output voltage is in the range of 200-600 V for the coupling factor in the range of 0.22-0.32. The selected parameters of the LCC-S network are listed in Table 5-2. The efficiency and output voltage of this system will be compared in this Section.

TABLE 5-2
RESONANT NETWORK AND SYSTEM SPECIFICATIONS

Parameter	SYMBOL	Design Value
Primary side resonant inductor	L_f	49.18 μH
Primary side parallel capacitor	C_f	71.05 nF
Primary side series capacitor	C_{1s}	10.19 nF
Secondary side series capacitor	C_{2s}	9.23 nF
Maximum Power	P_{max}	3.3 kW
Nominal power range	P_n	540W~3300 W
Nominal coupling factor range	K_n	0.22~0.32
Air gap	-	125 mm
Switching frequency	f	85 kHz
Input DC voltage	V_{dc}	200 V

In this setup, the inverter is built by IPW65R037C6 power Si MOSFET switching at 85 kHz. The diode bridge on the receiver side is built with DSEI120-06A. The output of the diode rectifier is connected to a DC-DC converter supplying the load and provide a regulated output voltage. The resonant capacitors are Metalized Film Propylene (MFP) from EPCOS with a low Equivalent Series Resistance (ESR) and high rated AC voltage withstand at 85 kHz.

The conventional Litz wire coils are built with 500 strands of AWG38 Litz wire. The four-layer PCB-based magnetic coupler is built according to the specification listed in Table 5-2. The magnetic couplers based on Litz wire and PCB-based magnetic coupler are shown in Fig. 5-27 (a) and (b), respectively. The dimension of the ferrite bars is 510 mm × 38 mm × 7 mm and the material of the ferrite core is N87 from EPCOS which has core loss at the high operating frequency.

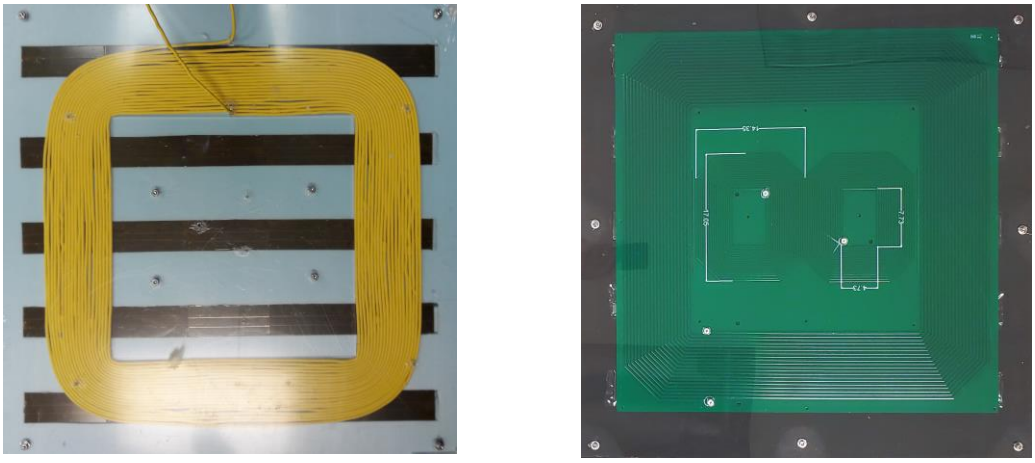

(a) Litz wire (b) PCB coil

Fig. 5-27. Magnetic couplers built by Litz wire and PCB.

In the proposed configuration, the transmitter side coil is built using the Litz wire and the receiver side is built using a PCB. The measured self-inductance of the magnetic coupler made by Litz wire on the primary side, L_p, is 386.6 μH and the self-inductance of the PCB-based magnetic coupler on the secondary side, L_s, is 380.1 μH.

The output voltage of the inverter (V_{in}), inverter current (I_{in}), output DC voltage (I_d), and output DC 20 (I_d) waveforms in the aligned position under 3.3 kW and 500W loading conditions are shown in Fig. 5-28. It can be seen that the Zero Voltage Switching (ZVS) is realized due to the inverter current phase lag. In another word, the current is passing through the anti-parallel diode of the Mosfet before the switching moment. Therefore, the turn-on voltage of the switch is close to zero and soft switching is realized.

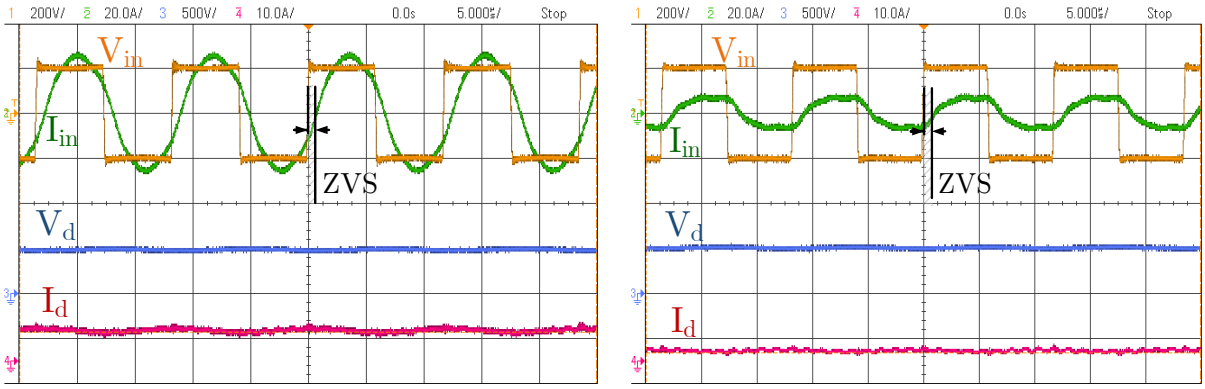

Fig. 5-28. Experimental output waveforms when magnetic couplers are fully aligned: (a) 3.3 kW (b) 500W.

The efficiency of the proposed configuration is measured experimentally and compared with calculation results as shown in Fig. 5-29. In this figure, the measured DC to DC power efficiency is reported. It can be seen that the measured efficiency is close to the calculation results. In the next step, the proposed combination that has PCB coil on the secondary side and Litz wire on the primary side is compared with the conventional dual-side Litz wire magnetic couplers. The coil inherent quality factor comparison is presented in 5-30. In this figure, the interpolation between the measured data is plotted as solid lines. It can be seen that the proposed PCB-based magnetic coupler, offers a competitive quality factor compared to the conventional magnetic coupler which ensures high efficiency of the proposed PCB-based magnetic coupler.

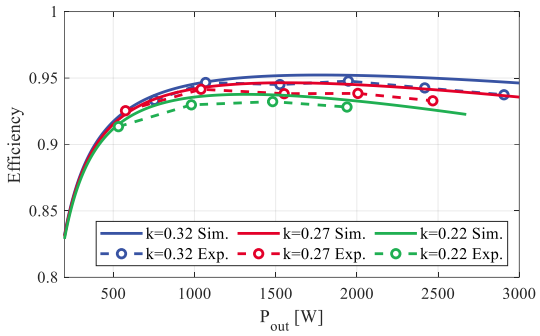

Fig. 5-29. Measured experimental efficiency values versus calculation results.

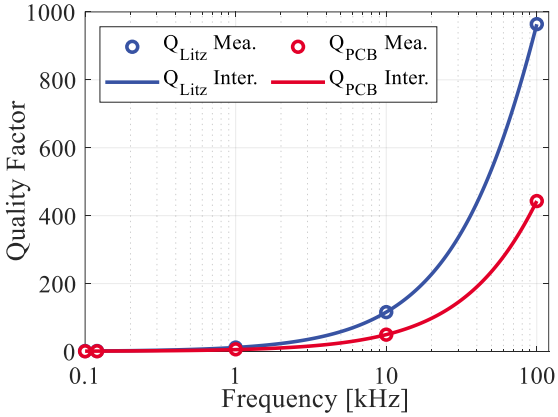

Fig. 5-30. Coil quality factor comparison between the conventional magnetic coupler made by Litz wire and PCB coil on the receiver side.

5.5. Conclusion

In this chapter, a cost-effective, simple to manufacture, and efficient magnetic coupler based on the Printed Circuit Board (PCB) is developed. The main advantage of the proposed magnetic coupler is the reduction of weight, fabrication error, cost, and maintaining high efficiency.

To design a competitive and efficient coil based on PCB, different design parameters are considered. In this study, copper cross-section, the number of

parallel branches, dielectric layer thickness, and magnetic core effect on the AC resistance is studied. To evaluate the effect of each design parameter on the AC resistance of the coil, finite element analysis is presented. According to the FEA results, when the track width is smaller than twice the size of the skin depth, the design showed the highest resistance even at high copper weights. Although having multiple parallel branches resulted in lower AC resistance as the number of branches increases, the changes are not large. As the number of branches increases, the clearance between the turns will be reduced; therefore, having many parallel branches results in higher AC resistance due to the proximity effect.

The dielectric layer thickness is also considered in the FEA analysis. It was shown that generally as the layer thickness reduces, the AC resistance reduces as well. When the copper tracks are wider, the coil AC resistance is more sensitive to the dielectric thickness between the layers. Moreover, it was concluded that the presence of the ferrite material has a negligible effect on the AC resistance. An optimal 4-layer PCB design was selected to replace the Litz wire in the magnetic couplers. To investigate the temperature rise of the proposed printed coil, a thermal analysis based on FEA is presented. It was shown that the maximum temperature of the copper will remain in the safe operating region of the board material.

Finally, a 3.3 kW wireless charging system based on the PCB coil on the receiver side is built. The efficiency of the system versus output power is measured experimentally which showed good accordance with the simulations. It was shown that the proposed PCB coil can replace the vehicle side Litz wire without sacrificing considerable system efficiency.

Chapter 6

A New Modular Resonant Topology for High-Power WPT Systems

6.1. Introduction

Electric vehicles already showed a great performance in terms of efficiency, and greenhouse gas emissions compared to conventional gasoline vehicles. Despite these outstanding features, few barriers need to be addressed to expect full domination of the EVs in the future market. One of the challenges is the range anxiety of the EVs which is related to the battery technology and charging time. In order to move the competition to the next level, EVs should offer a fast, convenient charging process close to gasoline refueling. Fast chargers are the solution to this challenge by reducing the changing time from several hours to few minutes.

Besides the battery technology that needs to be further improved, the power converters should be adopted for high-power applications as well. Increasing the power level of the converters and magnetic couplers faces several practical challenges that require introducing new topologies. The power level of the magnetic coupler can be increased by increasing the Litz wire gauge or using multi-phase systems [71]. In order to increase the power level of the transmitter side inverter, the current or the voltage level of the input needs to be increased.

Besides, commercial and fleet vehicles such as electric buses require huge a battery pack, and a high-power charging infrastructure. Wireless charging can address some of the shortcomings such that the vehicles equipped with wireless charging can carry smaller batteries because they can be charged throughout the day. This also means that the fleet does not have to account for wired charging time and thus the fleet can purchase fewer EVs and still maintain service levels [156].

Fig. 6-1 shows a high-power wireless charging system. In these applications, a high-power transmitter circuit to supply hundreds of kW is a requirement [18].

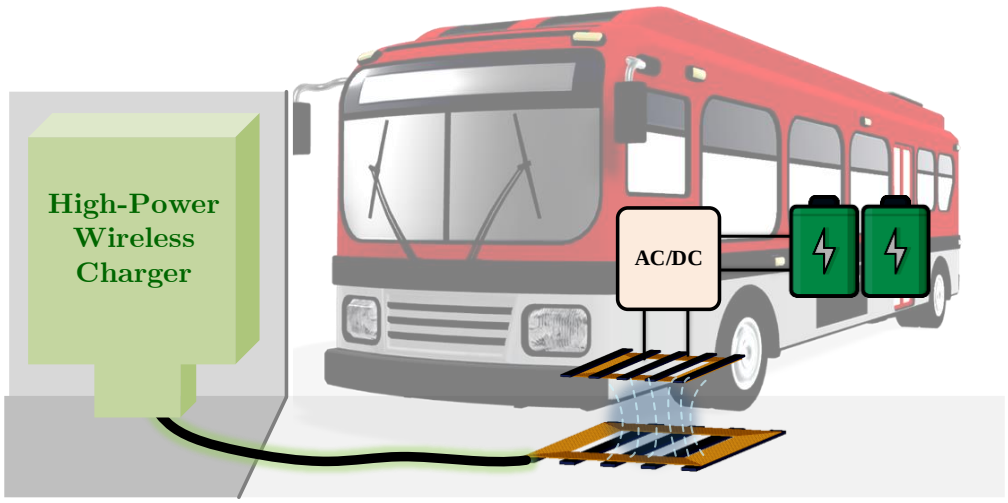

Fig. 6-1. Concept of high-power wireless charging application.

Increasing the power rating of the inverter could be achieved by increasing the rating of the semiconductors, using multilevel topologies [124-126], and modular structures [127]. Currently, the voltage rating of high-frequency switches such as SiC devices is limited in commercialized products. Moreover, at high voltage operation, the dv/dt and maximum current rating of the switches are other limiting factors [128]. Furthermore, the cost of the inverter switches increases significantly by increasing the switch ratings.

In order to increase the power level of the transmitter side inverter, modular structure is proposed in [128, 134, 136]. This topology is shown in Fig. 6-2. This topology requires multiple Intercell Transformers (ITC) to eliminate the circulating current between the inverter legs.

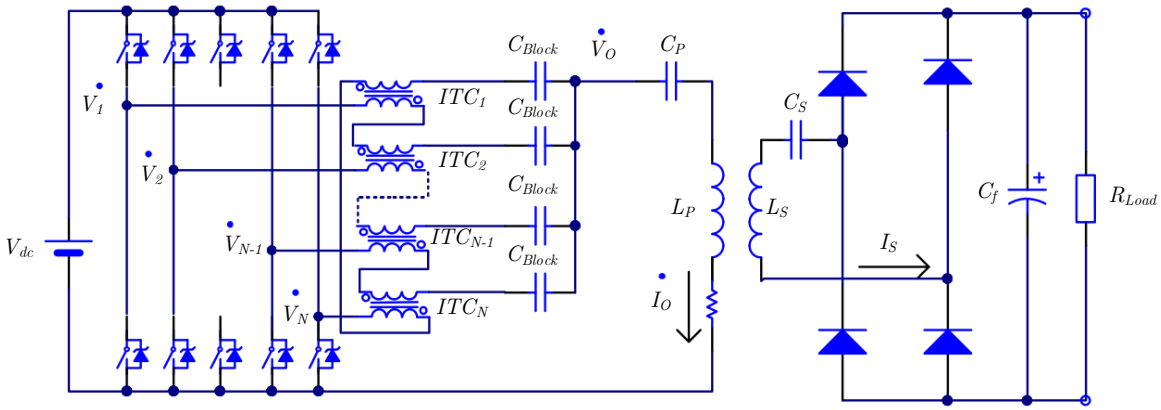

Fig. 6-2. Modular inverter topology for WPT applications proposed in [128].

In this structure which uses a half-bridge topology, a DC blocking capacitor should be connected to each ITC to avoid transformer saturation. These bulky transformers and DC blocking capacitors increase the complexity of the system and implementation cost. Moreover, this structure employs a series resonant network on the transmitter side. In this resonant topology, the impedance seen by the inverter is close to zero when the receiver side (vehicle) is not present which causes inverter failure. Furthermore, the resonant capacitors, C_p and C_s should be rated for the nominal power. Therefore, the size, rating, and cost of the resonant network are similar to a conventional high-power WPT system.

To address the associated issues with high-power wireless charging, a new modular inverter based on an LCC resonant network is proposed in this chapter. By using the proposed modular topology, no ICT is required for surpassing the circulating current.

The proposed modular system is compared with a conventional high-power wireless charging system from different aspects. The proposed system showed a better component rating, lower resonant element energy, and lower kVA/kW ratio which is an indicator of the higher power density. The proposed modular topology is simulated and the performance of the proposed topology is evaluated under different operating conditions.

6.2. The Proposed Modular Resonant Network

The proposed structure is shown in Fig. 6-3. The objective of the proposed structure is to have a modular resonant network that can be used to scale the output power of the WPT system.

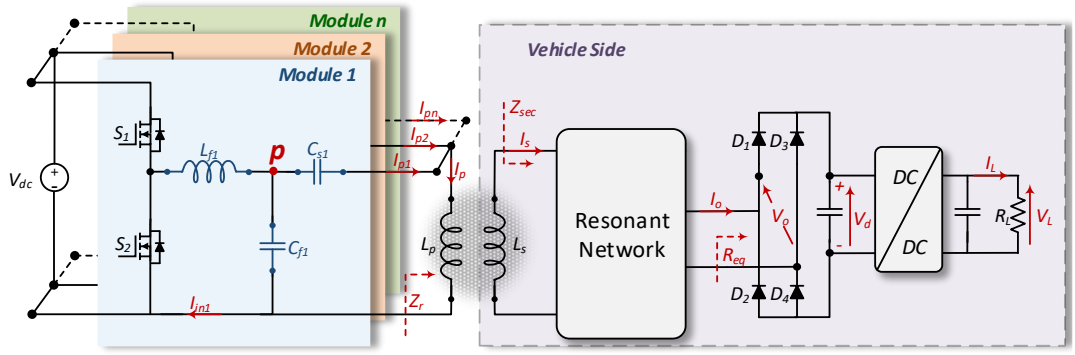

Fig. 6-3. The proposed modular resonant network for high-power wireless charging application.

In the proposed structure, the legs of the inverter are connected to an LCC network and the output of the LCC modules are connected in parallel to feed the transmitter side coil. Due to the current source behavior of the LCC network, the

output current of the LCC modules is constant and independent of the loading condition. Therefore, the transmitter coil current, I_p, is equal to the sum of the output currents of the LCC modules.

In the following, the tuning of the resonant network will be discussed and the problem of current sharing will be addressed.

6.3. Resonant Network Tuning

In a modular topology with n legs, each LCC network is connected to the primary side coil. Therefore, it can be assumed that each LCC network feeds $n \times L_p$ inductor and the total value of these parallel inductances would be equal to the primary side self-inductance, L_p. Therefore, at the resonant frequency the following equations should be satisfied for each LCC network:

$$C_f = \frac{1}{\omega^2 L_f} \tag{5.1}$$

$$C_s = \frac{1}{\omega^2 (n \times L_p - L_f)} \tag{5.2}$$

where n is the number of cells and ω is the angular operating frequency of the inverter. The value of the resonant inductor, L_f, should be selected according to the required output power or primary side coil current. An interesting point to design the series capacitor C_s is that n, the number of modules, is located in the

denominator of the C_s in (5.2). Therefore, the C_s value decreases as the number of modules increases. This reduction of the required capacitance for each module will help to reduce the cost of the design.

Assuming all the modules has identical components and neglecting the parasitic elements, the transmitter side circuit of each module can be described by:

$$\begin{aligned} V_{in} &= \left(L_{fi}\omega j + \frac{1}{C_{fi}\omega j}\right) I_{ini} - \left(\frac{1}{C_{fi}\omega j}\right) I_{pi} \\ 0 &= \left(\frac{-1}{C_{fi}\omega j}\right) I_{ini} + \left(\frac{1}{C_{fi}\omega j} + \frac{1}{C_{is}\omega j} + n\left(L_p\omega j + Z_r\right)\right) I_{pi} \end{aligned} \tag{5.3}$$

where I_{ini} is the inverter leg current of module i, I_{pi} is the generated output current of the LCC module i, and Z_r is the reflected impedance of the receiver side circuit to the primary side which is given by:

$$Z_r = \frac{M^2\omega^2}{Z_{\text{sec}}}. \tag{5.4}$$

Z_{sec} is the secondary side circuit impedance. By solving (5.3) at the resonant condition, I_{ini} and I_p can be defined by:

$$I_{ini} = \left(C_{fi} n Z_r \omega j\right) I_{pi} \tag{5.5}$$

$$I_{pi} = \left(-C_{fi}\omega j\right) V_{in} = \frac{V_{in}}{j\omega L_{fi}} \tag{5.6}$$

$$I_p = \sum I_{pi} = n \times \frac{V_{in}}{j\omega L_f} \tag{5.7}$$

where I_{pi} is the output current of each LCC network.

It can be seen that the primary side coil current, I_p, is load-independent and its value is only dependent on the selected resonant inductor, L_f. Therefore, the current source feature of the LCC network is realized at the resonant frequency.

6.3.1. Current Sharing

In practice, the resonant elements can have some manufacturing error or their value deviates from the nominal value due to temperature changes. These changes in the component's values can cause imbalanced current sharing between the modules. Therefore, it is essential to study the effect of the component tolerance on the current sharing between the modules.

The multi-parallel LCC network on the primary side is studied here using the features of the two-port networks. In this analysis, the effect of each resonant element of the LCC network on the module input and output current is investigated. Here, it is assumed that there is no delay between the inverter legs.

A. Generalized Model

For a general system with n modules, the total admittance matrix, Y_t is given by:

$$[Y_t] = \sum_{i=1}^{n} [Y_i] \tag{5.8}$$

where Y_i is the admittance matrix of module i. For each module, the Y parameters can be calculated by using the impedance matrix, Z, as follows:

$$[Y_i] = [Z_i]^{-1} \tag{5.9}$$

$$[Z_i] = \begin{bmatrix} L_{fi}\omega j + \dfrac{1}{C_{fi}\omega j} & \dfrac{-1}{C_{fi}\omega j} \\ \dfrac{-1}{C_{fi}\omega j} & \dfrac{1}{C_{fi}\omega j} + \dfrac{1}{C_{is}\omega j} \end{bmatrix}. \tag{5.10}$$

In this system, the relation of the input and output current of parallel networks and each module can be expressed by:

$$\begin{bmatrix} I_{in} \\ I_p \end{bmatrix} = [Y_t] \begin{bmatrix} V_{in} \\ V_p \end{bmatrix} \tag{5.11}$$

$$\begin{bmatrix} I_{ini} \\ I_{pi} \end{bmatrix} = [Y_i] \begin{bmatrix} V_{in} \\ V_p \end{bmatrix} \tag{5.12}$$

where I_{ini} is the module input current and V_p is the primary side voltage (voltage of the coil terminals) defined by:

$$V_p = Z_p I_p = \left(j\omega L_p + Z_r\right) I_p \tag{5.13}$$

where Z_p is the impedance seen by the LCC network. By substituting (5.13) and (5.10) into (5.12), the input current of each module (inverter leg current) and the LCC output current, I_{pi} can be calculated.

In order to consider the tolerance of the components and its effect on current sharing a deviation factor for each parameter of the LCC network is assumed as follows:

$$\begin{aligned} L_{fi} &= \alpha_i L_f \\ C_{fi} &= \beta_i C_f \\ C_{is} &= \gamma_i C_s \end{aligned} \tag{5.14}$$

where L_f, C_f, and C_s are the designed resonant elements tuned at the resonant frequency. It is assumed that the first module has $\alpha_1=\beta_1=\gamma_1=1$. Without losing the generality, two parallel modules are studied here:

B. Two Parallel Modules

In this case, n is equal to 2 and there are only three deviation factors for the second module. According to the presented analysis, the input and output current of the first module is calculated as:

$$\begin{bmatrix} I_{in1} \\ I_{p1} \end{bmatrix} = \begin{bmatrix} \dfrac{V_{in}}{j\omega L_f}\left[\left(1+\dfrac{\left(2L_p-L_f\right)}{L_f}\right)+\dfrac{Z_p\left(\dfrac{j}{\omega L_f}-\dfrac{\gamma_2}{\sigma_1}\right)}{\dfrac{\gamma_2\left(\alpha_2\beta_2-1\right)Z_p}{\sigma_1}+1}\right] \\ \dfrac{V_{in}}{j\omega L_f} \end{bmatrix}. \tag{5.15}$$

It can be seen that the deviation of the second module parameters can affect the input current of the first module too. Similarly, the input and output current of the second module is calculated as:

$$\begin{bmatrix} I_{in2} \\ I_{p2} \end{bmatrix} = \begin{bmatrix} \dfrac{V_{in}}{\omega}\left[\dfrac{\left(\dfrac{\beta_2}{L_f}+\dfrac{\gamma_2}{\left(2L_p-L_f\right)}\right)}{\sigma_3}+\dfrac{Z_p\gamma_2\left(\dfrac{j}{\omega L_f}-\dfrac{\gamma_2}{\sigma_3\omega\left(2L_p-L_f\right)}\right)}{\sigma_2}\right] \\ \dfrac{V_{in}\gamma_2}{\omega\left(2L_p-L_f\right)\sigma_2}-\dfrac{V_{in}\left(\dfrac{j}{\omega L_f}-\dfrac{\gamma_2}{\sigma_4\left(2L_p-L_f\right)}\right)\left(\alpha_2\beta_2-1\right)Z_p}{\sigma_2} \end{bmatrix} \tag{5.16}$$

where:

$$\begin{aligned} \sigma_1 &= j\omega\left(2L_p-L_f\right)\left(\alpha_2\beta_2+\frac{L_f\alpha_2\gamma_2}{\left(2L_p-L_f\right)}-1\right) \\ \sigma_2 &= j\omega\sigma_1\left(\frac{\gamma_2\left(\alpha_2\beta_2-1\right)}{\omega\left(2L_p-L_f\right)\sigma_3}+1\right) \\ \sigma_3 &= \sigma_1 \,/\, j\left(2L_p-L_f\right). \end{aligned} \tag{5.17}$$

It can be seen that when $a_2.\beta_2$ is equal to 1, the effect of mistuned C_{is} (γ_2) on the current will be eliminated. This will happen because, at this condition, the mistuned L_f and C_f on the second module are operating at resonant too ($a_2L_f.\beta_2C_f = 1/\omega^2$). Therefore, the output current of the mistuned LCC network is not dependent on the output load. However, if these values are not unity or $a_2.\beta_2 \neq 0$, all the deviation factors affect the current sharing of the parallel modules. Moreover, if $a_2=\beta_2=\gamma_2=1$, all the equations presented in Section 6.3 will be achieved.

To solve this issue, a passive current sharing method can be used [157]. This method can be simply applied to this modular structure by connecting point P of

all the cells as shown in Fig. 6-3. In this circuit, any difference between the values of resonant capacitors will not affect the power-sharing between the phases of the inverter. In this case, the impedance seen by each inductor is the parallel network of the $Z_p \,||\, \sum C_{fi}$. Therefore, the voltage of the capacitor C_{fi}, and output current of the modules, I_{pi} would be all equal to I_p/n. Consequently, the voltage of the series capacitors, C_{is} would be equal too. The effectiveness of this method will further be evaluated in Section 6.4.

6.3.2. Output Characteristics

For transportation applications, typically an LCC resonant topology is adopted on the primary side due to its outstanding performance. On the secondary side of the WPT system, two cases can be considered: LCC-LCC or LCC-S [154]. Both LCC and Series resonant topologies on the vehicle-side show a high-efficiency profile for the whole output power range and show a good constant output current and constant voltage, respectively. In this chapter, the LCC-LCC topology is selected; however, this modular transmitter side can be extended to other vehicle side topologies such as LCC-S.

For a given output voltage, and assuming perfect tuning, the output power of a conventional LCC-LCC (P_{out}) topology can be expressed by [38]:

$$P_{out} = \frac{M}{\omega L_f L_b} V_{in} V_o \tag{5.18}$$

where L_f, and L_b are the resonant inductors of the LCC networks on the primary and secondary side, respectively. M is the mutual inductance between the primary and secondary.

The parameters of the LCC-LCC resonant network can be designed according to (5.18) assuming L_f=L_b. In a modular WPT system for given output power, input and output voltage, the value of L_f and L_b can be designed as follows:

$$L_{fi} = \sqrt{\frac{M}{\omega \frac{P_{out}}{n}} V_o V_{in}} \tag{5.19}$$

$$L_b = \sqrt{\frac{M}{\omega P_{out}} V_o V_{in}} = \frac{1}{\sqrt{n}} L_{fi} \tag{5.20}$$

It can be seen that each LCC module of the primary side is designed for $1/n$ share of the total power and the LCC of the secondary side will be designed for the total power. In the case of using a module LCC network on the secondary side, the value of L_f=L_b can be used and the inductance can be calculated according to (5.20). According to (5.19), the value of the required inductance as the power level increases will be reduced. On the other hand, as the number of modules, n,

increases, the required inductance will be increased by the factor of $\sqrt{n}$, compared to the conventional single-cell LCC-LCC topology.

The value of resonant capacitors can be calculated according to (5.1), and (5.2) Similarly, the secondary side resonant capacitors can be selected, assuming n=1. The current of the inductor (I_{Lfi}=I_{ini}) and voltage of the resonant capacitors on the primary side is calculated as follows:

$$I_{ini} = \frac{M}{\omega\sqrt{n}L_{fi}L_b}V_o \tag{5.21}$$

$$V_{C_{fi}} = \left|V_{in} - j\omega L_{fi}I_{ini}\right| \tag{5.22}$$

$$V_{C_{si}} = \left|\frac{I_{pi}}{j\omega C_{si}}\right| = \frac{V_{in}}{\omega^2 n L_{fi}C_{si}} \tag{5.23}$$

It can be seen that as the number of parallel LCC modules on the primary side increases, the current of the inductor reduces $1/\sqrt{n}$. Moreover, for a given output power value, as the number of modules increases, the value of L_{fi} increases by a factor of $\sqrt{n}$; therefore, the inductor current rating will be reduced by $1/n$.

6.4. Design and Simulation Studies

6.4.1. Design

A modular structure can help to reduce the manufacturing cost, rating of the resonant elements and semiconductor devices, and cost of the devices. Moreover, a modular structure increases the reliability, flexibility, and scalability of the system. In this part, a comparison between the proposed modular topology and the conventional system and the design procedure of the proposed modular system are presented.

In this analysis, the values of the output voltage (V_{out}), input voltage (V_{dc}), magnetic coupler parameters, nominal coupling factor, and the number of paralleled modules are known parameters and the output power will change. The magnetic coupler is a rectangular type with the nominal coupling factor of k_n=0.32. It is assumed that the input DC voltage is 900 V, and the nominal output voltage is 800 V. It should be noted that at each power rating the designed values of the resonant elements are identical for any number of the modules except the primary side series capacitor, C_{si}. Therefore, the values of the resonant elements for each power level are selected.

Besides the switch and inductor current rating, and rated voltage of the resonant capacitors, the total energy of the resonant inductor (E_{Lp}) and resonant capacitors (E_{Cp}) of the primary side are considered as follows:

$$E_{Lp} = n.\left(\tfrac{1}{2} L_{fi} I_{ini}^2\right) \tag{5.24}$$

$$E_{Cp} = n.\left(\tfrac{1}{2} C_{fi} V_{Cfi}^2 + \tfrac{1}{2} C_{si} V_{Csi}^2\right) \tag{5.25}$$

Similarly, the energy of the resonant capacitors and inductors of the vehicle side LCC network can be calculated. The energy of the resonant inductor is proportional to the physical size of the inductor [41]. Therefore, the lower energy of the resonant inductor is preferable to achieve higher power density designs. Similarly, the apparent power rating of the resonant components to the total output power of the system (kVA/kW) can be considered as an index of the physical size of the resonant networks defined by [41]:

$$r_n = n.\omega.\left(L_{fi} I_{ini}^2 + C_{fi} V_{Cfi}^2 + C_{si} V_{Csi}^2\right) / P_{out} \tag{5.26}$$

Two steps are considered:

- Determining the module power rating
- Determining the number of the modules

6.4.2. Determining the Module Power Rating

At first, the conventional LCC-LCC (n=1) is compared with a modular LCC-LCC topology with a different number of the LCC modules on the primary side (n=2, 3, 4). In this analysis, the input and output voltage, and output power is the same for all the WPT systems. In this section, the power rating is changed and consequently, the values of the resonant networks are changed. Fixed power rating of the modules will be considered in the next step. In the following, different aspects of the modular and conventional WPT systems are compared:

A. Device Rating

Fig. 6-4 shows that for designing a system for a given total output power how the rating of the component will change as the number of modules increases. According to Fig. 6-4, the input currents of the modular systems are $1/n$ of the conventional WPT systems as expected. Therefore, the inverter switches current rating and resonant inductor current rating are $1/n$ of the conventional system. It should be noted that since the resonant topologies are operating at the perfect resonance mode, the input phase angle is zero.

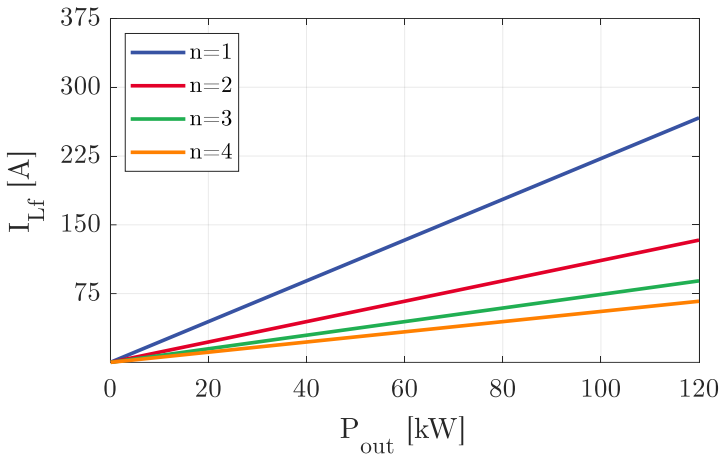

Fig. 6-4. Comparison of the input current rating (inverter, and inductor current).

The voltage rating of the parallel resonant capacitor, C_f is calculated according to (5.22) and the results are shown in Fig. 6-5. It can be seen that the voltage rating of C_f is reduced as the number of the modules increased at each power rating.

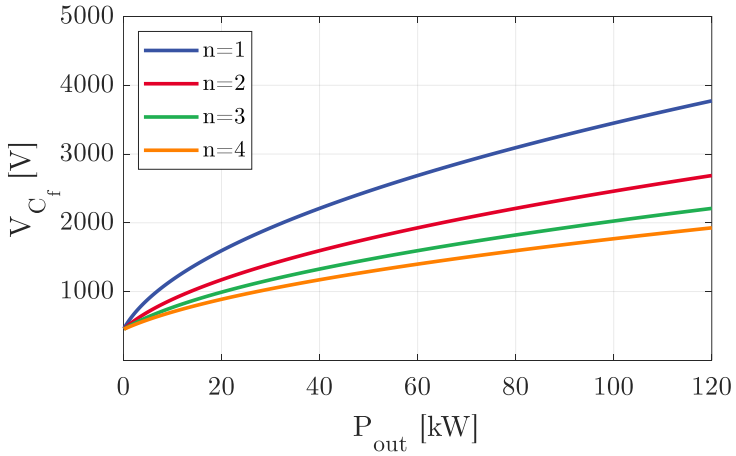

Fig. 6-5. Comparison of the parallel resonant capacitor voltage rating.

The voltage rating of C_s is also calculated versus the variation of the nominal output power and the results are shown in Fig. 6-6. It can be seen that the voltage rating of the series primary side capacitor versus output power is increased as the number of the parallel modules increased. Because at each power rating, by increasing the number of the modules, the value of this capacitor will be reduced. For the same current flowing through the capacitor, the voltage rating of the capacitor will be increased consequently.

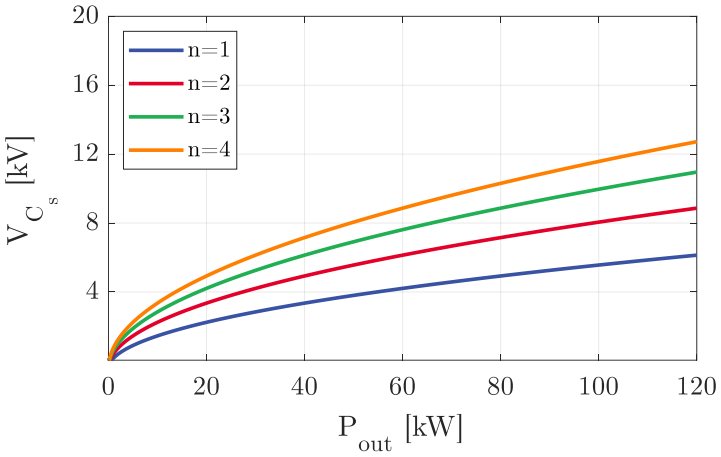

Fig. 6-6. Comparison of the series resonant capacitor voltage rating.

B. Components Energy

The inductor energy is calculated according to (5.24) and the results are presented in Fig. 6-7 for a different number of modules.

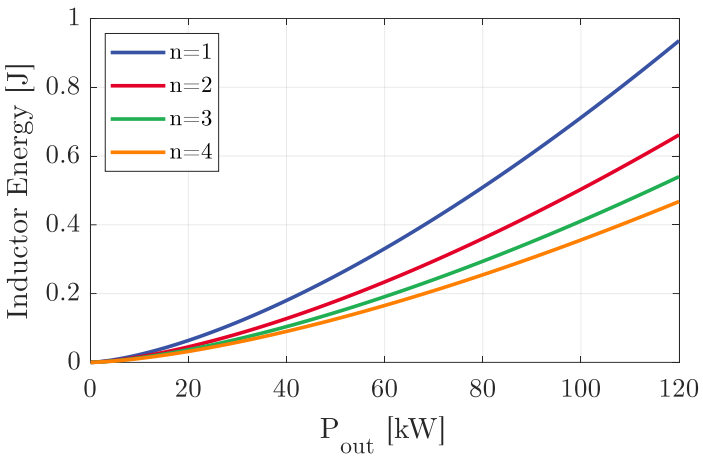

Fig. 6-7. Comparison of the resonant inductor energy (E_{Lp}).

It can be seen that due to the reduction of the input current, the energy of the resonant inductor is reduced as expected. Similarly, the total energy of the primary side resonant capacitors, E_{Cp}, is calculated and the results are presented in Fig. 6-8.

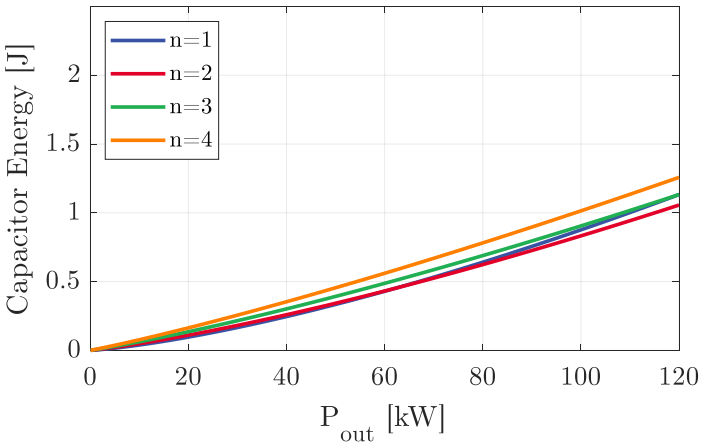

Fig. 6-8. Comparison of the resonant capacitor energy (E_{Cp}).

C. Apparent Power to Real Power Ratio

The apparent power ratio to the output power of the resonant topologies is compared in Fig. 6-9. It can be seen that as the nominal output power increases the kVA/kW ratio of the conventional and modular topologies increases. Moreover, it can be seen the conventional LCC-LCC topology is showing better performance for low power rating below a specific point (15 kW) by gaining lower r_n values. The two-cell LCC network performed better than the conventional system from 15 kW up to 80 kW. Above 80 kW, the modular topology with three LCC networks outperforms the other designs.

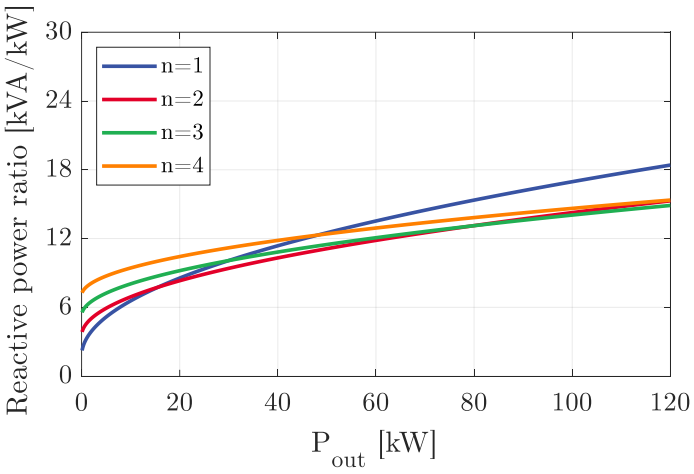

Fig. 6-9. Comparison of the rating of the components between the conventional WPT system with modular LCC topology with a different number of cells.

From the designer's perspective, it can be concluded that the maximum power rating in which the conventional design is performing better than modular structures should be selected as the module power rating. In this example, the

optimal power rating of the module is around 15-20 kW. Although this analysis can help the designer to select an optimal power rating for the modules, other parameters such as cost, availability of the components (such as switches, capacitors, etc.), and thermal concerns should be considered.

6.4.3. Determining the Number of Modules

Although Fig. 6-10 presents a comparison of the conventional topology and modular topologies designed for specific output power, it does not reflect the modularity of the system. In order to evaluate the modularity of the proposed LCC-based WPT system, fixed values of the module power should be considered. In practice, the manufacturer would select the power rating of each cell based on the cost, availability of the components, and thermal concerns. In this case, an LCC module with a fixed power rating of 20 kW is designed. In this part, all the resonant parameters are fixed except C_{si} which should be changed with the number of modules and according to (5.2).

Fig. 6-10 illustrates the comparison between the conventional (n=1) and modular topologies designed for 20 kW. It can be seen that the current of the switch (inductor current) is reduced by increasing the number of modules.

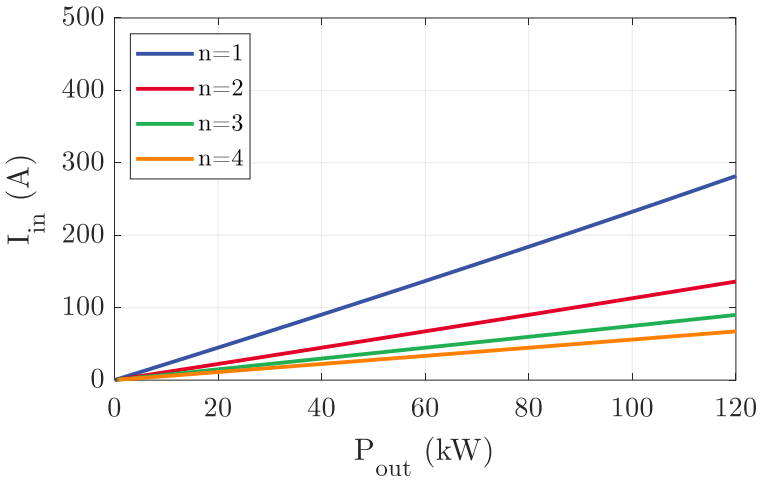

Fig. 6-10. Comparison of the input current of different number of modules designed for specific power versus total output power.

According to (5.7), the coil current is the sum of the LCC modules output currents (I_{pi}). Fig. 6-11 shows the primary side coil current. It can be seen that I_{pi} increased as the number of the modules increased. However, the value of the current is not affected by increasing the output power; because the LCC network operates as a current source independent of the loading condition.

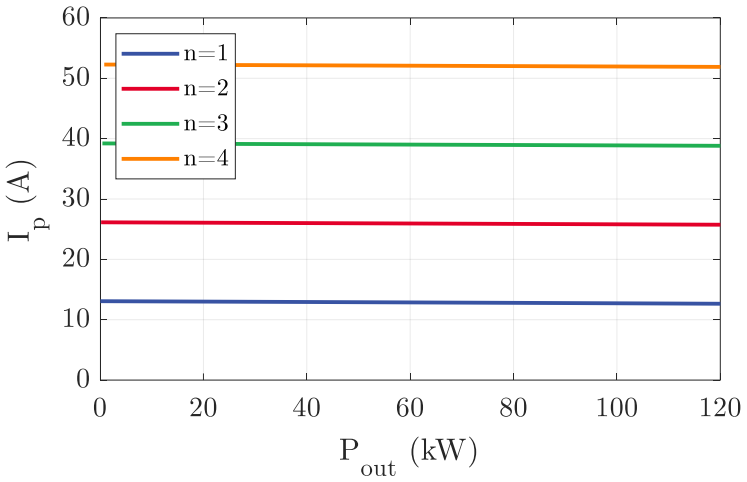

Fig. 6-11. Comparison of the transmitter coil current of different number of modules designed for specific power versus total output power.

To realize ZVS for the inverter switches, the impedance seen by the inverter should have an inductive characteristic. The input impedance phase angle is calculated and the results are shown in Fig. 6-12. It can be seen that the conventional LCC-LCC network stays in the inductive region (positive phase angle) for the whole operating region. Similarly, the modular topologies showed a positive input impedance phase angle.

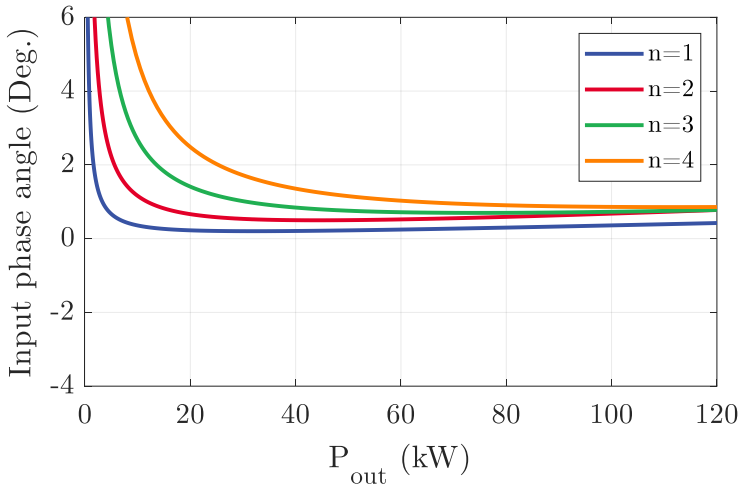

Fig. 6-12. Comparison of the input phase angle of different number of modules designed for specific power versus total output power.

Finally, the efficiency of the WPT system versus output power is presented in Fig. 6-13. According to this figure, at low power applications, up to 32 kW, the efficiency of the system with a single LCC module designed for 20 kW is superior. However, as the total power increases, the system with two modules (each rated for 20 kW) is performing at higher efficiency compared to the other topologies. Similarly, as the output power reaches a specific point (96 kW), the efficiency of the system with three modules would be the highest. This can be concluded, when the modules are designed for specific rated power, there is an optimal operating range according to the number of the modules.

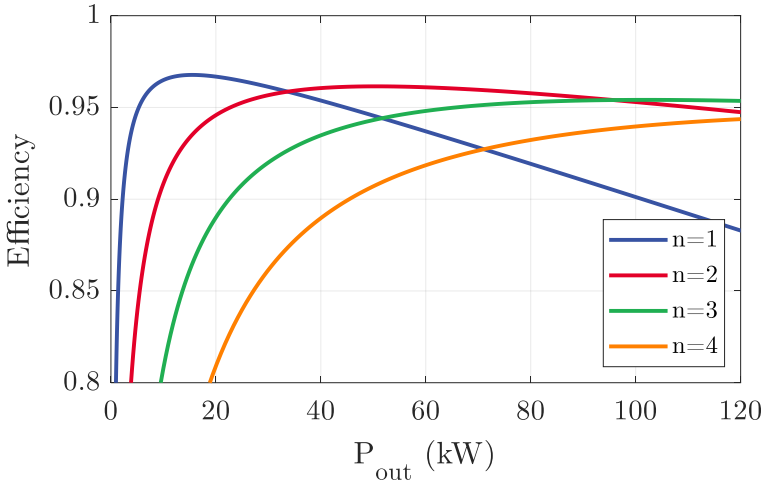

Fig. 6-13. Comparison of the efficiency profile of different number of modules designed for specific power versus total output power.

6.5. Current Sharing

To investigate the current sharing between the modules in the case of the resonant component tolerance. The analysis of these deviation parameters is studied in Section 6.3. Here, a time-domain simulation of a 22kW/85 kHz LCC3-LCC modular system with three modules on the primary side (n=3) is presented.

Fig. 6-14 (a) and (d) show the inverter current and primary side currents under normal operation of the system. It can be seen that the I_p is the sum of the LCC modules output current (I_{pi}) which is according to (5.7). To study the current sharing of the system due to component tolerance, the value of the parallel resonant

capacitor, C_{f1} (first module) is increased by 5%, and the inverter currents and LCC modules currents are shown in Fig. 6-14 (b) and (e), respectively.

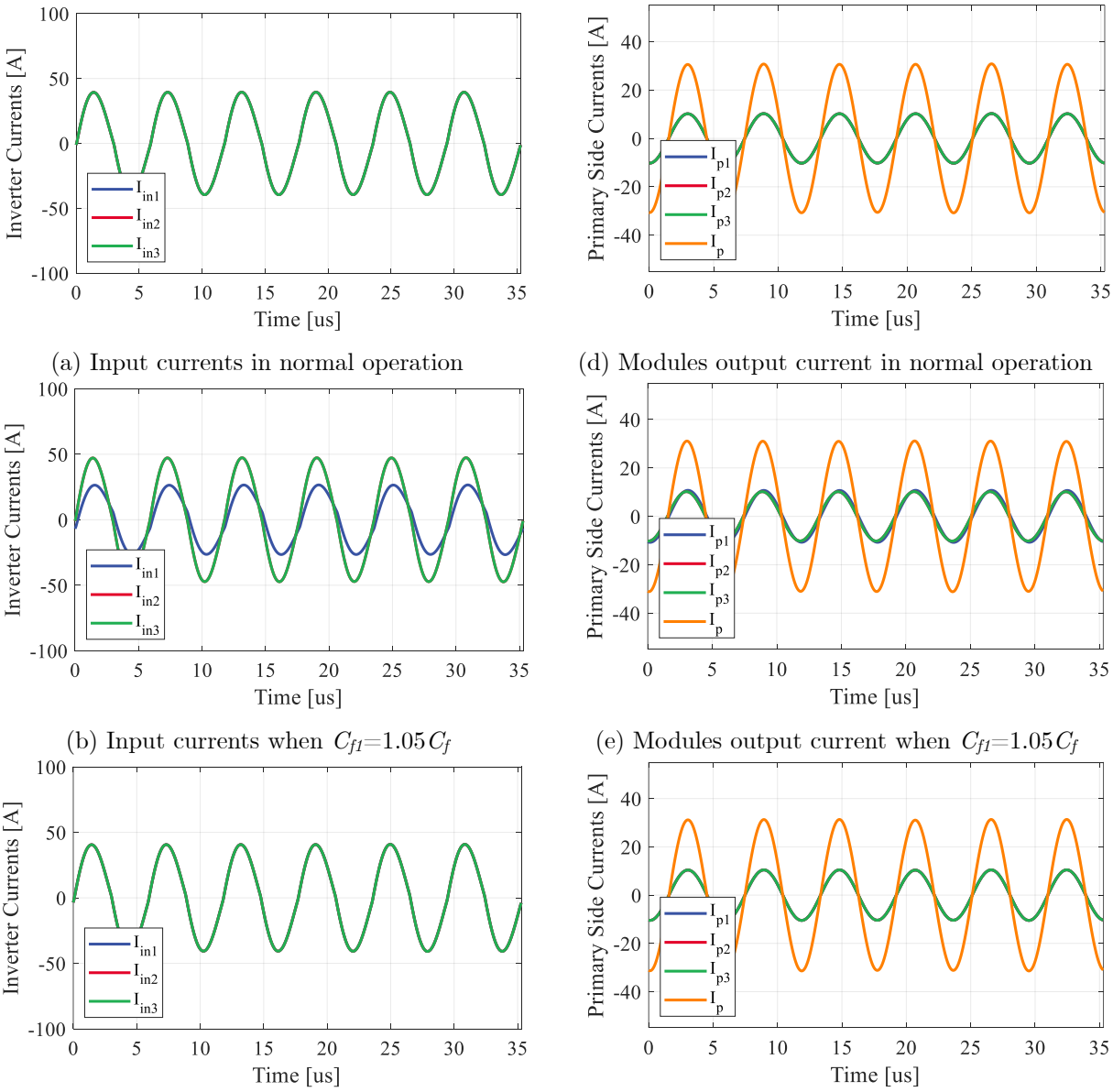

(a) Input currents in normal operation

(d) Modules output current in normal operation

(b) Input currents when C_{f1}=1.05C_f

(e) Modules output current when C_{f1}=1.05C_f

(c) Input currents with passive current sharing when C_{f1}=1.05C_f

(f) Modules output current with passive current sharing when C_{f1}=1.05C_f

Fig. 6-14. Current sharing of the modular WPT system in case of component tolerance in one module.

It can be seen that the first module's input current (I_{in1}) is decreased compared to the normal operation. Additionally, the input current of the other two modules increased to compensate for the reduction of the input power. Similarly, the primary side coil currents are shown in Fig. 6-14 (e). It can be seen that the changes in the amplitude of the currents are negligible; however, the output current of the first module (I_{p1}) showed a small phase difference compared to the other modules.

To solve the current sharing issue due to component tolerance, a passive current sharing method is used as discussed in Section 6.3.1. The inverter current and LCC modules output currents are shown in Fig. 6-14 (c) and (f). It can be seen that the inverter currents and output currents are balanced and there is no phase shift between the currents. This can be concluded that the proposed passive current sharing method can effectively, eliminate the issue of component tolerance.

6.6. Modular Magnetic Structure

An extended version of the proposed modular structure is presented here. In this system, the single-phase magnetic coupler is replaced by a decoupled magnetic structure. Therefore, the total power rating can be scaled up. The proposed fully-modular system is shown in Fig. 5-15. In this structure, the magnetic couplers should be decoupled from each other to avoid any interreference between the modules.

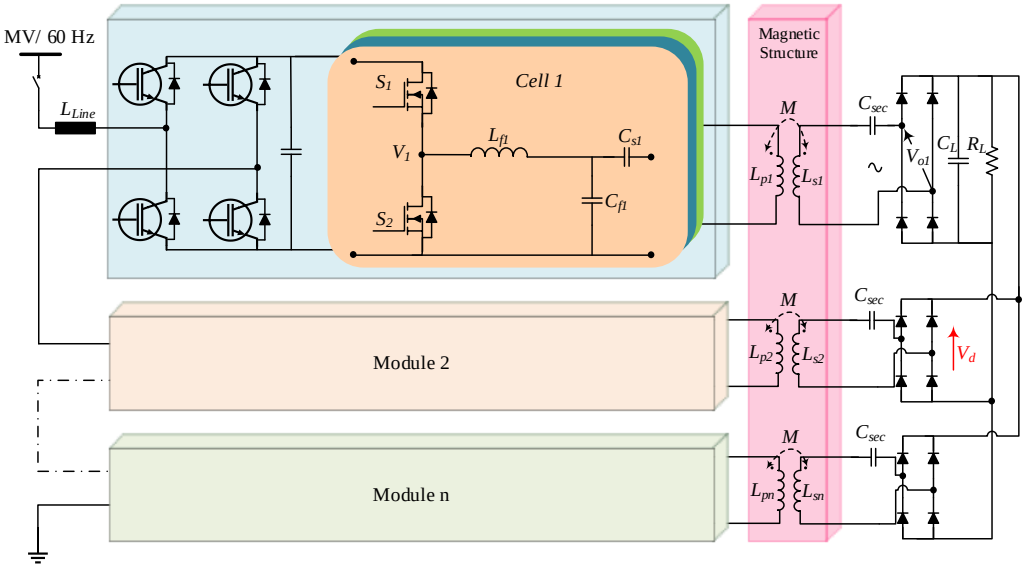

Fig. 6-15. Proposed modular system with modular inverter and modular magnetic structure.

6.6.1. Magnetic Coupler Design

In order to study the decoupling feature and design procedure, at first a one primary to two decoupled secondaries with overlapped coils is modeled. In this magnetic coupler a ferrite plate is placed and the 3D model is shown in Fig. 6-16. The coupling factor between the primary side and receiver coils and the coupling factor between the receivers are shown in Fig. 6-17 respectively. It can be seen that at 100 mm spacing between the centers of the receiver coils their mutual coupling is zero. At this point, the coupling factor between the primary and receiver coils is around 0.24. It can be concluded that by applying a specific distance between the coils a null point can be find where the mutual coupling between the receivers is eliminated.

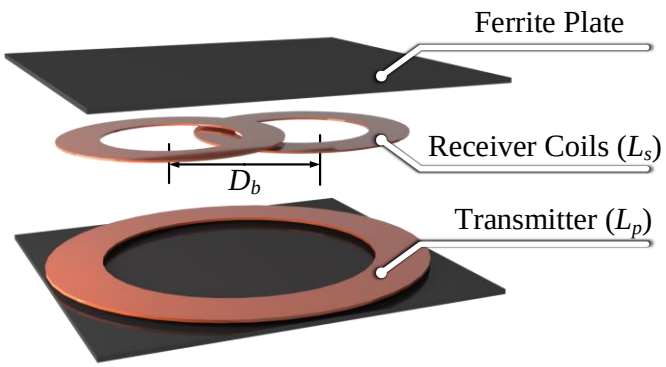

Fig. 6-16. One-primary and two-secondary magnetic structure with a full ferrite cover.

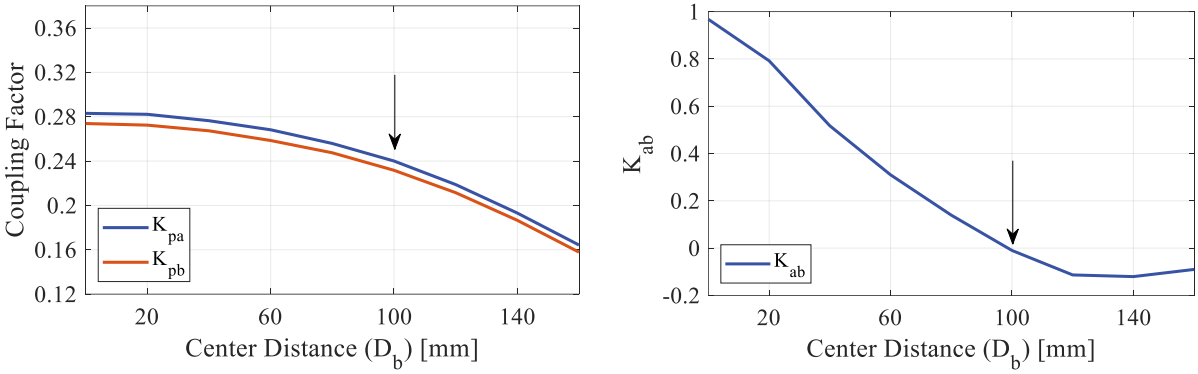

(a) Between the primary and receiver coils (b) Between the receiver coils

Fig. 6-17. FEA results of the overlapped one-transmitter two-receiver magnetic coupler.

Similarly, a one-transmitter and three-receiver magnetic coupler with overlapped configuration is modeled. The 3D model and FEA results are presented in Fig. 6-18 and Fig. 6-19, respectively. According to Fig. 6-19 (b) there is a null point that the mutual inductance between the three receiver coils is zero. The corresponding point of the coupling factor between the transmitter and receivers is also shown in Fig. 6-19 (a). It can be seen that by increasing the distance of the coils from the center of the structure, the main coupling factor between the

transmitter and receiver coils decreases. Moreover, the coupling factor of the three-receiver coil structure is lower than the two-receiver coil at the null point.

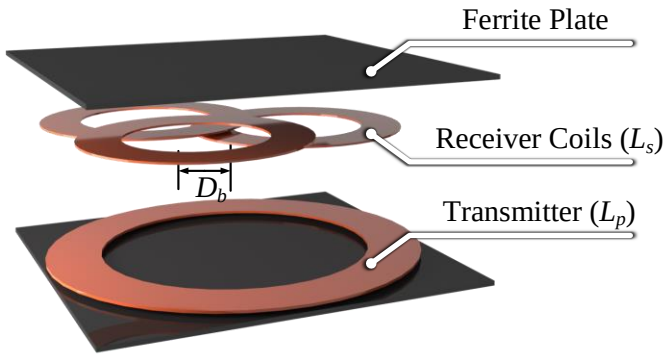

Fig. 6-18. One-primary and Three-secondary magnetic structure with a full ferrite cover.

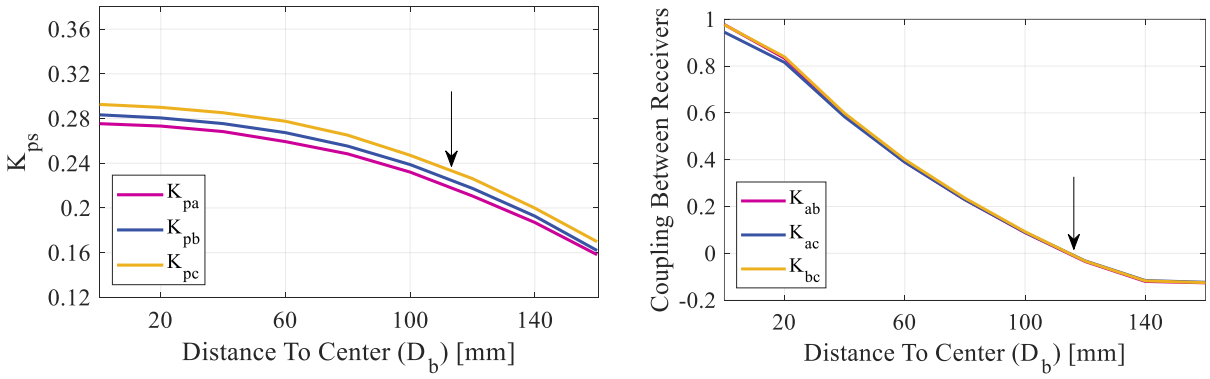

(a) Between the primary and receiver coils (b) Between the receiver coils

Fig. 6-19. FEA results of the overlapped one-transmitter three-receiver magnetic coupler.

By using this feature, a three transmitter and three-receiver coil structure is modeled in as shown in Fig. 6-20. Similarly, the distance of the center of the transmitter and receiver coils from the center of the ferrite pad is changed to find the null point. FEA results of the coupling factor between the primary and secondary side coils and between the secondary side coils are shown in Fig. 6-21 (a)

and (b), respectively. According to Fig. 6-21 (b), the null point is achieved by applying 110 mm spacing to the center of the ferrite plate. At this point the coupling factor between the primary and secondary is not affected because of having three coils on the transmitter side. Compared to the one-primary configuration the value of the nominal coupling factor at the null point is larger which helps to increase the power level, quality factor of the coil and efficiency of the system.

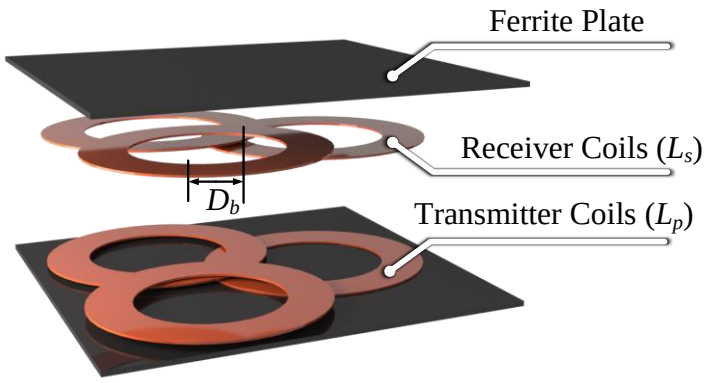

Fig. 6-20. Three-primary and three-secondary magnetic structure with a full ferrite cover.

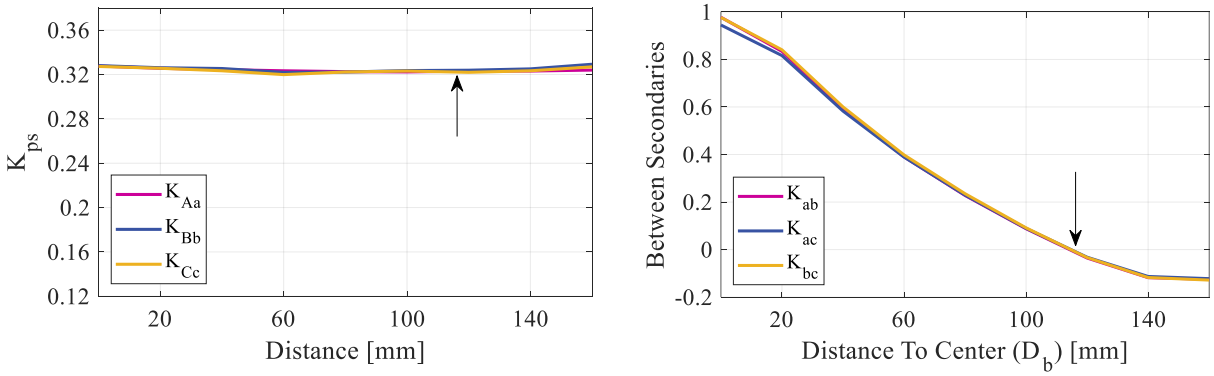

(a) Between each primary and receiver coils (b) Between the receiver coils

Fig. 6-21. FEA results of the overlapped three-transmitter three-receiver magnetic coupler.

6.6.2. Loss Analysis and Optimization

Since the proposed magnetic structure offers a decoupled transmitter and receiver coils, different phase angles can be considered for excitation of the transmitters. In order to present a more practical analysis, ferrite plate is replaced by the ferrite bars as shown in Fig. 6-22. At first, the phase angle of the excitation currents is assumed to be zero. The core loss and maximum amplitude of the magnetic field density (B) for a 20 A maximum current is shown in Fig. 6-23.

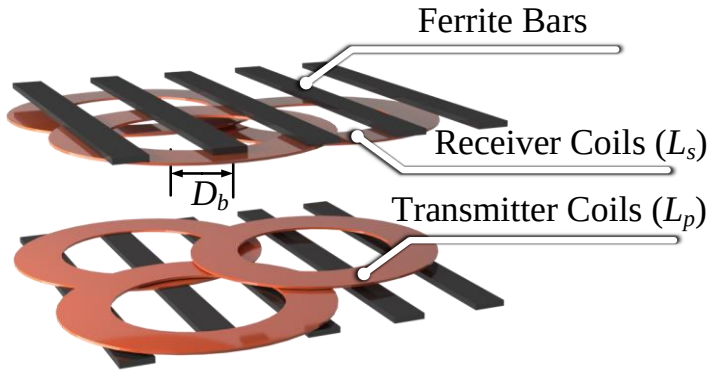

Fig. 6-22. Three-primary and three-secondary magnetic structure with ferrite bars.

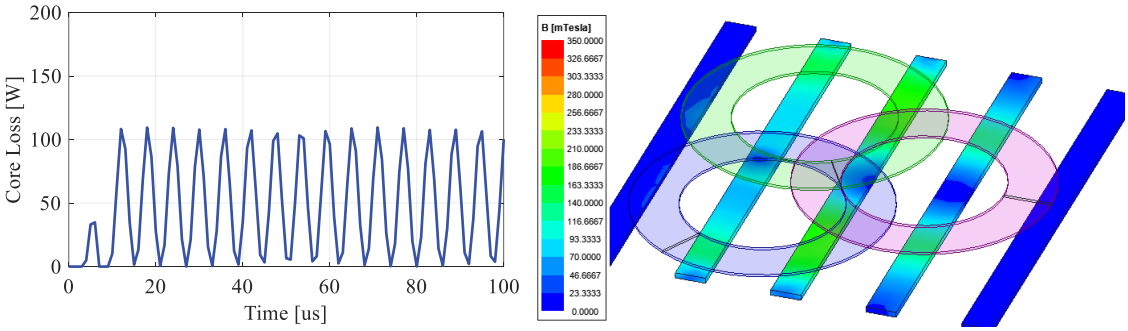

(a) Core loss whith no phase angle (b) Magnetic field density whith no phase angle

Fig. 6-23. FEA results of the overlapped three-transmitter three-receiver magnetic coupler with magnetic bars.

In the next step, the phase angle between the phase set to 120 ° to compare the losses and amplitude of the magnetic field density. The FEA results of this case are shown in Fig. 6-24. Compared to the previous case, the amplitude of the magnetic field density and core loss increased. In order to find the optimal phase angle of the excitation currents, the phase angles changed between 0 to 180 and the results are shown in Fig. 6-25. It can be seen that the when β and θ are equal to 1.8 rad the average loss of the magnetic structure is minimized. As discussed before, the phase angles of the excitation currents can be applied independently due to the decoupling of the adjacent coils. Moreover, the magnitude of the field magnetic density is decreased compared the two previous cases.

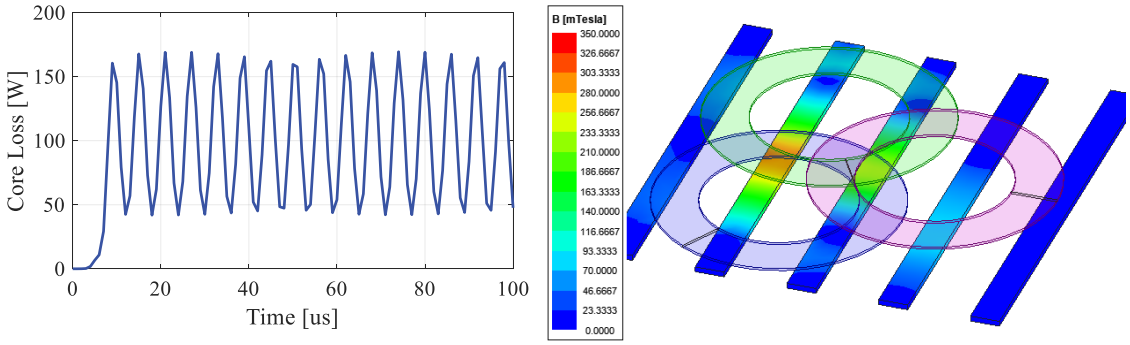

(a) Core loss with 120 ° phase angle differnece

(b) Magnetic field density with 120 ° phase angle differnece

Fig. 6-24. FEA results of the overlapped three-transmitter three-receiver magnetic coupler with magnetic bars.

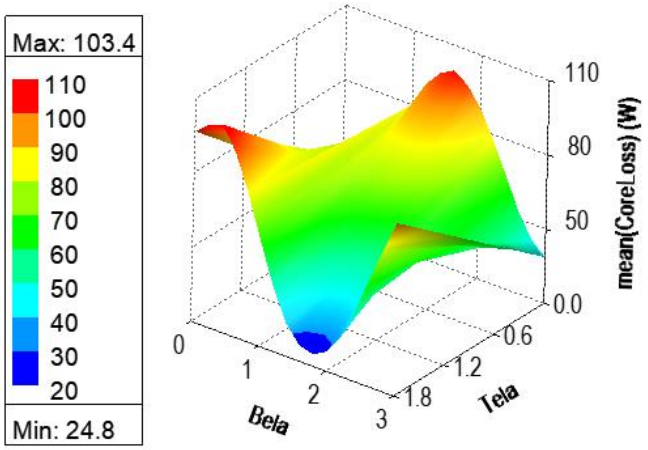

Fig. 6-25. Core loss versus the phase angle of the modules for a three-coil transmitter.

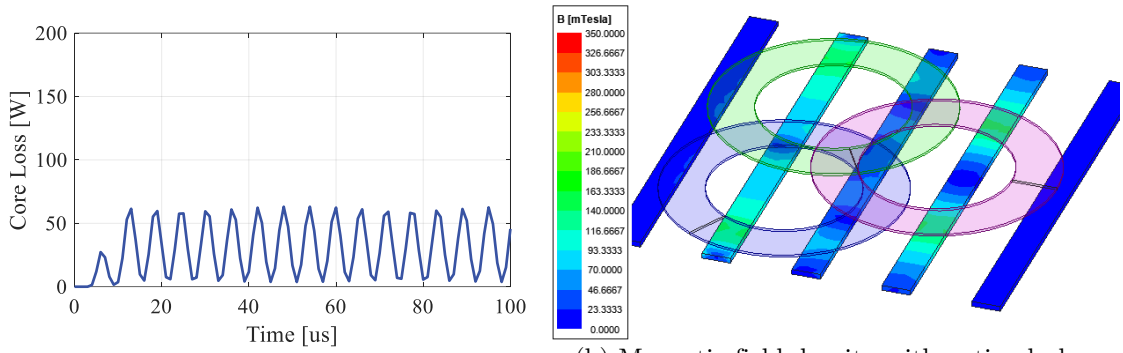

(a) Core loss with optimal phase angle

(b) Magnetic field density with optimal phase angle

Fig. 6-26. FEA results of the overlapped three-transmitter three-receiver magnetic coupler with magnetic bars.

6.7. Experimental Results

A scaled-down wireless power transfer system is implemented. However, the design principle of the modular design is the same for different power ratings. A modular LCC network with three LCC parallel networks is designed. Each module is designed for 500 W to deliver 1.5 kW at full load conditions.

In this setup, the magnetic coupler is a rectangular coil made by 500 strands of AWG 38 Litz wire. The transmitter and receiver side coils are identical with 20 turns on each side. The total dimension of the magnetic coupler is 510×510 mm^2. Five ferrite bars are placed in the back of the magnetic coupler. The ferrite core is N87 from EPCOS and its dimension is 510×38×70 mm^3. The nominal coupling factor, k_n, is around 0.32 at the nominal air-gap of 125 mm.

The transmitter converter is made of three half-bridge inverters and each half-bridge is supplying one module. The inverter is built by IPW65R037C6 *CoolMOS* and the gate signals are generated by TMS320F28379D DSP. The inductor of the LCC network is constructed by an E-type ferrite core and the resonant capacitors are 2 kV metalized polypropylene film capacitors made EPCOS. Fig. 6-27 shows the experimental setup of the proposed modular system.

At first, the normal operation of the proposed modular system is studied. In this case, the system is operating at the full-load condition and the resonant networks of the modules are identical. The first leg inverter voltage (V_{in1}), the first leg inverter current (I_{in1}), output voltage, and output current are measured and the results are shown in Fig. 6-28 (a). It can be seen that the inverter current has a small lagging phase angle relative to the inverter voltage which satisfies the ZVS condition for the inverter switches.

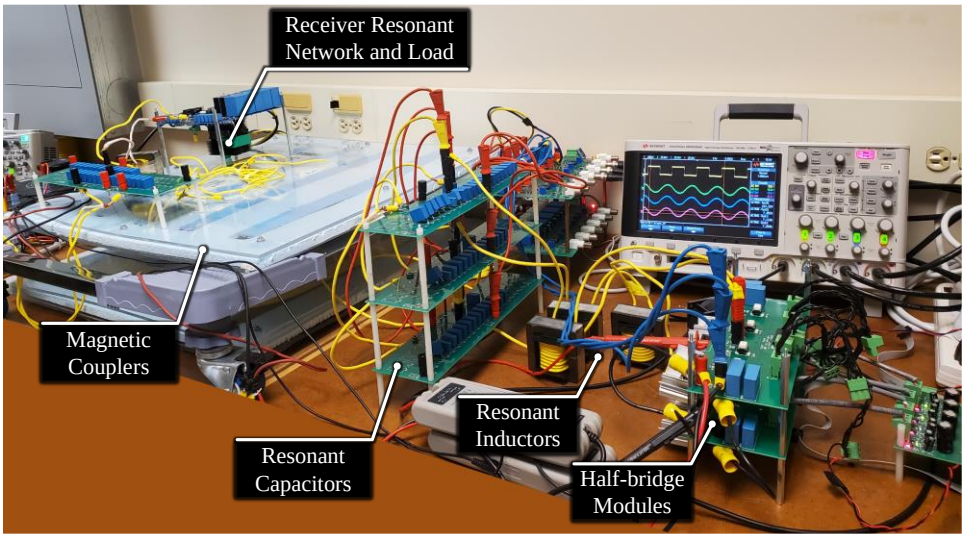

Fig. 6-27. Structure of the proposed modular LCC-based wireless charging system.

In Fig. 6-28 (b), the first leg inverter voltage (I_{in1}), and the inverter output currents (I_{in1}, I_{in2}, I_{in3}) are shown. It can be seen that the currents are balanced and there is no phase difference between them at normal operating conditions. The primary side coil current (I_p), and the output currents of the LCC modules (I_{p1}, I_{p2}, I_{p3}) are shown in Fig. 6-28 (c). It can be seen that I_p is the sum of the modules currents as expected. Moreover, it can be seen that the currents are balanced and their amplitude and phase angles are equal.

In the next step, the current sharing of the modular system is studied. When the LCC modules are identical, the inverter currents are balanced without any phase difference as shown in Fig. 6-29 (a). In the normal condition, the RMS value of the inverter currents is around 4.2 A. To study the component tolerance effect

on the modules current sharing, a 42% error for the value of the first module capacitor is considered, C_{f1}=1.42×C_f. Although in practice the component tolerance is around 10%, in this experiment a 42% error is considered to magnify the component tolerance effect in the experimental waveforms.

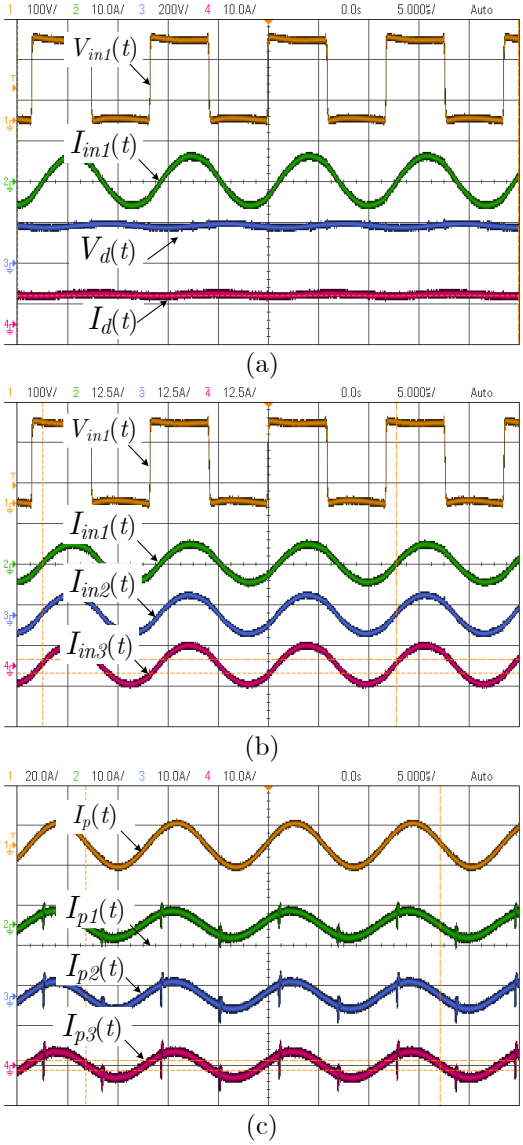

Fig. 6-28. Normal operation of the proposed modular wireless charging system: (a) Input and output waveforms (b) Inverter voltage and input currents of the LCC modules (c) output currents of the LCC modules and the primary side coil current.

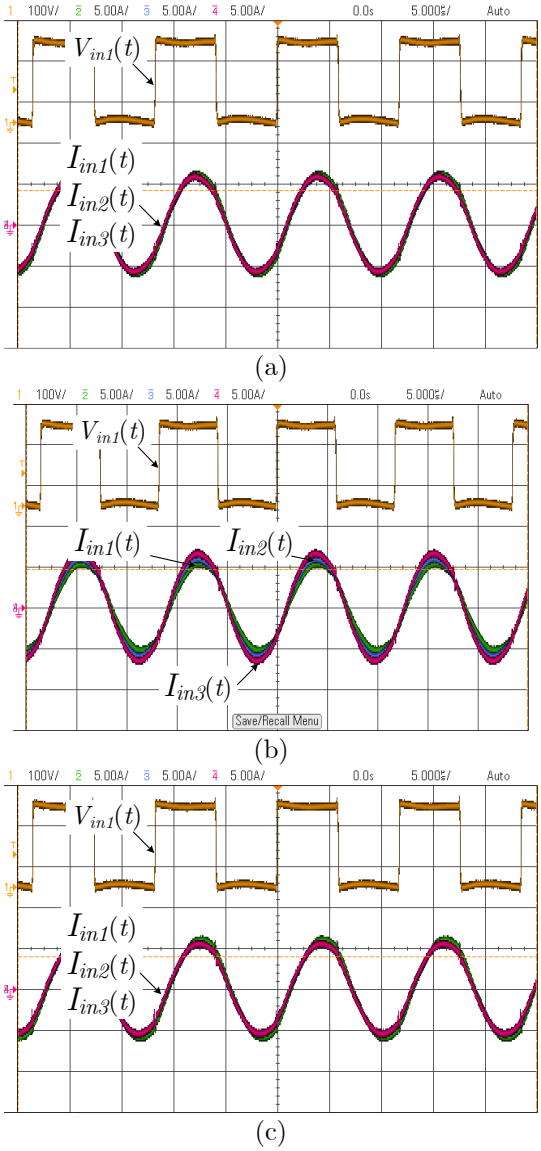

Fig. 6-29. Operation of the proposed modular wireless charging system under: (a) Normal condition (b) 42% tolerance of C_{f1} (c) passive current sharing.

The inverter currents under unbalanced condition are shown in Fig. 6-29 (b). It can be seen that the amplitude and phase of the currents are not equal. The first module inverter current is reduced to 3.7 A and the second and third cell currents

are 4.3 A and 4.8 A, respectively. As discussed before, the component tolerance involves all the modules and unbalances the current sharing among all the modules.

Using the passive current sharing method, the inverter currents can be balanced as shown in Fig. 6-29 (c). It can be seen that there is no phase difference and a negligible amplitude difference among the module's currents. In this case, the inverter currents are 4.15 A, 4.0 A, and 4.0 A. The small difference between the currents is due to the imperfection of the other components in the experiment. It can be seen that the proposed passive current sharing method successfully balanced the current of the modules.

6.8. Conclusion

In this chapter, a new LCC-based modular resonant network is proposed for high-power wireless charging applications. The proposed system employs multiple LCC modules in parallel to build a high-power transmitter side converter. In this way, the rating of the switches and resonant elements would be lower compared to a conventional wireless charging system. Moreover, the reliability, scalability, and thermal management of the system will be improved.

The proposed modular system is analyzed and the effect of the tolerance of the resonant components on the power-sharing of the modules is studied in detail. A

passive current sharing method is used in this chapter to solve this issue. It was shown that when the systems are designed for a given power, by using the modular topologies the inverter current (switch and inductor current), the voltage of the resonant capacitor, and the energy of the resonant elements are lower compared to the conventional system. Moreover, the reactive power to the output power ratio (kVA/kW) which can be interpreted as the reflection of the physical size of the resonant elements is considered as another figure of merit to compare to a modular system with the conventional wireless charging system. It was shown that by increasing the total rated power, the modular topologies have superior performance.

The normal operation and component tolerance effect on the current sharing is studied through a time-domain simulation study. It was shown that the primary side coil current is the sum of the LCC modules output currents as expected. Moreover, the passive current sharing method successfully surpassed the unbalancing of the modules' power-sharing.

Chapter 7

Conclusions and Future Work

7.1. Conclusions

This thesis is focused on the analysis, design, optimization, and implementation of novel magnetic structures and converter topologies for wireless charging applications. The outcome of this thesis is a high-power cost-effective wireless charging system with improved power density.

At first, the fundamentals of the wireless charging system were introduced. Different types of wireless charging systems and key features of each type were described. A review of different components of the wireless charging system was

presented. Inverter topologies and high-power application requirements were studied. The advantages and disadvantages of each resonant topology are outlined in detail and practical design considerations were presented. It was shown that rectangular and circular magnetic structures are suitable for stationary charging applications due to higher power density, lower loss, and lower cost. Finally, different types of control methods based on the converter architecture are described.

A comprehensive analysis of common resonant networks used in wireless charging was presented. Loss modeling and efficiency calculations for each topology described in detail. Besides the efficiency, sensitivity function with respect to the misalignment of the magnetic couplers is derived for each resonant topology. A new optimization procedure for tuning the resonant network was proposed and four resonant topologies were optimally designed for maximum efficiency and minimum voltage variation respect with to the misalignment of the magnetic couplers. Among the different resonant topologies, LCC-LCC presented the best performance in terms of output voltage variation (4.7%) for the wide range of coupling factors between 0.18 to 0.32. However, the number of components and their values in the LCC-LCC topology are higher than the other topologies. The next best candidate considering the number of components is LCC-Series with 5.3% output voltage fluctuation in the desired misalignment range. Moreover, the average efficiency of

LCC-Series was slightly lower than LCC-LCC. Therefore, taking the volume and weight of the design (power density) into account, especially in EV applications, LCC-Series can be considered as the best candidate with the least output voltage sensitivity and good average efficiency over a wide range of coupling factor variations.

A new integrated magnetic structure was proposed to save ferrite material and increase the power density of the converter. At first, partial integration of the DC-DC inductor into the vehicle side main wireless charging magnetic coupler was analyzed. The loss modeling and efficiency calculations were presented in detail. It was shown that by appropriate design of the integrated coil, the parasitic effect, and cross-coupling can be minimized. Similarly, the resonant inductor of the transmitter converter is integrated with the transmitter side main wireless charging magnetic coupler. It was shown that unwanted magnetic coupling between the integrated coils could affect the system performance. Therefore, a two-level optimization was proposed to minimize the cross-couplings and select the best magnetic structure and tune the resonant network accordingly. Moreover, the core and conduction losses of the magnetic coupler, inverter, and diode-bridge losses, and resonant capacitor losses are included in the resonant network optimization. The optimization problem picks the best optimized magnetic structure based on

the design requirements and cross-couplings and finds the best values for the resonant capacitors.

An efficient PCB-based wireless charging magnetic coupler was also introduced to replace the Litz wire. This approach results in improving the power density, simplification of the fabrication, and cost reduction. In order to compete with a conventional Litz wire design, the proposed PCB-based magnetic coupler is designed to show a low AC resistance. At first, 2D-FEA studies were presented to evaluate the effect of different design parameters such as track width, copper cross-section, etc. It was shown that there exists an optimal copper cross-section that the AC resistance is minimized. Moreover, it was shown that ferrite material does not have a meaningful effect on the AC resistance. The layer thickness showed a significant effect on the coil AC resistance. Considering these conclusions from 2D studies, the search for the 3D design was limited to feasible designs. An optimal integrated PCB-based magnetic design considering practical aspects was selected. Thermal analysis showed that the proposed PCB-based magnetic coupler can operate safely with a considerable margin. It was shown that the proposed design reduced the volume by around 50% while presenting a competitive efficiency profile compared to a conventional magnetic coupler made by Litz wire.

To overcome the issues with high-power wireless charging, a new modular inverter based on the LCC resonant network was proposed. The proposed system eliminates the requirement of bulky ICTs on the transmitter side. At first, an analytical model of the system for a generalized system was presented. In the next step current sharing between the modules due to resonant network elements tolerance was analyzed. A simple passive current sharing method was used to solve the current sharing issue. In order to design a high-power modular wireless charging system, two steps were considered. First, the module power rating was selected according to the kVA/kW ratio to maximize the power density. It was shown that the primary side coil current will scale up linearly as the number of the modules increases. Second, the number of modules is selected according to the system efficiency versus the output power. Time-domain simulation results were presented to verify the operation of the proposed modular topology. It was shown that the primary side coil current is the sum of the LCC modules output currents as expected. Moreover, the passive current sharing method successfully surpassed the unbalancing of the modules' power-sharing.

7.2. Future Work

Regarding the future work on wireless charging for EV application, the following improvements are suggested:

In Chapter 3, a new optimization procedure for designing the resonant network of the wireless system was proposed. Although the optimization guarantees the best resonant elements for different loading and misalignment conditions, magnetic structure optimization was not included. Including the optimization of the magnetic couplers into the resonant network design can result in finding the global maximum efficiency of the system for given output power and misalignment range. Moreover, other practical design objectives such as converter weight, cost, and power density can be added to the optimization problem.

The integration of the DC-DC inductor and resonant inductor into the main wireless charging system was presented in Chapter 4. It was shown that the power density of the system can be improved, and implementation cost reduced by a considerable margin. However, the size of the DC-DC inductor was limited to the available space in the middle of the coil. Therefore, the achievable inductance value is restricted to a limited range. Proposing a new integrated magnetic structure that can offer larger inductance values and mitigate the cross-coupling effect while

offering a high-efficiency profile can be considered as an improvement of the proposed magnetic integration in this thesis.

In direct continuation of the presented work in Chapter 5 on the PCB-based magnetic coupler, the pickup converter including the DC-DC converter can be integrated with the PCB of the wireless charging coils. In this way, the cable connecting the integrated coils to the converter will be eliminated and will reduce EMI issues and conductive losses. Moreover, by using wide-bandgap devices such as GaN the size of the converter can be further reduced. Additionally, larger PCB-based magnetic couplers can be considered to increase the power level and efficiency. For instance, instead of a single-phase PCB-based magnetic coupler, multi-phase structures can be used. The final design would be a high-power magnetic coupler with integrated DC-DC inductors and a DC-DC converter mounted on the same PCB that improves the power density significantly.

In Chapter 6, a new modular LCC-based resonant network was proposed for high-power applications. Although the proposed configuration solves the issues regarding the inverter and resonant network, other improvements can be considered. For instance, the front-end AC-DC converter topology can be further modified for this high-power application. Moreover, the magnetic coupler can be improved by using multi-phase structures that are suitable for high-power

applications. The pickup converter topology including the DC-DC converter can be further improved by introducing new topologies.

References

[1] (2020). *National Aeronautics and Space Administration (NASA).* Available: https://climate.nasa.gov/causes/

[2] (2020). *Global EV Outlook.* Available: https://webstore.iea.org/download/direct/3007

[3] W. Liu, *Hybrid electric vehicle system modeling and control.* John Wiley & Sons, 2017.

[4] H. Tu, H. Feng, S. Srdic, and S. Lukic, "Extreme Fast Charging of Electric Vehicles: A Technology Overview," *IEEE Transactions on Transportation Electrification,* vol. 5, no. 4, pp. 861-878, 2019.

[5] I. Aghabali, J. Bauman, P. Kollmeyer, Y. Wang, B. Bilgin, and A. Emadi, "800V Electric Vehicle Powertrains: Review and Analysis of Benefits, Challenges, and Future Trends," *IEEE Transactions on Transportation Electrification,* pp. 1-1, 2020.

[6] C. Urmson and W. Whittaker, "Self-Driving Cars and the Urban Challenge," *IEEE Intelligent Systems,* vol. 23, no. 2, pp. 66-68, 2008.

[7] S. Kuutti, R. Bowden, Y. Jin, P. Barber, and S. Fallah, "A Survey of Deep Learning Applications to Autonomous Vehicle Control," *IEEE Transactions on Intelligent Transportation Systems,* vol. 22, no. 2, pp. 712-733, 2021.

[8] J. J. Q. Yu and A. Y. S. Lam, "Autonomous Vehicle Logistic System: Joint Routing and Charging Strategy," *IEEE Transactions on Intelligent Transportation Systems,* vol. 19, no. 7, pp. 2175-2187, 2018.

[9] A. A. S. Mohamed, L. Zhu, A. Meintz, and E. Wood, "Planning Optimization for Inductively Charged On-Demand Automated Electric Shuttles Project at Greenville, South Carolina," *IEEE Transactions on Industry Applications,* vol. 56, no. 2, pp. 1010-1020, 2020.

[10] A. Khaligh and M. D. Antonio, "Global Trends in High-Power On-Board Chargers for Electric Vehicles," *IEEE Transactions on Vehicular Technology,* vol. 68, no. 4, pp. 3306-3324, 2019.

[11] D. Patil, M. K. McDonough, J. M. Miller, B. Fahimi, and P. T. Balsara, "Wireless Power Transfer for Vehicular Applications: Overview and Challenges," *IEEE Transactions on Transportation Electrification,* vol. 4, no. 1, pp. 3-37, 2018.

[12] A. A. S. Mohamed, C. R. Lashway, and O. Mohammed, "Modeling and Feasibility Analysis of Quasi-Dynamic WPT System for EV Applications," *IEEE Transactions on Transportation Electrification,* vol. 3, no. 2, pp. 343-353, 2017.

[13] A. A. S. Mohamed, A. A. Shaier, H. Metwally, and S. I. Selem, "A comprehensive overview of inductive pad in electric vehicles stationary charging," *Applied Energy,* vol. 262, p. 114584, 2020/03/15/ 2020.

[14] Z. Zhang, H. Pang, A. Georgiadis, and C. Cecati, "Wireless Power Transfer—An Overview," *IEEE Transactions on Industrial Electronics,* vol. 66, no. 2, pp. 1044-1058, 2019.

[15] A. Calabro, B. Cohen, A. Daga, J. Miller, and F. McMahon, "Performance of 200-kW Inductive Charging System for Range Extension of Electric Transit Buses," in *2019 IEEE Transportation Electrification Conference and Expo (ITEC)*, 2019, pp. 1-5.

[16] A. Ahmad, M. S. Alam, and R. Chabaan, "A Comprehensive Review of Wireless Charging Technologies for Electric Vehicles," *IEEE Transactions on Transportation Electrification,* vol. 4, no. 1, pp. 38-63, 2018.

[17] M. G. L. Roes, J. L. Duarte, M. A. M. Hendrix, and E. A. Lomonova, "Acoustic Energy Transfer: A Review," *IEEE Transactions on Industrial Electronics,* vol. 60, no. 1, pp. 242-248, 2013.

[18] H. Feng, R. Tavakoli, Z. Pantic, and O. C. Onar, "Advances in High-Power Wireless Charging Systems: Overview and Design Considerations," *IEEE Transactions on Transportation Electrification,* pp. 1-1, 2020.

[19] A. Kurs, A. Karalis, R. Moffatt, J. D. Joannopoulos, P. Fisher, and M. Soljačić, "Wireless Power Transfer via Strongly Coupled Magnetic Resonances," *Science,* vol. 317, no. 5834, pp. 83-86, 2007.

[20] S. L. Ho, W. Junhua, W. N. Fu, and S. Mingui, "A Comparative Study Between Novel Witricity and Traditional Inductive Magnetic Coupling in Wireless Charging," *Magnetics, IEEE Transactions on,* vol. 47, no. 5, pp. 1522-1525, 2011.

[21] A. Ramezani, S. Farhangi, H. Iman-Eini, and B. Farhangi, "High efficiency wireless power transfer system design for circular magnetic structures," in *2016 7th Power Electronics and Drive Systems Technologies Conference (PEDSTC)*, 2016, pp. 565-570.

[22] H. H. Wu, A. Gilchrist, K. D. Sealy, and D. Bronson, "A high efficiency 5 kW inductive charger for EVs using dual side control," *Industrial Informatics, IEEE Transactions on,* vol. 8, no. 3, pp. 585-595, 2012.

[23] B. Esteban, M. Sid-Ahmed, and N. C. Kar, "A Comparative Study of Power Supply Architectures in Wireless EV Charging Systems," *Power Electronics, IEEE Transactions on,* vol. 30, no. 11, pp. 6408-6422, 2015.

[24] S. Li and C. C. Mi, "Wireless power transfer for electric vehicle applications," *Emerging and Selected Topics in Power Electronics, IEEE Journal of,* vol. 3, no. 1, pp. 4-17, 2015.

[25] A. Berger, M. Agostinelli, S. Vesti, J. Oliver, J. Cobos, and M. Huemer, "A Wireless Charging System Applying Phase-Shift and Amplitude Control to Maximize Efficiency and Extracted Power," *IEEE Transactions on Power Electronics,* vol. 30, no. 11, pp. 6338-6348, 2015.

[26] M. K. Kazimierczuk and D. Czarkowski, *Resonant power converters*. John Wiley & Sons, 2012.

[27] S. Kim *et al.*, "Thermal Evaluation of an Inductive Power Transfer Pad for Charging Electric Vehicles," *IEEE Transactions on Industrial Electronics,* pp. 1-1, 2021.

[28] Y. Li, J. Hu, F. Chen, Z. Li, Z. He, and R. Mai, "Dual-Phase-Shift Control Scheme With Current-Stress and Efficiency Optimization for Wireless Power Transfer Systems," *IEEE Transactions on Circuits and Systems I: Regular Papers,* vol. 65, no. 9, pp. 3110-3121, 2018.

[29] J. Liu, K. W. Chan, C. Y. Chung, N. H. L. Chan, M. Liu, and W. Xu, "Single-Stage Wireless-Power-Transfer Resonant Converter with Boost Bridgeless Power-Factor-Correction Rectifier," *IEEE Transactions on Industrial Electronics,* vol. PP, no. 99, pp. 1-1, 2017.

[30] A. Ramezani and M. Narimani, "Optimized Electric Vehicle Wireless Chargers with Reduced Output Voltage Sensitivity to Misalignment," *IEEE Journal of Emerging and Selected Topics in Power Electronics,* pp. 1-1, 2019.

[31] W. Liu, K. T. Chau, C. H. T. Lee, W. Han, X. Tian, and W. H. Lam, "Full-Range Soft-Switching Pulse Frequency Modulated Wireless Power Transfer," *IEEE Transactions on Power Electronics,* pp. 1-1, 2019.

[32] S. Huang, T. Lee, W. Li, and R. Chen, "Modular On-Road AGV Wireless Charging Systems Via Interoperable Power Adjustment," *IEEE Transactions on Industrial Electronics,* vol. 66, no. 8, pp. 5918-5928, 2019.

[33] P. S. Huynh and S. S. Williamson, " Analysis and Design of Soft-Switching Active-Clamping Half-Bridge Boost Inverter for Inductive Wireless Charging Applications " *IEEE Transactions on Transportation Electrification,* vol. 5, no. 4, pp. 1027-1039, 2019.

[34] A. Namadmalan, "Self-Oscillating Pulse Width Modulation for Inductive Power Transfer Systems," *IEEE Journal of Emerging and Selected Topics in Power Electronics,* pp. 1-1, 2019.

[35] R. Mai, Z. Yan, Y. Chen, S. Liu, and Z. He, "A Hybrid Transmitter Based Efficiency Improvement Controller with Full-Bridge Dual Resonant Tank for Misalignment Condition," *IEEE Transactions on Power Electronics,* pp. 1-1, 2019.

[36] J. L. Villa, J. Sallan, J. F. S. Osorio, and A. Llombart, "High-Misalignment Tolerant Compensation Topology For ICPT Systems," *IEEE Transactions on Industrial Electronics,* vol. 59, no. 2, pp. 945-951, 2012.

[37] Y. Wang, Y. Yao, X. Liu, and D. Xu, "S/CLC Compensation Topology Analysis and Circular Coil Design for Wireless Power Transfer," *IEEE Transactions on Transportation Electrification,* vol. 3, no. 2, pp. 496-507, 2017.

[38] W. Li, H. Zhao, J. Deng, S. Li, and C. C. Mi, "Comparison Study on SS and Double-Sided LCC Compensation Topologies for EV/PHEV Wireless Chargers," *IEEE Transactions on Vehicular Technology,* vol. 65, no. 6, pp. 4429-4439, 2016.

[39] B. Wang, A. P. Hu, and D. Budgett, "Maintaining middle zero voltage switching operation of parallel-parallel tuned wireless power transfer system under bifurcation," *IET Power Electronics,* vol. 7, no. 1, pp. 78-84, 2014.

[40] H. Feng, T. Cai, S. Duan, J. Zhao, X. Zhang, and C. Chen, "An LCC-Compensated Resonant Converter Optimized for Robust Reaction to Large Coupling Variation in Dynamic Wireless Power Transfer," *IEEE Transactions on Industrial Electronics,* vol. 63, no. 10, pp. 6591-6601, 2016.

[41] M. Borage, S. Tiwari, and S. Kotaiah, "Analysis and design of an LCL-T resonant converter as a constant-current power supply," *IEEE Transactions on Industrial Electronics,* vol. 52, no. 6, pp. 1547-1554, 2005.

[42] W. Chwei-Sen, G. A. Covic, and O. H. Stielau, "Investigating an LCL load resonant inverter for inductive power transfer applications," *Power Electronics, IEEE Transactions on,* vol. 19, no. 4, pp. 995-1002, 2004.

[43] J. Zhang *et al.*, "Total Harmonic Distortion and Output Current Optimization Method of Inductive Power Transfer System for Power Loss Reduction," *IEEE Access,* vol. 8, pp. 4724-4736, 2020.

[44] D. Shen, G. Du, W. Zeng, Z. Yang, and J. Li, "Research on Optimization of Compensation Topology Parameters for a Wireless Power Transmission System with Wide Coupling Coefficient Fluctuation," *IEEE Access,* pp. 1-1, 2020.

[45] S. Chen *et al.*, "An Operation Mode Selection Method of Dual-side Bridge Converters for Efficiency Optimization in Inductive Power Transfer," *IEEE Transactions on Power Electronics,* pp. 1-1, 2020.

[46] Y. Li *et al.*, "Efficiency Analysis and Optimization Control for Input-Parallel Output-Series Wireless Power Transfer Systems," *IEEE Transactions on Power Electronics,* vol. 35, no. 1, pp. 1074-1085, 2020.

[47] L. Yang, X. Li, S. Liu, Z. Xu, and C. Cai, "Analysis and Design of an LCCC/S Compensated WPT System with Constant Output Characteristics for Battery Charging Applications," *IEEE Journal of Emerging and Selected Topics in Power Electronics,* pp. 1-1, 2020.

[48] W. Zhang and C. C. Mi, "Compensation Topologies of High-Power Wireless Power Transfer Systems," *IEEE Transactions on Vehicular Technology,* vol. 65, no. 6, pp. 4768-4778, 2016.

[49] B. V. Vu, V. Phan, M. Dahidah, and V. Pickert, "Multiple Output Inductive Charger for Electric Vehicles," *IEEE Transactions on Power Electronics,* pp. 1-1, 2018.

[50] Y. Chen, H. Zhang, C. Shin, C. Jo, S. Park, and D. Kim, "An Efficiency Optimization-Based Asymmetric Tuning Method of Double-Sided LCC Compensated WPT System for Electric Vehicles," *IEEE Transactions on Power Electronics,* pp. 1-1, 2020.

[51] X. Zhang, Y. Zhang, Z. Zhang, and M. Li, "Mode Conversion and Structure Optimization of Quadrature Coils for Electric Vehicles Wireless Power Transfer," *IEEE Transactions on Energy Conversion,* pp. 1-1, 2020.

[52] G. Yang *et al.*, "Interoperability Improvement for Wireless Electric Vehicle Charging System Using Adaptive Phase-Control Transmitter," *IEEE Access,* pp. 1-1, 2019.

[53] Y. Guo, L. Wang, Y. Zhang, S. Li, and C. Liao, "Rectifier Load Analysis for Electric Vehicle Wireless Charging System," *IEEE Transactions on Industrial Electronics,* vol. 65, no. 9, pp. 6970-6982, 2018.

[54] V. Vu, D. Tran, and W. Choi, "Implementation of the Constant Current and Constant Voltage Charge of Inductive Power Transfer Systems With the Double-Sided LCC Compensation Topology for Electric Vehicle Battery Charge Applications," *IEEE Transactions on Power Electronics,* vol. 33, no. 9, pp. 7398-7410, 2018.

[55] A. Ramezani, S. Farhangi, H. Iman-Eini, B. Farhangi, R. Rahimi, and G. R. Moradi, "Optimized LCC-Series Compensated Resonant Network for Stationary Wireless EV Chargers," *IEEE Transactions on Industrial Electronics,* vol. 66, no. 4, pp. 2756-2765, 2018.

[56] S. Y. R. Hui, Z. Wenxing, and C. K. Lee, "A Critical Review of Recent Progress in Mid-Range Wireless Power Transfer," *Power Electronics, IEEE Transactions on,* vol. 29, no. 9, pp. 4500-4511, 2014.

[57] G. Covic and J. T. Boys, "Inductive power transfer," *Proceedings of the IEEE,* vol. 101, no. 6, pp. 1276-1289, 2013.

[58] M. Bartoli, N. Noferi, A. Reatti, and M. K. Kazimierczuk, "Modeling Litz-wire winding losses in high-frequency power inductors," in *PESC Record. 27th Annual IEEE Power Electronics Specialists Conference*, 1996, vol. 2, pp. 1690-1696 vol.2.

[59] P. L. Dowell, "Effects of eddy currents in transformer windings," *Electrical Engineers, Proceedings of the Institution of,* vol. 113, no. 8, pp. 1387-1394, 1966.

[60] R. P. Wojda and M. K. Kazimierczuk, "Winding resistance of litz-wire and multi-strand inductors," *IET Power Electronics,* vol. 5, no. 2, pp. 257-268, 2012.

[61] A. Reatti and M. K. Kazimierczuk, "Comparison of various methods for calculating the AC resistance of inductors," *IEEE Transactions on Magnetics,* vol. 38, no. 3, pp. 1512-1518, 2002.

[62] C. R. Sullivan, "Optimal choice for number of strands in a litz-wire transformer winding," *IEEE Transactions on Power Electronics,* vol. 14, no. 2, pp. 283-291, 1999.

[63] S. Wang and D. Dorrell, "Copper Loss Analysis of EV Charging Coupler," *Magnetics, IEEE Transactions on,* vol. PP, no. 99, pp. 1-1, 2015.

[64] R. Bosshard *et al.*, "Modeling and η-α Pareto Optimization of Inductive Power Transfer Coils for Electric Vehicles," *IEEE Journal of Emerging and Selected Topics in Power Electronics,* vol. 3, no. 1, pp. 50-64, 2015.

[65] J. Kim *et al.*, "Coil Design and Shielding Methods for a Magnetic Resonant Wireless Power Transfer System," *Proceedings of the IEEE,* vol. 101, no. 6, pp. 1332-1342, 2013.

[66] S. Cruciani, T. Campi, F. Maradei, and M. Feliziani, "Active Shielding Design for Wireless Power Transfer Systems," *IEEE Transactions on Electromagnetic Compatibility,* vol. 61, no. 6, pp. 1953-1960, 2019.

[67] M. Budhia, G. A. Covic, and J. T. Boys, "Design and Optimization of Circular Magnetic Structures for Lumped Inductive Power Transfer Systems," *IEEE Transactions on Power Electronics,* vol. 26, no. 11, pp. 3096-3108, 2011.

[68] Z. Bi, T. Kan, C. C. Mi, Y. Zhang, Z. Zhao, and G. A. Keoleian, "A review of wireless power transfer for electric vehicles: Prospects to enhance sustainable mobility," *Applied Energy,* vol. 179, pp. 413-425, 2016.

[69] R. Bosshard and J. W. Kolar, "All-SiC 9.5 kW/dm3 On-Board Power Electronics for 50 kW/85 kHz Automotive IPT System," *IEEE Journal of Emerging and Selected Topics in Power Electronics,* vol. 5, no. 1, pp. 419-431, 2017.

[70] G. Rituraj, B. K. Kushwaha, and P. Kumar, "A Unipolar Coil Arrangement Method for Improving the Coupling Coefficient Without Ferrite Material in Wireless Power Transfer Systems," *IEEE Transactions on Transportation Electrification,* vol. 6, no. 2, pp. 497-509, 2020.

[71] J. Pries, V. P. Galigekere, O. C. Onar, and G. Su, "A 50kW Three–Phase Wireless Power Transfer System using Bipolar Windings and Series Resonant Networks for Rotating Magnetic Fields," *IEEE Transactions on Power Electronics,* pp. 1-1, 2019.

[72] W. Liu, K. T. Chau, C. H. T. Lee, C. Jiang, W. Han, and W. H. Lam, "Wireless Energy-On-Demand Using Magnetic Quasi-Resonant Coupling," *IEEE Transactions on Power Electronics,* vol. 35, no. 9, pp. 9057-9069, 2020.

[73] S. Kim, G. A. Covic, and J. T. Boys, "Tripolar pad for inductive power transfer systems for EV charging," *IEEE Transactions on Power Electronics,* vol. 32, no. 7, pp. 5045-5057, 2017.

[74] R. Bosshard, U. Iruretagoyena, and J. W. Kolar, "Comprehensive Evaluation of Rectangular and Double-D Coil Geometry for 50 kW/85 kHz IPT System," *IEEE Journal of Emerging and Selected Topics in Power Electronics,* vol. 4, no. 4, pp. 1406-1415, 2016.

[75] R. Bosshard, J. Muhlethaler, J. W. Kolar, and I. Stevanovic, "Optimized magnetic design for inductive power transfer coils," in *Applied Power Electronics Conference and Exposition (APEC), 2013 Twenty-Eighth Annual IEEE*, 2013, pp. 1812-1819.

[76] W. Choi, W. Ho, X. Liu, and S. Hui, "Comparative study on power conversion methods for wireless battery charging platform," in *Power Electronics and Motion Control Conference (EPE/PEMC), 2010 14th International*, 2010, pp. S15-9-S15-16: IEEE.

[77] R. L. Steigerwald, "A comparison of half-bridge resonant converter topologies," *IEEE Transactions on Power Electronics,* vol. 3, no. 2, pp. 174-182, 1988.

[78] N. Mohan, T. M. Undeland, and W. P. Robbins, *Power electronics: converters, applications, and design*. John wiley & sons, 2003.

[79] K. Colak, E. Asa, M. Bojarski, D. Czarkowski, and O. C. Onar, "A Novel Phase-Shift Control of Semibridgeless Active Rectifier for Wireless Power Transfer," *IEEE Transactions on Power Electronics,* vol. 30, no. 11, pp. 6288-6297, 2015.

[80] M. Fan, L. Shi, Z. Yin, F. Zhang, and L. Jiang, "Improved Pulse Density Modulation for Semi-bridgeless Active Rectifier in Inductive Power Transfer System," *IEEE Transactions on Power Electronics,* pp. 1-1, 2018.

[81] T. Diekhans and R. W. De Doncker, "A Dual-Side Controlled Inductive Power Transfer System Optimized for Large Coupling Factor Variations and Partial Load," *Power Electronics, IEEE Transactions on,* vol. 30, no. 11, pp. 6320-6328, 2015.

[82] A. K. Swain, M. J. Neath, U. K. Madawala, and D. J. Thrimawithana, "A Dynamic Multivariable State-Space Model for Bidirectional Inductive Power Transfer Systems," *Power Electronics, IEEE Transactions on,* vol. 27, no. 11, pp. 4772-4780, 2012.

[83] L. Grajales, J. A. Sabate, K. R. Wang, W. A. Tabisz, and F. C. Lee, "Design of a 10 kW, 500 kHz phase-shift controlled series-resonant inverter for induction heating," in *Conference Record of the 1993 IEEE Industry Applications Conference Twenty-Eighth IAS Annual Meeting*, 1993, pp. 843-849 vol.2.

[84] B. Esteban, M. Sid-Ahmed, and N. C. Kar, "A Comparative Study of Power Supply Architectures in Wireless EV Charging Systems," *IEEE Transactions on Power Electronics,* vol. 30, no. 11, pp. 6408-6422, 2015.

[85] A. Azad, A. Echols, V. Kulyukin, R. Zane, and Z. Pantic, "Analysis, Optimization, and Demonstration of a Vehicular Detection System Intended for Dynamic Wireless Charging Applications," *IEEE Transactions on Transportation Electrification,* pp. 147-161, 2018.

[86] I. Iam *et al.*, "Constant-Frequency and Non-Communication-Based Inductive Power Transfer Converter for Battery Charging," *IEEE Journal of Emerging and Selected Topics in Power Electronics,* pp. 1-1, 2020.

[87] R. Mai, Y. Liu, Y. Li, P. Yue, G. Cao, and Z. He, "An Active-Rectifier-Based Maximum Efficiency Tracking Method Using an Additional Measurement Coil for Wireless Power Transfer," *IEEE Transactions on Power Electronics,* vol. 33, no. 1, pp. 716-728, 2018.

[88] W. Zhong and S. Y. R. Hui, "Charging Time Control of Wireless Power Transfer Systems Without Using Mutual Coupling Information and Wireless Communication System," *IEEE Transactions on Industrial Electronics,* vol. 64, no. 1, pp. 228-235, 2017.

[89] Y. Yang, W. Zhong, S. Kiratipongvoot, S.-C. Tan, and S. R. Hui, "Dynamic Improvement of Series-Series Compensated Wireless Power Transfer Systems Using Discrete Sliding Mode Control," *IEEE Transactions on Power Electronics,* 2017.

[90] H. Li, K. Wang, J. Fang, and Y. Tang, "Pulse Density Modulated ZVS Full-Bridge Converters for Wireless Power Transfer Systems," *IEEE Transactions on Power Electronics,* pp. 1-1, 2018.

[91] Z. Cong, M. Hongbo, L. Jih-sheng, and Z. Lanhua, "Design Considerations to Reduce Gap Variation and Misalignment Effects for the Inductive Power Transfer

System," *Power Electronics, IEEE Transactions on,* vol. 30, no. 11, pp. 6108-6119, 2015.

[92] L. Zhao, D. J. Thrimawithana, U. K. Madawala, P. Hu, and C. C. Mi, "A Misalignment Tolerant Series-hybrid Wireless EV Charging System with Integrated Magnetics," *IEEE Transactions on Power Electronics,* pp. 1-1, 2018.

[93] Y. Chen, Z. Kou, Y. Zhang, Z. He, R. Mai, and G. Cao, "Hybrid Topology With Configurable Charge Current and Charge Voltage Output-Based WPT Charger for Massive Electric Bicycles," *IEEE Journal of Emerging and Selected Topics in Power Electronics,* vol. 6, no. 3, pp. 1581-1594, 2018.

[94] X. Dai, X. Li, Y. Li, and A. P. Hu, "Maximum Efficiency Tracking for Wireless Power Transfer Systems With Dynamic Coupling Coefficient Estimation," *IEEE Transactions on Power Electronics,* vol. 33, no. 6, pp. 5005-5015, 2018.

[95] I. Karakitsios, F. Palaiogiannis, A. Markou, and N. D. Hatziargyriou, "Optimizing the Energy Transfer, With a High System Efficiency in Dynamic Inductive Charging of EVs," *IEEE Transactions on Vehicular Technology,* vol. 67, no. 6, pp. 4728-4742, 2018.

[96] W. Zhong and S. Y. R. Hui, "Maximum Energy Efficiency Operation of Series-Series Resonant Wireless Power Transfer Systems Using On-Off Keying Modulation," *IEEE Transactions on Power Electronics,* vol. 33, no. 4, pp. 3595-3603, 2018.

[97] Z. Li, K. Song, J. Jiang, and C. Zhu, "Constant Current Charging and Maximum Efficiency Tracking Control Scheme for Supercapacitor Wireless Charging," *IEEE Transactions on Power Electronics,* pp. 1-1, 2018.

[98] G. Guidi and J. A. Suul, "Minimizing Converter Requirements of Inductive Power Transfer Systems With Constant Voltage Load and Variable Coupling Conditions," *IEEE Transactions on Industrial Electronics,* vol. 63, no. 11, pp. 6835-6844, 2016.

[99] H. Feng, T. Cai, S. Duan, X. Zhang, H. Hu, and J. Niu, "A Dual-Side-Detuned Series-Series Compensated Resonant Converter for Wide Charging Region in a Wireless Power Transfer System," *IEEE Transactions on Industrial Electronics,* vol. 65, no. 3, pp. 2177-2188, 2018.

[100] R. Bosshard and J. W. Kolar, "Multi-Objective Optimization of 50 kW/85 kHz IPT System for Public Transport," *IEEE Journal of Emerging and Selected Topics in Power Electronics,* vol. 4, no. 4, pp. 1370-1382, 2016.

[101] N. Keeling, G. A. Covic, F. Hao, L. George, and J. T. Boys, "Variable tuning in LCL compensated contactless power transfer pickups," in *2009 IEEE Energy Conversion Congress and Exposition*, 2009, pp. 1826-1832.

[102] S. Aldhaher, P. C. Luk, A. Bati, and J. F. Whidborne, "Wireless Power Transfer Using Class E Inverter With Saturable DC-Feed Inductor," *IEEE Transactions on Industry Applications,* vol. 50, no. 4, pp. 2710-2718, 2014.

[103] S. Aldhaher, P. C. Luk, and J. F. Whidborne, "Electronic Tuning of Misaligned Coils in Wireless Power Transfer Systems," *IEEE Transactions on Power Electronics,* vol. 29, no. 11, pp. 5975-5982, 2014.

[104] K. A. Cota, P. A. Gray, M. Pathmanathan, and P. W. Lehn, "An Approach for Selecting Compensation Capacitances in Resonance-Based EV Wireless Power Transfer Systems With Switched Capacitors," *IEEE Transactions on Transportation Electrification,* vol. 5, no. 4, pp. 1004-1014, 2019.

[105] J. Zhao, J. Zhang, and Y. Zhu, "A Flexible Wireless Power Transfer System With Switch Controlled Capacitor," *IEEE Access,* vol. 7, pp. 106873-106881, 2019.

[106] D. Kim and D. Ahn, "Self-Tuning LCC Inverter Using PWM-Controlled Switched Capacitor for Inductive Wireless Power Transfer," *IEEE Transactions on Industrial Electronics,* vol. 66, no. 5, pp. 3983-3992, 2019.

[107] J. Zhang, J. Zhao, Y. Zhang, and F. Deng, "A Wireless Power Transfer System With Dual Switch-Controlled Capacitors for Efficiency Optimization," *IEEE Transactions on Power Electronics,* vol. 35, no. 6, pp. 6091-6101, 2020.

[108] L. Zhao, D. Thrimawithana, and U. Madawala, "A Hybrid Bi-directional Wireless EV Charging System Tolerant to Pad Misalignment," *IEEE Transactions on Industrial Electronics,* vol. PP, no. 99, pp. 1-1, 2017.

[109] R. Mai, Y. Chen, Y. Li, Y. Zhang, G. Cao, and Z. He, "Inductive Power Transfer for Massive Electric Bicycles Charging Based on Hybrid Topology Switching With a Single Inverter," *IEEE Transactions on Power Electronics,* vol. 32, no. 8, pp. 5897-5906, 2017.

[110] Y. Li, Q. Xu, T. Lin, J. Hu, Z. He, and R. Mai, "Analysis and Design of Load-Independent Output Current or Output Voltage of a Three-Coil Wireless Power Transfer System," *IEEE Transactions on Transportation Electrification,* vol. 4, no. 2, pp. 364-375, 2018.

[111] Y. Li, J. Hu, F. Chen, S. Liu, Z. Yan, and Z. He, "A New-Variable-Coil-Structure-Based IPT System With Load-Independent Constant Output Current or Voltage for Charging Electric Bicycles," *IEEE Transactions on Power Electronics,* vol. 33, no. 10, pp. 8226-8230, 2018.

[112] Y. Chen, B. Yang, Z. Kou, Z. He, G. Cao, and R. Mai, "Hybrid and Reconfigurable IPT Systems With High-Misalignment Tolerance for Constant-Current and Constant-Voltage Battery Charging," *IEEE Transactions on Power Electronics,* vol. 33, no. 10, pp. 8259-8269, 2018.

[113] J. Zhao, T. Cai, S. Duan, H. Feng, C. Chen, and X. Zhang, "A General Design Method of Primary Compensation Network for Dynamic WPT System Maintaining Stable Transmission Power," *IEEE Transactions on Power Electronics,* vol. 31, no. 12, pp. 8343-8358, 2016.

[114] Q. Zhu, Y. Guo, L. Wang, C. Liao, and F. Li, "Improving the Misalignment Tolerance of Wireless Charging System by Optimizing the Compensate Capacitor," *IEEE Transactions on Industrial Electronics,* vol. 62, no. 8, pp. 4832-4836, 2015.

[115] Y. Yao, Y. Wang, X. Liu, Y. Pei, D. G. Xu, and X. Liu, "Particle Swarm Optimization Based Parameter Design Method for S/CLC Compensated IPT Systems Featuring High Tolerance to Misalignment and Load Variation," *IEEE Transactions on Power Electronics,* pp. 1-1, 2018.

[116] Y. Wang, J. Mai, Y. Yao, and D. Xu, "Analysis and Design of an IPT System Based on S/SP Compensation with Improved Output Voltage Regulation," *IEEE Transactions on Industrial Informatics,* pp. 1-1, 2019.

[117] Y. Yao, Y. Wang, X. Liu, K. Lu, and D. Xu, "Analysis and Design of an S/SP Compensated IPT System to Minimize Output Voltage Fluctuation Versus Coupling Coefficient and Load Variation," *IEEE Transactions on Vehicular Technology,* vol. 67, no. 10, pp. 9262-9272, 2018.

[118] W. Li, H. Zhao, S. Li, J. Deng, T. Kan, and C. C. Mi, "Integrated LCC Compensation Topology for Wireless Charger in Electric and Plug-in Electric Vehicles," *IEEE Transactions on Industrial Electronics,* vol. 62, no. 7, pp. 4215-4225, 2015.

[119] T. Kan, T. Nguyen, J. C. White, R. K. Malhan, and C. C. Mi, "A New Integration Method for an Electric Vehicle Wireless Charging System Using LCC Compensation Topology: Analysis and Design," *IEEE Transactions on Power Electronics,* vol. 32, no. 2, pp. 1638-1650, 2017.

[120] N. Rasekh, J. Kavianpour, and M. Mirsalim, "A Novel Integration Method for a Bipolar Receiver Pad Using LCC Compensation Topology for Wireless Power Transfer," *IEEE Transactions on Vehicular Technology,* vol. 67, no. 8, pp. 7419-7428, 2018.

[121] F. Lu, H. Zhang, H. Hofmann, W. Su, and C. Mi, "A Dual-Coupled LCC-Compensated IPT System with a Compact Magnetic Coupler," *IEEE Transactions on Power Electronics,* vol. 33, no. 7, pp. 6391 - 6402, 2017.

[122] T. Kan, F. Lu, T. D. Nguyen, P. P. Mercier, and C. Mi, "Integrated Coil Design for EV Wireless Charging Systems Using LCC Compensation Topology," *IEEE Transactions on Power Electronics,* vol. 33, no. 11, pp. 9231-9241, 2018.

[123] D. Junjun, L. Weihan, T. D. Nguyen, L. Siqi, and C. C. Mi, "Compact and Efficient Bipolar Coupler for Wireless Power Chargers: Design and Analysis," *Power Electronics, IEEE Transactions on,* vol. 30, no. 11, pp. 6130-6140, 2015.

[124] A. R. Dekka, A. Ramezani, S. Ounie, and M. Narimani, "A New Five-Level Voltage Source Inverter: Modulation and Control," *IEEE Transactions on Industry Applications,* vol. 56, no. 5, pp. 5553-5564, 2020.

[125] A. Bahrami and M. Narimani, "A New Five-Level T-Type Nested Neutral Point Clamped (T-NNPC) Converter," *IEEE Transactions on Power Electronics,* pp. 1-1, 2019.

[126] M. Narimani, B. Wu, and N. R. Zargari, "A Novel Five-Level Voltage Source Inverter With Sinusoidal Pulse Width Modulator for Medium-Voltage Applications," *IEEE Transactions on Power Electronics,* vol. 31, no. 3, pp. 1959-1967, 2016.

[127] X. Zhang, T. C. Green, and A. Junyent-Ferré, "A New Resonant Modular Multilevel Step-Down DC–DC Converter with Inherent-Balancing," *IEEE Transactions on Power Electronics,* vol. 30, no. 1, pp. 78-88, 2015.

[128] Q. Deng, J. Liu, D. Czarkowski, W. Hu, and H. Zhou, "An Inductive Power Transfer System Supplied by a Multiphase Parallel Inverter," *IEEE Transactions on Industrial Electronics,* vol. 64, no. 9, pp. 7039-7048, 2017.

[129] Z. Zeng, X. Zhang, and Z. Zhang, "Imbalance Current Analysis and Its Suppression Methodology for Parallel SiC MOSFETs with Aid of a Differential Mode Choke," *IEEE Transactions on Industrial Electronics,* vol. 67, no. 2, pp. 1508-1519, 2020.

[130] Q. Wu, M. Wang, W. Zhou, and X. Wang, "Current Balancing of Paralleled SiC mosfets for a Resonant Pulsed Power Converter," *IEEE Transactions on Power Electronics,* vol. 35, no. 6, pp. 5557-5561, 2020.

[131] B. Wu and M. Narimani, *High-power converters and AC drives*. John Wiley & Sons, 2017.

[132] H. R. Rahnamaee, U. K. Madawala, and D. J. Thrimawithana, "A modified hybrid multi-level converter for high-power high-frequency IPT systems," in *2014 International Power Electronics and Application Conference and Exposition*, 2014, pp. 624-629.

[133] S. Piriienko, W. V. Wang, M. Neuburger, D. J. Thrimawithana, and A. Balakhontsev, "Nacelle-to-Tower Multilevel IPT System for Small-Scale Wind Turbines," *IEEE Transactions on Power Electronics,* pp. 1-1, 2020.

[134] M. Bojarski, E. Asa, K. Colak, and D. Czarkowski, "Analysis and Control of Multiphase Inductively Coupled Resonant Converter for Wireless Electric Vehicle Charger Applications," *IEEE Transactions on Transportation Electrification,* vol. 3, no. 2, pp. 312-320, 2017.

[135] M. Bojarski, E. Asa, K. Colak, and D. Czarkowski, "A 25 kW industrial prototype wireless electric vehicle charger," in *2016 IEEE Applied Power Electronics Conference and Exposition (APEC)*, 2016, pp. 1756-1761.

[136] Q. Deng, P. Sun, W. Hu, D. Czarkowski, M. K. Kazimierczuk, and H. Zhou, "Modular Parallel Multi-Inverter System for High-Power Inductive Power Transfer," *IEEE Transactions on Power Electronics,* pp. 1-1, 2019.

[137] Q. Deng *et al.*, "Modeling and Control of Inductive Power Transfer System Supplied by Multiphase Phase-Controlled Inverter," *IEEE Transactions on Power Electronics,* pp. 1-1, 2018.

[138] H. Hao, G. A. Covic, and J. T. Boys, "A Parallel Topology for Inductive Power Transfer Power Supplies," *IEEE Transactions on Power Electronics,* vol. 29, no. 3, pp. 1140-1151, 2014.

[139] S. Samanta and A. K. Rathore, "A New Inductive Power Transfer Topology Using Direct AC–AC Converter With Active Source Current Waveshaping," *IEEE Transactions on Power Electronics,* vol. 33, no. 7, pp. 5565-5577, 2018.

[140] M. Moghaddami and A. I. Sarwat, "Single-Phase Soft-Switched AC–AC Matrix Converter With Power Controller for Bidirectional Inductive Power Transfer Systems," *IEEE Transactions on Industry Applications,* vol. 54, no. 4, pp. 3760-3770, 2018.

[141] S. Weerasinghe, U. K. Madawala, and D. J. Thrimawithana, "A Matrix Converter-Based Bidirectional Contactless Grid Interface," *IEEE Transactions on Power Electronics,* vol. 32, no. 3, pp. 1755-1766, 2017.

[142] M. Moghaddami, A. Anzalchi, and A. I. Sarwat, "Single-Stage Three-Phase AC-AC Matrix Converter for Inductive Power Transfer Systems," *IEEE Transactions on Industrial Electronics,* vol. 63, no. 10, pp. 6613-6622, 2016.

[143] Z. Fang, T. Cai, S. Duan, and C. Chen, "Optimal Design Methodology for LLC Resonant Converter in Battery Charging Applications Based on Time-Weighted Average Efficiency," *IEEE Transactions on Power Electronics,* vol. 30, no. 10, pp. 5469-5483, 2015.

[144] A. Ramezani, S. Farhangi, H. Iman-Eini, B. Farhangi, R. Rahimi, and G. R. Moradi, "Optimized LCC-Series Compensated Resonant Network for Stationary Wireless EV Chargers," *IEEE Transactions on Industrial Electronics,* pp. 1-1, 2018.

[145] N. V. Sahinidis, "BARON: A general purpose global optimization software package," *Journal of Global Optimization,* journal article vol. 8, no. 2, pp. 201-205, 1996.

[146] M. Tawarmalani and N. V. Sahinidis, "A polyhedral branch-and-cut approach to global optimization," *Mathematical Programming,* vol. 103, no. 2, pp. 225-249, 2005.

[147] N. S. M. Tawarmalani, BARON User Manual v. 2019.7.13: Global Optimization of Mixed-Integer Nonlinear Programs: User's Manual, 2019. [Online]. Available.

[148] C.-S. Wang, G. Covic, and O. H. Stielau, "Power transfer capability and bifurcation phenomena of loosely coupled inductive power transfer systems," *Industrial Electronics, IEEE Transactions on,* vol. 51, no. 1, pp. 148-157, 2004.

[149] K. Aditya and S. S. Williamson, "Design Guidelines to Avoid Bifurcation in a Series–Series Compensated Inductive Power Transfer System," *IEEE Transactions on Industrial Electronics,* vol. 66, no. 5, pp. 3973-3982, 2019.

[150] M. Budhia, J. T. Boys, G. Covic, and C.-Y. Huang, "Development of a single-sided flux magnetic coupler for electric vehicle IPT charging systems," *Industrial Electronics, IEEE Transactions on,* vol. 60, no. 1, pp. 318-328, 2013.

[151] A. Ramezani and M. Narimani, "A New Wireless EV Charging System with Integrated DC-DC Magnetic Element," *IEEE Transactions on Transportation Electrification,* vol. 5, no. 4, pp. 1112-1123, 2019.

[152] T. Yilmaz, N. Hasan, R. Zane, and Z. Pantic, "Multi-Objective Optimization of Circular Magnetic Couplers for Wireless Power Transfer Applications," *IEEE Transactions on Magnetics,* vol. 53, no. 8, pp. 1-12, 2017.

[153] S. Bandyopadhyay, P. Venugopal, J. Dong, and P. Bauer, "Comparison of Magnetic Couplers for IPT-Based EV Charging Using Multi-Objective Optimization," *IEEE Transactions on Vehicular Technology,* vol. 68, no. 6, pp. 5416-5429, 2019.

[154] A. Ramezani and M. Narimani, "Optimized Electric Vehicle Wireless Chargers With Reduced Output Voltage Sensitivity to Misalignment," *IEEE Journal of Emerging and Selected Topics in Power Electronics,* vol. 8, no. 4, pp. 3569-3581, 2020.

[155] *Wireless Power Transfer for Light-Duty Plug-In/Electric Vehicles and Alignment Methodology, Standard SAEJ2954, 2020.* Available: https://www.sae.org/standards/content/j2954_202010/

[156] (2021). *Wireless Charging Unleashes Electric Vehicle Fleets.* Available: https://utilityfleetprofessional.com/departments/smart-fleets/wireless-charging-unleashes-electric-vehicle-fleets

[157] H. Wang, Y. Chen, and Y. Liu, "A Passive-Impedance-Matching Technology to Achieve Automatic Current Sharing for a Multiphase Resonant Converter," *IEEE Transactions on Power Electronics,* vol. 32, no. 12, pp. 9191-9209, 2017.